# Thermoelectric transport through quantum dots

Von der Fakultät für Mathematik, Informatik und Naturwissenschaften der RWTH Aachen University zur Erlangung des akademischen Grades eines Doktors der Naturwissenschaften genehmigte Dissertation

vorgelegt von

Dipl.-Phys. Lukas Heinrich Merker

aus Steinfurt

| | | |
|---|---|---|
| Berichter: | Dr. rer. nat. | Theo Costi |
| | Univ. Prof. Dr. rer. nat. | Volker Meden |
| | Apl. Prof. Dr. rer. nat. | Ralf Bulla |

Tag der mündlichen Prüfung: 30. Juni 2016

# Summary

In this thesis the thermoelectric properties (electrical conductance, Seebeck coefficient and thermal conductance) of quantum dots described by the Anderson impurity model have been investigated by using the numerical renormalization group (NRG) method.

In order to make accurate calculations for thermoelectric properties of quantum impurity systems, a number of recent developments and refinements of the NRG have been implemented. These include the z-averaging and Campo discretization scheme, which enable the evaluation of physical quantities on an arbitrary temperature grid and at large discretization parameter $\Lambda$ and the full density matrix (FDM) approach, which allows a more accurate calculation of spectral functions and transport coefficients.

The implementation of the z-averaging and Campo discretization scheme has been tested within a new method for specific heats of quantum impurities. The accuracy of this new method was established by comparison with the numerical solution of the Bethe-ansatz equations for the Anderson model.

The FDM approach was implemented and tested within a new approach to the calculation of impurity contributions to the uniform susceptibilities. Within this method a non-negligible contribution from the "environmental" degrees of freedom needs to be taken into account to recover the correct susceptibility, as shown by comparison with the Bethe-ansatz approach.

An accurate method to calculate the conductance of a quantum dot is implemented, enabling the extraction of the Fermi liquid scaling coefficients $c_T$ and $c_B$ to high accuracy, being able to verify the results of the renormalized super perturbation theory approach (within its regime of validity). The method was generalized to higher order moments of the local level spectral function. This, as well as reduction of the $SU(2)$ code to the $U(1)$ symmetry, enabled the investigation of the effect of a magnetic field on the thermoelectric properties of quantum dots. Furthermore the model could be used to qualitatively describe and predict the behavior of the thermopower of $CeCu_{6-x}Au_x$ in a magnetic field.

Motivated by the large thermopower realized in a negative-U Anderson model, a generalized Anderson impurity model with screening to the leads was introduced and investigated with the NRG. A two-channel NRG code

needed to be developed, since the decoupling of the odd parity channel is no longer valid in the presence of a screening term. Sufficiently large screening terms can make the Coulomb interaction negative (at particle-hole symmetry), thereby enhancing the thermopower by the negative-U effect. Experimentally, screening interactions are always expected to be present and may be particularly important in molecular quantum dots, where the leads are metallic. We showed the effect of the conductance electron screening term at $T = 0$ on the conductance and on the local occupation number as well as the charge and spin susceptibility. These results verify functional renormalization group results for these quantities within their range of validity, i.e. for small Coulomb interactions and screening interactions, but go beyond these since they allow investigating quantitatively also in the non perturbative limit. It is shown that for strong screening interaction (relative to the local Coulomb repulsion) the physics is consistent (at particle-hole symmetry) with a charge Kondo effect.

*Ich widme diese Arbeit meinem Sohn Eduard, der vor zwei Jahren das Licht der Welt erblickt hat.*

# Danksagung

Ich möchte einer Reihe von Leuten danken ohne die diese Arbeit nicht möglich gewesen wäre: Dr. Theo Costi, der meine Promotionsarbeit betreut hat, Professor David DiVincenco, der mich in das Jülicher Institut aufgenommen hat, Andreas Weichselbaum und Stefan Kirchner und Enrique Muñoz für die wissenschaftliche Zusammenarbeit, Prof. von Löhneysen für die Erlaubnis die experimentellen Daten von $CeCu_{6-x}Au_x$ zu benutzen, David Hämmerler und Sabine Andergassen, die uns die fRG Berechnungen zur Verfügung gestellt haben, Hoa, Luise und den anderen Mitglieder des PGI für die schöne Arbeitsatmosphere, meinen Eltern und Schwiegereltern, die meiner Frau und mir im Alltag unter die Arme gegriffen haben, sowie viele weitere Freunde und Bekannte, die uns tatkräftig unterstützt haben.

# Contents

# Chapter 1

# Introduction

The physics of quantum dots has been of continuous interest in research. Modern realizations of quantum dots are highly tunable devices [1, 2, 3, 4]. In artificial quantum dots, for example, one can manipulate the gate voltage and the tunneling barrier to the quantum dot (see Figure 1.1). Other more complex realizations, like double quantum dots, have been of recent interest also in the context of quantum computing [6, 7]. A different approach to create artificial quantum dots is to attach molecules between two leads [8, 9, 10, 11, 12]. These provide a large variety of systems that can be investigated.

Investigating the thermoelectric properties of such devices, i.e. their thermopower and their electrical and thermal conductance, is of interest from the fundamental physics point of view as well as for future applications to harvest waste energy in space constrained environments. Measuring these properties can also be used to probe the electronic structure of molecules (see e.g. Reddy et al. [13]).

To investigate the properties of quantum dots we will use the numerical renormalization group (NRG) method. It was introduced by Wilson [14] to solve the Kondo problem. The model, introduced by Kondo [15], described a mechanism explaining the resistance minimum appearing in metals doped with magnetic impurities. The same effect can increase the conductance of quantum dots at low temperatures [16, 17]. Since its introduction in the 1970's the NRG has been further developed and proved to give accurate results for a wide range of models and parameters (see Bulla et al. [18]). The details of this method will be introduced in Chapter 2.

In this thesis we were particularly motivated by recent experiments on the conductance scaling coefficients [4, 12, 19] (see Figure 1.2). While these coefficients take defined values in the Kondo limit, deviations are expected, and found, away from this limit (Chapter 5). While previous work (Costi and Zlatić [20]) has investigated the thermoelectric properties of quantum dots in zero magnetic field, a systematic study of these properties in a magnetic field is absent. We supply this in Chapter 6, where we also apply our re-

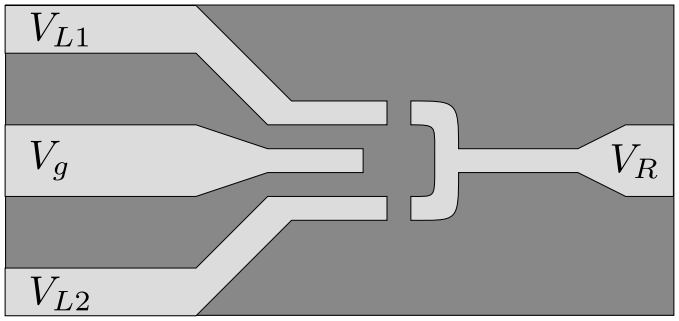


*Figure 1.1: Schematic picture of a single electron transistor [5]. The surrounding electrodes ($V_{L1}$, $V_{L2}$ and $V_R$) control the tunnel barrier and create the quantum dot in the 2D electron gas. the middle left electrode acts as a gate voltage $V_g$ and controls the level of the dots with respect to the Fermi level $E_F$ of the leads. Source and drain on the top and bottom are not visible here.*

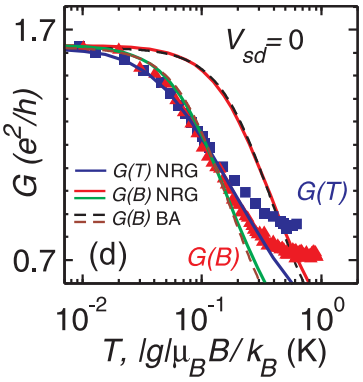


*Figure 1.2: Low temperature measurements of the conductance of a InAs nanowire quantum dot depending on the ($G(T)$) temperature and on the magnetic field ($G(B)$) (taken from Kretinin et al. [4]). The experimental data has been compared to theoretical predictions by the NRG (solid lines) and Bethe ansatz (dashed lines).*

sults for the magnetothermopower to interpret, in a semi-phenomenological manner, the recent measurements of von Löhneysen et al. [21] on the system $CeCu_{6-x}Au_x$. Finally, the high thermopower observed in a negative-U Anderson model [22] raises the question of how to realize an attractive Coulomb energy in quantum dots. This motivates our study of the screened two-channel Anderson model in Chapter 7 as a possible route to a negative-U model.

To be able to calculate these effects the existing NRG program was extended to include a series of recent developments. First, z-averaging improved different aspects of the calculation. It allows to calculate results on an arbitrary temperature grid, largely reduces oscillations introduced by the discretization, and in turn allows the use of larger discretization parameters, which thus reduces also the computational time. Second, a different discretization scheme introduced by Campo Jr and Oliveira [23] corrects a systematic overestimation of the hybridization. Last, the full density matrix (FDM) approach eliminates the need to choose the best energy shell at which to calculate a physical quantity within the NRG. These general advancements have to be complemented by some problem specific extensions.

The first two advancements, the z-averaging and the improved discretization scheme, were implemented in connection to a new method to calculate the internal energy and specific heat contribution of an impurity in Chapter 3. Within this approach, the impurity specific heat contribution can be extracted with just a single NRG calculation for the total system, as opposed to the usual approach that further requires the calculation of the pure host system. This method is independent of the NRG and may find use in other impurity solvers or problems. To show the accuracy of the new method (and the new NRG developments) we solve the thermodynamic Bethe-ansatz equations for the Anderson model numerically and extract from these the specific heat at finite temperatures (and also the susceptibility, which we use in Chapter 4).

The FDM approach was explored in the context of the impurity contribution of the specific heat and the magnetic susceptibility in Chapter 4. There we also address a delicate problem arising when calculating the total spin susceptibility and numerically confirm the Clogston-Anderson compensation theorem.

With these developments, we were able to address the question of how the universal conductance scaling behavior changes away from the Kondo regime in Chapter 5. For this work a reliable method to calculate the conductance [24] enables extraction of the scaling parameters to new precision. The simpler $U(1)$ symmetry has to be incorporated as well to allow the inclusion of a magnetic field.

Extending the method for the conductance calculation to higher moments of the local level Green's function, enabled us to analyze the behavior of different thermoelectric properties in a magnetic field. Besides extending

the work of Costi and Zlatić [20], we show that the low temperature behavior of the Seebeck coefficient of $CeCu_{6-x}Au_x$, a heavy Fermion material, indeed shows the signature of a Kondo effect, within a certain Au concentration range.

Finally, we investigate the effect of a conduction electron screening term on the low temperature conductance in Chapter 7. An electron screening term is discussed as one mechanism that can lower the effective Coulomb repulsion [25, 26]. This model has previously only been investigated by an effective one-channel approximation [27] for its thermoelectric properties. The more accurate description requires the need of a two-channel Anderson model and comes with its own set of challenges, as the diagonalization needs a different set of coefficients in the iterative diagonalization procedure, and the methods used for the calculation of thermoelectric properties are no longer valid in presence of an electron screening term. Benchmarking the results against functional renormalization group calculations for the same model gave good agreement for the zero temperature conductance and dot level occupation number [28].

# Chapter 2

# Numerical renormalization group

When liquid helium became available in the early 20'th century, in metals doped with magnetic impurities an unexpected resistance minimum was observed (for example Iron in Gold [29]). Jun Kondo [15] made a significant advancement in explaining this phenomenon. His explanation was based on the s-d model which for a single impurity takes the form

$$H_{\text{s-d}} = \sum_{k,k'} J_{k,k'} S^+ c^\dagger_{k,\downarrow} c_{k',\uparrow} + S^- c^\dagger_{k,\uparrow} c_{k',\downarrow} + S_z (c^\dagger_{k,\uparrow} c_{k',\uparrow} - c^\dagger_{k,\downarrow} c_{k',\downarrow}), \tag{2.1}$$

where $S_z$ and $S^\pm = S_x \pm iS_y$ are the spin operators of the local state of spin S.

The s-d model assumes that there already is a localized spin. A more general model was proposed by Anderson [30]:

$$H = H_{\text{imp}} + H_{\text{int}} + H_{\text{cond}} \tag{2.2}$$

where

$$H_{\text{imp}} = U n_{d,\uparrow} n_{d,\downarrow} + \sum_\sigma \varepsilon_d n_{d,\sigma} \tag{2.3}$$

$$H_{\text{int}} = \sum_{k,\sigma} V_k \left( c^\dagger_{k,\sigma} d_\sigma + d^\dagger_\sigma c_{k,\sigma} \right) \tag{2.4}$$

$$H_{\text{cond}} = \sum_{k,\sigma} \epsilon_k c^\dagger_{k,\sigma} c_{k,\sigma}. \tag{2.5}$$

The symmetric Anderson impurity model ($\varepsilon_d = -\frac{1}{2}U$) and the s-d model are connected by the Schrieffer-Wolff transformation [31] for $U/V_k \gg 1$

$$J_{k,k'} = 2V^*_k V_{k'} \left( \frac{1}{U + \varepsilon_d - \epsilon_{k'}} + \frac{1}{\epsilon_k - \varepsilon_d} \right) \left[ = -\frac{8\,|V|^2}{U} \right],$$

where the results in brackets indicate the particle-hole symmetric case for $k \approx k_F$. The Anderson model will play a fundamental role in this thesis.

Though the underlying models are rather simple, it took until 1975 until Wilson [14] found a method to solve this problem essentially exactly non-perturbatively: the numerical renormalization group (NRG).

Kenneth Wilson was awarded the Nobel Prize in Physics in 1982 for his work on the renormalization group and the solution of the Kondo problem. The extensive papers by Krishna-murthy et al. [32][33] give a good introduction into the NRG, while the review article of Bulla et al. [18] surveys the more recent developments and applications of this method. Unlike other renormalization theories it is non-perturbative in any of the interaction parameters and thereby produces a set of energies that are a good description of the system on all relevant energy scales.

## 2.1 Introduction to the NRG

The derivation of the NRG will follow the lines of Bulla et al. [18]. The single impurity Anderson model (SIAM) will be the starting point for the derivation in this chapter. Its Hamiltonian takes the form

$$H = H_{\text{imp}} + H_{\text{hyb}} + H_{\text{band}} \tag{2.6}$$

$$H_{\text{imp}} = \sum_{\sigma} \varepsilon_d d_\sigma^\dagger d_\sigma + U n_{d,\uparrow} n_{d,\downarrow} \tag{2.7}$$

$$H_{\text{hyb}} = \sum_{k,\sigma} V_k (d_\sigma^\dagger c_{k,\sigma} + c_{k,\sigma}^\dagger d_\sigma) \tag{2.8}$$

$$H_{\text{band}} = \sum_{k,\sigma} \epsilon_k c_{k,\sigma}^\dagger c_{k,\sigma}. \tag{2.9}$$

The method can be easily extended to arbitrary $H_{\text{imp}}$ and multiple bands even though the number of bands that can be treated at present is 3 or less [34]. The two band case and the addition of a screening term of the impurity will be discussed in more detail in Chapter 7.

In this chapter we will first introduce the three main steps needed for the NRG calculation (Section 2.1). The following section will go into the details of an alternative discretization scheme that eliminates some problem of the original scheme. Sections 2.3-2.5 will introduce how different observables are calculated within the NRG. The last section then explains the full density matrix (FDM) approach as a further improvement to determine observables using the full energy spectrum of the NRG.

### 2.1.1 Band Discretization

The overall strategy of the NRG is to convert the starting Hamiltonian into a tridiagonal chain, where the hopping terms from one site to the next

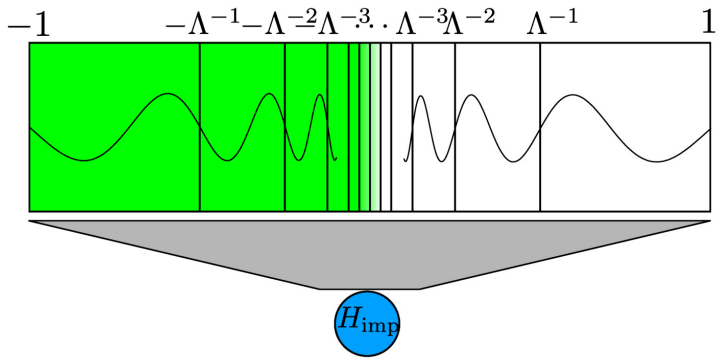


*Figure 2.1: This sketch visualizes the logarithmic discretization of the band. The band is split into logarithmically decreasing parts ranging from energies $D\Lambda^{-n}$ to $D\Lambda^{-(n-1)}$ for positive energies or $-D\Lambda^{-(n-1)}$ to $-D\Lambda^{-n}$ for negative energies. These strips will then be decomposed into a Fourier series (or another suitable basis) as represented by the sine wave.*

decrease exponentially. It is therefore possible to iteratively treat each new chain element as a perturbation to the previously diagonalized chain. As one is interested in low energy behavior it is justified to neglect some high energy states from the previous iteration.

### Relation between dispersion and hybridization

To simplify the derivation for the NRG we introduce the hybridization function $\Delta(\omega)$ of the SIAM:

$$\Delta(\omega) = \pi \sum_k V_k^2 \delta(\omega - \epsilon_k). \tag{2.10}$$

Assuming there is no support for $\Delta(\omega)$ outside the interval $[-D, D]$, we can use $D$ as the energy unit and rewrite the Hamiltonian as:

$$\begin{aligned} H = H_{\text{imp}} &+ \int_{-1}^{1} \sum_\sigma g(\epsilon) a^\dagger_{\epsilon,\sigma} a_{\epsilon,\sigma} \\ &+ \int_{-1}^{1} \sum_\sigma h(\epsilon)(d^\dagger_\sigma a_{\epsilon,\sigma} + \text{H.c.}), \end{aligned} \tag{2.11}$$

where $g(\epsilon)$ is the dispersion relation and $h(\epsilon)$ the hybridization. $a_{\epsilon,\sigma}$ fulfills the fermionic commutator relation $[a_{\epsilon,\sigma}, a^\dagger_{\epsilon',\sigma'}]_+ = \delta(\epsilon - \epsilon')\delta_{\sigma\sigma'}$. The functions $g(\epsilon)$ and $h(\epsilon)$ are then related by

$$\Delta(\omega) = \pi \frac{d\epsilon(\omega)}{d\omega} h(\epsilon(\omega))^2, \tag{2.12}$$

where $\epsilon(\omega)$ is the inverse of $g(\epsilon)$ (see Reference [35] for the derivation). Therefore the NRG is only dependent on the hybridization function $\Delta(\omega)$.

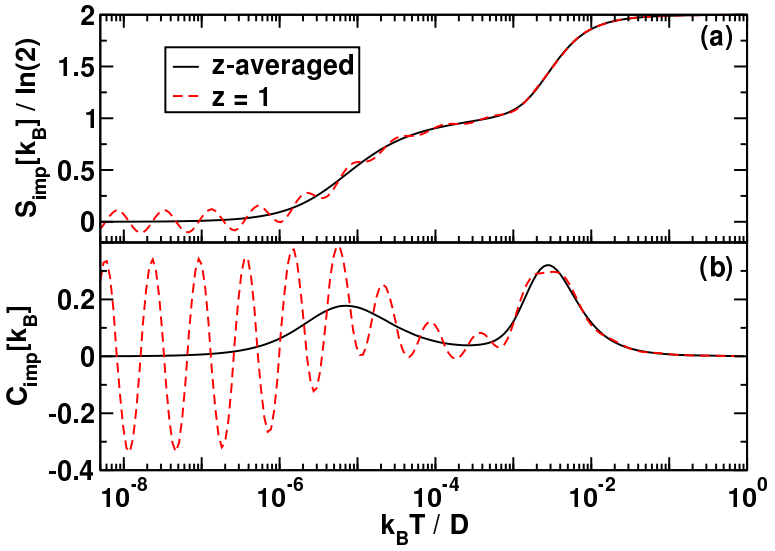


*Figure 2.2: Temperature dependence of (a) the impurity entropy $S_{imp}(T)$ and (b) the impurity specific heat $C_{imp}(T)$. The curves are calculated for the symmetric Anderson model using $\Delta_0 = 0.001D$, $U/\Delta_0 = 12$ and $\Lambda = 4$, $e_c(\Lambda = 4) = 40$. The figure depicts the difference before (dashed lines) and after (solid lines) z-averaging. For $\Lambda = 4$ two z-values [$z = 1/4, 3/4$] are sufficient to eliminate the oscillations.*

### Logarithmic intervals

To achieve exponentially decreasing hopping terms, the band will first be split into a set of logarithmically decreasing intervals with respect to the Fermi energy. As it is more convenient, the Fermi energy is set to zero throughout the thesis. Further the energies are rescaled to the half bandwidth $D$. Figure 2.1 sketches how a flat band is split into intervals reaching from $-\Lambda^{-n}$ to $-\Lambda^{-(n+1)}$ and into intervals from $\Lambda^{-(n+1)}$ to $\Lambda^{n}$.

Note that one would like to let $\Lambda \to 1$ to return to the continuum limit while numerically large values of $\Lambda$ make the calculation easier, but introduce discretization artifacts. The oscillation artifacts (see Figure 2.2) can be reduced by averaging over a set of results obtained from the following discretization scheme (Frota and Oliveira [36], Oliveira and Olilveria [37], Yoshida et al. [38]): The interval end points will be shifted by a factor $\Lambda^{-z}$ for $z \in (0, 1]$ to $x_n = \pm\Lambda^{-n-1-z}$, $n$ now running from $n \in \{1, 2, 3, \dots\}$ and $x_0 = \pm 1$. Averaging over a set of equally spaced z values greatly reduces the oscillations seen for a large discretization parameter $\Lambda$. This averaging will be denoted as the z-trick or as z-averaging. The derivation for this trick is equivalent to the usual derivation, any $\Lambda^{-n}$ will be replaced by $\Lambda^{-n-1-z}$ with an exception for the first intervals.

Other discretization artifacts remain. An effective change in the hy-

bridization for large $\Lambda$, can be overcome by a different decomposition than given in the next subsection (see Section 2.2). It is therefore advised to make calculations with the smallest $\Lambda$ feasible or at least vary $\Lambda$ to make sure the coarse discretization does not effect the results.

**Discretization**

To justify a replacement of each interval with a $\delta$-function representing the average of the interval, the interval will be decomposed into a Fourier series. Note that this decomposition leads to a shifted effective hybridization for large $\Lambda$, which can be averted by using a different decomposition (Campo and Oliveira [23] and Section 2.2). Denoting the length of an interval $d_n$ with

$$d_n = \Lambda^{-n}(1 - \Lambda^{-1}), \quad n = 0, 1, 2, \ldots \tag{2.13}$$

and the interval borders $x_n$

$$x_n = \pm\Lambda^{-n} \tag{2.14}$$

the complete set of orthonormal basis is given by:

$$\psi^{\pm}_{n,p}(\epsilon) = \begin{cases} \frac{1}{\sqrt{d_n}} \exp(\pm\omega_n p\epsilon) & \text{if } x_n < \pm\epsilon < x_{n+1} \\ 0 & \text{else} \end{cases}, \tag{2.15}$$

where $p$ is an integer $p \in (-\infty, \infty)$. The fundamental frequencies of each interval are given by $\omega_n = 2\pi/d_n$. The conduction electron operator $a_{\epsilon,\sigma}$ can now be expressed in this basis:

$$a_{\epsilon,\sigma} = \sum_{n,p} a_{n,p,\sigma}\psi^{+}_{n,p}(\epsilon) + b_{n,p,\sigma}\psi^{-}_{n,p}(\epsilon), \tag{2.16}$$

where the corresponding Fourier coefficients are given by the inverse transformation:

$$a_{n,p,\sigma} = \int \mathrm{d}\epsilon\, [\psi^{+}_{n,p}(\epsilon)]^* a_{\epsilon,\sigma} \tag{2.17}$$

$$b_{n,p,\sigma} = \int \mathrm{d}\epsilon\, [\psi^{-}_{n,p}(\epsilon)]^* a_{\epsilon,\sigma}. \tag{2.18}$$

The operators $a^{(\dagger)}_{n,p,\sigma}$ and $b^{(\dagger)}_{n,p,\sigma}$ fulfill the fermionic commutation relation. We can rewrite the Hamiltonian in terms of the new set of operators. The hybridization part can be rewritten as:

$$\begin{aligned} \int \mathrm{d}\epsilon\, h(\epsilon) d^{\dagger}_{\sigma} a_{\epsilon,\sigma} = d^{\dagger} \sum_{n,p} \Bigg[ & a_{n,p,\sigma} \int^{+.n} \mathrm{d}\epsilon\, h(\epsilon)\psi^{+}_{n,p}(\epsilon) \\ & + b_{n,p,\sigma} \int^{-.n} \mathrm{d}\epsilon\, h(\epsilon)\psi^{-}_{n,p}(\epsilon) \Bigg], \end{aligned} \tag{2.19}$$

where we defined

$$\int^{\pm.n} := \pm \int_{\pm x_{n+1}}^{\pm x_n}. \tag{2.20}$$

We can use any non-zero hybridization $h(\epsilon)$ due to the relation given in Equation 2.12. Choosing a step function

$$h(\epsilon)^2 = h_n^{\pm 2} = \frac{1}{d_n} \int^{\pm.n} \mathrm{d}\epsilon \, \frac{1}{\pi} \Delta(\epsilon). \tag{2.21}$$

has two advantages. On the one hand, this choice will ensure a linear dispersion at the discretization points $g(x_n) = x_n$ or $\epsilon(x_n) = x_n$. This can be proved by using Equations (2.12) and (2.21) and has been introduced by Bulla et al.[35]. On the other hand, it will also couple the band only to the Fourier coefficients $a_{n,0,\sigma}$ and $b_{n,0,\sigma}$. The other coefficients will only couple indirectly via the dispersion relation. This is crucial for Wilson's argument in neglecting the $p \neq 0$ terms [32]. In Section 2.2 we will see that it is possible to completely uncouple $a_{n,0,\sigma}$ and $b_{n,0,\sigma}$ from the other Fourier coefficients, but at the cost of not having a fully orthogonal basis $\{a_{n,p,\sigma}, b_{n,p,\sigma}\}$ anymore. Evaluating Equation (2.19) for step function hybridization leads to

$$\int \mathrm{d}\epsilon \, h(\epsilon) d_\sigma^\dagger a_{\epsilon,\sigma} = \frac{1}{\sqrt{\pi}} d_\sigma^\dagger \sum_n \gamma_n^+ a_{n,0,\sigma} + \gamma_n^- b_{n,0,\sigma}, \tag{2.22}$$

where $\gamma_n^{\pm 2} = \int^{\pm.n} \mathrm{d}\epsilon \, \Delta(\epsilon)$.

Rewriting the conduction electron part in terms of the new basis yields

$$\begin{aligned} \int \mathrm{d}\epsilon \, g(\epsilon) a_{\epsilon,\sigma}^\dagger a_{\epsilon,\sigma} = &\sum_n \xi_n^+ a_{n,p,\sigma}^\dagger a_{n,p,\sigma} + \xi_n^- b_{n,p,\sigma}^\dagger b_{n,p,\sigma} \\ &+ \sum_{n,p\neq p'} \alpha_n^+(p,p') a_{n,p,\sigma}^\dagger a_{n,p',\sigma} - \alpha_n^-(p,p') b_{n,p,\sigma}^\dagger b_{n,p',\sigma} \end{aligned} \tag{2.23}$$

where the coefficients for the diagonal elements are given by

$$\xi_n^\pm = \frac{\int^{\pm.n} \mathrm{d}\epsilon \, \epsilon \Delta(\epsilon)}{\int^{\pm.n} \mathrm{d}\epsilon \, \Delta(\epsilon)} \left[ = \frac{1}{2} \Lambda^{-n} (1 + \Lambda^{-1}) \right], \tag{2.24}$$

where the result for a constant $\Delta(\epsilon)$ is given in the bracket. When using a linear dispersion $g(\epsilon) = \epsilon$ the off-diagonal elements are given by

$$\alpha_n^\pm(p,p') = \frac{1-\Lambda^{-1}}{2\pi i} \frac{\Lambda^{-n}}{p-p'} \exp\left[ \frac{2\pi i (p-p')}{1-\Lambda^{-1}} \right]. \tag{2.25}$$

So far the results given by Equation (2.22) and (2.23) are exact. The discretization is made when dropping the terms using $p \neq 0$. The justification for this step is that the impurity only couples directly to the $p = 0$ coefficients. Further, the coupling between different $a_{n,p,\sigma}$, $b_{n,p,\sigma}$ is proportional to $(1 - \Lambda^{-1})$ and vanishes at the continuum limit $\Lambda \to 1$. Neglecting it could

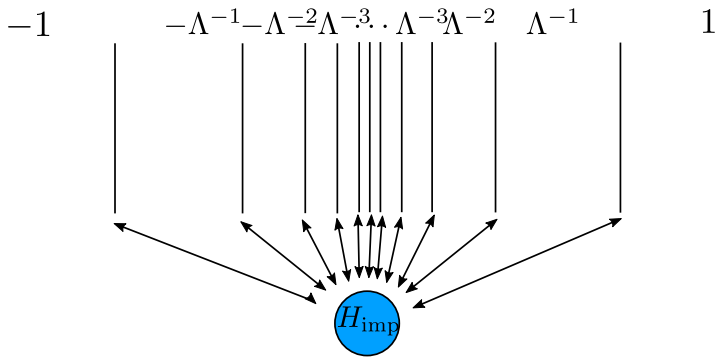


*Figure 2.3: The band Hamiltonian has been reduced to a set of discrete states coupling to the impurity.*

be interpreted as a zeroth order step in a perturbation expansion with respect to $\alpha_n^{\pm}(p,p')$. Relabeling $a_{n,0,\sigma} \equiv a_{n,\sigma}$ the discretized Hamiltonian takes the form

$$\begin{aligned} H = H_{\text{imp}} &+ \sum_{n,\sigma} \xi_n^+ a_{n,\sigma}^\dagger a_{n,\sigma} + \xi_n^- b_{n,\sigma}^\dagger b_{n,\sigma} \\ &+ \frac{1}{\sqrt{\pi}} \sum_\sigma d_\sigma^\dagger \sum_n \gamma_n^+ a_{n,\sigma} + \gamma_n^- b_{n,\sigma} \\ &+ \frac{1}{\sqrt{\pi}} \sum_\sigma \left[ \sum_n \gamma_n^+ {a_{n,\sigma}}^\dagger + \gamma_n^- {b_{n,\sigma}}^\dagger \right] d_\sigma . \end{aligned} \tag{2.26}$$

Figure 2.3 depicts the discretized version of the band in Figure 2.1.

### 2.1.2 Mapping to semi-infinite chain

The standard Gram-Schmidt procedure can be used to transform the Hamiltonian (2.26) onto a tridiagonal Hamiltonian. The off diagonal parts will correspond to the hopping terms of the semi-infinite chain. An initial state $f_{0,\sigma}$ has to be selected for the Gram-Schmidt procedure. This state is chosen to correspond to the hybridization of the impurity with the conduction electrons.

$$f_{0,\sigma} = \frac{1}{\sqrt{\xi_0}} \sum_n \gamma_n^+ a_{n,\sigma} + \gamma_n^- b_{n,\sigma} \tag{2.27}$$

$$= \frac{1}{\sqrt{\xi_0}} \int h(\epsilon) a_{\epsilon,\sigma}, \tag{2.28}$$

where $\xi_0 = \int \mathrm{d}\epsilon\, \Delta(\epsilon) = \sum_n {\gamma_n^+}^2 + {\gamma_n^-}^2$ is the normalization constant for $f_{0,\sigma}$. The hybridization can therefore be rewritten as

$$H_{\text{hyb}} = \sum_\sigma \sqrt{\frac{\xi_0}{\pi}} (f_{0,\sigma}^\dagger d + \text{H.c.}). \tag{2.29}$$

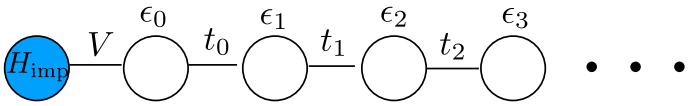


*Figure 2.4: After the mapping the Hamiltonian takes the form of a semi-infinite chain with exponentially decreasing hopping terms $t_n$.*

The total Hamiltonian therefore takes the form

$$H = H_{\text{imp}} + \sum_{\sigma} \sqrt{\frac{\xi_0}{\pi}} (f^{\dagger}_{0,\sigma} d_{\sigma} + d^{\dagger}_{\sigma} f_{0,\sigma}) \tag{2.30}$$
$$+ \sum_{n,\sigma} \epsilon_n f^{\dagger}_{n,\sigma} f_{n,\sigma} + t_n \left( f^{\dagger}_{n,\sigma} f_{n+1,\sigma} + f^{\dagger}_{n+1,\sigma} f_{n,\sigma} \right).$$

Figure 2.4 depicts this chain. The factors $t_n$ and $\epsilon_n$ will be recovered using the Gram-Schmidt algorithm. The first state is initialized as

$$|0\rangle = f^{\dagger}_{0,\sigma} |\varnothing\rangle, \tag{2.31}$$

where $|\varnothing\rangle$ denotes the vacuum. The next states will be created by applying the discretized conduction electron Hamiltonian $H_{\text{band}}$ as it appears in Equation 2.26 to $|0\rangle$. The resulting state has to be orthogonalized and normalized. The first new state is given by

$$|1\rangle = \frac{1}{n_1} \left( H_{\text{band}} |0\rangle - |0\rangle \langle 0| H_{\text{band}} |0\rangle \right), \tag{2.32}$$

where $n_i$ normalize the created states. Using the fact that the Hamiltonian is hermitian one can show that $\langle j | H_{\text{band}} | i \rangle = 0$ if $j < i - 1$. Therefore the general case takes the following form

$$|i+1\rangle = \frac{1}{n_{i+1}} \left( H_{\text{band}} |i\rangle - |i\rangle \langle i| H_{\text{band}} |i\rangle - |i-1\rangle \langle i-1| H_{\text{band}} |i\rangle \right). \tag{2.33}$$

An entry of $|i\rangle$ will be referred to as $v_i{}^{\pm}_k$. Applying the scheme to the actual Hamiltonian yields

$$\bar{v}_0 = \frac{1}{\sqrt{\xi_0}} (\gamma^+_0, \gamma^+_1, \gamma^+_2, \cdots, \gamma^-_2, \gamma^-_1, \gamma^-_0)^T, \tag{2.34}$$

and

$$\bar{v}_1 = \frac{1}{n_1} \left( (\xi^+_0 - \epsilon_0)\gamma^+_0, (\xi^+_1 - \epsilon_0)\gamma^+_1, \cdots, (\xi^-_1 - \epsilon_0)\gamma^-_1, (\xi^-_0 - \epsilon_0)\gamma^-_0 \right)^T, \tag{2.35}$$

where $\epsilon_0 = \sum_{k,\pm} \xi^{\pm}_0 {v_0}^{\pm 2}_k$ is the on-site energy. The hopping terms $t_n$ and on-site energies $\epsilon_n$ can be calculated as

$$t_{n-1} = \sum_{k,\pm} v_n{}^{\pm}_k \xi_k v_{n-1}{}^{\pm}_k \tag{2.36}$$

$$\epsilon_n = \sum_{k,\pm} \xi^{\pm}_k {v_n}^{\pm 2}_k. \tag{2.37}$$

The remaining states are then given by

$$\bar{v}_{n+1} = \frac{1}{n_{n+1}} \left(\xi_0^+ v_{n0}^+, \xi_1^+ v_{n1}^+, \cdots, \xi_1^- v_{n1}^-, \xi_0^- v_{n0}^-\right)^T \tag{2.38}$$

$$- \frac{1}{n_{n+1}} (\epsilon_n \bar{v}_n + t_{n-1} \bar{v}_{n-1}). \tag{2.39}$$

While the implementation is very easy it has to be stated that a wide range of numbers enter into the calculation of the coefficients. It is therefore important to use multiple precision routines to calculate the parameters, else the algorithm breaks down after approximately 15-20 iterations. The on-site and hopping terms generally fall off exponentially. For a flat symmetric band Wilson [32] showed that the hopping terms $t_n$ behave like

$$t_n = \frac{(1+\Lambda^{-1})(1-\Lambda^{-n-1})}{2\sqrt{1-\Lambda^{-2n-1}}\sqrt{1-\Lambda^{-2n-3}}} \Lambda^{-n/2} \xrightarrow{n\to\infty} \frac{1}{2}(1+\Lambda^{-1})\Lambda^{-n/2}, \tag{2.40}$$

while $\epsilon_n = 0$ due to the particle-hole symmetric band. Exponentially decreasing hopping elements are crucial to justify the cut-off scheme used in the next step.

### 2.1.3 Iterative diagonalization

For the iterative diagonalization we consider the tridiagonal Hamiltonian as the limit $N \to \infty$ of a series $H_n$

$$H_{n+1} = H_n + \sum_\sigma t_n (f_{n,\sigma}^\dagger f_{n+1,\sigma} + f_{n+1,\sigma}^\dagger f_{n,\sigma}) + \epsilon_{n+1} f_{n+1,\sigma}^\dagger f_{n+1,\sigma}, \tag{2.41}$$

where the starting Hamiltonian $H_0$ is given by

$$H_0 = H_{\text{imp}} + \sum_\sigma \sqrt{\frac{\xi_0}{\pi}} (d_\sigma^\dagger f_{0,\sigma} + f_{0,\sigma}^\dagger d) + \epsilon_0 f_{0,\sigma}^\dagger f_{0,\sigma}. \tag{2.42}$$

Many authors choose to rescale $H_n$ by $\Lambda^{(N-1)/2}$ to cancel the $N$ dependence of $t_{n-1}$. When investigating the renormalization group flow this is important to ensure the energies are on the same energy scale. Assuming we already know each energy and eigenstate of $H_n$, we can calculate $H_{n+1}$.

Without the coupling term

$$V_{n+1} = \underbrace{\sum_\sigma t_n (f_{n,\sigma}^\dagger f_{n+1,\sigma} + f_{n+1,\sigma}^\dagger f_{n,\sigma})}_{H_{\text{hopping}}} + \underbrace{\sum_\sigma \epsilon_{n+1} f_{n+1,\sigma}^\dagger f_{n+1,\sigma}}_{H_{\text{on-site}}}. \tag{2.43}$$

the shell belonging to $f_{n+1,\sigma}^\dagger$ just creates a fourfold degeneracy. Denoting

the eigenstates of $H_n$ as $|r_n\rangle$ a basis of $H_{n+1}$ can be created as

$$\begin{aligned}
|r_n;1\rangle &= |r_n\rangle && \propto |r_n\rangle|\varnothing\rangle_{n+1} \\
|r_n;2\rangle &= f^\dagger_{n+1,\uparrow}|r_n\rangle && \propto |r_n\rangle|\uparrow\rangle_{n+1} \\
|r_n;3\rangle &= f^\dagger_{n+1,\downarrow}|r_n\rangle && \propto |r_n\rangle|\downarrow\rangle_{n+1} \\
|r_n;4\rangle &= f^\dagger_{n+1,\uparrow}f^\dagger_{n+1,\downarrow}|r_n\rangle && \propto |r_n\rangle|\uparrow\downarrow\rangle_{n+1}, d
\end{aligned}$$

where the proportionality is due to the possible phase factor. The eigenstates and eigenvalues of $H_{n+1}$ are then simply a matter of diagonalizing the matrix $\langle r_n;i|H_{n+1}|r'_n,j\rangle$. In practice the Hamiltonian can be divided into various sub Hamiltonians due to symmetry. These greatly reduce the needed matrix sizes and, in case of the $SU(2)$ symmetry, even allows to work on only a subset of otherwise degenerate energies [32]. The new basis states that reflect that symmetry will therefore be a rearrangement and linear combination of the states generated by $f^\dagger_{n+1,\sigma}$. As the tridiagonalized SIAM Hamiltonian commutes with the total particle number $N$ and the z-component of the total spin $S_z$ (and in absence of a local magnetic field the total spin $S$), we can use $N$ and $S_z$ as quantum numbers for the sub Hamiltonians. The new states, spanning the sub Hamiltonian, will consist of

$$\begin{aligned}
|N,S_z,r;1\rangle_{n+1} &= |N,S_z,r\rangle_n \\
|N,S_z,r;2\rangle_{n+1} &= f^\dagger_{n+1,\uparrow}|N-1,S_z-\frac{1}{2},r\rangle_n \\
|N,S_z,r;3\rangle_{n+1} &= f^\dagger_{n+1,\downarrow}|N-1,S_z+\frac{1}{2},r\rangle_n \\
|N,S_z,r;4\rangle_{n+1} &= f^\dagger_{n+1,\uparrow}f^\dagger_{n+1,\downarrow}|N-2,S_z,r\rangle_n.
\end{aligned}$$

To calculate ${}_{n+1}\langle N,S_z,r,i|H_{n+1}|N,S_z,r',j\rangle_{n+1}$ we split the Hamiltonian into

$$H_{n+1} = H_n + H_{\text{hopping}} + H_{\text{on-site}}.$$

The elements

$${}_{n+1}\langle N,S_z,r,i|H_n|N,S_z,r',j\rangle_{n+1} = \delta_{r,r'}\delta_{i,j}E^n_r$$

are the diagonal energies calculated in the previous step. The elements

$${}_{n+1}\langle N,S_z,r,i|H_{\text{on-site}}|N,S_z,r',j\rangle_{n+1} = \delta_{r,r'}\delta_{i,j}\tilde{n}_{n+1}\epsilon_{n+1},$$

where $\tilde{n}_{n+1}$ is the occupation number of the newly added shell, give constant contribution to the diagonal depending on $i$. To calculate

$${}_{n+1}\langle N,S_z,r,i|H_{\text{hopping}}|N,S_z,r',j\rangle_{n+1}$$

we need to access the occupation of the previous last shell. We use the transformation of the previous step

$$|N, S_z, r\rangle_n = \sum_{w,i} U^n_{N,S_z}(w, j; r)|N, S_z, w, j\rangle_n$$

to access these elements. After the diagonalization the energies are shifted by the lowest energy state of the shell $E^n_i \to E^n_i - E^n_{\mathrm{GS}}$. The coefficients needed for the SU(2) symmetry are listed in Appendix A. See also Krishna-murthy et al. [32] for a detailed derivation of the one-channel SU(2) symmetry.

In each step we will get four times the number of eigenvalues as in the previous step. This exponential growth reaches its computational limits after a few iterations, even if as many symmetries as possible are used. Luckily, a simple truncation scheme will solve this problem. Starting from a chain of length $m_0$ (typically $m_0 = 4, 5$ or 6), in each step we will keep only the lowest energy values. Either a fix amount of states $N_{\mathrm{keep}}$ is kept every step or a energy dependent method can be used where only energies $E^n_i < e_c t_n$ will be kept.

It is not guaranteed that this cut-off scheme works. A numerical hint is that the low energy spectrum does not change when varying the number of kept states $N_{\mathrm{keep}}$. Further the results obtained by the NRG have proven to be correct within a few percent or better when compared to other methods. Nevertheless we can try to explain why dropping the high energy states does not affect the low energy spectrum.

The Hamiltonian (Equation (2.43)) added with each chain element can be understood as a perturbation to the previous Hamiltonian. Due to the exponentially decreasing hopping parameters ($t_n \propto \Lambda^{-n/2}$) we can assume that the added term counts as small compared to the previous energies. The standard quantum perturbation theory states that the eigenstates will receive the corrections

$$|r\rangle_{n+1} = |r^0\rangle_{n+1} + |r^1\rangle_{n+1} + O(t_n^2) \tag{2.44}$$

$$|r^1\rangle_{n+1} = \sum_{q \neq r} |q^0\rangle_{n+1} \frac{{}_{n+1}\langle q^0|V_{n+1}|r^0\rangle_{n+1}}{E^0_r - E^0_q}. \tag{2.45}$$

The superscript 0 denotes the unperturbed state the superscript 1 denotes corrections of the first order. We see that for low energy states, high energy corrections are not very important. Their importance drops with the energy difference $E^0_r - E^0_q$. On top of that the matrix elements $\langle q^0|V_{n+1}|r^0\rangle_{n+1}$ typically give smaller contributions for bigger energy differences. Keep in mind that the NRG itself is non-perturbative.

## 2.2 Alternative discretization

Using the Fourier decomposition introduced by Wilson [32, 14] to justify the discretization leads to a shift of the effective hybridization $\Delta \to A_\Lambda \Delta$, where

$$A_\Lambda = \frac{\ln\Lambda}{2}\frac{1+\Lambda^{-1}}{1-\Lambda^{-1}}. \tag{2.46}$$

While this effect may be corrected "manually" for each $\Lambda$, it is clearly advantageous to have a built-in procedure within the NRG that does this automatically. Campo Jr and Oliveira [23] accomplished this within a logarithmic discretization scheme by using a Fourier decomposition in terms of non-orthogonal basis functions. As in the case of the linear grid, this correctly estimated $\Delta(\omega)$. This section will give an alternative derivation for the discretization following Section 2.1 and Reference [35] and [18] for general $\Delta(\omega)$ and was published in the appendix of Reference [39]. The starting point will be the idea that the original Fourier decomposition behaves unsteady on the interval borders. Using a modified decomposition will lead to an uncoupling of the used subset for a flat band. Realizing that this is the key property we can review the equations to generalize this to an arbitrary hybridization function.

We start with the single-channel Anderson impurity model, given by

$$\begin{aligned} H =& H_{imp} + \sum_{k,\sigma} \epsilon_{k,\sigma} c^\dagger_{k,\sigma} c_{k,\sigma} \\ &+ \sum_{k,\sigma} V_k (f^\dagger_\sigma c_{k,\sigma} + c^\dagger_{k,\sigma} f_\sigma), \end{aligned}$$

which may be written in the energy representation as [35]

$$\begin{aligned} H =& H_{imp} + \sum_\sigma \int_{-D_-}^{D_+} h(\epsilon)(f^\dagger_\sigma a_{\epsilon,\sigma} + a^\dagger_{\epsilon,\sigma} f_\sigma) d\epsilon \\ &+ \sum_\sigma \int_{-D_-}^{D_+} g(\epsilon) a^\dagger_{\epsilon,\sigma} a_{\epsilon,\sigma} d\epsilon. \end{aligned} \tag{2.47}$$

Here, $a_{\epsilon,\sigma}$ and $a^\dagger_{\epsilon',\sigma'}$ obey the standard anticommutation relations $\{a_{\epsilon,\sigma}, a^\dagger_{\epsilon',\sigma'}\} = \delta_{\sigma,\sigma'}\delta(\epsilon-\epsilon')$, $g(\epsilon)$ is the dispersion, $h(\epsilon)$ is the hybridization amplitude, and $\pm D_\pm$ are the upper/lower conduction electron band edges.

We consider the following set of orthonormal Fourier functions in each interval of a linear grid,

$$\psi_{n,p}(\eta) = \begin{cases} e^{-2\pi i p \eta}, & \text{if } \eta \in [n, n+1], n = -1, 0, 1, \dots \\ 0, & \text{otherwise.} \end{cases}$$

The inverse functions are given by $\Psi_{n,p}(\eta) = \psi^*_{n,p}(\eta)$ fulfilling the usual orthonormality condition:

$$\int_{-\infty}^{\infty} \psi_{n,p}(\eta)\Psi_{n',p'}(\eta) d\eta = \delta_{n,n'}\delta_{p,p'}. \tag{2.48}$$

We will transform this relation to a logarithmic grid such that $[n, n+1]$ will be transformed to $D_+[\Lambda^{-n-z-1}, \Lambda^{-n-z}]$ for $n = 0, 1, \ldots$ . The first interval $[-1, 0]$ is special and transforms to the first logarithmic interval containing the band edge, i.e. to $D_+[\Lambda^{-z}, 1]$. One possible choice, the obvious one, is $\epsilon = D_+\Lambda^{-\eta-z} \leftrightarrow \eta(\epsilon) = -\ln|\epsilon/D_+|/\ln\Lambda - z, n = 0, 1, \ldots$ ($\epsilon = D_+\Lambda^{-z(\eta+1)}$, $n = -1$) , but other choices are possible for defining the transformation between linear and logarithmic grids (and hence $\eta(\epsilon)$)[1]. Thus, for $n = 0, 1, \ldots$ we have[2]

$$\int_0^\infty \underbrace{\frac{1}{|\epsilon|\ln\Lambda}\psi_{n,p}\Big(-\frac{\ln\frac{|\epsilon|}{D_+}}{\ln\Lambda} - z\Big)}_{=\phi^+_{n,p}(\epsilon)/c^+_n} \underbrace{\Psi_{n',p'}\Big(-\frac{\ln\frac{|\epsilon|}{D_+}}{\ln\Lambda} - z\Big)}_{=c^+_n\cdot\Phi^+_{n',p'}(\epsilon)} d\epsilon$$
$$= \delta_{n,n'}\delta_{p,p'}. \tag{2.49}$$

For the expansion of the negative part of the band we use $\epsilon = -D_-\Lambda^{-\eta-z}$ and do not reverse the integration boundaries yielding the same function inside the integration.

$$\int_{-\infty}^0 \underbrace{\frac{1}{|\epsilon|\ln\Lambda}\psi_{n,p}\Big(-\frac{\ln\frac{|\epsilon|}{D_-}}{\ln\Lambda} - z\Big)}_{=\phi^-_{n,p}(\epsilon)/c^-_n} \underbrace{\Psi_{n',p'}\Big(-\frac{\ln\frac{|\epsilon|}{D_-}}{\ln\Lambda} - z\Big)}_{=c^-_n\cdot\Phi^-_{n',p'}(\epsilon)} d\epsilon$$
$$= \delta_{n,n'}\delta_{p,p'}. \tag{2.50}$$

The normalization factor $c^\pm_n$ can be distributed freely between the new basis $\phi^\pm_{n,p}$ and its inverse $\Phi^\pm_{n,p}$. $a_{\epsilon,\sigma}$ is expressed in terms of the new basis:

$$a_{\epsilon,\sigma} = \sum_{n,p} a_{n,p,\sigma}\phi^+_{n,p}(\epsilon) + b_{n,p,\sigma}\phi^-_{n,p}(\epsilon),$$

where

$$a_{n,p,\sigma} = \int^{+n} a_{\epsilon,\sigma}\Phi^+_{n,p}(\epsilon)d\epsilon$$
$$b_{n,p,\sigma} = \int^{-n} b_{\epsilon,\sigma}\Phi^-_{n,p}(\epsilon)d\epsilon,$$

where we defined

$$\int^{+n} = \int_{D_+\Lambda^{-n-z-1}}^{D_+\Lambda^{-n-z}}, \quad \int^{-n} = \int_{-D_-\Lambda^{-n-z}}^{-D_-\Lambda^{-n-z-1}}.$$

[1] A different choice will be made later in Equation (2.52). At present, the only requirement on $\eta(\epsilon)$ is that $\eta(\pm D_\pm\Lambda^{-n-z}) = n$ and $\eta(\pm D_\pm\Lambda^{-n-1-z}) = n+1$, i.e., the boundaries of $[n, n+1]$ map onto the mesh points of the logarithmic grid.

[2] For $n = -1$ a similar expression applies on using $\epsilon = D_+\Lambda^{-z(\eta+1)}$.

Evaluating the anticommutator $\left\{a_{n,p,\sigma}, a^{\dagger}_{n',p',\sigma'}\right\}$ we find

$$\begin{aligned}
& \left\{a_{n,p,\sigma}, a^{\dagger}_{n',p',\sigma'}\right\} \\
= \quad & \int^{+n} a_{\epsilon,\sigma}\Phi^{+}_{n,p}(\epsilon)d\epsilon \int^{+n'} a^{\dagger}_{\epsilon',\sigma'}\Phi^{+}_{n',p'}{}^{*}(\epsilon')d\epsilon' \\
& + \int^{+n'} a^{\dagger}_{\epsilon',\sigma'}\Phi^{+}_{n',p'}{}^{*}(\epsilon')d\epsilon \int^{+n} a_{\epsilon,\sigma}\Phi^{+}_{n,p}(\epsilon)d\epsilon \\
= \quad & \delta_{n,n'}\int^{+n}\int^{+n}[a_{\epsilon,\sigma}, a^{\dagger}_{\epsilon',\sigma'}]\Phi^{+}_{n,p}(\epsilon)\Phi^{+}_{n,p'}{}^{*}(\epsilon')d\epsilon d\epsilon' \\
= \quad & \delta_{n,n'}\delta_{\sigma,\sigma'}\int^{+n}\Phi^{+}_{n,p}(\epsilon)\Phi^{+}_{n,p'}{}^{*}(\epsilon)d\epsilon \\
= \quad & \delta_{n,n'}\delta_{\sigma,\sigma'}\int^{+n}\frac{1}{|c^{+}_{n}|^{2}}\mathrm{e}^{2\pi i(p-p')(\frac{\ln\frac{|\epsilon|}{D_{\pm}}}{\ln\Lambda}+z)}
\end{aligned}$$

with an analogous expression for $\left\{b_{n,p,\sigma}, b^{\dagger}_{n',p',\sigma'}\right\}$. Setting $\left\{a_{n,p,\sigma}, a^{\dagger}_{n,p,\sigma}\right\} = \left\{b_{n,p,\sigma}, b^{\dagger}_{n,p,\sigma}\right\} = 1$ fixes the constants $c^{\pm}_{n}$ in Equations (2.49) and (2.50), leading to

$$\begin{aligned}
|c^{\pm}_{n}|^{2} &= D_{\pm}\Lambda^{-n-z}(1-\Lambda^{-1}) \quad = d^{\pm}_{n} \\
&\left(= D_{\pm}(1-\Lambda^{-z}) \quad \text{for } n=-1\right)
\end{aligned}$$

and

$$\left\{a_{n,p,\sigma}, a^{\dagger}_{n',p',\sigma'}\right\} = \delta_{n,n'}\delta_{\sigma,\sigma'}\begin{cases}1, & \text{if } p=p' \\ \frac{\ln\Lambda}{2\pi i(p-p')+\ln\Lambda}, & \text{otherwise,}\end{cases}$$

with an analogous expression for $\left\{b_{n,p,\sigma}, b^{\dagger}_{n',p',\sigma'}\right\}$. Thus, only for the continuum limit $\Lambda \to 1$ is the above an orthonormal basis for all $p, p'$ [23]. However, as we show below, an approximate discretized Hamiltonian can be formulated in terms of the orthonormal subset of $p = 0$ states only, within which the NRG calculation is carried out. We show that for general $\Delta(\omega)$, (i), only $p = 0$ states couple to the impurity, and, (ii), off-diagonal terms in $p, p'$ can always be eliminated from the Hamiltonian by a suitable choice of the function $\eta(\epsilon)$ relating the linear to the logarithmic discretization $\epsilon = \pm D_{\pm}\Lambda^{-\eta(\epsilon)-z}$.

With the new basis functions we follow the derivation of Bulla et al. [18], reformulating first the hybridization part of Equation (2.47)

$$\begin{aligned}
\int_{-D_{-}}^{D_{+}} h(\epsilon)a_{\epsilon,\sigma}d\epsilon = & \sum_{n,p} a_{n,p,\sigma}\int^{+n} h(\epsilon)\phi^{+}_{n,p}(\epsilon)d\epsilon \\
& + \sum_{n,p} b_{n,p,\sigma}\int^{-n} h(\epsilon)\phi^{-}_{n,p}(\epsilon)d\epsilon.
\end{aligned}$$

The requirement that the hybridization only couples to the $p = 0$ terms can be satisfied by choosing $h(\epsilon) \propto \Phi^{\pm}_{n,0}(\epsilon) = \frac{1}{\sqrt{d_n}}$, which by Equation (2.49)

and (2.50) implies that $p \neq 0$ do not hybridize. Therefore we can choose the same $h(\epsilon)$ as in Section 2.1.1 (i.e. a step function in the discrete intervals),

$$h(\epsilon)^2 \equiv h_n^{\pm 2} = \frac{1}{d_n^{\pm}} \int^{\pm n} \frac{1}{\pi} \Delta(\omega) d\omega, \tag{2.51}$$

for $D_{\pm}\Lambda^{-n-z} < \pm\epsilon < D_{\pm}\Lambda^{-n-1-z}$. This choice guarantees that $\epsilon(\pm D_{\pm}\Lambda^{-n-z}) = \pm D_{\pm}\Lambda^{-n-z}$ and that the dispersion is linear at the grid points $g(\pm D_{\pm}\Lambda^{-n-z}) = \pm D_{\pm}\Lambda^{-n-z}$ (see Equation (2.21)). The first part of the hybridization may be written as

$$\begin{aligned}\sum_{\sigma} \int_{-D_-}^{+D_+} h(\epsilon) f_{\sigma}^{\dagger} a_{\epsilon,\sigma} d\epsilon &= \frac{1}{\sqrt{\pi}} \sum_n f_{\sigma}^{\dagger} \left(\gamma_n^{+} a_{n,0,\sigma} + \gamma_n^{-} b_{n,0,\sigma}\right) \\ &\equiv \sqrt{\frac{\xi_0}{\pi}} \sum_{\sigma} f_{\sigma}^{\dagger} f_{0\sigma},\end{aligned}$$

where $\gamma_n^{\pm 2} = \int^{\pm n} \Delta(\omega) d\omega$, and the conduction electron Wannier orbital at the impurity site is defined as $f_{0\sigma} = \frac{1}{\sqrt{\xi_0}} \sum_n \gamma_n^{+} a_{n,0,\sigma} + \gamma_n^{-} b_{n,0,\sigma}$, with $\xi_0 = \sum_n \left(\gamma_n^{+}\right)^2 + \left(\gamma_n^{-}\right)^2$.

Next, we reformulate the conduction electron kinetic energy term:

$$\begin{aligned}&\int_{-D_-}^{D_+} g(\epsilon) a_{\epsilon,\sigma}^{\dagger} a_{\epsilon,\sigma} d\epsilon \\ &\qquad = \sum_n \sum_{p,p'} a_{n,p,\sigma}^{\dagger} a_{n,p',\sigma} \int^{+n} g(\epsilon) \phi_{n,p}^{+}(\epsilon) {\phi_{n,p'}^{+}}^{*}(\epsilon) d\epsilon \\ &\qquad\qquad + b_{n,p,\sigma}^{\dagger} b_{n,p',\sigma} \int^{-n} g(\epsilon) \phi_{n,p}^{-}(\epsilon) {\phi_{n,p'}^{-}}^{*}(\epsilon) d\epsilon \\ &\qquad = \sum_n \sum_{p,p'} a_{n,p,\sigma}^{\dagger} a_{n,p',\sigma} \xi_{n,p,p'}^{+} + b_{n,p,\sigma}^{\dagger} b_{n,p',\sigma} \xi_{n,p,p'}^{-}\end{aligned}$$

$$\begin{aligned}\xi_{n,p,p'}^{\pm} &= \int^{\pm n} g(\epsilon) \phi_{n,p}^{\pm}(\epsilon) {\phi_{n,p'}^{\pm}}^{*}(\epsilon) d\epsilon \\ &= \int^{\pm n} \omega \Delta(\omega) \frac{1}{\pi h(\epsilon)^2} \phi_{n,p}^{\pm}(\epsilon) {\phi_{n,p'}^{\pm}}^{*}(\epsilon) d\omega \\ &= \frac{\int^{\pm n} \omega \Delta(\omega) d_n^{\pm} \phi_{n,p}^{\pm}(\epsilon(\omega)) {\phi_{n,p'}^{\pm}}^{*}(\epsilon(\omega)) d\omega}{\int^{\pm n} \Delta(\omega) d\omega} \\ &= \frac{\int^{\pm n} \frac{\omega \Delta(\omega) {d_n^{\pm}}^2}{\left(|\epsilon(\omega)| \ln \Lambda\right)^2} \mathrm{e}^{2\pi i (p-p') \left(\frac{\ln \frac{|\epsilon(\omega)|}{D_{\pm}}}{\ln \Lambda} + z\right)} d\omega}{\int^{\pm n} \Delta(\omega) d\omega}.\end{aligned}$$

For $\Delta(\omega) = \Delta_0$ we obtain $\epsilon(\omega) = \omega$ and only $\xi_{n,p=p'}^{\pm} = \pm \frac{d_n^{\pm}}{\ln \Lambda}$ are unequal to zero and agree with the result of Campo Jr and Oliveira [23]. Thus,

the impurity, which by construction couples only to the $p = 0$ state via the hybridization term, is completely decoupled from the $p \neq 0$ states. We now show that the same can be achieved for a general $\Delta(\omega)$ by a suitable choice of $\eta(\epsilon)$.

Following the same derivation as above, but substituting

$$\eta(\epsilon) = \int_{k_n^{(2)}}^{\epsilon} \frac{k_n^{(1)}}{g(\epsilon')} d\epsilon' \tag{2.52}$$

in Equation (2.48) leads to diagonal $\xi_{n,p,p'}$ for an arbitrary $\Delta(\omega)$. $k_n^{(1)}$ and $k_n^{(2)}$ are given by the boundary conditions $\int_{k_n^{(2)}}^{\pm D_\pm \Lambda^{-n-z}} \frac{k_n^{(1)}}{g(\epsilon')} d\epsilon' = n$ and $\int_{k_n^{(2)}}^{\pm D_\pm \Lambda^{-n-z-1}} \frac{k_n^{(1)}}{g(\epsilon')} d\epsilon' = n+1$. $c_n^\pm$ and $\gamma_n^\pm$ remain unchanged but

$$\begin{aligned}
\xi^\pm_{n,p,p'} &= \int^{\pm n} g(\epsilon) \phi^\pm_{n,p}(\epsilon) {\phi^\pm_{n,p'}}^*(\epsilon) d\epsilon \\
&= \int^{\pm n} \frac{d_n^\pm {k_n^{(1)}}^2}{g(\epsilon)} \mathrm{e}^{2\pi i (p-p') \int_{k_n^{(2)}}^{\epsilon} \frac{k_n^{(1)}}{g(\epsilon')} d\epsilon'} d\epsilon \\
&= \mp k_n^{(1)} d_n^\pm \delta_{p,p'}.
\end{aligned}$$

The $k_n^{(1)}$ can be obtained by taking the difference of the boundary conditions (as defined above), and using $\epsilon(\pm D_\pm \Lambda^{-n-z}) = \pm D_\pm \Lambda^{-n-z}$ and Equation (2.12),

$$k_n^{(1)} = \frac{\int^{\pm n} \Delta(\omega) d\omega}{\mp d_n^\pm \int^{\pm n} \frac{\Delta(\omega)}{\omega} d\omega}$$

As in Ref. [23] the resulting $\xi^\pm_{n,p=p'} \equiv \xi^\pm_{n,p=p'}(C)$ are given by[3]

$$\xi^\pm_{n,p=p'}(C) = \frac{\int^{\pm n} \Delta(\omega) d\omega}{\int^{\pm n} \frac{\Delta(\omega)}{\omega} d\omega} \tag{2.53}$$

The corresponding result, denoted by $\xi^\pm_{n,p=p'} = \xi^\pm_{n,p=p'}(B)$, in the usual logarithmic discretization scheme is given by[35, 40]

$$\xi^\pm_{n,p=p'}(B) = \frac{\int^{\pm n} \omega \Delta(\omega) d\omega}{\int^{\pm n} \Delta(\omega) d\omega}. \tag{2.54}$$

[3]Note that the derivation in Ref. [23] was actually for the two-impurity Anderson model, where the energy dependent couplings arise via the non-trivial $k$-dependence of the hybridization term $H_{\mathrm{hyb}} = V \sum_{\vec{k},j=1,2} (e^{i\vec{k}\vec{R}_j} c^\dagger_{\vec{k}} d_j + H.c.)$.

Evaluating (2.53-2.54) for a flat band with $D_+ = D_- = 1$, gives

$$\xi^{\pm}_{n,p=p'}(C) = \pm\frac{1}{2}(1+\Lambda^{-1})\Lambda^{-n-z}/A_\Lambda,\ n = 0,1,\ldots$$
$$\xi^{\pm}_{n,p=p'}(C) = \pm\frac{1}{2}(1+(\Lambda^z)^{-1})/A_{\Lambda^z},\ n = -1$$
$$\xi^{\pm}_{n,p=p'}(B) = \pm\frac{1}{2}(1+\Lambda^{-1})\Lambda^{-n-z},\ n = 0,1,\ldots$$
$$\xi^{\pm}_{n,p=p'}(B) = \pm\frac{1}{2}(1+(\Lambda^z)^{-1}),\ n = -1.$$

We see that $\xi^{\pm}_{n,p=p'}(B)/\xi^{\pm}_{n,p=p'}(C)$ is given by the factor $A_\Lambda$ ($A_{\Lambda^z}$ for $n = -1$), indicating that the Campo discretization achieves the correct estimate for $\Delta(\omega)$ via a reduction of the effective bandwidth of the discretized model. For energies close to the band edge, where the Campo discretization gives a different correction to the desired one ($A_{\Lambda^z}$ instead of $A_\Lambda$) further corrections are needed.[41]

## 2.3 Static correlation functions

The thermal average of an observable is given by

$$\langle O\rangle = \mathrm{Tr}[\rho O] \tag{2.55}$$

$$= \frac{1}{Z}\sum_n \langle n|\mathrm{e}^{-\beta H}O|n\rangle \tag{2.56}$$

$$= \frac{1}{Z}\sum_n O_{n,n}\mathrm{e}^{-\beta E_n}, \tag{2.57}$$

where $Z = \sum_n \mathrm{e}^{-\beta E_n}$ is the partition function, $O_{n,n} = \langle n|O|n\rangle$, and $|n\rangle$ and $E_n$ are the eigenstates and eigenenergies of the system.

Some observations are needed to calculate this expectation value within the standard NRG: First, energies that are much higher than the temperature do not contribute as $\exp(-\beta E_n) \approx 0$ in this case. Second, the NRG calculation can be stopped at some shell length $N$ for which the hopping term $t_n$ is of the order of the temperature. The NRG assumption then is that $H \approx H_N$ and therefore $\exp(-\beta H)|l\rangle_N \approx \exp(-\beta E_l^N)|l\rangle_N$. As a hand-waving argument, the temperature will destroy the correlations to lower energy shells. Krishna-murthy et al. [32] make a more rigorous calculation for certain quantities. The observable is therefore evaluated in shell N:

$$\langle O\rangle \approx \frac{1}{Z_N}\sum_r \mathrm{e}^{-\beta E_r^N}O_{r,r}^N, \tag{2.58}$$

where $Z_N = \sum_r \exp(-\beta E_r^N)$ is the partition function of shell length $N$.

Figure 2.5 shows results for this method only look well behaved when looking at the impurity contribution. Before the host is subtracted from the total system non local quantities like the total spin susceptibility typically look meaningless. This is partly due to the fact that for many non local quantities, the environmental degrees of freedom would give a contribution (see also Chapter 4). Local quantities on the other hand are usually well behaved and they develop smaller oscillations due to the discretization.

The optimal shell $N$ is chosen to be the one for which the hopping term $t_N$ is the smallest to be greater than the temperature [36, 38, 37]:

$$N = \max(M : \alpha t_M > T), \tag{2.59}$$

where $\alpha \approx 1$. The need to choose a best shell can be avoided by using the FDM scheme described in Section 2.6 which makes use of the complete set discarded states from all shells.

The elements $O_{l,l}^N$ can in some cases be derived from the energies and the used quantum numbers (i.e. specific heat or total spin susceptibility). For other (local) observables the operator has to be given for one of the

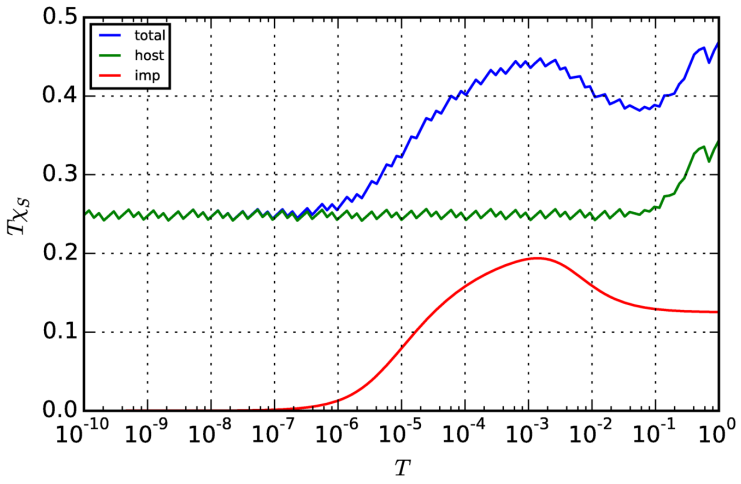


*Figure 2.5: The figure shows the total spin susceptibility. The curve looks smooth only after the host has been subtracted from the total system even though the curves are already z-averaged ($n_z = 16$, $\Lambda = 8$).*

first shells. It is then transformed along with the iterative diagonalization to lower shells.

$$ {}_N\langle r|O|r'\rangle_N = \sum_{k,i,k',j} U^N(k,i;r)^T \, {}_{N-1}\langle k,i|O|k',j\rangle_{N-1} U^N(k',j;r'). \tag{2.60} $$

While this representation is formally true, the computational effort is reduced when considering that most operators can only connect certain subspaces. Some derivations for the coefficients in the case of $SU(2)$ symmetry can be found in Appendix A.

### Temperature derivative of a thermodynamic observable

The straight forward formulation leads to

$$ \frac{\delta \langle O\rangle_T}{\delta T} = \frac{\delta\left(\frac{1}{Z(T)}\sum O_{n,n} \mathrm{e}^{-\beta E_n}\right)}{\delta T}. \tag{2.61} $$

Using product and chain rules and $\frac{d\beta}{dT} = -k_\mathrm{B}\beta^2$ yields

$$ \frac{\delta \langle O\rangle_T}{\delta T} = k_\mathrm{B}\beta^2 \left( \frac{\sum O_{n,n} E_n \mathrm{e}^{-\beta E_n}}{Z(T)} - \langle O\rangle \langle H\rangle \right) \tag{2.62} $$

$$ = k_\mathrm{B}\beta^2 \left( \langle OH\rangle - \langle O\rangle \langle H\rangle \right). \tag{2.63} $$

For example for $O = H$ we have the specific heat

$$ C(T) = k_\mathrm{B}\beta^2 (\langle H^2\rangle - \langle H\rangle^2). \tag{2.64} $$

## 2.4 Green's functions

This section will summarize briefly the definition for the retarded Green's function, the Lehmann representation and the spectral function as well as a standard NRG approach to calculate it. More detailed derivations can be found in standard literature (e.g. Reference [42, 43, 44, 45])

The retarded Green's function is defined as

$$\mathcal{G}^r_{A,B}(t-t') = -i\theta(t-t')\langle\left[A_H(t), B_H(t')\right]_\pm\rangle, \tag{2.65}$$

where

$$X_H = \mathrm{e}^{-iHt} X \mathrm{e}^{iHt}. \tag{2.66}$$

Using the Fourier transform this can be rewritten as

$$\mathrm{G}_{A,B}(\omega + i\delta) = \langle\langle A, B\rangle\rangle(\omega) = \frac{1}{Z}\sum_{n,m}\frac{\langle n|A|m\rangle\langle m|B|n\rangle}{\omega + i\delta + E_n - E_m}(\mathrm{e}^{-\beta E_n} \pm \mathrm{e}^{-\beta E_m}). \tag{2.67}$$

It fulfills the equation of motion

$$z\,\mathrm{G}_{A,B}(z) - \langle[A,B]_\pm\rangle = \mathrm{G}_{[A,H]_-,B}(z) = \mathrm{G}_{A,[H,B]_-}(z). \tag{2.68}$$

One interesting property is its role in linear response theory (see Section 2.5). Another interesting related function is the spectral function

$$\mathcal{A}_{\mathrm{A,B}}(\omega) = -\frac{1}{\pi}\,\mathrm{Im}(\mathrm{G}_{A,B}(\omega + i\delta)) \tag{2.69}$$

$$= \frac{1}{Z}\sum_{n,m}\langle n|A|m\rangle\langle m|B|n\rangle\delta(\omega + E_n - E_m)(\mathrm{e}^{-\beta E_n} \pm \mathrm{e}^{-\beta E_m}). \tag{2.70}$$

The moments of the local level spectral function will play an important role in the calculation of thermoelectric properties (see Chapter 6).

There is a successful method to calculate these quantities within the standard NRG. For static correlation functions the only relevant energy of the system was the temperature. For Green's function or spectral functions the frequency is a second energy dependence. Costi and Hewson [46] showed that evaluating $\mathcal{A}_{\mathrm{A,B}}(\omega)$ at the shell according to

$$N = \max(M : \alpha t_M > \max(T, |\omega|)), \tag{2.71}$$

where $\alpha \approx 1$ gives reasonable results for the local level spectral function. Therefore

$$\mathcal{A}_{\mathrm{A,B}}(\omega) = \sum_{N(\omega,T)}\frac{1}{Z_N}\sum_{r,r'}{}_N\langle r|A|r'\rangle_N\,{}_N\langle r'|B|r\rangle_N\delta(\omega + E^N_r - E^N_{r'})(\mathrm{e}^{E^N_r} \pm \mathrm{e}^{E^N_{r'}}). \tag{2.72}$$

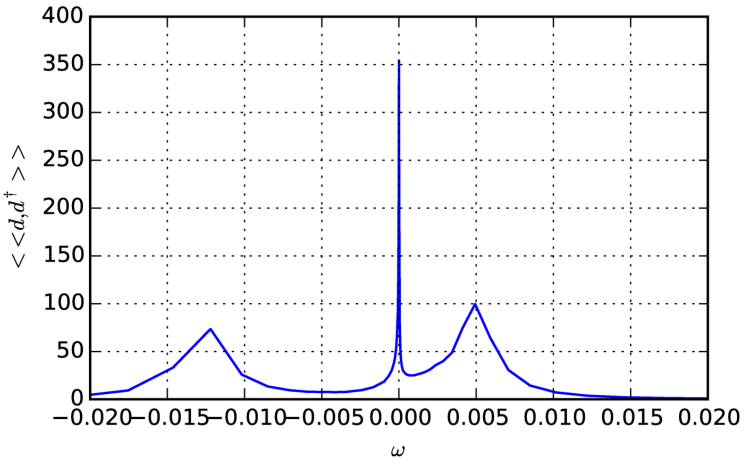


*Figure 2.6: The figure shows the spectral function $\mathcal{A}_{\mathrm{d,d}^\dagger}(\omega)$ evaluated at single shells. The discretization parameters used were $n_z = 64$ and $\Lambda = 8$.*

The delta functions have to be broadened to get a smooth result. Typically a Gaussian is used for broadening that depends on the shell $N$.

$$\delta(\omega + E_r^N - E_{r'}^N) \to \frac{1}{\sqrt{2\pi\sigma_N^2}} \mathrm{e}^{-(\omega + E_r^N - E_{r'}^N)^2/(2\sigma_N^2)}, \tag{2.73}$$

where $\sigma_N \propto t_N$. The resolution for the low energy frequencies is therefore limited by the temperature. The problem remains for the FDM approach in Section 2.6 and is discussed in more detail in Appendix C.

Figure 2.6 shows an example using this method for a low temperature. Though it is possible to calculate Green's functions in this way the FDM approach introduced in Section 2.6 tends to be more reliable. The FDM approach is therefore used in the remainder of the thesis to calculate spectral functions.

## 2.5 Linear response

This section gives a brief summery for the linear response theory. A more detailed derivation can be found in the script of Müller-Hartmann [42].

Given a small perturbation $F(t)$ coupling to the Hamiltonian $H_0$ via the operator $B$

$$H = H_0 + BF(t), \tag{2.74}$$

the effect of this perturbation on a given observable $A$ can be expressed in terms of a Green's function:

$$\langle A(t)\rangle - \overline{A} = \int_{-\infty}^{\infty} \mathrm{d}t' X_{A,B}(t-t')F(t'), \tag{2.75}$$

where the linear response function $X_{A,B}(t)$ is given by the (bosonic) negative retarded Green's function

$$X_{A,B}(t) = -\mathcal{G}^r_{A,B}(t). \tag{2.76}$$

Through Fourier transform we obtain the dynamic susceptibility

$$A_\omega = \chi_{A,B}(\omega)F_\omega, \tag{2.77}$$

where

$$\chi_{A,B}(\omega) = -\mathrm{G}_{A,B}(\omega + i\delta). \tag{2.78}$$

The adiabatic static susceptibility is then defined as

$$\chi^{\text{static}}_{A,B} = \chi_{A,B}(0) = -\mathrm{G}_{A,B}(i\delta). \tag{2.79}$$

The retarded Green's function and its calculation within the NRG are described in Section 2.4 and Section 2.6. Note that entries where the energies are roughly equal ($E_i \approx E_j$) would be excluded to avoid numerical difficulties as the principal value yields zero.

In experiments, on the other hand, the isothermal susceptibility is often measured. The adiabatic case depicts an out of equilibrium situation, where the ground states are not affected, in the isothermal case the perturbation changes the ground states. It can be calculated as

$$\chi^{\text{isothermal}}_{A,B} = \frac{\partial}{\partial F_0}\langle A\rangle_H|_{F_0=0}, \tag{2.80}$$

leading to

$$\chi^{\text{isothermal}}_{A,B} = \int_0^\beta \mathrm{d}\tau\, \langle B_\tau(A-\overline{A})\rangle_{H_0} = -G^{(0)}_{A-\overline{A},B}. \tag{2.81}$$

Here we partly introduced the Matsubara Green's function $\langle B_\tau(A-\overline{A})\rangle$ and its zero frequency coefficient $G^{(0)}_{A-\overline{A},B}$. The operator $X_\tau$ is short notation for

$$X_\tau = \mathrm{e}^{H\tau} X \mathrm{e}^{-H\tau}, \quad 0 < \tau < \beta. \tag{2.82}$$

Evaluating Equation 2.81 leads to

$$\chi_{A,B}^{\text{isothermal}} = \int_0^\beta \mathrm{d}\tau \, \langle B_\tau (A - \overline{A}) \rangle_{H_0} \tag{2.83}$$

$$= \int_0^\beta \mathrm{d}\tau \sum_{n,m} \langle n | \mathrm{e}^{-\beta H} \mathrm{e}^{\tau H} B | m \rangle \langle m | \mathrm{e}^{-\tau H} (A - \overline{A}) | n \rangle \tag{2.84}$$

$$= \int_0^\beta \mathrm{d}\tau \sum_{n,m} \mathrm{e}^{-\beta E_n} \mathrm{e}^{\tau (E_n - E_m)} [A - \overline{A}]_{m,n} B_{n,m} \tag{2.85}$$

$$= \begin{cases} \sum_{n,m} -\frac{\mathrm{e}^{-\beta E_n} - \mathrm{e}^{-\beta E_m}}{E_n - E_m} [A - \overline{A}]_{n,m} B_{m,n} & \text{if } E_n \neq E_m \\ \sum_{n,m} \beta \mathrm{e}^{-\beta E_n} [A - \overline{A}]_{n,m} B_{m,n} & \text{if } E_n = E_m \end{cases} . \tag{2.86}$$

In the last step we switched $n$ and $m$ to make the equation look similar to the regular Green's function at zero frequency. In Section 2.6.4 we will see that this can be naively implemented into the NRG scheme.

## 2.6 Full reduced density matrix

It is not always clear which shell is the most suited to evaluate a quantity. A series of developments in recent years gives rise to a method that uses all discarded states generated by the NRG thus eliminating the need to choose a shell. Hofstetter [47] introduced the reduced density matrix. Anders and Schiller [48] showed that the discarded states form a complete basis. Peters et al. [49] applied these approaches to finite temperatures. Weichselbaum and von Delft [50] developed this approach into the full density matrix (FDM). It was further extended to non abelian symmetry by Tóth et al. [51]. A short derivation can also be found in Reference [20].

### 2.6.1 Complete Basis Set

It is possible to define a complete basis set using the discarded states of a NRG run.

$$\mathbb{I} = \mathbb{I}_M^- + \mathbb{I}_M^+ \tag{2.87}$$

$$\mathbb{I}_M^- = \sum_{n\le M, l_n, e_n} |l_n\rangle|e_n\rangle\langle e_n|\langle l_n| \tag{2.88}$$

$$\mathbb{I}_M^+ = \sum_{n>M, l_n, e_n} |l_n\rangle|e_n\rangle\langle e_n|\langle l_n| \tag{2.89}$$

$$= \sum_{n=M, k_M, e_M} |k_M\rangle|e_M\rangle\langle e_M|\langle k_M|, \tag{2.90}$$

where $|e_n\rangle = |e\rangle_{n+1}|e'\rangle_{n+2}\cdots|e^{(N-n-1)}\rangle_N$ represent a environmental degrees of freedom of the uncoupled chain elements (each $e^{(n)} \in \{\varnothing, \uparrow, \downarrow, \uparrow\downarrow\}$ in the one channel case). $N$ is the total chain length. $M$ is an intermediate shell where discarded states are available $m_0 < M \le N$. $|l_n\rangle$ denote the discarded states of shell $n$ while $|k_n\rangle$ denote the kept states of shell $n$.

### 2.6.2 Static correlation functions

Using the complete basis it is straightforward to calculate static correlation functions as

$$\langle O\rangle = \frac{1}{Z}\,\mathrm{Tr}\left[\exp(-\beta H)O\right] \tag{2.91}$$

$$= \frac{1}{Z}\sum_{n, l_n, e_n} \langle e_n|\langle l_n|O\exp(-\beta H)|l_n\rangle|e_n\rangle \tag{2.92}$$

$$\approx \frac{1}{Z}\sum_{n, l_n} O^n_{l,l}\exp(-\beta E^n_l) n_e^{N-n}, \tag{2.93}$$

where the energy $E_l^n$ is measured with respect to the ground state energy of the last diagonalized shell, $N$ is the number of shells in the chain and $n_e$ is

the number of environmental states per shell ($n_e = 4$ for the 1 channel SIAM for $|\varnothing\rangle$, $|\uparrow\rangle$, $|\downarrow\rangle$ and $|\uparrow\downarrow\rangle$). The partition function is given by

$$\begin{aligned} Z &= \sum_{n,l_n,e_n} \langle e_n|\langle l_n|\mathrm{e}^{-\beta H}|l_n\rangle|e_n\rangle \\ &\approx \sum_{n,l_n} n_e^{N-n}\mathrm{e}^{-\beta E_l^n}. \end{aligned} \tag{2.94}$$

Equation (2.93) only holds if the observable $O$ is independent of the environment for example for local observables. In Chapter 4 it will be discussed that the non local total spin susceptibility $\chi_S$ will need an additional term to account for this dependency. Chapter 7 will also give a brief description for the total charge susceptibility.

In practice one has to avoid large exponentials to make sure the partition function stays within numerical limits. In later chapters this was achieved by defining a weighting for each shell $w_n$. As the energies within the NRG are usually measured with respect to the lowest energy of the current shell and not to the lowest energy of the last shell, the factor will incorporate this difference so it can act as a prefactor of the Boltzmann factors.

$$\log w_n^* = (N-n)\log n_e - \beta E_n^{\mathrm{GS}}, \tag{2.95}$$

where $E_n^{\mathrm{GS}}$ is the energy difference between the lowest energies of the current and last shell. These values are then shifted so $w_n$ will be smaller or equal to one:

$$\log w_n = \log w_n^* - \max_m\{\log w_m^*\}, \tag{2.96}$$

A similar but slightly different approach was used in Chapter 4.

### 2.6.3 Green's functions

Applying the FDM to the Green's function formalism will yield a black box approach for their calculation. The derivation is not that straightforward. Using the Lehmann representation as a starting point and fully projecting all low energy contributions to higher shells leads to a computationally complex method described in Appendix E. To make better use of the NRG approximation the starting point will be the definition of the retarded Green's function

$$\mathcal{G}_{A,B}^r(t) = -i\theta(t)\frac{1}{Z}\operatorname{Tr}\left[\mathrm{e}^{-\beta H}[A, B(t)]_\pm\right] \tag{2.97}$$

$$= -i\theta(t)\frac{1}{Z}\sum_n \langle n|\mathrm{e}^{-\beta H}(A\mathrm{e}^{iHt}B\mathrm{e}^{-iHt} \pm \mathrm{e}^{iHt}B\mathrm{e}^{-iHt}A)|n\rangle. \tag{2.98}$$

We substitute $|n\rangle$ by the complete basis set 2.87 and insert a complete basis in between $A$ and $B$.

$$\begin{aligned}\mathcal{G}^r_{A,B}(t) = -i\theta(t)\frac{1}{Z}\sum_{n,l_n,e_n}\sum_{m,l'_m e'_m} & \\ \langle e_n|\langle l_n|\mathrm{e}^{-\beta H}A\mathrm{e}^{iHt}|l'_m\rangle|e'_m\rangle\langle e'_m|\langle l'_m|B\mathrm{e}^{-iHt}|l_n\rangle|e_n\rangle & \quad (2.99)\\ \pm\langle e_n|\langle l_n|\mathrm{e}^{-\beta H}\mathrm{e}^{iHt}B|l'_m\rangle|e'_m\rangle\langle e'_m|\langle l'_m|\mathrm{e}^{-iHt}A)|l_n\rangle|e_n\rangle &\end{aligned}$$

Splitting the sums into three parts, $n > m$, $n < m$ and $n = m$, leads to

$$\begin{aligned}\mathcal{G}^{r,I}_{A,B}(t) &= -i\theta(t)\frac{1}{Z}\sum_{n=m,l_n,e_n,l'_n,e'_n} \\ &\quad \langle e_n|\langle l_n|\mathrm{e}^{-\beta H}A\mathrm{e}^{iHt}|l'_n\rangle|e'_n\rangle\langle e'_n|\langle l'_n|B\mathrm{e}^{-iHt}|l_n\rangle|e_n\rangle \quad (2.100)\\ &\quad \pm\langle e_n|\langle l_n|\mathrm{e}^{-\beta H}\mathrm{e}^{iHt}B|l'_n\rangle|e'_n\rangle\langle e'_n|\langle l'_n|\mathrm{e}^{-iHt}A|l_n\rangle|e_n\rangle \\ &= -i\theta(t)\frac{1}{Z}\sum_{n=m,l_n,e_n,l'_n,e'_n} \\ &\quad \mathrm{e}^{i(E^n_{l'}-E^n_l)t}\langle e_n|\langle l_n|\mathrm{e}^{-\beta H}A|l'_n\rangle|e'_n\rangle\langle e'_n|\langle l'_n|B|l_n\rangle|e_n\rangle \quad (2.101)\\ &\quad \pm\mathrm{e}^{i(E^n_l-E^n_{l'})t}\langle e_n|\langle l_n|\mathrm{e}^{-\beta H}B|l'_n\rangle|e'_n\rangle\langle e'_n|\langle l'_n|A|l_n\rangle|e_n\rangle \\ \mathcal{G}^{r,II}_{A,B}(t) &= -i\theta(t)\frac{1}{Z}\sum_{n>m,l_n,e_n,l'_m,e'_m} \\ &\quad \langle e_n|\langle l_n|\mathrm{e}^{-\beta H}A\mathrm{e}^{iHt}|l'_m\rangle|e'_m\rangle\langle e'_m|\langle l'_m|B\mathrm{e}^{-iHt}|l_n\rangle|e_n\rangle \quad (2.102)\\ &\quad \pm\langle e_n|\langle l_n|\mathrm{e}^{-\beta H}\mathrm{e}^{iHt}B|l'_m\rangle|e'_m\rangle\langle e'_m|\langle l'_m|\mathrm{e}^{-iHt}A|l_n\rangle|e_n\rangle \\ &= -i\theta(t)\frac{1}{Z}\sum_{n=m,k_n,e_n,l'_n,e'_n} \\ &\quad \mathrm{e}^{i(E^n_{l'}-E^n_k)t}\langle e_n|\langle k_n|\mathrm{e}^{-\beta H}A|l'_n\rangle|e'_n\rangle\langle e'_n|\langle l'_n|B|k_n\rangle|e_n\rangle \quad (2.103)\\ &\quad \pm\mathrm{e}^{i(E^n_k-E^n_{l'})t}\langle e_n|\langle k_n|\mathrm{e}^{-\beta H}B|l'_n\rangle|e'_n\rangle\langle e'_n|\langle l'_n|A|k_n\rangle|e_n\rangle \\ \mathcal{G}^{r,III}_{A,B}(t) &= -i\theta(t)\frac{1}{Z}\sum_{n<m,l_n,e_n,l'_n,e'_n} \\ &\quad \langle e_n|\langle l_n|\mathrm{e}^{-\beta H}A\mathrm{e}^{iHt}|l'_m\rangle|e'_m\rangle\langle e'_m|\langle l'_m|B\mathrm{e}^{-iHt}|l_n\rangle|e_n\rangle \quad (2.104)\\ &\quad \pm\langle e_n|\langle l_n|\mathrm{e}^{-\beta H}\mathrm{e}^{iHt}B|l'_m\rangle|e'_m\rangle\langle e'_m|\langle l'_m|\mathrm{e}^{-iHt}A|l_n\rangle|e_n\rangle \\ &= -i\theta(t)\frac{1}{Z}\sum_{n=m,l_n,e_n,k_n,e'_n} \\ &\quad \mathrm{e}^{i(E^n_k-E^n_l)t}\langle e_n|\langle l_n|\mathrm{e}^{-\beta H}A|k_n\rangle|e'_n\rangle\langle e'_n|\langle k_n|B|l_n\rangle|e_n\rangle \quad (2.105)\\ &\quad \pm\mathrm{e}^{i(E^n_l-E^n_k)t}\langle e_n|\langle l_n|\mathrm{e}^{-\beta H}B|k_n\rangle|e'_n\rangle\langle e'_n|\langle k_n|A|l_n\rangle|e_n\rangle,\end{aligned}$$

where we substituted the discarded states by kept states according to Equation (2.90) where appropriate. This is also where the NRG approximation enters as $\mathrm{e}^{iHt}|x_n\rangle = \mathrm{e}^{iE^n_x t}|x_n\rangle$, $x \in \{l, k\}$.

It turns out that, unlike for the time evolution $e^{iHt}$, for the approximate density matrix

$$\rho = \frac{1}{Z}e^{-\beta H} \approx \sum_{n,l_n,e_n} |l_n\rangle|e_n\rangle\frac{e^{-\beta E_l^n}}{Z}\langle e_n|\langle l_n|, \tag{2.106}$$

knowledge of lower shells is needed. We will achieve this by projecting the density matrix between kept and discarded states from the lower shells to the current shell. In Appendix D we will look into a different approach that allows the straightforward approximation $e^{-\beta H}|k_n\rangle = e^{-\beta E_k^n}|k_n\rangle$ by an energy shift. We define $A^n_{x,x'}$ and $B^n_{x,x'}$ as

$$O^n_{x,x'}\delta_{e_n,e'_n} \equiv \langle e_n|\langle x_n|O|x'_n\rangle|e'_n\rangle, \tag{2.107}$$

with $x, x' \in \{l, k\}$. Further the sums over the environmental degrees of freedom may yield a factor $\sum_{e_n,e'_n}\delta_{e_n,e'_n} = n_e^{N-n}$. Substituting the approximate density matrix (Equation (2.106)) into equations (2.100-2.105), we see that $\mathcal{G}^{r,I}_{A,B}(t)$ and $\mathcal{G}^{r,III}_{A,B}(t)$ can be directly evaluated as

$$\langle e_n|\langle l_n \mid l''_m\rangle|e''_m\rangle = \delta_{m,n}\delta_{l_n,l''_m}\delta_{e_n,e''_m}, \tag{2.108}$$

leading to

$$\begin{aligned}\mathcal{G}^{r,I}_{A,B}(t) = -i\theta(t)\frac{1}{Z}\sum_n n_e^{N-n} \\ \sum_{l,l'} e^{-\beta E_l^n}\left(e^{i(E^n_{l'}-E^n_l)t}A^n_{l,l'}B^n_{l',l} \pm e^{i(E^n_l-E^n_{l'})t}B^n_{l,l'}A^n_{l',l}\right)\end{aligned} \tag{2.109}$$

$$\begin{aligned}\mathcal{G}^{r,III}_{A,B}(t) = -i\theta(t)\frac{1}{Z}\sum_n n_e^{N-n} \\ \sum_{l,k} e^{-\beta E_l^n}\left(e^{i(E^n_k-E^n_l)t}A^n_{l,k}B^n_{k,l} \pm e^{i(E^n_l-E^n_k)t}B^n_{l,k}A^n_{k,l}\right).\end{aligned} \tag{2.110}$$

The first part inside the sum of $\mathcal{G}^{r,II}_{A,B}(t)$ is given by

$$\begin{aligned}\sum_{m,l''_m,e''_m} e^{i(E^n_{l'}-E^n_k)t}\langle e_n|\langle k_n \mid l''_m\rangle|e''_m\rangle e^{-\beta E^m_{l''}}\times \\ \langle e''_m|\langle l''_m|A|l'_n\rangle|e'_n\rangle\delta_{e_n,e'_n}B^n_{l',k} \pm \cdots.\end{aligned} \tag{2.111}$$

Here $\langle e_n|\langle k_n \mid l''_m\rangle|e''_m\rangle = 0$ if $m \leq n$. Therefore, when inserting a complete basis set $\mathbb{I}$ between $\rho$ and $A$, we can ignore the discarded states $\mathbb{I}_n^-$ leaving

$$\begin{aligned}\sum_{k'}\overbrace{\sum_{e_n}\sum_{m>n,l''_m,e''_m,}\langle e_n|\langle k_n \mid l''_m\rangle|e''_m\rangle e^{-\beta E^m_{l''}}\langle e''_m|\langle l''_m \mid k'_n\rangle|e_n\rangle}^{R^n_{k,k'}}\times \\ A^n_{k',l'}\delta_{e_n,e'_n}B^n_{l',k} \pm \cdots.\end{aligned} \tag{2.112}$$

Here we defined the full reduced density (FDM) matrix $R^n_{k,k'}$. It can calculated recursively. Defining

$$\underline{\underline{\mathcal{R}}}^n = \begin{pmatrix} \frac{n_e^{N-n}}{Z} \mathrm{e}^{-\beta E^n_{l_M}} & & & \\ & \ddots & & \\ & & \frac{n_e^{N-n}}{Z} \mathrm{e}^{-\beta E^n_{l_1}} & \\ & & & \underline{\underline{R}}^n \end{pmatrix}, \tag{2.113}$$

a combination of the Boltzmann factors and the FDM, where $M$ is the number of discarded states in shell $n$. The matrix $\mathcal{R}^N$ of the last shell will only contain the diagonal Boltzmann factors as all states are counted as discarded states. Further we denote the transformation ${}_{n+1}\langle e|\langle k_n \mid x_{n+1}\rangle = U^{n+1}_{e,k,x}$, where $|e\rangle_{n+1}$ is the environmental degree of freedom of shell $n+1$

$$R^n_{k,k'} = \sum_e \sum_{x,x'} U^{n+1}_{e,k,x} \mathcal{R}^{n+1}_{x,x'} {U^{n+1}_{e,k',x'}}^T. \tag{2.114}$$

The coefficients needed when $SU(2)$ symmetry is used can be found in Appendix A. The expression for $\mathcal{G}^{r,II}_{A,B}(t)$ now reads

$$\begin{aligned} \mathcal{G}^{r,II}_{A,B}(t) = -i\theta(t)\frac{1}{Z}\sum_n n_e^{N-n} \\ \sum_{l,k,k'} \mathrm{e}^{i(E^n_l - E^n_k)t} R^n_{k,k'} A^n_{k',l} B^n_{l,k} \pm \mathrm{e}^{i(E^n_k - E^n_l)t} R^n_{k,k'} B^n_{k',l} A^n_{l,k}. \end{aligned} \tag{2.115}$$

To reach to a frequency dependent representation similar to the Lehmann representation we will Fourier transform the expressions.

$$\mathrm{G}^I_{A,B}(\omega) = \sum_n \frac{n_e^{N-n}}{Z} \sum_{l,l'} \frac{\mathrm{e}^{-\beta E^n_l} \pm \mathrm{e}^{-\beta E^n_{l'}}}{\omega + E^n_l - E^n_{l'}} A^n_{l,l'} B^n_{l',l} \tag{2.116}$$

$$\begin{aligned} \mathrm{G}^{II}_{A,B}(\omega) &= \sum_n \sum_{l,k,k'} \frac{R^n_{k,k'} A^n_{k',l} B^n_{l,k}}{\omega + E^n_k - E^n_l} \\ &\pm \sum_n \sum_{l,k,k'} \frac{R^n_{k,k'} A^n_{l,k} B^n_{k',l}}{\omega + E^n_l - E^n_k} \end{aligned} \tag{2.117}$$

$$\begin{aligned} \mathrm{G}^{III}_{A,B}(\omega) &= \sum_n \frac{n_e^{N-n}}{Z} \sum_{l,k} \frac{\mathrm{e}^{-\beta E^n_l}}{\omega + E^n_l - E^n_k} A^n_{l,k} B^n_{k,l} \\ &\pm \sum_n \frac{n_e^{N-n}}{Z} \sum_{l,k} \frac{\mathrm{e}^{-\beta E^n_l}}{\omega + E^n_k - E^n_l} A^n_{k,l} B^n_{l,k}. \end{aligned} \tag{2.118}$$

Using the definition of $\mathcal{R}^n$ in Equation (2.113) it is possible to write this into one short matrix equation.

$$\mathrm{G}_{A,B}(\omega) = \sum_n \sum_{i,j} \left[ \underline{\underline{\mathcal{K}}}^n(\omega) \odot (\underline{\underline{\mathcal{R}}}^n \underline{\underline{B}}^{nT} \pm \underline{\underline{B}}^{nT} \underline{\underline{\mathcal{R}}}^n) \odot \underline{\underline{A}}^{0^n} \right]_{i,j}, \tag{2.119}$$

where in $A^{0n}_{i,j}$ the kept-kept entries of the operator $A$ have been set to zero, $\odot$ denotes the element wise product $[X \odot Y]_{i,j} = X_{i.j}Y_{i,j}$. In the case of the Green's function $\mathcal{K}^n_{i,j}(\omega) = 1/(\omega + E^n_i - E^n_j)$, but for a different quantity like the spectral function it can represent the broadened $\delta$-functions.

Examples for this method can be seen in Chapter 7 for the calculation of the conductance. A discussion about the low frequency problem and different kernels for the spectral function can be found in Appendix C.

### 2.6.4 Isothermal susceptibility

Even though the derivation is different, the structure of $\chi^{\text{iso}}_{A,B}$ (see Equation (2.86)) is very similar to the regular Green's function for $\omega = 0$. We therefore represent the isothermal susceptibility in the usual way

$$\chi^{\text{iso}}_{A,B} = -G^{(0)}_{A-\overline{A},B} \tag{2.120}$$

$$= \sum_n \sum_{i,j} \left[ \underline{\underline{\mathcal{K}}}^n \odot (\underline{\underline{\mathcal{R}}}^n \underline{\underline{B}}^{nT} - \underline{\underline{B}}^{nT} \underline{\underline{\mathcal{R}}}^n) \odot \underline{\underline{(A - \overline{A})^{0^n}}} \right]_{i,j}. \tag{2.121}$$

But we have to manipulate the entries where $E_i \approx E_j$. A possible way is to choose

$$\left[\underline{\underline{\mathcal{K}}}^n\right]_{i,j} = \begin{cases} \beta & \text{if } E_i \approx E_j \\ -\frac{1}{E_i - E_j} & \text{else} \end{cases} \tag{2.122}$$

and

$$\left[\underline{\underline{\mathcal{R}}}^n \underline{\underline{B}}^{nT} - \underline{\underline{B}}^{nT} \underline{\underline{\mathcal{R}}}^n\right]_{i,j} = \frac{n_e^{N-n}}{Z} \frac{\mathrm{e}^{-\beta E_i} + \mathrm{e}^{-\beta E_j}}{2} \left[\underline{\underline{B}}^n\right]_{i,j} \quad \text{if } E_i \approx E_j. \tag{2.123}$$

As it turns out this method yields good results for all tested linear responses and temperatures. The results are part of Chapter 7. The approach is developed independently by Fang et al. [52] to accurately calculate the local spin susceptibility. Hanl and Weichselbaum [53] use a similar approach collecting the diagonal terms separately and obtaining the remaining parts via a Kramers-Kronig relation.

### 2.6.5 Performance

Calculating spectral functions using the FDM approach can be computationally demanding. Any reformulation that reduces the number of matrix multiplications gives a significant boost in speed. Typically one is interested in the full spectrum of the Green's function or the spectral function. Optimizing the code for many different $\omega$ values is therefore expected to have the biggest speedup. Using the compact notation of Equation (2.119) we can save computation time by storing

$$(\underline{\underline{\mathcal{R}}}^n \underline{\underline{B}}^{nT} \pm \underline{\underline{B}}^{nT} \underline{\underline{\mathcal{R}}}^n) \odot \underline{\underline{A^{0^n}}}$$

and reusing it for each frequency before calculating the contribution of the next sub-Hamiltonian. Further it is worth noting that i.e. for an energy dependent Gaussian broadening scheme for the spectral function the calculated standard deviations can be reused for all frequencies. Last notice that the compact notation of Equation (2.119) uses unnecessary large matrix products. The implementation should again separate the equations into kept-discarded, discarded-kept and discarded-discarded contributions.

# Chapter 3

# New approach to specific heats

## 3.1 Introduction

Thermodynamics properties such as the specific heats are of particular interest for bulk systems. They can give information about a Fermi-liquid behavior thus the low-energy excitations. This chapter has several purposes. First we show how z-averaging significantly improves the specific heat curves calculated at large $\Lambda$. In Section 3.3 we will derive the new approach (published in Merker and Costi [54]) that is well approximated by $C_{\rm imp} = \frac{\partial E_{\rm ionic}}{\partial T} + \frac{1}{2}\frac{\partial E_{\rm hyb}}{\partial T}$. In Section 3.4 we discuss the specific heat curves for the Anderson model. Last we show that the approach can be generalized to more complex systems (Section 3.5).

At the technical level, this chapter (i) extends the NRG program by implementing z-averaging [37] thereby enabling the choice of an arbitrary temperature grid as well as a large discretization parameter $\Lambda$ and, (ii), solves numerically the thermodynamic Bethe-ansatz equations for the Anderson impurity model, allowing for reliable comparison of our NRG calculations for the specific heat (and also susceptibilities in the following chapter).

## 3.2 Conventional Approach

The usual approach to calculate the specific heat within the NRG is a two stage procedure. First the total system $H = H_{\rm imp} + H_{\rm int} + H_0$ is diagonalized followed by the diagonalization of the host Hamiltonian $H_0$. The specific heat contribution of the impurity $C_{\rm imp}(T)$ is calculated by subtracting spe-

cific heat of the host $C_0(T)$ system from the total system $C(T)$:

$$C(T) = -T\frac{\partial^2\Omega(T)}{\partial T^2} = k_B\beta^2\langle(H - \langle H\rangle)^2\rangle \tag{3.1}$$

$$C_0(T) = -T\frac{\partial^2\Omega_0(T)}{\partial T^2} = k_B\beta^2\langle(H_0 - \langle H_0\rangle)^2\rangle \tag{3.2}$$

$$C_{\text{imp}}(T) = C(T) - C_0(T). \tag{3.3}$$

Here, $\Omega(T) = -k_BT\ln Z$ is the thermodynamical potential with $Z$ being the grand canonical partition function and $\beta = 1/k_BT$ the inverse temperature.

The most reliable approaches to calculate specific heat properties so far are the Bethe ansatz method [55, 56, 57, 58, 59, 60, 61] and the NRG method. Throughout this chapter we use Bethe ansatz calculations to compare the NRG results to. For a detailed description of the Bethe ansatz calculations see Appendix G.

With the NRG method the specific heat is calculated within the approach of Campo Jr and Oliveira [23]. The Hamiltonian used after tridiagonalization reads

$$H = H_{\text{imp}} + H_{\text{int}} + \sum_{n,\sigma}\epsilon_n f^\dagger_{n,\sigma}f_{n,\sigma} + t_n(f^\dagger_{n,\sigma}f_{n+1,\sigma} + f^\dagger_{n+1,\sigma}f_{n,\sigma}). \tag{3.4}$$

A energy dependent cut-off scheme is used. Energy states $E_n^{(N)}$ with $E_n^{(N)} - E_{GS}^{(N)} < e_c t_N$ will be kept, where $E_{GS}^{(N)}$ denotes the ground state energy of the chain of length $N$. The thermodynamic function will be evaluated at the lowest shell for which $t_N > T$. A $U(1)$ symmetry for the electron number and a $SU(2)$ symmetry for the total spin is used throughout the calculation. If not mentioned otherwise a flat band with half-width $D$ is used and a constant density of states of $N_F = 1/2D$. The hybridization strength $\Delta_0$ is defined as half-width of the resonant level given by $\Delta_0 = \pi N_F V^2$. Chapter 2 offers more details on the calculation of static correlation functions or specific heat. In Figure 3.1 the result of a NRG run is depicted. The oscillations that appear due to the discretization can be canceled out effectively by averaging the results over several z-values. Figure 3.2 shows a comparison between a Bethe ansatz calculation and the corresponding NRG calculation which show good agreement. We will see that the new approach nevertheless offers advantages over the conventional method later in this chapter.

## 3.3 New Approach

In the new approach the specific heat can be expressed within one NRG run in purely local quantities:

$$C_{\text{imp}}(T) = \frac{\partial E_{\text{ionic}}}{\partial T} + \frac{1}{2}\frac{\partial E_{\text{hyb}}}{\partial T}, \tag{3.5}$$

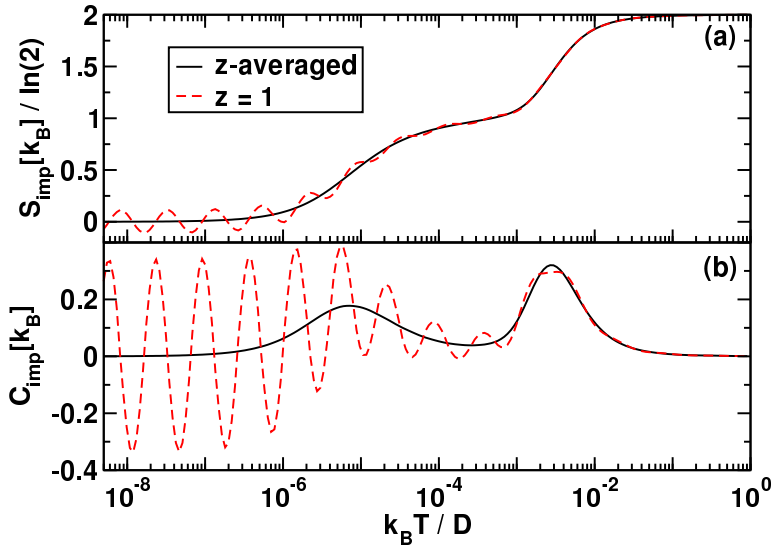


*Figure 3.1: Temperature dependence of (a) the impurity entropy $S_{imp}(T)$ and (b) the impurity specific heat $C_{imp}(T)$. The curves are calculated for the symmetric Anderson model using $\Delta_0 = 0.001D$, $U/\Delta_0 = 12$ and $\Lambda = 4$, $e_c(\Lambda = 4) = 40$. The figure depicts the difference before (dashed lines) and after (solid lines) z-averaging. For $\Lambda = 4$ two z-values [$z = 1/4, 3/4$] are sufficient to eliminate the oscillations.*

where $E_{\text{ionic}} = \langle H_{\text{imp}} \rangle$ and $E_{\text{hyb}} = \langle H_{\text{int}} \rangle$. This approach is not restricted to the NRG but can be used by any impurity solver.

The derivation is based on the Anderson impurity model (AIM) and is exact in the wide band limit, but the small derivation for the finite band width can be calculated within the one NRG run as well. Further the approach can be generalized to other models. For the AIM the three parts of the Hamiltonian consist of:

$$H = H_{\text{ionic}} + H_{\text{int}} + H_0 \tag{3.6}$$

$$H_{\text{ionic}} = \varepsilon_d n_d + U n_{d\uparrow} n_{d,\downarrow} \tag{3.7}$$

$$H_{\text{int}} = \sum_{k,\sigma} V_k (d_\sigma^\dagger c_{k,\sigma} + c_{k,\sigma}^\dagger d_\sigma) \tag{3.8}$$

$$H_0 = \sum_{k,\sigma} \epsilon_k c_{k,\sigma}^\dagger c_{k,\sigma}. \tag{3.9}$$

The impurity internal energy is given by $E_{\text{imp}} = E_{\text{total}} - E_0$, where $E_{\text{total}} = \langle H \rangle$ and $E_0 = \langle H_0 \rangle = \sum_{k,\sigma} \epsilon_k \langle c_{k,\sigma}^\dagger c_{k,\sigma} \rangle_0$, where the subscript 0 denotes the thermodynamic average for the noninteracting conduction band. The energy of the noninteracting band can also be expressed as

$$E_0 = \int f(\epsilon) \epsilon N(\epsilon) \, \mathrm{d}\epsilon \,, \tag{3.10}$$

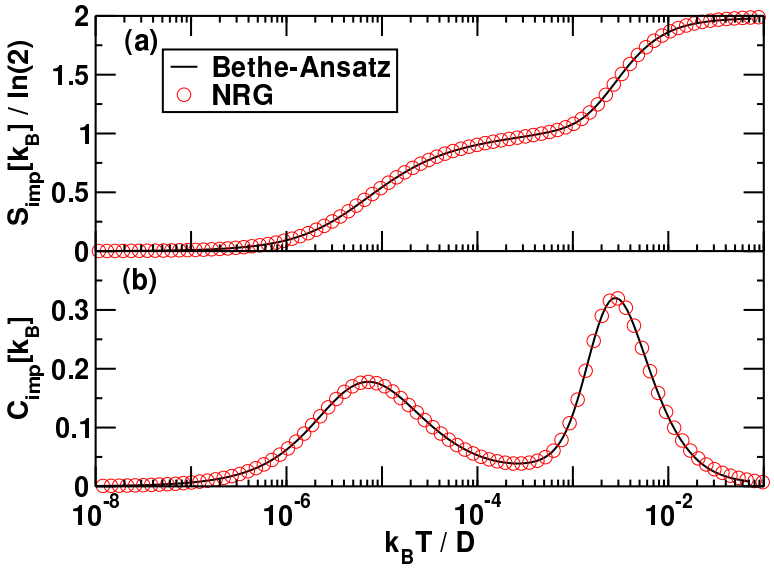


*Figure 3.2: Comparison of the NRG calculation with the Bethe ansatz results. Figure (a) shows the entropy contribution of the impurity $S_{imp}(T)$. Figure (b) shows the specific heat contribution $C_{imp}(T) = T \cdot \frac{\partial S_{imp}}{\partial T}$. Solid lines (Bethe ansatz calculation) and symbols (conventional NRG approach) are in good agreement. The same parameters as in Figure 3.1 have been used. The NRG curves were averaged using $n_z = 2$.*

where $f(\epsilon)$ is the Fermi function and $N(\epsilon) = \sum_k \delta(\epsilon - \epsilon_k)$ is the noninteracting conduction electron density of states per spin. We can separate $E_{\text{total}}$ on the other hand into

$$E_{\text{total}} = E_{\text{occ}} + E_{\text{docc}} + E_{\text{hyb}} + E_{\text{cond}}, \tag{3.11}$$

where $E_{\text{occ}} = \varepsilon_d \langle n_d \rangle$, $E_{\text{docc}} = U \langle n_{d\uparrow} n_{d\downarrow} \rangle$, $E_{\text{hyb}} = V \sum_{k,\sigma} \langle d_\sigma^\dagger c_{k,\sigma} + c_{k,\sigma}^\dagger d \rangle$ and $E_{\text{cond}} = \sum_{k,\sigma} \epsilon_k \langle c_{k,\sigma}^\dagger c_{k,\sigma} \rangle$. As $E_{\text{hyb}}$ can be expressed in terms of the impurity and the first NRG shell $E_{\text{hyb}} = V \langle d_\sigma^\dagger f_{0,\sigma} + f_{0,\sigma}^\dagger d \rangle$, the first three expressions can be calculated within the NRG. Given the local level Green's function $G_{d\sigma}(\omega) = \langle\langle d, d^\dagger \rangle\rangle_{\omega + i\delta}$ and the hybridization function $\Delta(\omega) = V^2/(\omega - \epsilon_k + i\delta)$ $E_{\text{hyb}}$ can be also expressed as

$$E_{\text{hyb}} = -\frac{2}{\pi} \int f(\omega) \operatorname{Im}(G_{d\sigma}(\omega)\Delta(\omega)) \, \mathrm{d}\omega \,. \tag{3.12}$$

This can be seen from $E_{\text{hyb}} = V \sum_{k,\sigma} \langle d_\sigma^\dagger c_{k,\sigma} + c_{k,\sigma}^\dagger d \rangle$ by using the equation of motion on $\langle\langle c_k, d^\dagger \rangle\rangle$ and using

$$\lim_{t \to 0} \langle B A_H(t) \rangle = \int \mathcal{A}_{\text{A,B}}(\omega) f(\omega) \, \mathrm{d}\omega \,, \tag{3.13}$$

where $\mathcal{A}_{\text{A,B}} = -\frac{1}{\pi} \operatorname{Im}(G_{A,B}(\omega))$.

The last term $E_{\text{cond}} = \sum_{k,\sigma} \epsilon_k \langle c_{k,\sigma}^\dagger c_{k,\sigma} \rangle$ is different from $E_0$ since the impurity affects the band contribution. Denoting the conduction electron Green's function $G_{k\sigma} = \langle\langle c_{k,\sigma}, c_{k,\sigma}^\dagger \rangle\rangle_{\omega + i\delta}$ we can use

$$G_{k\sigma} = G_{k\sigma}^0 + G_{k\sigma}^0 \mathcal{T}_\sigma G_{k\sigma}^0, \tag{3.14}$$

where $\mathcal{T}_\sigma(\omega) = V^2 G_{d\sigma}(\omega)$ is the local T matrix. $G_{k\sigma}^0(\omega) = 1/(\omega - \epsilon_k + i\delta)$ is the noninteracting conduction electron Green's function. This can be derived by applying the equation of motion to $G_{k\sigma}(\omega)$. Using Equation (3.13) we find that

$$E_{\text{cond}} = E_0 + E_{\text{int}}, \tag{3.15}$$

where

$$E_{\text{int}} = -\frac{1}{\pi} \sum_\sigma \int \mathrm{d}\omega \, f(\omega) \int \mathrm{d}\epsilon \, \operatorname{Im} \left[ \frac{\epsilon V^2 N(\epsilon)}{(\omega + i\delta - \epsilon)^2} G_{d,\sigma}(\omega) \right] \tag{3.16}$$

$$= -\frac{1}{\pi} \sum_\sigma \int \mathrm{d}\omega \, f(\omega) \operatorname{Im} \left[ G_{d\sigma}(\omega) I(\omega) \right]. \tag{3.17}$$

Here,

$$I(\omega) = -\frac{1}{\pi} \int \mathrm{d}\epsilon \, \frac{\epsilon \Delta_I(\epsilon)}{(\omega + i\delta - \epsilon)^2} = -\frac{\partial}{\partial \omega} \left[ \omega \Delta(\omega) \right], \tag{3.18}$$

where $\Delta_I(\epsilon) = \operatorname{Im}\Delta(\epsilon + i\delta) = -\pi V^2 N(\epsilon)$. For the last equivalence see Equation (3.40-3.47) at the end of the chapter. We can split $E_{\text{int}} = E_{\text{int}}^{(1)} + E_{\text{int}}^{(2)}$ into two parts

$$E_{\text{int}}^{(1)} = \frac{1}{\pi}\sum_\sigma \int \mathrm{d}\omega\, f(\omega) \operatorname{Im}\left[G_{d\sigma}(\omega)\Delta(\omega)\right] \tag{3.19}$$

$$E_{\text{int}}^{(2)} = \frac{1}{\pi}\sum_\sigma \int \mathrm{d}\omega\, f(\omega) \operatorname{Im}\left[G_{d\sigma}(\omega)\omega\frac{\partial}{\partial\omega}\Delta(\omega)\right]. \tag{3.20}$$

We note that the first part of the internal energy is proportional to the hybridization energy $E_{\text{int}}^{(1)} = -\frac{1}{2}E_{\text{hyb}}$ (compare to Equation (3.12)). Hence the impurity contribution to the energy can be summarized as

$$E_{\text{imp}} = E_{\text{occ}} + E_{\text{docc}} + \frac{1}{2}E_{\text{hyb}} + E_{\text{int}}^{(2)} \tag{3.21}$$

$$= E_{\text{ionic}} + \frac{1}{2}E_{\text{hyb}} + E_{\text{int}}^{(2)}. \tag{3.22}$$

Although $E_{\text{int}}^{(2)}$ can be calculated within a NRG run, unlike the other parts of the solution, it can not be expressed in terms of static correlation functions. For calculating the specific heat we can argue that its contribution will be small enough to be neglected in many cases. The main contribution arises from the Fermi-window $|\omega| < T$. But this region is suppressed due to the factor $\omega$ in $E_{\text{int}}^{(2)}$. Additionally in many cases $\frac{\partial}{\partial\omega}\Delta(\omega)$ is small and vanishes for example in the wide band limit of the flat band ($D \to \infty$, $\Delta_0 = \pi N(0)V^2$ fixed). For example for a constant density of states it equals $\frac{2\Delta_0}{\pi D}[1 - (\omega/D)^2]^{-1} \propto \Delta_0/D$ for $\omega \ll D$.

The impurity specific heat contributions using this approach will be calculated from $\bar{E}_{\text{imp}} = E_{\text{ionic}} + \frac{1}{2}E_{\text{hyb}}$ as

$$C_{\text{imp}} = \frac{\partial \bar{E}_{\text{imp}}}{\partial T} \tag{3.23}$$

$$= \frac{\partial E_{\text{occ}}}{\partial T} + \frac{\partial E_{\text{docc}}}{\partial T} + \frac{1}{2}\frac{\partial E_{\text{hyb}}}{\partial T} \tag{3.24}$$

$$= \frac{\partial E_{\text{ionic}}}{\partial T} + \frac{1}{2}\frac{\partial E_{\text{hyb}}}{\partial T}. \tag{3.25}$$

We quantify the error made by neglecting the $\partial E_{\text{int}}^{(2)}/\partial T$ first by comparing the different methods to the Bethe ansatz results (see Figure 3.3). The relative deviation is below 1% for all temperatures $T < 0.01D = 10\Delta_0$. For $T \ll T_K$ the relative error is 0.1% for the internal energy and 0.5% for the conventional approach. The relative error exhibits remnants of the discretization oscillations which are not completely eliminated by z-averaging. Notice also that the error correlates for both methods especially for $T \gg \Delta_0$, hinting that the error due to neglecting $\partial E_{\text{int}}^{(2)}/\partial T$ is not the main error

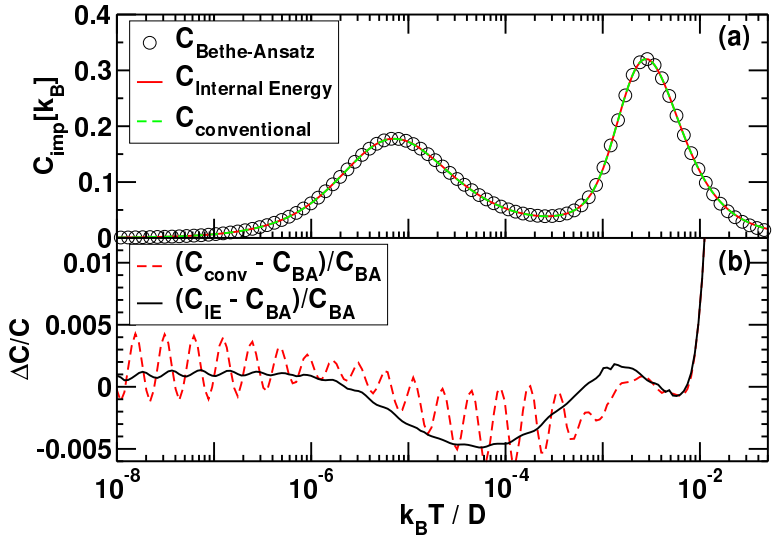


*Figure 3.3: Temperature dependence of (a) the impurity specific heat $C_{imp}(T)$ and (b) error relative to the Bethe ansatz calculation. The same parameters as in Figure 3.2 are used.*

source. The high temperature behavior instead reflects different high energy cut-off schemes between NRG and Bethe ansatz and errors introduced due to finite size effects that are largest in the shortest chains diagonalized (typically $m = 4 - 6$) which are the most sensitive to the logarithmic discretization. An explicit calculation of the error can be seen in Figure 3.4. $E_{\rm int}^{(2)}$ is of the order of $\Delta_0/\pi$ but its temperature dependence is negligible small relative to the other contributions.

The new approach offers several advantages. (i) Numerical errors are reduced as Equation (3.5) only involves a first temperature derivative with respect to the temperature. Equation (3.1-3.3) involve the second temperature derivative of the thermodynamic potential or the calculation of the total energy fluctuation. Additionally the subtraction of $C_0(T)$ from $C(T)$ can introduce numerical difficulties for low temperatures. Typically $C_0(T)$ and $C(T)$ reach a finite value for low temperatures. For the Wilson ratio for example $R \propto C_{\rm imp}/T = (C(T) - C_0(T))/T$ is needed which can not be calculated at arbitrary low temperatures due to double precision limitations (even though usually sufficiently low temperatures well below the Kondo temperature can be reached). (ii) Only one NRG calculation is needed as the host contribution $\langle H_0 \rangle$ has been subtracted analytically. (iii) Only local static correlation functions are required. Such quantities can be calculated very accurately within the NRG method. (iv) The approach is less sensitive to the oscillations introduced by the discretization. Comparing Figure 3.1 (conventional) with Figure 3.5 (new approach) one sees the drastic reduction

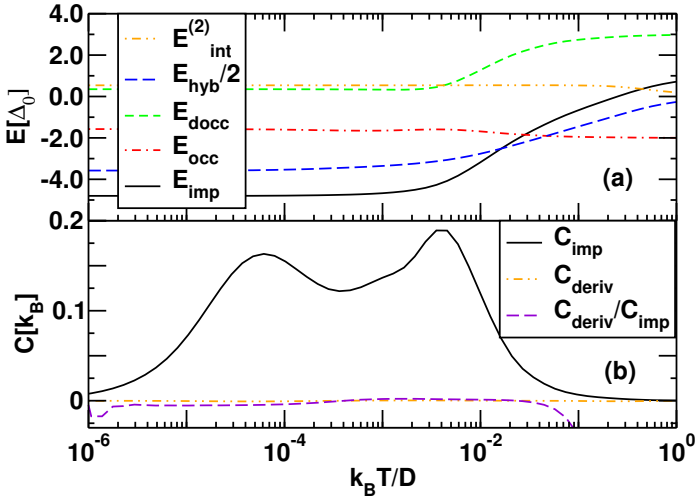


*Figure 3.4: (a) Contribution of $E^{(2)}_{int}$ to $E_{imp}$ as a function of temperature compared with the other contributions $E_{occ}$, $E_{docc}$ and $E_{hyb}/2$. This calculation uses a semi-elliptic hybridization $\mathrm{Im}(\Delta(\omega)) = -\frac{\Delta_0}{D}\sqrt{D^2-\omega^2}$ with parameters $\Delta_0 = 0.001D$, $U = 12\Delta_0$ and $\varepsilon_d = -1\Delta_0$. A small $\Lambda = 1.5$ was used which allowed to good results without z-averaging. (b) The impurity specific heat $C_{imp}(T)$ compared to $C_{deriv} = \partial E^{(2)}_{int}/\partial T$. The relative contribution lies below 0.2% to 0.5% all all temperatures except temperatures approaching the bandwidth $D = 1$.*

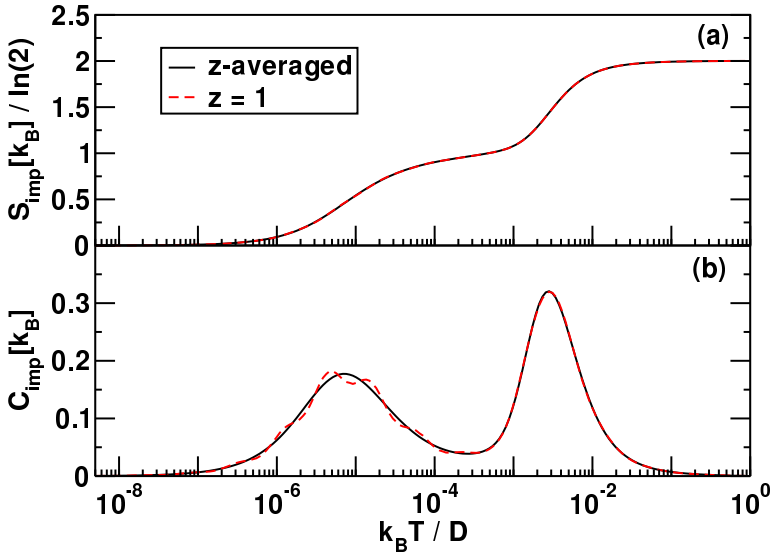


*Figure 3.5: Temperature dependence of (a) the impurity entropy $S_{imp}(T)$ and (b) the impurity specific heat $C_{imp}(T)$ using the new approach. The same parameters as in Figure 3.1 are used. The figure depicts the difference before (dashed lines) and after (solid lines) z-averaging. For $\Lambda = 4$ two z-values [$z = 1/4, 3/4$] are sufficient to eliminate the oscillations. Compared to Figure 3.1 the oscillations are drastically smaller.*

of the oscillations.

## 3.4 Results

In Figure 3.6(a), we show the different contributions $E_{\rm occ}$, $E_{\rm docc}$ and $E_{\rm hyb}/2$ to the impurity internal energy for the symmetric Anderson model. Their temperature derivatives $C_{\rm occ}$ , $C_{\rm docc}$ and $C_{\rm hyb}$ give the relative contributions of these terms to the impurity specific heat $C_{\rm imp}$ and are shown in Figure 3.6(b). Notice, that the Kondo induced peak in $C_{\rm imp}$ at low temperatures results from a delicate balance of the hybridization ($C_{\rm hyb}$) and Coulomb contributions ($C_{\rm docc}$), while the peak due to the resonant level at high temperatures is mainly due to the Coulomb term. The latter trend persists also for the asymmetric model, as shown in Figure 3.7. Notice also that the gain in energy due to hybridization diminishes at high temperatures, reflecting the decoupling of the impurity from the conduction electrons in this limit. In general, however, the interaction of the impurity with the environment via the hybridization term provides an essential contribution at all non-zero hybridization strengths.

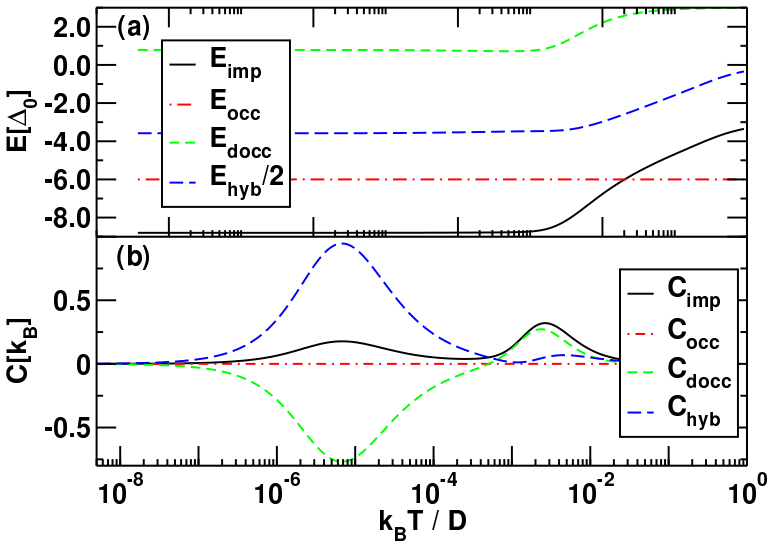


*Figure 3.6: Individual contribution of (a) $E_{occ}$, $E_{docc}$ and $E_{hyb}/2$ to $E_{imp}$ as a function of temperature for the symmetric model with parameters as in Figure 3.1. (b) Temperature derivative of the above yielding the individual contributions $C_{occ}$, $C_{docc}$ and $C_{hyb}$ to the impurity specific heat $C_{imp}$.*

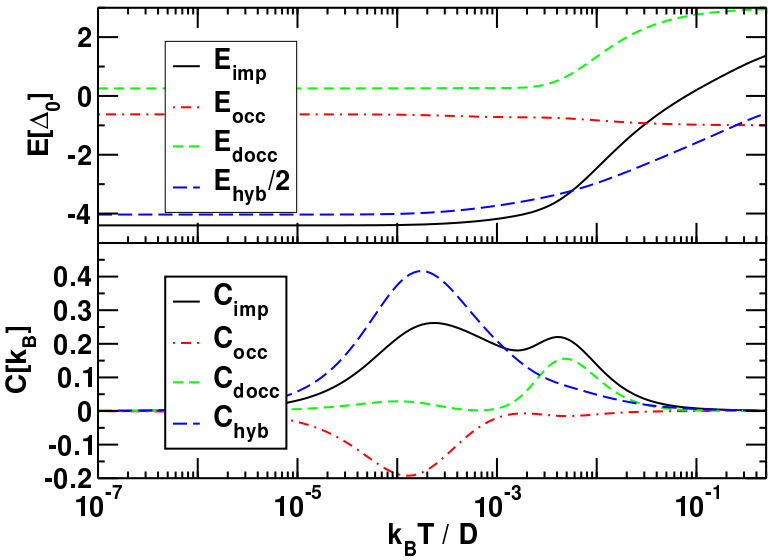


*Figure 3.7: Individual contribution of (a) $E_{occ}$, $E_{docc}$ and $E_{hyb}/2$ to $E_{imp}$ as a function of temperature for the asymmetric model with parameters as in Figure 3.1 but $\varepsilon_d = -1\Delta_0$. (b) Temperature derivative of the above yielding the individual contributions $C_{occ}$, $C_{docc}$ and $C_{hyb}$ to the impurity specific heat $C_{imp}$.*

### 3.4.1 Symmetric model

In this subsection we show results for the entropy and specific heat of the Anderson model at the particle-hole symmetric point $\varepsilon_d = -U/2$ and show the results for zero magnetic field and increasing correlation strength $U/\Delta_0$ and results for finite magnetic fields.

The symmetric Anderson model has been investigated in detail [62] and is well understood. For $U/\Delta_0 \gg 1$ and $-\varepsilon_d \gg \Delta_0$, a local spin $S = 1/2$ magnetic moment forms on the impurity. In this limit, the physics of the symmetric model at low temperatures $T \ll \min(|\varepsilon_d + U|, |\varepsilon_d|, D)$ is that of the Kondo model

$$H_{\mathrm{K}} = H_0 + J\vec{S}.\vec{s}_0, \tag{3.26}$$

where, $J$ is an antiferromagnetic exchange coupling between the local spin $S$ and the conduction electron spin-density $\vec{s}_0$ at the impurity site. The value of $J$ is given by the Schrieffer-Wolff transformation[31] $J = 8V^2/U$. The low temperature properties (for $U \gg \Delta_0$) are universal functions of $T/T_{\mathrm{K}}$ and $B/T_{\mathrm{K}}$ where we choose to define the Kondo scale from the Bethe ansatz result for the $T = 0$ susceptibility $\chi(0)$ via $\chi(0) = (g\mu_{\mathrm{B}})^2/4T_{\mathrm{K}}$. For $U \gg \Delta_0$, $T_{\mathrm{K}}$ is given by

$$T_{\mathrm{K}} = \sqrt{U\Delta_0/2}e^{-\pi U/8\Delta_0 + \pi\Delta_0/2U}, \tag{3.27}$$

within corrections which are exponentially small in $U/\pi\Delta_0$ (see Reference [62]). For $U = 0$, the symmetric Anderson model reduces to a resonant level model and the relevant low temperature scale is then $\Delta_0$.

#### Zero magnetic field

A comparison of the new approach with Bethe ansatz calculations is shown in Figure 3.8 for the temperature dependence of the impurity specific heat and entropy for increasing values of the Coulomb interaction $U/\Delta_0$. For $U/\Delta_0 = 12$, the Kondo induced peak in the specific heat at $T_{\mathrm{p}} = \alpha T_{\mathrm{K}}$ with $\alpha \approx 0.29$ is well separated from the peak at $T \approx |\varepsilon_d|$ due to the resonant level. With decreasing $U/\Delta_0$, the Kondo effect is suppressed and the Kondo induced peak in $C(T)$ eventually merges with the peak due to the resonant level for $U/\Delta_0 \to 0$. Good agreement between the NRG and the exact Bethe ansatz calculations is seen for all values of $U/\Delta_0$.

#### Finite magnetic field

At finite magnetic fields $B > 0$, the SU(2) spin symmetry which we use in the NRG calculations, is broken. Therefore, in order to carry out calculations at finite magnetic field $B > 0$, preserving the numerical advantages of the full SU(2) symmetry, such as the increased number of states that can be retained, we obtained the finite field results by mapping the symmetric positive

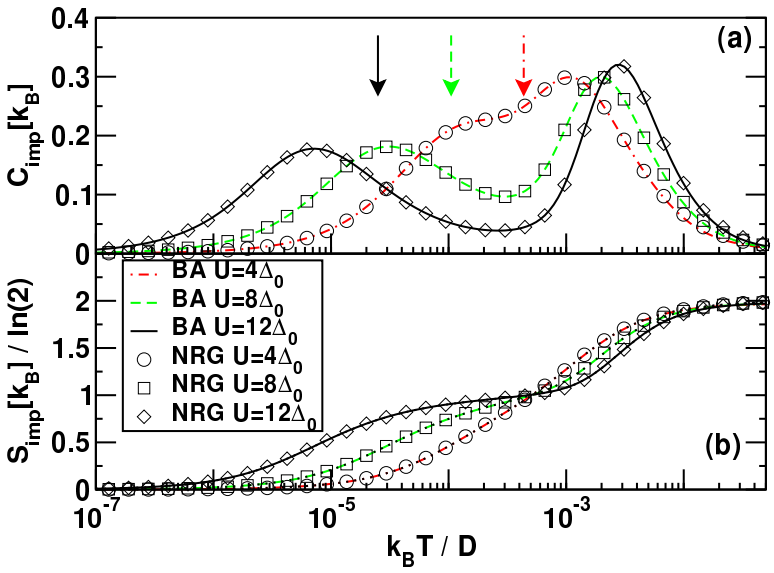


*Figure 3.8: Temperature dependence of, (a), the impurity specific heat, $C_{\rm imp}(T)$, and, (b), the impurity entropy, $S_{\rm imp}(T)/\ln(2)$, for the symmetric Anderson model with $\Delta_0 = 0.001D$ and increasing values of the Coulomb interaction: $U/\Delta_0 = 4, 8, 12$. Arrows in (a) indicated the Kondo scale $T_{\rm K}$ defined in Equation (3.27). Symbols: new approach using NRG with $\Lambda = 4$ with an energy cut-off $e_c(\Lambda = 4) = 40$, and z-averaging [$n_z = 2$, $z = 1/4, 3/4$]. Lines: corresponding Bethe ansatz calculations.*

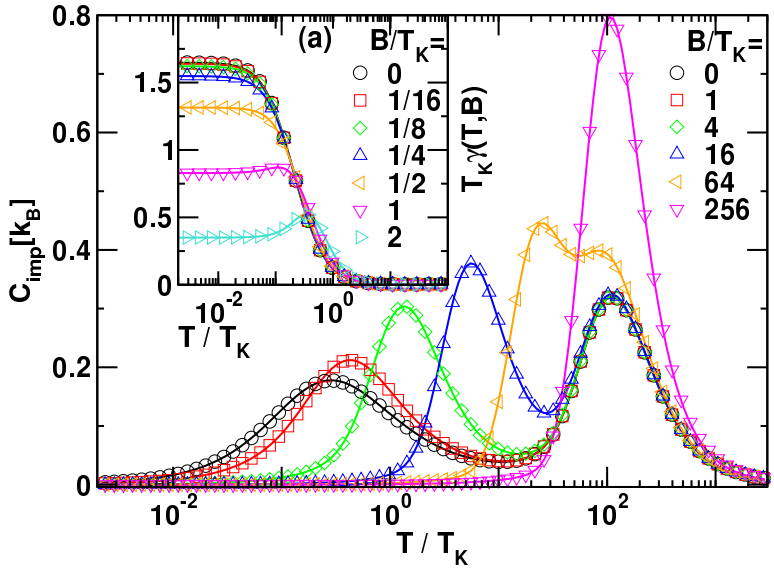


*Figure 3.9: Temperature dependence of the impurity specific heat, $C_{\rm imp}(T,B)$, for the symmetric Anderson model for $U/\Delta_0 = 12$, $\Delta_0 = 0.001D$ and increasing values of the magnetic field $B/T_{\rm K} \geq 1$ where the Kondo scale $T$ is defined in Equation (3.27). Symbols: NRG calculations $\Lambda = 4$ with an energy cut-off $e_c(\Lambda = 4) = 40$, and z-averaging [$n_z = 2$, $z = 1/4, 3/4$]. Lines: Bethe ansatz calculations. Inset (a): $T_{\rm K}\gamma(T,B)$ versus $T/T_{\rm K}$ for several values of $B/T_{\rm K} \leq 2$, where $\gamma(T,B) = C_{\rm imp}(T,B)/T$.*

$U$ Anderson model onto the negative-$U$ Anderson model in the absence of a magnetic field but with local level given by $\varepsilon_d = -U/2 - B/2$ with $U$ negative. [63, 64] This correspondence results from a particle-hole transformation on the down spins only: $d_\downarrow \to d_\downarrow^\dagger$, $d_\uparrow \to d_\uparrow$, and $c_{k\downarrow} \to c_{-k\downarrow}^\dagger, c_{k\uparrow} \to c_{k\uparrow}$ with a particle-hole symmetric band $\epsilon_k = -\epsilon_{-k}$. Figure 3.9 shows the temperature dependence of $C_{\rm imp}(T,B)$ for $B/T_{\rm K} \geq 1$ using our new approach and compared with Bethe ansatz calculations. The Kondo peak in the specific heat shifts to higher fields with increasing $B$ and its position scales as $B^2/T_{\rm K}$ for $T_{\rm K} \ll B \ll \varepsilon_d$. In contrast, the resonant level peak remains approximately fixed at $T \approx \varepsilon_d$. As $B$ approaches the value $\varepsilon_d$, the two peaks merge into one peak at $T \approx \varepsilon_d$, with approximately twice the height of the $B = 0$ resonant level peak, and containing the whole entropy $S_{\rm imp}/k_{\rm B} = \ln(4)$. The low field behavior of $C_{\rm imp}(T,B)$, also compared to Bethe ansatz calculations, is shown in Figure 3.9(a) as $T_{\rm K}\gamma(T,B) = C_{\rm imp}(T,B)/(T/T_{\rm K})$ versus $T/T_{\rm K}$ for $B/T_{\rm K} \leq 2$. For $T, B \to 0$, $\gamma(T,B) \to \gamma(0,0) \sim 1/T_{\rm K}$ where $\gamma(0,0)$ is the linear coefficient of specific heat. This is strongly enhanced for $U/\Delta_0 \gg 1$ due to the exponential decrease of $T_{\rm K}$. A finite magnetic field of order $T_{\rm K}$ significantly suppresses the Kondo effect and results in smaller values of $\gamma(0,B)$. As another check on the accuracy of our calculations, we estimate the Wilson

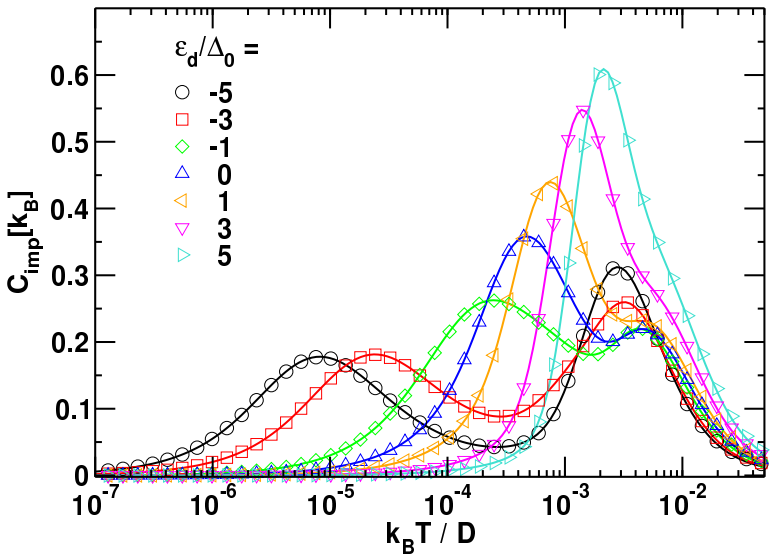


*Figure 3.10: Temperature dependence of $C_{\rm imp}(T)$ for $U/\Delta_0 = 12$, $\Delta_0 = 0.001D$ and local level positions $\varepsilon_d/\Delta_0$ ranging from Kondo ($\varepsilon_d/\Delta_0 \leq -1$), mixed valence ($|\varepsilon_d/\Delta_0| \leq 1$), and empty orbital ($\varepsilon_d/\Delta_0 > 1$) regimes. Symbols: NRG calculations (new approach, z-averaging and NRG parameters as in Figure 3.1). Lines: Bethe ansatz calculations.*

ratio $R_{\rm W} = 4\pi^2\chi(0)/3\gamma(0,0)$. This takes the value 2 in the Kondo regime of the symmetric Kondo model (i.e., for $U \gg \Delta_0$) From the definition of $T_{\rm K}$, we have that the susceptibility $\chi(0) = 1/4T_{\rm K}$, and from Figure 3.9(a) we extract $\gamma(0,0) \approx 1.64/T_{\rm K}$, resulting in $R_{\rm W} \approx 2.006$, that is, a relative error in $R_{\rm W}$ below 1%.

### 3.4.2 Asymmetric model

Figure 3.10 shows the impurity specific heat versus temperature for the asymmetric Anderson model, that is, for $\varepsilon_d > -U/2$, calculated within the new approach. For comparison, we also show the corresponding Bethe ansatz calculations. One sees again excellent agreement at all temperatures between the two methods. Results for $\varepsilon_d < -U/2$ are not shown, since these can be obtained from results for $\varepsilon_d > -U/2$ by noting that the Anderson model with parameters $\varepsilon_d, U, V$ transforms, under a particle-hole transformation applied to both spin species, to an Anderson model with parameters $-(\varepsilon_d+U), U, V$. This holds for a particle-hole symmetric constant density of states, the case considered here.

The specific heat curves for the asymmetric model are more complicated than those of the symmetric model. In the latter, the relevant excitations were the low temperature spin flip excitations, characterized by the Kondo

scale $T_K$, and the excitations involving addition or removal of an electron from the resonant level, both characterized by an energy $|\varepsilon_d| = U/2$. This accounts for the two peaks in the specific heat of the symmetric model: A high temperature peak at $T \approx |\varepsilon_d|$ and a low temperature Kondo induced peak at $T \approx T_K$. For the asymmetric Anderson model, three types of excitation are possible: Low-temperature spin flip excitations, associated with the Kondo scale $T_L = \sqrt{U\Delta_0/2}e^{-\pi|\varepsilon_d||\varepsilon_d+U|/2U\Delta_0}$ of the asymmetric model,[62] and excitations associated with, (i), removing an electron from a singly occupied level (with energy scale $|\varepsilon_d|$) and (ii), removing an electron from a doubly occupied level (with energy scale $|\varepsilon_d + U|$). Thus, three peaks can be present in $C_{\rm imp}(T)$: a Kondo induced peak at $T \approx T_L$, and two charge fluctuation induced peaks at $T \approx T_1 = |\varepsilon_d|$ and $T \approx T_2 = |\varepsilon_d + U|$, respectively. In Figure 3.10, the two high temperature peaks are seen in the mixed valence regime and partly also in the empty orbital regime (where the upper peak at $T_2$ appears as a shoulder of the main peak at $T_1$). However, in the Kondo regime, the cases $\varepsilon_d/\Delta_0 = -5, -3$ with the choice $U = 12\Delta_0$ result in $T_1/\Delta_0 = 5, 3$ and $T_2/\Delta_0 = 7, 9$. In these cases, $T_1$ and $T_2$ are too close for separate peaks to be seen. In order to clarify this, we carried out calculations for $U = 48\Delta_0 \gg \Delta_0$, and $\varepsilon_d/\Delta_0 = -10, -8, -6, -4, -2$ in the Kondo regime, for which $T_1/\Delta_0 = 10, 8, 6, 4, 2$ and $T_2/\Delta_0 = 38, 40, 42, 44, 46 \gg T_1/\Delta_0$ are disparate scales. Figure 3.11 shows how the peaks at $T \approx T_1$ and $T \approx T_2$ evolve from the peak at $T \approx |\varepsilon_d| = U/2$ of the symmetric model (dashed line in Figure 3.11) on increasing $\varepsilon_d$ above $-U/2$. Simultaneously, the Kondo peak in the specific heat at $T_L$ shifts to higher temperatures and eventually merges with the peak at $T_1$ when the mixed valence regime is reached (i.e., for $\varepsilon_d = -\Delta_0$). Thereafter, only the high temperature peaks at $T_1$ and $T_2$ are present. Notice also, that in the mixed valence regime $T_1$ differs significantly from $|\varepsilon_d|$, a result of non-trivial renormalizations present in the mixed valence regime, but absent in the empty orbital regime.

## 3.5 Generalization to other models

### 3.5.1 Multiorbital and multichannel Anderson models

The approach of Section 3.3 can be generalized to models having the form

$$H = H_{\rm imp} + H_0 + H_{\rm int} \tag{3.28}$$

$$H_{\rm imp} = \sum_{\alpha,\sigma} \varepsilon_\alpha d^\dagger_{\alpha,\sigma} d_{\alpha,\sigma} + H_C(U, U', J) \tag{3.29}$$

$$H_0 = \sum_{\alpha,k,\sigma} \epsilon_{k,\alpha} c^\dagger_{k,\alpha,\sigma} c_{k,\alpha,\sigma} \tag{3.30}$$

$$H_{\rm int} = \sum_{k,\alpha,\sigma} V_\alpha (c^\dagger_{k,\alpha,\sigma} d_{\alpha,\sigma} + d^\dagger_{\alpha,\sigma} c_{k,\alpha,\sigma}), \tag{3.31}$$

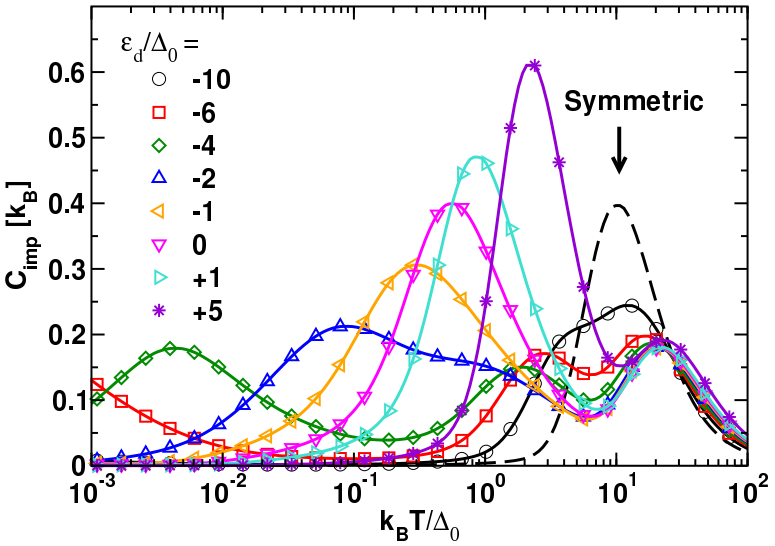


*Figure 3.11: Temperature dependence of* $C_{\rm imp}(T)$ *for* $U/\Delta_0 = 48$, $\Delta_0 = 0.0001D$ *and local level positions* $\varepsilon_d/\Delta_0 = -10, -6, -4, -2$ *(Kondo regime),* $\varepsilon_d/\Delta_0 = -1, 0, +1$ *(mixed valence regime) and* $\varepsilon_d/\Delta_0 = +5$ *(empty orbital regime). NRG using the new approach (symbols) and conventional approach (solid lines) [*$\Lambda = 20, n_z = 4, e_c(\Lambda) = 130$*]. Dashed line: resonant level peak in* $C_{\rm imp}$ *at* $T/\Delta_0 \approx |\varepsilon_d|/\Delta_0 = U/2\Delta_0 = 24$ *for the symmetric model (the Kondo induced peak at much lower* $T$ *is not shown). The two high temperature peaks of the asymmetric model evolve from this peak when the asymmetry is finite.*

where $\alpha = 1, \ldots, g$ is the band index. $H_C(U, U', J)$ is the local Coulomb interaction involving intraorbital $U$, interorbital $U'$ and Hund's exchange term $J$. $\varepsilon_\alpha$ denotes a set of local energy levels of the impurity. $\epsilon_{k,\alpha}$ is the kinetic energy of electrons in band $\alpha$. The bands hybridize with a hybridization strength $V_\alpha$. Denoting the hybridization function $\Delta_\alpha(\omega) = V_\alpha^2/(\omega - \epsilon_{k,\alpha})$. The derivation for analytically subtracting $E_{\text{imp}} = E_{\text{total}} - E_0$ is very similar to the single impurity Anderson model. The energy of the noninteracting conduction band is given by $E_0 = \sum_{k,\alpha,\sigma} \epsilon_{k,\alpha,\sigma} \langle c^\dagger_{k,\alpha,\sigma} c_{k,\alpha,\sigma} \rangle = \sum_{\alpha,\sigma} \int d\epsilon f(\epsilon) \epsilon N_\alpha(\epsilon)$, where $f(\epsilon)$ is the Fermi function and $N_\alpha(\epsilon) = \sum_k \delta(\epsilon - \epsilon_{k,\alpha})$ the noninteracting conduction electron density per spin for band $\alpha$. The total energy $E_{\text{total}}$ will be given by

$$E_{\text{total}} = E_{\text{occ}} + E_{\text{C}} + E_{\text{cond}} + E_{\text{hyb}}, \tag{3.32}$$

where the local occupation number contribution $E_{\text{occ}} = \sum_{\alpha,\sigma} \varepsilon_\alpha \langle d^\dagger_{\alpha,\sigma} d_{\alpha,\sigma} \rangle$, the local Coulomb terms $E_{\text{C}} = \langle H_C(U, U', J) \rangle$, the interacting band $E_{\text{cond}} = \sum_{\alpha,k,\sigma} \epsilon_{k,\alpha} \langle c^\dagger_{k,\alpha,\sigma} c_{k,\alpha,\sigma} \rangle$ and the hybridization energy $E_{\text{hyb}} = \sum_{\alpha,\sigma} V_\alpha \langle f^\dagger_{0,\alpha,\sigma} d_{\alpha,\sigma} + \text{H.c.} \rangle$. Following the same derivation as in Section 3.3 $E_{\text{hyb}}$ can be rewritten as:

$$E_{\text{hyb}} = -\frac{2}{\pi} \sum_{\alpha,\sigma} \int \mathrm{d}\omega \ \mathrm{Im}[G_{d,\alpha,\sigma}(\omega) \Delta_\alpha(\omega)], \tag{3.33}$$

and $E_{\text{cond}} = E_0 + E_{\text{int}}$, where

$$\begin{aligned} E_{\text{int}} &= \frac{1}{\pi} \sum_{\alpha\sigma} \int \mathrm{d}\omega \, f(\omega) \mathrm{Im} \left[ G_{d\alpha\sigma}(\omega) \frac{\partial}{\partial \omega} \left( \omega \Delta_\alpha(\omega) \right) \right] \\ &= E^{(1)}_{\text{int}} + E^{(2)}_{\text{int}}, \end{aligned} \tag{3.34}$$

$$E^{(1)}_{\text{int}} = \frac{1}{\pi} \sum_{\alpha\sigma} \int \mathrm{d}\omega \, f(\omega) \mathrm{Im} \left[ G_{d\alpha\sigma}(\omega) \Delta_\alpha(\omega) \right] \tag{3.35}$$

$$E^{(2)}_{\text{int}} = \frac{1}{\pi} \sum_{\alpha\sigma} \int \mathrm{d}\omega \, f(\omega) \mathrm{Im} \left[ G_{d\alpha\sigma}(\omega) \omega \frac{\partial \Delta_\alpha(\omega)}{\partial \omega} \right], \tag{3.36}$$

with $G_{d\alpha\sigma}(\omega)$ being the retarded Green's function for the local level $\alpha$. Now the band contribution can be analytically subtracted leading to

$$E_{\text{imp}} = E_{\text{occ}} + E_{\text{C}} + \frac{1}{2} E_{\text{hyb}} + E^{(2)}_{\text{int}}. \tag{3.37}$$

All contributions except $E^{(2)}_{\text{int}}$ can be calculated using local static correlation functions. The temperature dependence of $E^{(2)}_{\text{int}}$ can be neglected in many cases for the same reasons as stated in Section 3.3. The specific heat can be calculated to high accuracy via

$$C_{\text{imp}} = \frac{\partial E_{\text{occ}}}{\partial T} + \frac{\partial E_{\text{C}}}{\partial T} + \frac{1}{2} \frac{\partial E_{\text{hyb}}}{\partial T} \tag{3.38}$$

$$= \frac{\partial E_{\text{ionic}}}{\partial T} + \frac{1}{2} \frac{\partial E_{\text{hyb}}}{\partial T}, \tag{3.39}$$

where $E_{\text{ionic}} = \langle H_{\text{imp}} \rangle$.

## 3.6 Supplementary calculations

To prove the equivalence in Equation (3.18) we first performed an integration by parts using $\Delta(\omega) = \sum_k V^2/(\omega + i\delta - \epsilon_k) = \Delta_R(\omega) + \Delta_I(\omega)$

$$I(\omega) = -\frac{1}{\pi}\int \mathrm{d}\epsilon\, \frac{\epsilon\Delta_I(\epsilon)}{(\omega + i\delta - \epsilon)^2} \tag{3.40}$$

$$= -\frac{1}{\pi}\int \mathrm{d}\epsilon\, \epsilon\Delta_I(\epsilon)\frac{\partial}{\partial\epsilon}\frac{1}{(\omega + i\delta - \epsilon)} \tag{3.41}$$

$$= -\frac{1}{\pi}\frac{\epsilon\Delta_I(\epsilon)}{(\omega + i\delta - \epsilon)}\Bigg|_{-D}^{D} + \frac{1}{\pi}\int \mathrm{d}\epsilon\, \frac{1}{(\omega + i\delta - \epsilon)}\frac{\partial}{\partial\epsilon}(\epsilon\Delta_I(\epsilon)). \tag{3.42}$$

As there are no energies outside $[-D, D]$ the first integrated part is zero. Re-substituting $\Delta_I(\epsilon) = -\pi V^2 \sum_k \delta(\epsilon - \epsilon_k)$

$$I(\omega) = -\int \mathrm{d}\epsilon\, \frac{1}{(\omega + i\delta - \epsilon)}\frac{\partial}{\partial\epsilon}(\epsilon\sum_k V^2\delta(\epsilon - \epsilon_k)) \tag{3.43}$$

$$= -V^2\sum_k \int \mathrm{d}\epsilon\, \frac{\delta(\omega - \epsilon_k)}{(\omega + i\delta - \epsilon)} + \frac{\epsilon\frac{\partial}{\partial\epsilon}\delta(\omega - \epsilon_k)}{(\omega + i\delta - \epsilon)} \tag{3.44}$$

$$= -\Delta(\omega) + V^2\sum_k \int \mathrm{d}\epsilon\, \delta(\omega - \epsilon_k)\frac{\partial}{\partial\epsilon}\frac{\epsilon}{(\omega + i\delta - \epsilon)} \tag{3.45}$$

$$+\frac{1}{\pi}\frac{\epsilon\Delta_I(\epsilon)}{(\omega + i\delta - \epsilon)}\Bigg|_{-D}^{D}$$

$$= -\Delta(\omega) + V^2\sum_k \frac{\omega + i\delta}{(\omega + i\delta - \epsilon_k)^2} \tag{3.46}$$

$$= -\frac{\partial}{\partial\omega}\left[\omega\Delta(\omega)\right]. \tag{3.47}$$

# Chapter 4

# FDM approach to thermodynamics

.

## 4.1 Introduction

In this chapter we apply the full density matrix (FDM) approach to the calculation of static correlation functions, such as the spin susceptibility, of the SIAM and compare the results from this approach to the conventional approach and to the Bethe-ansatz results (published in Merker et al. [65]). We point out, in particular, that a non-negligible contribution of the uniform susceptibility arises from the environmental degrees of freedom. Furthermore, we will numerically confirm the Clogston-Anderson compensation theorem.

In Section 4.2 we specify the Anderson impurity model, and outline the conventional approach to thermodynamics within the NRG method [23]. The FDM approach to thermodynamics is described in Section 4.3. Section 4.4 contains our results. The impurity contribution to the specific heat, $C_{\mathrm{imp}}$, calculated within the FDM approach, is compared with Bethe ansatz calculations [66, 67, 57, 56, 68, 69, 55] and to calculations using the conventional approach in Section 4.4.1. The impurity contribution to the susceptibility, $\chi_{\mathrm{imp}}$, with the magnetic field acting on both impurity and conduction electron states, calculated within FDM is compared with corresponding results from Bethe ansatz and the conventional approach within NRG in Section 4.4.2). Results for the Wilson ratio as a function of the local Coulomb repulsion and the local level position are also given in Section 4.4.2). In Section 4.4.3 we consider also the local susceptibility of the Anderson model, $\chi_{\mathrm{loc}}$, with a magnetic field acting only on the impurity, and show by comparison with Bethe ansatz results for $\chi_{\mathrm{imp}}$, that $\chi_{\mathrm{loc}} = \chi_{\mathrm{imp}}$ for both the symmetric and asymmetric Anderson model in the wide-band

limit. In addition, we also compare the FDM and conventional approaches for another local quantity, the double occupancy, in Section 4.4.4. Section 4.5 contains our summary. Details of the numerical solution of the thermodynamic Bethe ansatz equations may be found in Appendix G.

## 4.2 Model, method and conventional approach to thermodynamics

We consider the Anderson impurity model [30] in a magnetic field $B$, described by the Hamiltonian

$$H = H_{\rm imp} + H_0 + H_{\rm int} + H_B.$$

The first term, $H_{\rm imp} = \sum_\sigma \varepsilon_d d^\dagger_\sigma d_\sigma + U n_{d\uparrow} n_{d\downarrow}$, describes the impurity with local level energy $\varepsilon_d$ and on-site Coulomb repulsion $U$, the second term, $H_0 = \sum_{k\sigma} \epsilon_k c^\dagger_{k\sigma} c_{k\sigma}$, is the kinetic energy of non-interacting conduction electrons with dispersion $\varepsilon_k$, the third term, $H_{\rm int} = V \sum_{k\sigma} (c^\dagger_{k\sigma} d_\sigma + d^\dagger_\sigma c_{k\sigma})$, is the hybridization between the local level and the conduction electron states, with $V$ being the hybridization matrix element, and, the last term $H_B = -g\mu_{\rm B} B\, S_{z,tot}$ where $S_{z,tot}$ is the $z$-component of the total spin (i.e. impurity plus conduction electron spin), is the uniform magnetic field acting on impurity and conduction electrons. $g$ is the electron g-factor, and $\mu_{\rm B}$ is the Bohr magneton. We choose units such that $g = \mu_{\rm B} = 1$ and assume a constant conduction electron density of states per spin $N(\epsilon) = 1/2D$, where $D = 1$ is the half-bandwidth. The hybridization strength is denoted by $\Delta_0 = \pi V^2 N(0)$ and equals the half-width of the non-interacting resonant level.

The NRG procedure[32, 33, 18] as described in Chapter 2 is used to iteratively diagonalize the Anderson model. Unless otherwise stated, we use conservation of total electron number $N_e$, total spin $S$, and total $z$-component of spin $S_z$ in the iterative diagonalization of $H$ at $B = 0$, so the eigenstate $|p; m\rangle$ is an abbreviation for the eigenstate $|N_e S S_z p; m\rangle$ of $H_m$, with energy $E^m_{N_e S p}$ (abbreviated as $E^m_p$) where the index $p = 1, \ldots$ distinguishes states with the same conserved quantum numbers. As long as $m \le m_0 - 1$, where typically $m_0 = 4 - 6$, all states are retained. For $m \ge m_0$, only the lowest energy states are used to set up the Hamiltonian $H_{m+1}$. These may be a fixed number $N_{\rm keep}$ of the lowest energy states, or one may specify a predefined $m_0$, and retain only those states with rescaled energies $(E^m_p - E^m_{GS})/t_m(z) < e_c(\Lambda)$, where $E^m_{GS}$ is the (absolute) ground state energy at iteration $m$ and $e_c(\Lambda)$ is $\Lambda$-dependent cut-off energy. [70, 37, 71] For most results in this chapter, we used $m_0 = 4, 5$, respectively for $H$, $H_0$, and $e_c(\Lambda) = 15\sqrt{\Lambda} \approx 47$ for $\Lambda = 10$ and found excellent agreement with exact continuum results from Bethe ansatz (after appropriate $z$-averaging,

see below). Calculations at smaller $\Lambda = 4$, using $m_0 = 5, 6$ for $H$, $H_0$, respectively, and $e_c(\Lambda) = 40$ were also carried out for the local susceptibility in Section 4.4.3. These showed equally good agreement with corresponding continuum Bethe ansatz results, indicating that the $m_0$ and $\Lambda$-dependence of our results (after $z$-averaging) is negligible. In our notation, the number of retained states at iteration $m$ (before truncation) grows as $4^{m+1}$, so the value of $m_0$ cannot be increased much beyond 5, in practice, due to the exponential increase in storage and computer time. As our calculations show, this is also not necessary, since agreement with exact Bethe ansatz calculations is achieved already for $m \geq m_0 = 4, 5$.

The impurity contribution to the specific heat is defined by $C_{\rm imp}(T) = C(T) - C_0(T)$, where $C(T)$ and $C_0(T)$ are the specific heats of $H$ and $H_0$, respectively. Similarly, the impurity contribution to the zero field susceptibility is given by $\chi_{\rm imp}(T) = \chi(T) - \chi_0(T)$, where $\chi(T)$ and $\chi_0(T)$ are the susceptibilities of $H$ and $H_0$, respectively. Denoting by $Z(T, B)$ and $Z_0(T, B)$ the partition functions of $H$ and $H_0$, and $\Omega(T, B) = -k_{\rm B}T \ln Z(T, B)$ and $\Omega_0(T, B) = -k_{\rm B}T \ln Z_0(T, B)$ the corresponding thermodynamic potentials, we have,

$$C(T) = -T\frac{\partial^2 \Omega(T)}{\partial\, T^2} = k_{\rm B}\beta^2 \langle (H - \langle\, H\rangle)^2\rangle, \tag{4.1}$$

$$C_0(T) = -T\frac{\partial^2 \Omega_0(T)}{\partial\, T^2} = k_{\rm B}\beta^2 \langle (H_0 - \langle\, H_0\rangle)^2\rangle_0, \tag{4.2}$$

$$\chi(T) = -\frac{\partial^2 \Omega(T, B)}{\partial\, B^2}|_{B=0} = \beta(g\mu_{\rm B})^2 \langle S^2_{z,tot}\rangle, \tag{4.3}$$

$$\chi_0(T) = -\frac{\partial^2 \Omega_0(T, B)}{\partial\, B^2}|_{B=0} = \beta(g\mu_{\rm B})^2 \langle {S^0_{z,tot}}^2\rangle_0, \tag{4.4}$$

where $S^0_{z,tot}$ is the $z$-component of total spin for $H_0$.

We follow the approach of Campo Jr and Oliveira [23], which we term the "conventional" approach, to calculate the thermodynamic averages appearing in (4.1-4.4) at large $\Lambda \gg 1$ (thermodynamic calculations at smaller values of $\Lambda \lesssim 3$ are also possible,[32, 72] however, truncation errors increase with decreasing $\Lambda$): for any temperature $T$, we choose the smallest $m$ such that $k_B T > t_m(z)$ and we use the eigenvalues of $H_m$ to evaluate the partition function $Z_m(T) = \sum_p e^{-E^m_p/k_{\rm B}T}$ and the expectation values appearing in (4.1-4.4). Calculations for several $z = (2i-1)/2n_z, i = 1, \ldots, n_z$ with typically $n_z = 2, 4$ or 8 are carried out and averaged in order to eliminate discretization induced oscillations at large $\Lambda \gg 1$. A dense grid of temperatures defined on a logarithmic scale from $10^{-4}T_{\rm K}$ to $2D$ was used throughout, where $T_K$ is the Kondo scale for the symmetric Anderson model for given $U$ [see Equation (4.15)]. An advantage of the FDM approach, which we describe next, is that such a dense grid of temperatures can be used without the requirement to choose a best shell for a given $T$ and $z$. This is possible within

the FDM approach, because the partition function of the latter contains all excitations from all shells.

## 4.3 Thermodynamics within the FDM approach

As an alternative approach, the FDM approach, as described in Chapter 2.6, can be used. In this Chapter we will use slightly different definitions for the weighting factors. In correspondence with Reference [20] the factors $w_m$ are defined as

$$w_m = d^{N-m}\frac{Z_m}{Z}, \tag{4.5}$$

where $d^{N-m}$ is the factor resulting from the trace over the environmental degrees of freedom ($d = 4$ for one-channel SIAM), $Z_m = \sum_l \mathrm{e}^{-\beta E_l^m}$ is the sum over the discarded states of one shell and the energies $E_l^m$ are measured with respect to the final ground state. This definition has the property $\sum_m w_m = 1$. The FDM is then defined as

$$\rho = \sum_{m=m_0}^{N}\sum_{le}|lem\rangle\frac{e^{-\beta E_l^m}}{Z(T)}\langle lem| = \sum_{m=m_0}^{N} w_m\tilde{\rho}_m, \tag{4.6}$$

where $\tilde{\rho}_m = \sum_{le}|lem\rangle\frac{e^{-\beta E_l^m}}{\tilde{Z}_m}\langle lem|$ using $\tilde{Z}_m = d^{N-m}Z_m$.

Substituting $\rho = \sum_{m'} w_{m'}\tilde{\rho}_{m'}$ into the expression for the thermodynamic average $\langle\hat{O}\rangle$ and making use of the decomposition of unity Equation (2.87), we have

$$\begin{aligned}
\langle\hat{O}\rangle_\rho &= \mathrm{Tr}\left[\rho\hat{O}\right] \\
&= \sum_{l'e'm'}\langle l'e'm'|\hat{O}\sum_{lem} w_m|lem\rangle\frac{e^{-\beta E_l^m}}{\tilde{Z}_m}\langle lem|l'e'm'\rangle \\
&= \sum_{lem} O_{ll}^m w_m\frac{e^{-\beta E_l^m}}{\tilde{Z}_m} \qquad (4.7)\\
&= \sum_{lm} d^{N-m}w_m O_{ll}^m\frac{e^{-\beta E_l^m}}{d^{N-m}Z_m} \\
&= \sum_{m=m_0,l}^{N} w_m O_{ll}^m\frac{e^{-\beta E_l^m}}{Z_m}, \qquad (4.8)
\end{aligned}$$

where orthonormality $\langle lem|l'e'm'\rangle = \delta_{ll'}\delta_{ee'}\delta_{mm'}$, and the trace over the $N-m$ environment degrees of freedom $\sum_{lem}\cdots = \sum_{lm} d^{N-m}\ldots$ has been used and $O_{ll}^m = \langle lm|\hat{O}|lm\rangle$. A similar expression applies for expectation values $\langle\hat{O}\rangle_{\rho_0}$ with respect to the host system $H_0$. For each temperature $T$ and shell $m$, we require $w_m(T)$ and the factor $B_l^m(T) = e^{-\beta E_l^m}/Z_m$ where $Z_m = \sum_l e^{-\beta E_l^m}$. Numerical problems due to large exponentials are avoided by calculating

$B_l^m(T) = e^{-\beta(E_l^m - E_0^m)}/Z'_m$ where $Z'_m = e^{\beta E_0^m} Z_m$ and $E_0^m$ is the lowest energy for shell $m$.

The calculation of the full partition function $Z(T)$, like the weights $w_m(T)$, requires care in order to avoid large exponentials (see Costi and Zlatić [20]). Note also, that the energies $E_l^m$ in the above expressions denote absolute energies of $H_m$. In this Chapter in the NRG calculation one defines rescaled Hamiltonians $\bar{H}_m$ in place of $H_m$, with rescaled energies $\bar{E}_l^m$ shifted so that the ground state energy of $\bar{H}_m$ is zero. In the FDM approach, information from different shells is combined. This requires that energies from different shells be measured relative to a common ground state energy, which is usually taken to be the absolute ground state energy of the longest chain diagonalized. Hence, it is important to keep track of rescaled ground state energies of the $\bar{H}_m$ so that the $\bar{E}_l^m$ can be related to the absolute energies $E_l^m$ used in the FDM expressions for thermodynamic averages (this relation is specific to precisely how the sequence $\bar{H}_m$, $m = 1, 2, \ldots$ is defined, so we do not specify it here).

The specific heat $C_{\rm imp}(T) = C(T) - C_0(T)$ is obtained from separate calculations for $H$ and $H_0$. For $H$, we first calculate $E = \langle H \rangle$ using (4.8):

$$\langle H \rangle_\rho = \sum_{m=m_0,l}^{N} w_m E_l^m B_l^m, \tag{4.9}$$

and then substituting this into Equation (4.1) to obtain

$$\begin{aligned} C(T) &= k_{\rm B}\beta^2 \langle (H - \langle H \rangle)^2 \rangle \\ &= k_{\rm B}\beta^2 \sum_{m=m_0,l}^{N} w_m (E_l^m - E)^2 B_l^m, \end{aligned} \tag{4.10}$$

with a similar calculation for $H_0$ to obtain $C_0(T)$. The specific heats are then $z$-averaged and subtracted to yield $C_{\rm imp}(T) = C(T) - C_0(T)$. Alternatively, the specific heat $C(T)$ may be obtained from the $z$-averaged entropy $S(T)$ via $C(T) = -T\partial S/\partial T$, where $S$ is calculated from $E$ and $Z$ using $S = -\partial\Omega/\partial T = k_{\rm B} \ln Z + E/T$ (with similar expressions for $C_0(T)$ and $S_0(T)$). We note that in cases where explicit numerical derivatives of the thermodynamic potential with respect to magnetic field or temperature are required, the NRG supplies a sufficiently smooth $\Omega(T, B)$ for this to be possible (see Costi et al. [72] for an early application). We show this within the FDM approach for the case of the local magnetic susceptibility in Section 4.4.3, a quantity that requires a numerical second derivative of $\Omega(T, B)$ with respect to $B$.

The susceptibility from (4.3-4.4) requires more care, since a uniform field acts also on the environment degrees of freedom, implying that we require the expectation value $\langle (S_z + S_{z,e})^2 \rangle$ in evaluating $k_{\rm B}T\chi(T, B = 0)/(g\mu_B)^2$ (and similarly for $k_{\rm B}T\chi_0(T, B = 0)/(g\mu_B)^2$), where $S_z$ refers to total $z$-component of spin for the system $H_m$ and $S_{z,e}$, the total $z$-component of

the $N-m$ environment states $e$. Now $\langle (S_z+S_{z,e})^2\rangle = \langle (S_z^2+S_{z,e}^2)\rangle$ since the trace over $S_z$ (or $S_{z,e}$) of the cross-term $2S_zS_{z,e}$ will vanish. Hence, the susceptibility will have an additional contribution $\chi_{\rm E} = \beta(g\mu_{\rm B})^2\langle S_{z,e}^2\rangle$ due the environment degrees of freedom in addition to the usual term $\chi_{\rm S} = \beta(g\mu_{\rm B})^2\langle S_z^2\rangle$ for the system $H_m$. Evaluating the latter via (4.8), indicating explicitly the conserved quantum number $S_z$ in the trace with all other conserved quantum numbers indicated by $l$, results in

$$\begin{aligned}\frac{k_{\rm B}T\chi_{\rm S}}{(g\mu_B)^2} &= \langle S_z^2\rangle = \sum_{m=m_0,S_z,l}^{N} w_m S_z^2 B_l^m \\ &= \sum_{m=m_0,l}^{N} f_1(S) w_m B_l^m, \end{aligned} \tag{4.11}$$

where $\sum_{S_z} S_z^2 = f_1(S) = (2S+1)((2S+1)^2-1)/12$ has been used. For the term $\chi_{\rm E}$, we have from (4.7)

$$\frac{k_{\rm B}T\chi_{\rm E}}{(g\mu_B)^2} \equiv \langle S_{z,e}^2\rangle = \sum_{m=m_0,S_z,l,e}^{N} w_m S_{z,e}^2 \frac{e^{-\beta E_l^m}}{\tilde{Z}_m}. \tag{4.12}$$

Since $\tilde{Z}_m = d^{N-m}Z_m$ and denoting by $Z_e = d^{N-m}$ the partition function of the $N-m$ environment degrees of freedom, we can rewrite the above as

$$\begin{aligned}&\sum_{m=m_0,S_z,l,e}^{N} w_m S_{z,e}^2 \frac{e^{-\beta E_l^m}}{\tilde{Z}_m} \\ =\ &\sum_{m=m_0,S_z,l}^{N} w_m {\rm Tr}_e\left[\frac{S_{z,e}^2}{Z_e}\right]\frac{e^{-\beta E_l^m}}{Z_m} \\ =\ &\sum_{m=m_0,l}^{N} w_m f_2(S)\frac{N-m}{8} B_l^m,\end{aligned}$$

where $f_2(S) = \sum_{S_z} = (2S+1)$ and we used the fact that ${\rm Tr}_e S_{z,e}^2/Z_e = (N-m)/8$ since for one environment state $\langle S_{z,e_i}^2\rangle_{e_i} \equiv {\rm Tr}_{e_i} S_{z,e_i}^2/Z_{e_i} = (1/4{+}1/4)/4 = 1/8$ (for $d=4$). Hence, we have

$$\frac{k_{\rm B}T\chi_{\rm E}}{(g\mu_B)^2} = \sum_{m=m_0,l}^{N} f_2(S)\frac{N-m}{8} w_m B_l^m, \tag{4.13}$$

and the total susceptibility $\chi(T) = \chi_{\rm S}(T) + \chi_{\rm E}(T)$ is given by

$$\begin{aligned}\frac{k_{\rm B}T\chi(T)}{(g\mu_B)^2} &\equiv \frac{k_{\rm B}T\chi_{\rm S}(T)}{(g\mu_B)^2} + \frac{k_{\rm B}T\chi_{\rm E}(T)}{(g\mu_B)^2} \\ &= \sum_{m=m_0,l}^{N} (f_1(S) + f_2(S)\frac{N-m}{8}) w_m B_l^m, \end{aligned} \tag{4.14}$$

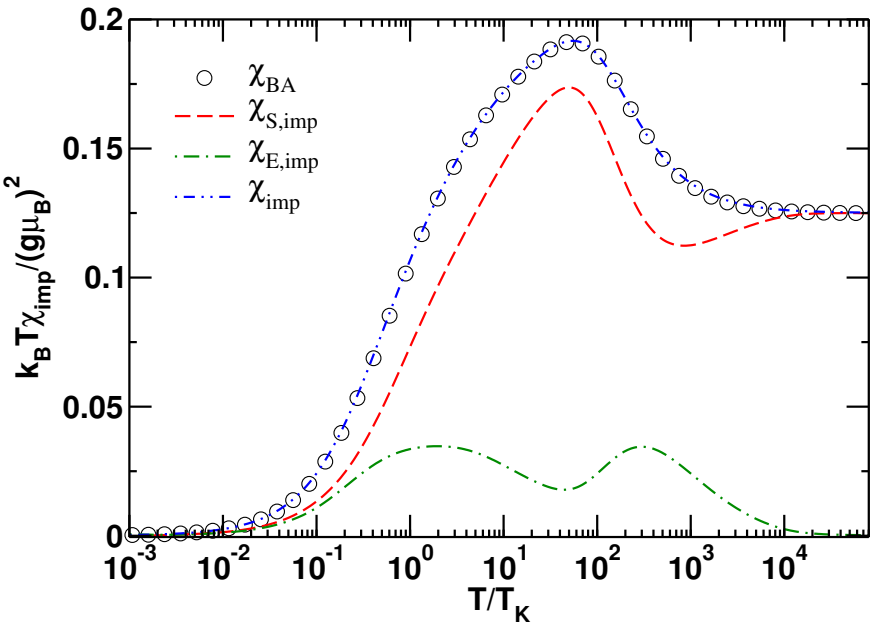


*Figure 4.1: Impurity contribution to the susceptibility from Bethe ansatz ($\chi_{\rm BA}$) and FDM ($\chi_{\rm imp}$) vs $T/T_{\rm K}$ for the symmetric Anderson model [$U/\Delta_0$ = 12 and $\Delta_0 = 0.001D$ with $T_{\rm K}$ defined in Equation (4.15)]. Also shown are the impurity contributions $k_{\rm B}T\chi_{\rm S,imp}(T)/(g\mu_{\rm B})^2$ and $k_{\rm B}T\chi_{\rm E,imp}(T)/(g\mu_{\rm B})^2$ as defined at the end of Section 4.3. The calculations are for $\Lambda = 10$ with an energy cut-off $e_c(\Lambda) = 15\sqrt{\Lambda} \approx 47$, with z-averaging [$n_z = 4$, $z = 1/8, 3/8, 5/8, 7/8$].*

with a similar expression for the host susceptibility $\chi_0(T)$. The impurity contribution is then obtained via $\chi_{\rm imp}(T) = \chi(T) - \chi_0(T)$.

Figure 4.1 illustrates the problem just discussed for the symmetric Anderson model in the strong correlation limit ($U/\Delta_0 = 12 \gg 1$). Denoting by $\chi_{\rm S,imp}$ and $\chi_{\rm E,imp}$ the *impurity* contributions to $\chi_{\rm S}$ and $\chi_{\rm E}$, i.e. with respective host contributions subtracted, we have $\chi_{\rm imp} \equiv \chi_{\rm S,imp} + \chi_{\rm E,imp}$. We see from Figure 4.1 that the contribution from the environment degrees of freedom, $\chi_{\rm E,imp}$, is significant at all temperatures and is required in order to recover the exact Bethe ansatz result for $\chi_{\rm imp}$.

## 4.4 Results

In this section we compare results for the impurity specific heat (Section 4.4.1), impurity susceptibilities in response to uniform (Section 4.4.2) and local (Section 4.4.3) magnetic fields, and the double occupancy (Section 4.4.4) of the Anderson model, calculated within the FDM approach, with corresponding results from the conventional approach. For the first two quantities we also show comparisons with Bethe ansatz calculations. Results for the Wilson ratio, as a function of Coulomb interaction and local level position, within FDM and Bethe ansatz, are also presented (Section 4.4.2). We show the results for all quantities as functions of the reduced temperature $T/T_{\rm K}$, where the Kondo scale $T_{\rm K}$ is chosen to be the symmetric Anderson model Kondo scale given by

$$T_K = \sqrt{U\Delta_0/2}e^{-\pi U/8\Delta_0 + \pi\Delta_0/2U}, \tag{4.15}$$

except for $U/\Delta_0 < 1$ when we set $T_K = \Delta_0$. The Kondo scale in Equation (4.15) is related to the $T = 0$ Bethe ansatz susceptibility $\chi_{\rm imp}(0)$ via $\chi_{\rm imp}(0) = (g\mu_{\rm B})^2/4T_{\rm K}$ in the limit $U \gg \Delta_0$ (see Hewson [62]). We continue to use $T_{\rm K}$ in comparing results from different methods, although we note that for the asymmetric Anderson model, the physical low energy Kondo scale, $T_{\rm L}$, will increasingly deviate from $T_{\rm K}$ with increasing level asymmetry $\delta = 2\varepsilon_d + U$. For example, second order poor Man's scaling for the Anderson model yields a low energy scale [73] $T_{\rm L} = \sqrt{U\Delta_0/2}e^{\pi\varepsilon_d(\varepsilon_d+U)/2\Delta_0 U}$.

### 4.4.1 Specific heat

Figure 4.2 shows the impurity specific heat ($C_{\rm imp}$) and impurity entropy ($S_{\rm imp}$) for the symmetric Anderson model versus temperature $T/T_{\rm K}$ for increasing Coulomb interaction $U/\Delta_0$. One sees from Figure 4.2 that there is excellent agreement between the results obtained within the FDM approach, within the conventional approach and within the exact Bethe ansatz calculations. This agreement is found for both the strongly correlated limit $U/\Delta_0 \gg 1$ where there are two peaks in the specific heat, a low temperature Kondo induced peak and a high temperature peak due to the resonant

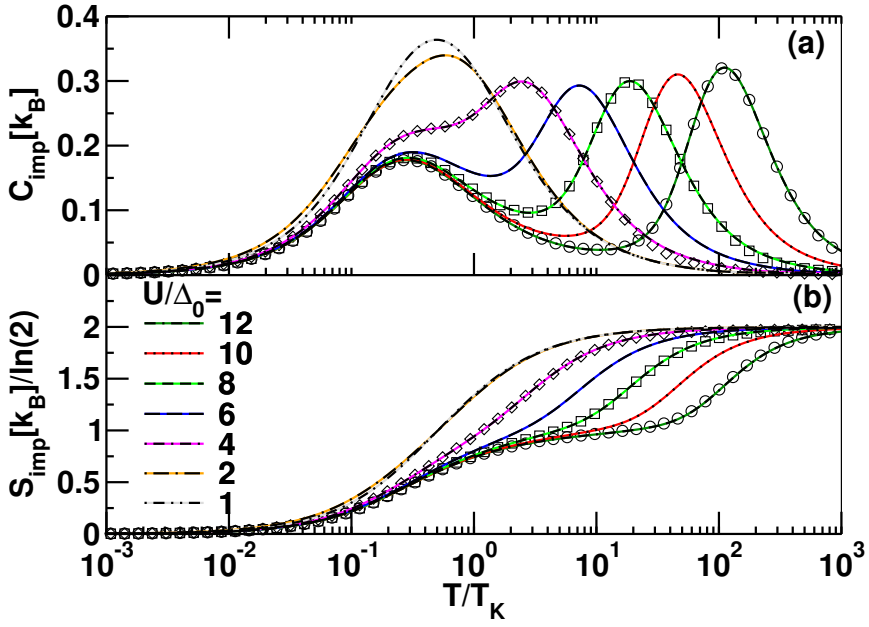


*Figure 4.2: (a) Impurity specific heat, $C_{\rm imp}(T)$, and, (b), impurity entropy, $S_{\rm imp}(T)$, vs reduced temperature $T/T_{\rm K}$ for the symmetric Anderson model with $U/\Delta_0 = 12, 10, 8, 6, 4, 2, 1$ and $\Delta_0 = 0.001D$. Broken lines: FDM approach. Solid lines: conventional approach. Selected Bethe ansatz results are shown as symbols for $U/\Delta_0 = 12, 8, 4$ (circles, squares, diamonds, respectively). The Kondo scale is defined in Equation (4.15). As a guide to the eye, note that the high temperature peak in $C_{\rm imp}$ shifts downwards with decreasing $U$. NRG and z-averaging parameters as in Figure 4.1.*

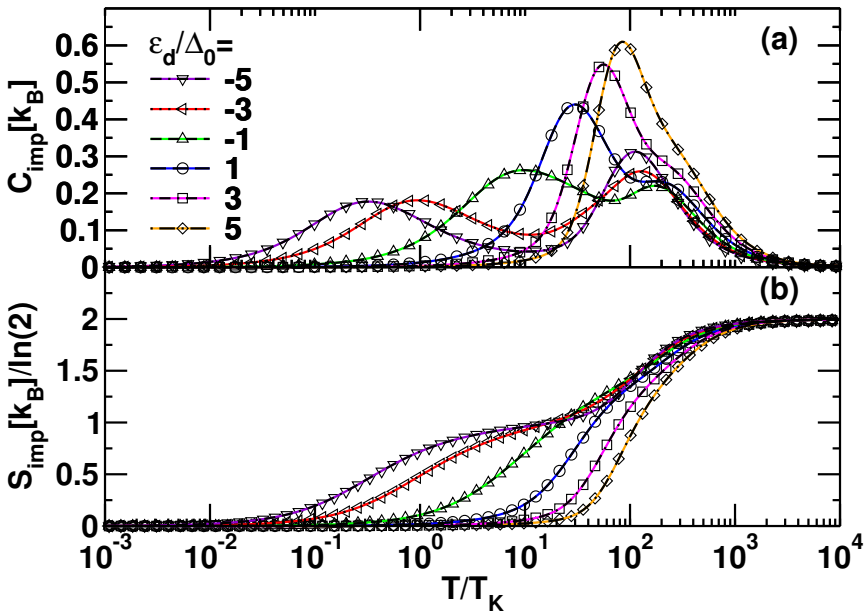


*Figure 4.3: (a) Impurity specific heat, $C_{\rm imp}(T)$, and, (b), impurity entropy $S_{\rm imp}(T)$, vs reduced temperature $T/T_{\rm K}$ for the asymmetric Anderson model with $U/\Delta_0 = 12$, $\Delta_0 = 0.001D$ and several values of $\varepsilon_d/\Delta_0 = -5, -3, \ldots, +5$. Broken lines: FDM approach. Solid lines: conventional approach. Bethe ansatz results are shown as symbols for $\varepsilon_d/\Delta$. For simplicity we used the symmetric $T_{\rm K}$ of Equation (4.15) for all $\varepsilon_d$ values. NRG and $z$-averaging parameters as in Figure 4.1.*

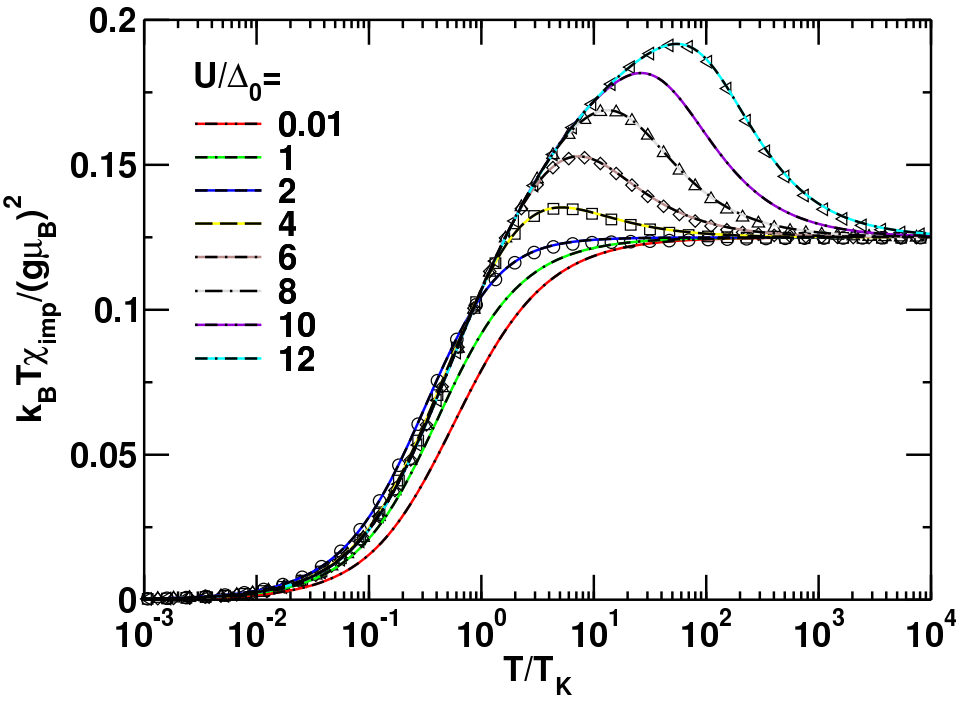


*Figure 4.4: Impurity susceptibility, $\chi_{\rm imp}(T)$, vs $T/T_{\rm K}$ for the symmetric Anderson model with $U/\Delta_0 = 12, 10, 8, 6, 4, 2, 1, 0.01$ and $\Delta_0 = 0.001D$ with $T_{\rm K}$ defined in Equation (4.15) for $U/\Delta_0 \geq 1$ and $T_K = \Delta_0$ for the $U/\Delta_0 = 0.01$ case. Broken lines: FDM approach. Solid lines: conventional approach. Symbols: Bethe ansatz (for selected values of $U/\Delta_0 = 12, 8, 6, 4, 2$). As a guide to the eye, note that $\chi_{\rm imp}$ is increasingly enhanced with increasing $U$. NRG and z-averaging parameters as in Figure 4.1.*

level, and for the weakly correlated limit $U/\Delta_0 \lesssim 1$, where there is only a single resonant level peak in the specific heat. The correct high temperature entropy $\ln 4$ is obtained in all cases.

The temperature dependence of the impurity specific heat and entropy, for the asymmetric Anderson model is shown in Figure 4.3 for local level positions ranging from $\varepsilon_d/\Delta_0 = -6$ to $+5$ in units of $\Delta_0$. For simplicity we continue to show the results as a function of $T/T_{\rm K}$, with $T_{\rm K}$ the symmetric Kondo scale (4.15), although, the true Kondo scale will deviate from this for $\varepsilon_d > -U/2$. The FDM results agree also here very well with the conventional approach and the Bethe ansatz calculations.

### 4.4.2 Susceptibility and Wilson ratio

Figure 4.4 compares the susceptibilities of the symmetric Anderson model calculated from FDM, conventional and Bethe ansatz approaches for several values of $U/\Delta_0$, again indicating good agreement over the whole tem-

| $U/\Delta_0$ | $k_B T_K \chi^a_{\rm imp}/(g\mu_B)^2$ | | $R^a$ | |
|---|---|---|---|---|
| | $a$ = BA | $a$ = NRG | $a$ = BA | $a$ = NRG |
| 12 | 0.250091 | 0.256 | 1.998 | 2.027 |
| 10 | – | 0.256 | – | 2.024 |
| 8 | 0.250715 | 0.256 | 1.986 | 2.013 |
| 6 | – | 0.2574 | – | 1.982 |
| 4 | 0.259130 | 0.2637 | 1.852 | 1.877 |
| 2 | – | 0.3085 | – | 1.578 |
| 1 | – | 0.2214 | – | 1.317 |
| 0.01 | – | 0.1599 | – | 1.003 |

*Table 4.1: Zero temperature susceptibilities $k_{\rm B}T_K\chi^a_{\rm imp}/(g\mu_{\rm B})^2$ and Wilson ratios $R^a \equiv \lim_{T\to 0} 4\pi^2\chi^a_{\rm imp}(T)/3C^a_{\rm imp}(T)/T$ for the symmetric Anderson model at several values of $U/\Delta_0$ using the Bethe ansatz/NRG FDM approach ($a$ = BA/NRG). Note that $T_{\rm K}$ is defined by Equation (4.15) for $U/\Delta_0 > 1$ and is set to $\Delta_0$ otherwise.*

perature range between these three approaches. Table 4.1 lists the zero temperature impurity susceptibilities ($k_{\rm B}T_K\chi_{\rm imp}/(g\mu_{\rm B})^2$) and Wilson ratios ($R \equiv \lim_{T\to 0} 4\pi^2\chi_{\rm imp}(T)/3C_{\rm imp}(T)/T$), for the symmetric Anderson model as calculated within FDM and for a range of Coulomb interactions from strong $U/\Delta_0 \gg 1$ to weak ($U/\Delta_0 \ll 1$). In these two limits, the Wilson ratio for the symmetric Anderson model approaches the well known values of 2, and 1, respectively within FDM ($a = NRG$) and Bethe ansatz. Comparison with Bethe ansatz results at selected values of $U/\Delta_0$ indicate an error in the susceptibility of around 2% with a similar error in the Wilson ratio.

Figure 4.5 shows results within FDM and conventional approaches for the asymmetric Anderson model ($\varepsilon_d > -U/2$) and for several local level positions ranging from the Kondo ($-\varepsilon_d/\Delta_0 \gg 1$) to the mixed valence $|\varepsilon_d/\Delta_0| \leq 1$ and empty orbital regimes $\varepsilon_d/\Delta_0 > 1$. Bethe ansatz results are also shown for selected local level positions, and we see again very good agreement between all three methods over the whole temperature range. Corresponding zero temperature susceptibilities and Wilson ratios are listed in Table 4.2. Note that the Wilson ratio approaches the value for a non-interacting system only in the empty orbital limit ($\varepsilon_d \gg \Delta_0$), being approximately $1.5 \pm 0.25$ in the mixed valence regime ($|\varepsilon_d/\Delta_0| \lesssim 1$). The Wilson ratio from NRG and Bethe ansatz deviate by less than 3% in all regimes.

### 4.4.3 Local susceptibility

It is also interesting to consider the susceptibility, $\chi_{\rm loc}$, in response to a local magnetic field acting only at the impurity site and to compare this

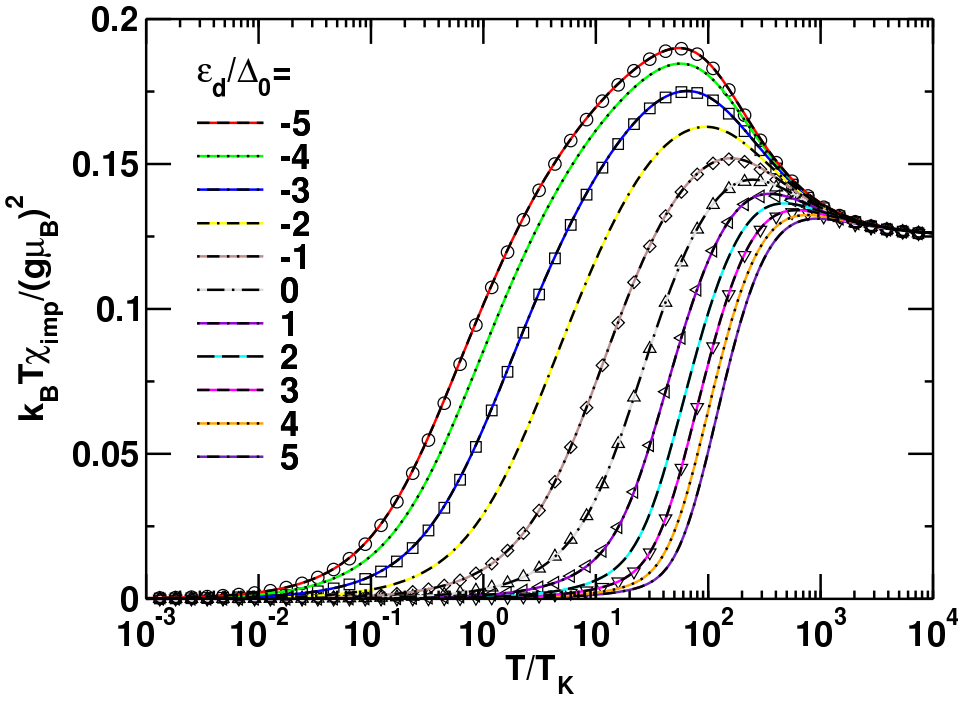


*Figure 4.5: Impurity susceptibility, $\chi_{\rm imp}(T)$, vs $T/T_{\rm K}$ for the asymmetric Anderson model with $U/\Delta_0 = 12$, $\Delta_0 = 0.001D$ and several values of $\varepsilon_d/\Delta_0$ with $T_{\rm K}$ defined in Equation (4.15). Broken lines: FDM approach. Solid lines: conventional approach. Symbols: Bethe ansatz (for selected values of $\varepsilon_d/\Delta_0 = -5, -3, -1, 0, +1, +3$). As a guide to the eye, note that the susceptibility curves shift to higher temperatures with increasing $\varepsilon_d$. NRG and z-averaging parameters as in Figure 4.1.*

| $\varepsilon_d/\Delta_0$ | $k_B T_K \chi^a_{\rm imp}/(g\mu_B)^2$ | | $R^a$ | |
|---|---|---|---|---|
| | $a = BA$ | $a = NRG$ | $a = BA$ | $a = NRG$ |
| -5 | 0.219482 | 0.2245 | 1.999 | 2.025 |
| -4 | – | 0.1515 | – | 2.023 |
| -3 | 0.077356 | 0.0785 | 1.990 | 2.00 |
| -2 | – | 0.0315 | – | 1.97 |
| -1 | 0.010337 | 0.0103 | 1.795 | 1.78 |
| 0 | 0.003303 | 0.0033 | 1.512 | 1.50 |
| 1 | 0.001250 | 0.0013 | 1.315 | 1.32 |
| 2 | – | 0.00059 | – | 1.18 |
| 3 | 0.000325 | 0.00033 | 1.086 | 1.12 |
| 4 | – | 0.00021 | – | 1.09 |
| 5 | – | 0.00014 | – | 1.06 |

*Table 4.2: Zero temperature susceptibilities* $k_{\rm B}T\chi^a_{\rm imp}/(g\mu_{\rm B})^2$ *and Wilson ratios* $R^a \equiv \lim_{T\to 0} 4\pi^2\chi^a_{\rm imp}(T)/3C^a_{\rm imp}(T)/T$ *for the asymmetric Anderson model at* $U/\Delta_0 = 12$ *and several local level positions* $\varepsilon_d/\Delta_0$ *using the Bethe ansatz/FDM NRG approach (*$a = $ BA/NRG*).*

with the susceptibility, $\chi_{\rm imp}$, discussed above, in which the magnetic field acts on both the impurity and conduction electron spins. The former is relevant, for example, in nuclear magnetic resonance and neutron scattering experiments, while the latter can be measured in bulk samples with and without magnetic impurities.

A local magnetic field term, $-g\mu_{\rm B}BS_{\rm z,d}$, in the Anderson model, with $S_{z,d} = (n_{d\uparrow} - n_{d\downarrow})/2$, is not a conserved quantity, i.e $S_{\rm z,d}$ is not conserved , and $\chi_{\rm loc}(T)$ cannot be expressed as a fluctuation as in Equation (4.3-4.4), which would obviate the need to explicitly evaluate a numerical second derivative with respect to $B$ of the thermodynamic potential. Such a derivative, however, poses no actual problem within NRG, so we proceed by explicitly diagonalizing the Anderson model in a local field, using only U(1) symmetries for charge and spin (for the symmetric Anderson model in a magnetic field, an SU(2) pseudo-spin symmetry may be exploited, by using the mapping of this model in a local magnetic field $B$ onto the SU(2) invariant negative-$U$ Anderson model in zero magnetic field at finite level asymmetry $2\varepsilon_d + U = B$ [63, 64]). The evaluation of $\chi_{\rm loc}$ then proceeds via $\chi_{\rm loc}(T, B = 0) = -\partial^2\Omega_{\rm loc}(T, B)/\partial B^2|_{B=0}$ where $\Omega_{\rm loc}(T, B) = \Omega(T, B) - \Omega_0(T)$ and $\Omega(T, B)$ and $\Omega_0(T)$ are the thermodynamic potentials of the total system in a local magnetic field $B$ and the host system, respectively.

Results for $\chi_{\rm loc}$ obtained in this way are shown in Figure 4.6 at several values of $U/\Delta_0$ as a function of $T/T_{\rm K}$. A comparison of $\chi_{\rm loc}$ to $\chi_{\rm imp}$ obtained from the Bethe ansatz, allows us to conclude that these two susceptibilities

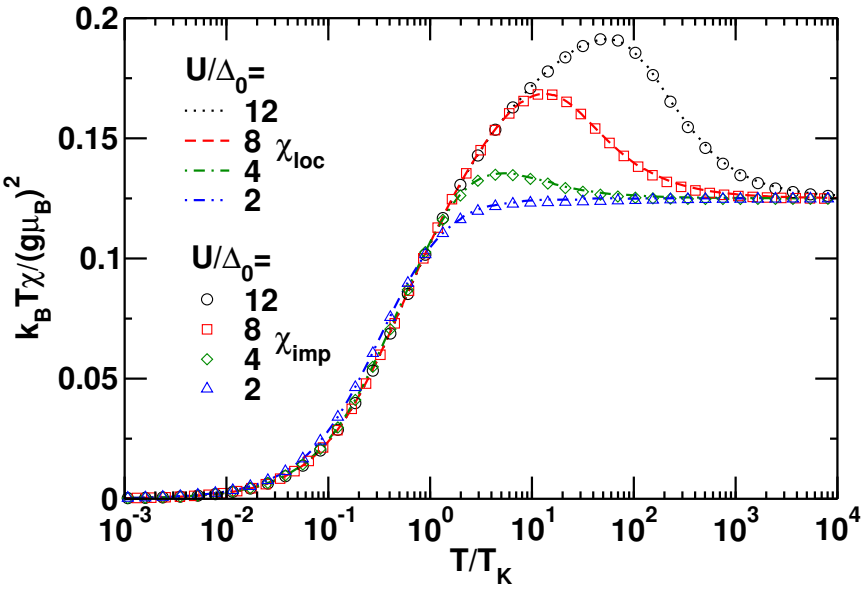


*Figure 4.6: Comparison of the local, $\chi_{\rm loc}(T)$, and impurity, $\chi_{\rm imp}$, susceptibilities vs $T/T_{\rm K}$ for the symmetric Anderson model with $U/\Delta_0 = 12, 8, 4, 2$ and $\Delta_0 = 0.001D$ with $T_{\rm K}$ defined in Equation (4.15). Broken lines: FDM approach. Symbols: Bethe ansatz (for selected values of $U/\Delta_0 = 12, 8, 4, 2$). NRG and z-averaging parameters as in Figure 4.1.*

are close to identical at all temperatures, i.e. $\chi_{\rm imp}(T) = \chi_{\rm loc}(T)$ and for all interaction strengths $U/\Delta_0$. This is not always the case. A prominent example is the anisotropic Kondo model [74], where $\chi_{\rm imp} = \alpha\chi_{\rm loc}$, with the dissipation strength $0 \le \alpha \le 1$ being determined by the anisotropy of the exchange interaction [74, 75].

Figure 4.7 compares local and impurity susceptibilities for the asymmetric Anderson model in the strong correlation limit ($U/\Delta_0 = 12$) for several local level positions, ranging from the Kondo ($\varepsilon_d/\Delta_0 = -5, -4, -3, -2$) to the mixed valence ($\varepsilon_d/\Delta_0 = -1, 0, +1$) and into the empty orbital regime ($\varepsilon_d/\Delta_0 = +2, \ldots, +5$). We see that, as for the symmetric Anderson model, local and impurity susceptibilities are almost identical at all temperatures and for all local level positions, i.e. $\chi_{\rm imp}(T) = \chi_{\rm loc}(T)$ for the parameter values used.

The result $\chi_{\rm imp}(T) = \chi_{\rm loc}(T)$, which we verified here, follows from the Clogston-Anderson compensation theorem [76] (see Hewson [62]). Consider the impurity contribution to the magnetization $M_{\rm imp}(B)$ in a uniform field.

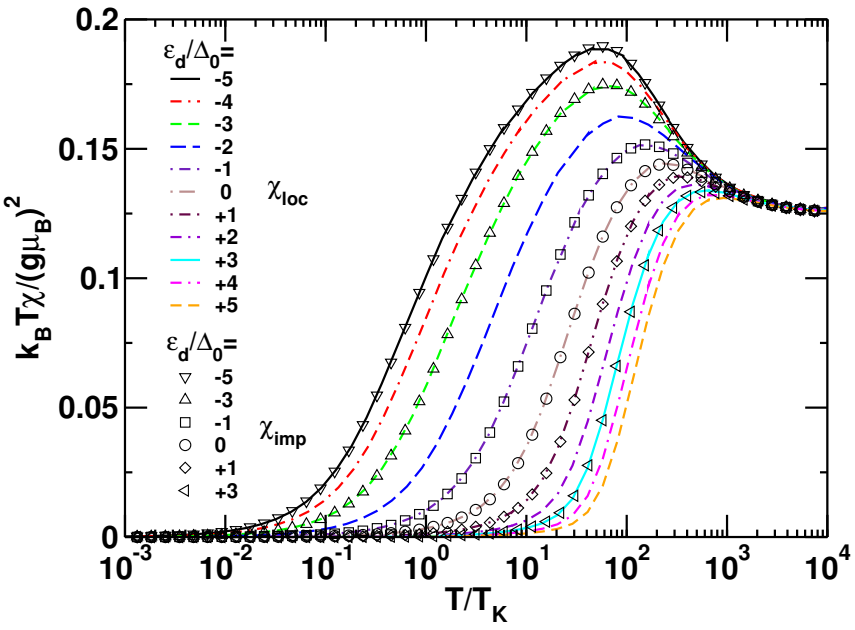


*Figure 4.7: Comparison of the local, $\chi_{\rm loc}$, and impurity, $\chi_{\rm imp}(T)$, susceptibilities vs $T/T_{\rm K}$ for the asymmetric Anderson model with $U/\Delta_0 = 12$, $\Delta_0 = 0.001D$ with $T_{\rm K}$ defined in Equation (4.15) and for several values of the local level position: $\varepsilon_d/\Delta_0 = -5, -4, \ldots, +5$. Broken lines: $\chi_{\rm loc}$ from the FDM approach. Symbols: $\chi_{\rm imp}$ from Bethe ansatz for selected values of $\varepsilon_d$. The NRG calculations are for $\Lambda = 4$ with an energy cut-off $e_c(\Lambda = 4) = 40$ with z-averaging [$n_z = 2$ with $z = 0$ and $z = 0.5$].*

This is given by $M_{\rm imp}/(g\mu_{\rm B}) = \langle S_{z,d} + S_{z,c}\rangle - \langle S_{z,c}\rangle_0$ where $S_{z,d}, S_{z,c}$ are the impurity and conduction electron $z-$components of spin. Using equations of motion, one easily shows [62], that the additional impurity magnetization $\delta M_{\rm imp}/(g\mu_{\rm B}) = \langle S_{z,c}\rangle - \langle S_{z,c}\rangle_0$ from the conduction electrons induced by the presence of the impurity is given by

$$\frac{\delta M_{\rm imp}}{(g\mu_{\rm B})} = \frac{1}{2\pi}\sum_{\sigma}\int d\omega f(\omega){\rm Im}\left[\sigma G_{d\sigma}(\omega,B)\frac{\partial\Delta(\omega)}{\partial\omega}\right], \qquad (4.16)$$

where $f(\omega)$ is the Fermi function, $G_{d\sigma}(\omega,B)$ is the spin $\sigma$ local level Green function of the Anderson model and $\Delta(\omega) = \sum_k |V_k|^2/(\omega - \epsilon_k + i\delta)$ is the hybridization function. For a flat band, $\partial\Delta(\omega)/\partial\omega \approx \Delta_0/D$ in the wide-band limit. Hence, $\delta M_{\rm imp}/(g\mu_{\rm B})$ is of order $(M_{\rm loc}(B)/g\mu_{\rm B})\Delta_0/D$ where $M_{\rm loc}(B)/(g\mu_{\rm B}) = \langle n_{d\uparrow} - n_{d\downarrow}\rangle/2 = \langle S_{z,d}\rangle$ is the local magnetization, which is linear in $B$ for $B \to 0$. From this we deduce that $M_{\rm imp}/(g\mu_{\rm B}) \approx \langle S_{z,d}\rangle \equiv M_{\rm loc}/(g\mu_{\rm B})$ to within corrections of order $(M_{\rm loc}(B)/g\mu_{\rm B})\Delta_0/D$, i.e. $\chi_{\rm imp}(T) = \chi_{\rm loc}(T)$ to within corrections of order $(\chi_{\rm loc}(T)/(g\mu_{\rm B})^2)\Delta_0/D \ll \chi_{\rm loc}(T)$. Away from the wide-band limit, or for strong energy dependence of $\Delta(\omega)$, the above susceptibilities will differ by the correction term given by the field derivative of $\delta M_{\rm imp}$ in Equation (4.16).

### 4.4.4 Double occupancy

Our conclusions concerning the accuracy of specific heat and the susceptibility calculations within the FDM approach, hold also for other thermodynamic properties, e.g. for the occupation number or the double occupancy. Figure 4.8(a) shows a comparison between the FDM and conventional approaches for the temperature dependence of the double occupancy $D_{\rm occ} = \langle n_{d\uparrow} n_{d\downarrow}\rangle$ of the symmetric model for different strengths of correlation $U/\Delta_0$, and Figure 4.8(b) shows the same for the asymmetric Anderson model for $U/\Delta_0 = 12$ and for several local level positions. The results of the two approaches agree at all temperatures, local level positions and Coulomb interactions. Notice that $D$ acquires its mean-field value of 1/4 for the symmetric model in the limit $U/\Delta_0 \to 0$ and is strongly suppressed with increasing Coulomb interaction away from this limit [see Figure 4.8(a)]. Similarly for the asymmetric model, increasing $\varepsilon_d/\Delta_0$ away from the correlated Kondo regime decreases the double occupancy significantly [see Figure 4.8(b)].

## 4.5 Summary

In this chapter we focused on the calculation of the impurity specific heat and the impurity susceptibility of the Anderson model within the FDM approach [50], finding that this method gives reliable results for these quantities, as shown by a comparison to both exact Bethe ansatz calculations

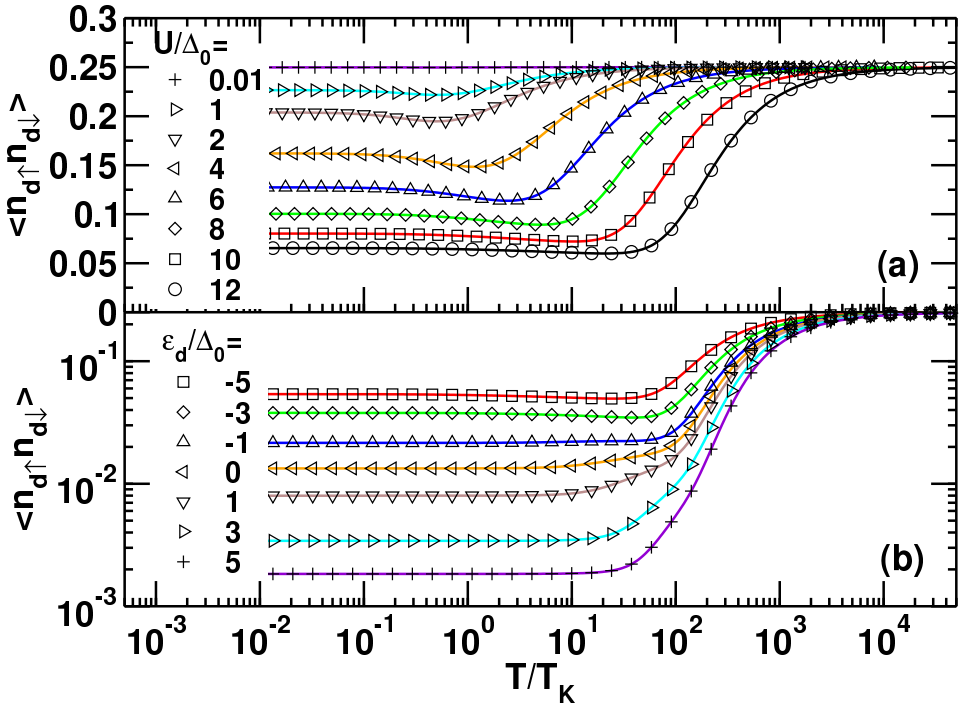


*Figure 4.8: (a) Double occupancy* $D_{\rm occ} = \langle n_{d\uparrow} n_{d\downarrow} \rangle$ *as a function of temperature* $T/T_{\rm K}$ *for the symmetric Anderson model and decreasing values of* $U/\Delta_0 = 12, 10, 8, 6, 4, 2, 1, 0.01$ *within FDM (solid lines) and conventional approaches (symbols). (b) Double occupancy* $D_{\rm occ} = \langle n_{d\uparrow} n_{d\downarrow} \rangle$ *as a function of temperature* $T/T_{\rm K}$ *for the asymmetric Anderson model and increasing values of* $\varepsilon_d/\Delta_0 = -5, -3, -1, 0, +1, +3, +5$ *for* $U/\Delta_0 = 12$ *within FDM (solid lines) and conventional approaches (symbols).* $T_{\rm K}$ *is defined in Equation* (4.15) *for* $U/\Delta_0 \geq 1$ *and is set to* $\Delta_0$ *for the case* $U/\Delta_0 = 0.01$*. NRG and* $z$*-averaging parameters as in Figure 4.1.*

[66, 67, 57, 56, 68, 69, 55] and to NRG calculations within the conventional approach [23]. Some care is needed in implementing the FDM approach for the susceptibility $\chi_{\rm imp}$ in a uniform field, i.e. when the applied magnetic field acts on both the impurity and conduction electron spins. In this case, an additional contribution from the environment degrees of freedom needs to be included. We also showed that the susceptibility in response to a local magnetic field on the impurity, $\chi_{\rm loc}$, could also be obtained within FDM and a comparison of this susceptibility with $\chi_{\rm imp}$ (from Bethe ansatz), showed that they are close to identical at all temperatures, and in all parameter regimes for $\Delta_0 \ll D$, thereby verifying the Clogston-Anderson compensation theorem. An arbitrary temperature grid can be used for thermodynamics in both the conventional and the FDM approaches, however, the former requires a specific best shell to be selected depending on $T$ and $z$, whereas the FDM approach avoids this step by incorporating all excitations from all shells in a single density matrix.

We also showed, that quantities such as the double occupancy can also be accurately calculated within the FDM approach. The double occupancy can be probed in experiments on cold atom realizations of Hubbard models in optical lattices. [77, 78] Flexible techniques, such as the FDM approach, for calculating them within a dynamical mean field theory [79, 80, 81] treatment of the underlying effective quantum impurity models could be useful in future investigations of such systems [82].

# Chapter 5

# Conductance scaling in quantum dots

Motivated by recent experiments on conductance scaling in correlated quantum dots exhibiting the Kondo effect [19, 4, 12], we present in this chapter a detailed study of the low-temperature and low-field scaling properties of the linear conductance of a quantum dot described by the single-level Anderson impurity model (published in Merker et al. [39] and Merker et al. [83]). Scaling in physical properties is a hallmark of the Kondo effect [62]. Thus, a Kondo model description of a quantum dot implies that the conductance $G(T, B)$ is a universal function of $T/T_0$ and $g\mu_{\mathrm{B}}B/k_{\mathrm{B}}T_0$ over all temperatures $T$ and magnetic fields $B$, with microscopic parameters (such as the Kondo exchange $J$) only entering through the dynamically generated low energy scale $T_0$ (to be defined explicitly in Section 5.2), with $g$, $\mu_{\mathrm{B}}$, $k_{\mathrm{B}}$ denoting the $g$-factor, Bohr magneton and Boltzmann's constant respectively. In particular for $T \ll T_0$ or $g\mu_{\mathrm{B}}B \ll k_{\mathrm{B}}T_0$ the functions $G(T, B = 0) = G(0,0)(1 - c_{\mathrm{T}}(T/T_0)^2)$ and $G(T = 0, B) = G(0,0)(1 - c_{\mathrm{B}}(g\mu_{\mathrm{B}}B/k_{\mathrm{B}}T_0)^2)$ exhibit Fermi liquid corrections about the unitary conductance $G(0,0)$ with deviations which are universal in the sense that the coefficients $c_T = \pi^4/16$ and $c_B = \pi^2/16$ are independent of microscopic details. Actual quantum dot devices, however, have a finite charging energy, and they are more realistically described by an Anderson model. The finite charging energy, and the ability to change the level energy of the quantum dot with a gate voltage, allow for charge fluctuations (even in the "Kondo regime" of the quantum dot) and can give rise to deviations from the expected Kondo scaling. It is therefore of some interest to quantify the effect of increasing charge fluctuations on the values of $c_T$ and $c_B$. Recently, this issue has also been addressed in Reference [84] by using a renormalized perturbation theory on the Keldysh contour [85, 86] formulated using dual fermions [87, 88, 89]. This approach, denoted henceforth as superperturbation theory (SPT) performed by Kirchner and Muñoz, yields both the linear and non-linear conductance. In this

chapter we shall compare the predictions of this theory for the linear conductance with results obtained within the numerical renormalization group (NRG) approach [14, 32, 33, 18].

At the technical level, this chapter rewrites the NRG code to use just total electron number and total $S_z$ as good quantum numbers instead of the $SU(2)$ for the total spin. This allows studying the effect of a local magnetic field on the conductance and on the thermopower (see next Chapter). Furthermore, a more accurate method of calculation, compared to the method used in e.g. Costi and Hewson [90], was used for the conductance [24] enabling the accurate extraction of the Fermi liquid coefficients $c_T$ and $c_B$. The same method has been used in the next chapter to obtain the magnetic field dependence of the thermopower (and the other transport coefficients).

The outline of the chapter is as follows. Section 5.1 describes the quantum dot model. Section 5.2 gives a brief description of the calculation of the finite temperature linear conductance $G(T, B)$ of the Anderson model within the NRG following the procedure in Reference [91]. In Section 5.3, some Fermi liquid results for $c_T$ and $c_B$ are given, and in Section 5.4 we briefly introduce the SPT, with which we shall compare. In Section 5.5 we present results for the dependence of the coefficients $c_{\rm T}$ and $c_{\rm B}$ on charging energy and gate voltage (local level energy). The latter are compared with the corresponding results from SPT. We conclude in Section 5.6 with a discussion of the relevance of our results for experiments on quantum dots.

## 5.1 Model

We consider the simplest model of a correlated quantum dot, the single-level Anderson model given by the Hamiltonian

$$H = \sum_{\sigma} \varepsilon_{d\sigma} n_{d\sigma} - g\mu_{\rm B} B\, s_z^d + U n_{d\uparrow} n_{d\downarrow} + \sum_{k\alpha\sigma} \epsilon_{k\alpha} c^\dagger_{k\alpha\sigma} c_{k\alpha\sigma} + \sum_{k\alpha\sigma} (t_\alpha c^\dagger_{k\alpha\sigma} d_\sigma + h.c.). \tag{5.1}$$

Here, $\varepsilon_d$ is the level energy, related to the gate voltage $V_g$ in the quantum dot via $\varepsilon_d \sim eV_g$,$B$ is a local magnetic field acting on the quantum dot with $s_z^d = \frac{1}{2}(n_{d\uparrow} - n_{d\downarrow})$, $U > 0$ is the Coulomb charging energy, $\sigma$ labels the spin, and $\alpha = L, R$ labels left and right electron lead states with kinetic energies $\epsilon_{k\alpha}$. The couplings of the dot to the leads are denoted by $\Delta_\alpha(\omega) = \pi\rho_\alpha(\omega)|t_\alpha|^2$, where $\rho_\alpha(\omega) = \sum_k \delta(\omega - \epsilon_{k\alpha})$ is the density of states of lead $\alpha$. For simplicity we assume a constant density of states $\rho_\alpha = N_{\rm F} = 1/2D$ with half-bandwidth $D = 1$ so that $\Delta_\alpha = \pi N_{\rm F} t_\alpha^2$. By using even and odd parity combinations of left and right lead states, model (5.1) is reduced to a single-channel Anderson model with a resonant level half-width at half-maximum given by $\Delta = \Delta_{\rm L} + \Delta_{\rm R}$. The spectral function of the latter model is required in the calculation of the linear conductance, which we describe next.

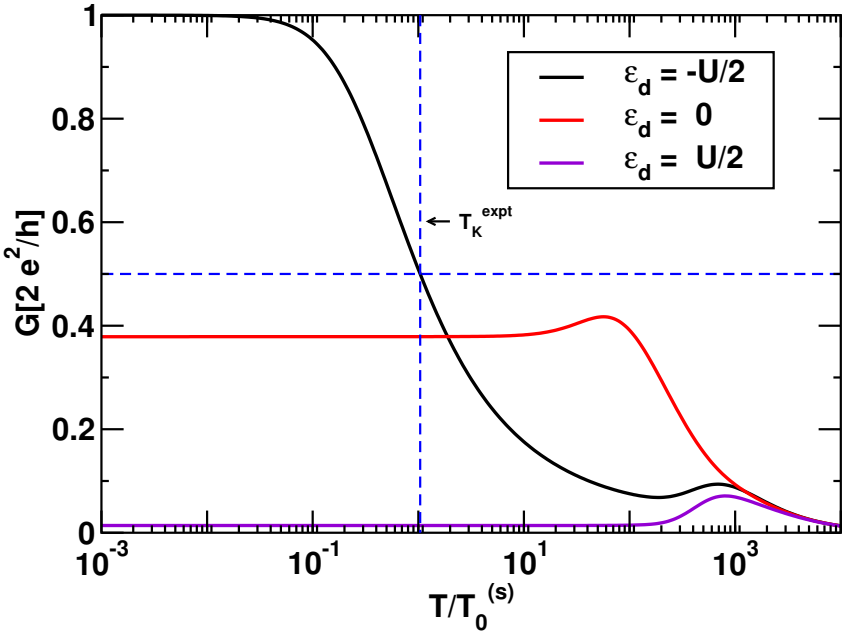


*Figure 5.1: Linear conductance $G(T)$ versus $T/T_0^s$ for $U/\Delta = 16$ and several values of $\varepsilon_d = -U/2, 0, +U/2$ using the approach of Ref. [91], with $T_0^s$ defined by Equations (5.6)-(5.7). We also indicate with horizontal and vertical dashed lines the extraction of the experimental Kondo scale, $T_{\rm K}^{\rm expt}$, from the mid-valley Kondo conductance (i.e. that for $\varepsilon_d = -U/2$) via $G(T = T_{\rm K}^{\rm expt}) = G(0)/2$. NRG parameters were for $\Lambda = 4$, with an energy cut-off $e_c(\Lambda = 4) = 30$ and $n_z = 2$.*

## 5.2 NRG calculation of conductance

The linear response electrical conductance $G(T, B)$ of (5.1) is given by [92, 93]

$$G(T,B) \;=\; \frac{e^2}{h}\int d\omega \left(-\frac{\partial f}{\partial \omega}\right) \sum_\sigma \mathcal{T}_\sigma(\omega, T, B), \tag{5.2}$$

where

$$\mathcal{T}_\sigma(\omega,T,B) = 4\pi \frac{\Delta_L \Delta_R}{\Delta_L + \Delta_R} A_\sigma(\omega, T, B) \tag{5.3}$$

is the transmission function for spin $\sigma$ electrons. It can be calculated from the single-particle spectral function of the dot $A_\sigma(\omega, T, B) = -\mathrm{Im}[G_{d\sigma}(\omega + i\delta)]/\pi$, where $G_{d\sigma}(\omega + i\delta) = \langle\langle d_\sigma; d_\sigma^\dagger \rangle\rangle$ is the Fourier transform of the retarded single-particle Green function of (5.1). In Equation (5.2), $e$ and $h$

are the electronic charge and Planck's constant respectively, and $f(\omega) = [1+\exp(\beta\omega)]^{-1}$ is the Fermi function.

We use the NRG to evaluate the spectral function $A_\sigma(\omega, T, B)$ via the Lehmann representation

$$A_\sigma(\omega,T,B) = \frac{1}{Z}\sum_{m,n}|M^\sigma_{mn}|^2(e^{-\beta E_m}+e^{-\beta E_n}) \times \delta(\omega-(E_m-E_n)), \tag{5.4}$$

where $M^\sigma_{mn}$ are the matrix elements of the spin $\sigma$ local d-electron operator between eigenstates $|m\rangle$ and $|n\rangle$ with energies $E_m$ and $E_n$ and $Z = \sum_m \exp(-\beta E_m)$ is the partition function (see Ref. [18] for details). The usual approach is to broaden the discrete spectral function in Equation (5.4) with Gaussians or Logarithmic Gaussians in order to obtain a smooth function [94, 95, 18], which is then substituted into Equation (5.2), thereby yielding $G(T, B)$ after a numerical integration. A more accurate procedure, introduced in Reference [91], is to substitute the discrete representation in Equation (5.4) directly into Equation (5.2) resulting in the expression

$$G(T,B) = \frac{\gamma\beta}{Z}\sum_\sigma\sum_{m,n}|M^\sigma_{mn}|^2\frac{1}{e^{\beta E_m}+e^{\beta E_n}}, \tag{5.5}$$

where $\gamma = 4\pi\frac{e^2}{h}\frac{\Delta_L\Delta_R}{\Delta_L+\Delta_R}$. This avoids errors from numerical integrations and from an artificial broadening of the spectral function and has been shown to give accurate results for the conductance [91]. A similar procedure has been used in Reference [50] to extract $c_T$ for the symmetric Anderson model to within 5% accuracy. This uses a full density matrix evaluation of the spectral function [50, 49] within the complete basis set [96] and is computationally more intensive than the approach which we use here, whose computational complexity is comparable to that of evaluating a local static correlation function.

For the remainder of this chapter we shall set the g-factor $g$, Bohr magneton $\mu_B$, Planck's constant $h$, electric charge $e$, and Boltzmann's constant $k_\mathrm{B}$ to unity, and also assume symmetric coupling to the leads ($\Delta_L = \Delta_R = \Delta/2, \gamma = \pi\Delta$). A finite asymmetry $\Delta_L \neq \Delta_R$ only influences the value of $G(0,0)$, but not our results for $c_B$ and $c_T$. Note that in experiments on quantum dots [4, 5]. the extracted full width at half maximum of the Coulomb blockade peaks is given by $\Gamma = 2\Delta$.

In evaluating Equation (5.5), we used $z$-averaging [37] within the band discretization scheme of Reference [23] (see Chapter 2.2). A discretization parameter of $\Lambda = 4$ with $n_z = 2$ values for the $z$-averaging was used and the cut-off for the rescaled energies at each NRG iteration was set to $e_c(\Lambda = 4) = 30$. Figure 5.1 shows typical examples for $G(T)$ versus $T/T_0$ at $B = 0$ for a strongly correlated quantum dot ($U/\Delta = 16 \gg 1$) in the Kondo ($\varepsilon_d = -U/2$),

| Fitting range | $R^2$ | $c_T$ | % error |
|---|---|---|---|
| $10^{-5}T_0 \le T \le T_0$ | 0.818 | 0.7447 | 87 |
| $10^{-5}T_0 \le T \le 0.1T_0$ | 0.9969 | 5.1277 | 16 |
| $10^{-5}T_0 \le T \le 0.05T_0$ | 0.99965 | 5.8002 | 4.7 |
| $10^{-5}T_0 \le T \le 0.02T_0$ | 0.999980 | 6.0820 | 0.086 |
| $10^{-5}T_0 \le T \le 0.01T_0$ | 0.9999894 | 6.1459 | 0.96 |
| $10^{-5}T_0 \le T \le 0.005T_0$ | 0.99985 | 6.1468 | 0.98 |
| $10^{-5}T_0 \le T \le 0.001T_0$ | 0.9381 | 6.2034 | 1.91 |

*Table 5.1: Optimal temperature range for fitting the conductance $G(T,0)$ to the Fermi liquid form $f(T/T_0) = a(1 - c_T(T/T_0)^2)$ for $U/\Delta = 12$ and $\varepsilon_d = -U/2$ using a goodness of fit based on the value of $R^2$. The latter is defined by $R^2 = 1 - \frac{\sum_{i=1}^{n}(y_i - f(x_i))^2}{\sum_{i=1}^{n}(y_i - <y>)^2}$, where $x_i = T_i/T_0$, $y_i = G(T_i,0)$, $\langle y\rangle = \frac{1}{n}\sum_{i=1}^{n} y_i$ and the number of data points in the fitting ranges was $n \approx 200$. The value $R^2 = 1$ would correspond to a perfect fit to the Fermi liquid form. The % error in $c_T$ in the last column is defined by % error $= 100\cdot|\frac{c_T - c_{T,exact}}{c_{T,exact}}|$ where $c_{T,exact}$ is the exact value at particle-hole symmetry given by Equation (5.15). From this table we see that the optimal range which maximizes $R^2$ and the accuracy of $c_T$ is close to $T \le 0.02T_0$. The NRG calculations used $\Lambda = 4$, $n_z = 2$ and an energy cut-off $e_c(\Lambda) = 30$.*

mixed valence ($\varepsilon_d = 0$) and empty orbital ($\varepsilon_d = U \gg \Delta$) regimes. The scale $T_0$ is defined from the $T = 0$ susceptibility of the Anderson model (5.1))

$$\chi(0) = 1/4T_0 \tag{5.6}$$

for all $U$ and $\varepsilon_d$. For the case of particle-hole symmetry ($\varepsilon_d = -U/2$) and strong correlations $U \gg \pi\Delta$, one also has from the Bethe ansatz solution for $\chi(0)$ an analytic expression for $T_0$

$$T_0(\varepsilon_d = -U/2) \equiv T_0^{(s)} \approx \sqrt{U\Delta/2}e^{-\pi U/8\Delta + \pi\Delta/2U}, \tag{5.7}$$

within corrections which are exponentially small in $U/\pi\Delta$ (see Ref. [62]).

The Kondo scale $T_0$ is useful in analytic calculations of $c_T$ and $c_B$ about the Fermi liquid fixed point at $T = 0$, such as those in Section 5.3. With this definition, the meaning of the coefficients $c_T$ and $c_B$ is fixed by

$$\frac{G(T, B=0)}{G(0,0)} = 1 - c_{\rm T}\left(\frac{T}{T_0}\right)^2, \qquad (T \ll T_0), \tag{5.8}$$

$$\frac{G(T=0, B)}{G(0,0)} = 1 - c_{\rm B}\left(\frac{B}{T_0}\right)^2, \qquad (B \ll T_0). \tag{5.9}$$

In extracting $c_B$ we do not use Equation (5.9), but instead use the Fermi liquid result in Equation (5.17) of Section 5.3. This allows $c_B$ to be obtained

directly from the $T = 0$ occupancy of the $d$-level, a quantity that can be calculated to high accuracy within the NRG. The coefficient $c_T$ is extracted numerically by fitting $G(T, 0)$ in the range $10^{-5}T_0 \leq T \leq 2 \times 10^{-2}T_0$ to the Fermi liquid form in Equation (5.8) with $T_0$ as defined in Equation (5.6). The range $T \leq 0.02T_0$ was found optimal for this purpose, as we now describe.[1] Specifically, we fit the NRG results for $G(T, 0)$ in the above range to $f(x) = a(1 - c_T x^2)$ where $x = T/T_0$. We find that $a = 2 \pm 10^{-5}$ at the particle-hole symmetric point, with $a = 2$ (in units of $e^2/h$) being the exact result from the Friedel sum rule. The effect of the fitting range on the accuracy of the extracted $c_T$ and the degree of confidence in the Fermi liquid form $f(x) = a(1 - c_T x^2)$ may be ascertained quantitatively by calculating the $R$ squared coefficient $R^2$ (also called the coefficient of determination and defined in Table 5.1). Table 5.1 lists $R^2$, together with the extracted $c_T$ and the % error in $c_T$ for different fitting ranges. We see that the range $10^{-5}T_0 \leq T \leq 0.02T_0$ is close to maximizing both $R^2$ and the accuracy of $c_T$ [as compared to the exact result in Equation (5.15) of Section 5.3]. We therefore used this range throughout, also for the asymmetric cases. Care is needed in the choice of the cut-off $e_c(\Lambda)$ in order to obtain correct results for $G(T)$ in the low-temperature limit when using Equation (5.5). If $e_c(\Lambda)$ is chosen to be too small, the correct saturation behavior of $G(T, 0)$ in the low-temperature limit (i.e. the "leveling-off" of the conductance) is not obtained. In this case, a fit of $G(T, 0)$ to $f(T/T_0)$ shows a drop in $R^2$ to small values, indicating a problem. This is remedied by increasing $e_c(\Lambda)$ (the used value $e_c(\Lambda = 4) = 30$ was sufficient, whereas $e_c(\Lambda = 4) = 12$, for example, is not). Thus, the $R^2$ criterion can be a useful check on appropriate choices of cut-off when evaluating the conductance via Equation (5.5).

In experiments on Kondo correlated quantum dots, $T_0$ is not measurable, and instead one extracts a Kondo scale, $T_{\mathrm{K}}^{\mathrm{expt}}$, from the temperature dependence of the $B = 0$ conductance via

$$G(T = T_{\mathrm{K}}^{\mathrm{expt}}) = G(0)/2. \tag{5.10}$$

In principle, this $T_{\mathrm{K}}^{\mathrm{expt}}$ can be extracted for each gate voltage (i.e., for each $\varepsilon_d$), but in practice, it is usually extracted only at mid-valley ($\varepsilon_d = -U/2$) where one is sure to be in the Kondo regime for large $U/\Delta$. This is illustrated in Figure 5.1 by the dashed lines.

With this definition of $T_{\mathrm{K}}^{\mathrm{expt}}$, one extracts the experimentally measured

[1] The lower bound of this range $T_{\mathrm{min}} = 10^{-5}T_0$ is the lowest temperature for NRG calculations. Provided it is small enough, its precise value does not affect the quality of the fits significantly.

coefficients $c_T^{\rm expt}$ and $c_B^{\rm expt}$ via

$$\frac{G(T,B=0)}{G(0,0)} = 1 - c_{\rm T}^{\rm expt}\left(\frac{T}{T_{\rm K}^{\rm expt}}\right)^2, \qquad (T \ll T_{\rm K}^{\rm expt}), \tag{5.11}$$

$$\frac{G(T=0,B)}{G(0,0)} = 1 - c_{\rm B}^{\rm expt}\left(\frac{B}{T_{\rm K}^{\rm expt}}\right)^2, \qquad (B \ll T_{\rm K}^{\rm expt}). \tag{5.12}$$

For the particle-hole symmetric Anderson model, the coefficients $c_T^{\rm expt}$ and $c_B^{\rm expt}$ are related to $c_T$ and $c_B$ via

$$c_T^{\rm expt} = c_T\left(\frac{T_{\rm K}^{\rm expt}}{T_0^{(s)}}\right)^2, \tag{5.13}$$

$$c_B^{\rm expt} = c_B\left(\frac{T_{\rm K}^{\rm expt}}{T_0^{(s)}}\right)^2. \tag{5.14}$$

For a precise translation of theoretical calculations of $c_B$ and $c_T$ in terms of $T_0$, into experimentally measured ones in terms of $T_{\rm K}^{\rm expt}$, one therefore requires the ratio $T_{\rm K}^{\rm expt}/T_0^s$ at mid-valley for all charging energies ($U/\Delta$), which we supply in Section 5.5.

## 5.3 Fermi liquid results for $G(T,B)$

For the case of particle-hole symmetry, the coefficient $c_T$ is known for arbitrary $U/\Delta$ within renormalized perturbation theory about the Fermi liquid fixed point [64]. The expression is given by

$$c_T = \frac{\pi^4}{12}\frac{1+2(R-1)^2}{R^2}, \tag{5.15}$$

where $R$ is the Wilson ratio

$$R = \frac{4\pi^2 k_B^2}{3(g\mu_B)^2}\frac{\chi_d}{\gamma_d}$$

with

$$\gamma_d \overset{T\to 0}{=} C_{\rm imp}(T)/T.$$

In the limit of strong correlations, $U/\Delta \gg 1$, the Wilson ratio approaches 2 and $c_T$ takes the well known universal Kondo value $c_T = \pi^4/16$ (see Reference [97, 72]). In the opposite limit $U/\Delta \to 0$ the Wilson ratio tends to 1 and $c_T$ acquires the value $\pi^4/12$. Evaluation of Equation (5.15) for general $U/\Delta$ requires knowledge of $R$, either from Bethe ansatz or from NRG.

Fermi liquid theory allows an exact analytic expression for $c_B$ to be obtained for all $U$ and $\varepsilon_d$. For this purpose we use the Friedel sum rule

$$A_\sigma(0,B) = \sin^2(\pi n_{d\sigma}(B))/\pi\Delta,$$

where $n_{d\sigma}(B)$ is the spin $\sigma$ local level occupancy in a small finite magnetic field $B \ll T_0$ at $T = 0$. Using the corrected [98] expansion for the local occupation

$$n_{d\sigma}(B) = n_d/2 + \sigma\alpha B + \frac{\partial^2 n_{d,\sigma}}{\partial B^2}\frac{B^2}{4} + O(B^3),$$

where $n_d$ is the total occupancy at $B = 0$, and the fact that $\alpha = \frac{1}{2}\frac{n_{d\uparrow}(B)-n_{d\downarrow}(B)}{B} = \chi(0)$ we easily find the exact result (correct to order $B^2$)

$$\frac{G(0,B)}{G(0,0)} = 1 - \left(\pi^2\chi^2(0)(1-\cot^2(\frac{\pi n_d}{2})) + \cot(\frac{\pi n_d}{2})\frac{\pi}{2}\frac{\partial^2 n_d}{\partial B^2}\right)B^2 \qquad (5.16)$$

$$= 1 - c_B\left(\frac{B}{T_0}\right)^2,$$

$$c_B = \frac{\pi^2}{16}(1-\cot^2(\frac{\pi n_d}{2})) - \frac{\pi}{2}\cot(\frac{\pi n_d}{2})T_0^2\frac{\partial^2 n_d}{\partial B^2}, \qquad (5.17)$$

where $\chi(0) = 1/4T_0$ has been used. Note that at the particle-hole symmetric point ($\varepsilon_d = -U/2$), where $n_d = 1$, $c_B$ takes the universal Kondo value $\pi^2/16$ for all $U$ [99]. This universal result could be tested in semiconductor quantum dots that can be tuned through complete valleys. It would then acquire the value $\pi^2/16$ at mid-valley for any valley. The expression in Equation (5.17) also shows that $c_B$ decreases monotonically with increasing gate voltage away from mid-valley as $\frac{\partial^2 n_d}{\partial B^2}$ is positive [98, 100]. Similar to $c_T$ the value of $\frac{\partial^2 n_d}{\partial B^2}$ was extracted by $G(0,B)$ in the range $10^{-5}T_0 \le B \le 2\times10^{-2}T_0$.

## 5.4 SPT calculation

The SPT approach [84] is based on a renormalized perturbation theory on the Keldysh contour [85, 86] using dual fermions [87, 88, 89]. This approach can be shown to be current conserving by construction [84] even in the nonlinear response regime, as opposed to finite-order perturbation theory in the bare parameters [101]. We compare the results of this theory for the linear conductance with NRG calculations. The details are available in the Supplemental Material of Reference [84, 39]. For the comparison the scaling coefficients will be given in the reference system of the symmetric Anderson

model, i.e., $c'_T, c'_B$ are defined via

$$\frac{G(T, B=0)}{G(0,0)} = 1 - c'_T \left(\frac{T}{T_0^{(s)}}\right)^2, \qquad (T \ll T_0^s), \tag{5.18}$$

$$\frac{G(T=0, B)}{G(0,0)} = 1 - c'_B \left(\frac{B}{T_0^{(s)}}\right)^2, \qquad (B \ll T_0^s), \tag{5.19}$$

where $T_0^{(s)} = 1/4\chi(0)$ is the susceptibility Kondo scale for the symmetric model and is given explicitly within SPT.

## 5.5 Results

### 5.5.1 Symmetric case ($\varepsilon_d = -U/2$)

Figure 5.2 shows $c_T$ vs $U$ for the symmetric model, both in terms of the scale $T_0(\varepsilon_d = -U/2) \equiv T_0^{(s)}$ and in terms of the Kondo scale from the conductance $T_{\rm K}^{\rm expt}$ (i.e., $c_T^{\rm expt}$, discussed below). The former is compared with the corresponding SPT prediction and we see very good agreement between this and the NRG calculations for all $U/\Delta$. For $U/\Delta \gtrsim 6$, the value of $c_T$ remains within 2% of the universal Kondo value $c_T = \pi^4/16 = 6.088$. The value $U/\Delta = \pi \approx 3$ separates the weakly correlated ($U/\pi\Delta < 1$) from the strongly correlated regime ($U/\pi\Delta > 1$) [62]. We see that in the moderately correlated regime $6 \gtrsim U/\Delta \gtrsim 1$, the deviation $c_T$ from the Kondo value increases, eventually reaching 7% at $U/\Delta \approx 3$. For weakly correlated (non-Kondo) quantum dots with $U/\pi\Delta \lesssim 1$, $c_T$ first decreases with decreasing $U$, reaches a minimum at $U/\Delta \approx 1.7$, and then increases to its non-interacting value of $\pi^4/12 \approx 8.117$ at $U = 0$. Note that this latter value differs by more than 30% from the Kondo value at $U \gg \Delta$.

In Figure 5.2(a) we show the ratio $T_{\rm K}^{\rm expt}/T_0^{(s)}$ vs $U$. This ratio allows obtaining $c_T^{\rm expt}$ from Equation (5.13), the coefficient measured in experiments, and which we show in Figure 5.2. Note the very different behavior between $c_T^{\rm expt}$ and $c_T$ for charging energies $U/\Delta \lesssim 5$. This is due to the strong dependence of $T_{\rm K}^{\rm expt}/T_0^{(s)}$ on $U/\Delta$ in this range of charging energies. In particular $c_T^{\rm expt}$ acquires a maximum value of $\approx 8.75$ at $U/\Delta \approx 3.5$. Since $T_{\rm K}^{\rm expt}/T_0^{(s)} \approx 1.041$ for $U/\Delta \gtrsim 10$ [Figure 5.2(a)], $c_T^{\rm expt} \approx 6.58$ for strongly correlated quantum dots in the Kondo regime.[2] In contrast, for $U/\Delta \lesssim 10$, the scale $T_{\rm K}^{\rm expt}$ differs appreciably from $T_0^{(s)}$. Thus, even for nominally Kondo correlated quantum dots with $U/\Delta \approx 4.5$, such as those

[2] A. Weichselbaum and M. Hanl find a similar value $T_{\rm K}^{\rm expt}/T_0^{(s)} \approx 1.06 \pm 0.03$ within a full density matrix approach to the spectral function[50] (private communication). The present result improves on an earlier estimate for the $S = 1/2$ Kondo model [102] which yielded $T_{\rm K}^{\rm expt}/T_0^{(s)} \approx 0.94$.

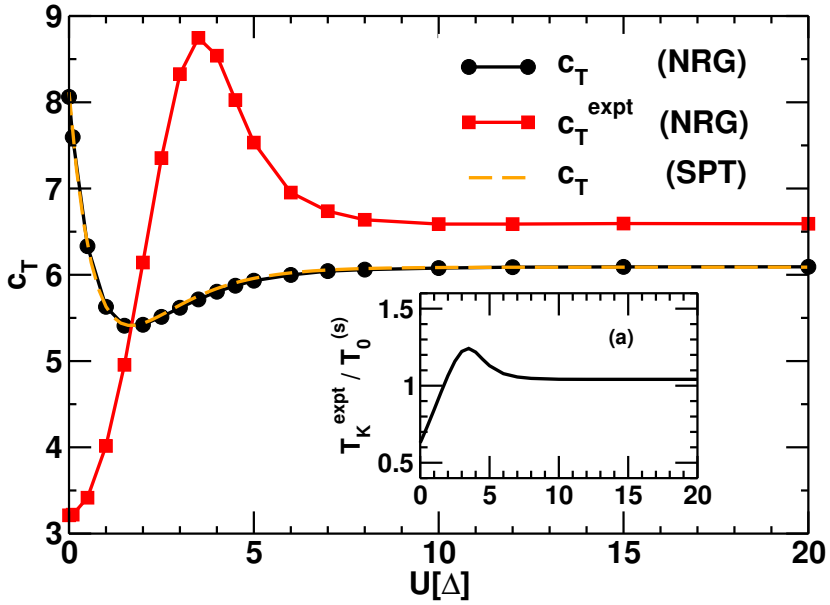


*Figure 5.2: $c_T$ vs $U/\Delta$ for the symmetric Anderson model calculated within NRG (solid lines with symbols) and SPT (dashed line). Filled circles show $c_T$ using the susceptibility scale $T_0^{(s)}$, while filled squares show $c_T$ upon using the scale from the conductance $T_K^{\rm expt}$. By comparing the value of $c_T$ at $U/\Delta \gg 1$ with the exact one $c_T = \pi^4/16 \approx 6.088$, we estimate the relative error in the NRG calculation of $c_T$ to lie below 0.2%, considerably more accurate than previous estimates. [72, 50] Inset (a): ratio $T_K^{\rm expt}/T_0^{(s)}$ vs $U/\Delta$. For $U/\Delta \gg 1$, the ratio $T_K^{\rm expt}/T_0^{(s)}$ approaches 1.04. NRG parameters were for $\Lambda = 4$ with an energy cut-off $e_c(\Lambda = 4) = 30$ and $n_z = 2$.*

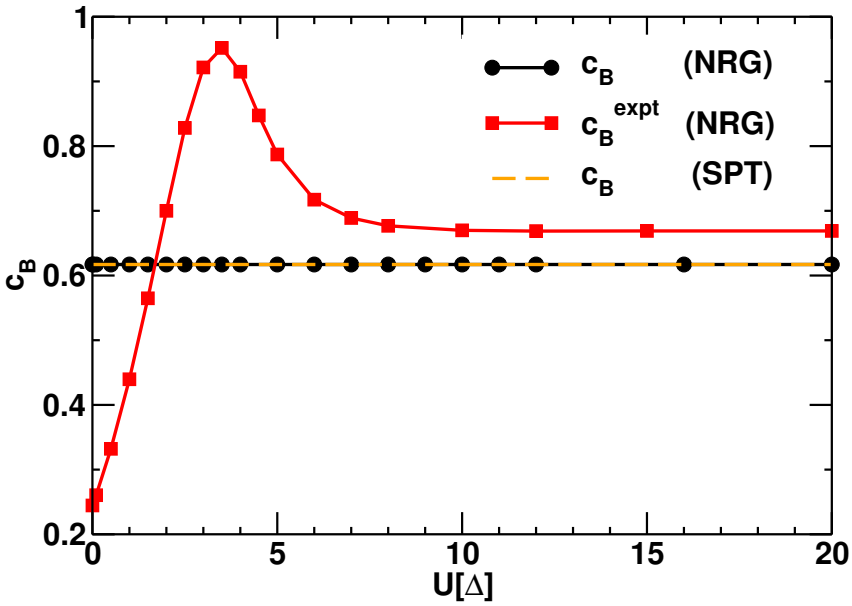


*Figure 5.3: $c_B$ (filled circles) and $c_B^{\rm expt}$ (filled squares) vs $U/\Delta$ for the symmetric Anderson model calculated within NRG NRG parameters were for $\Lambda = 4$ with an energy cut-off $e_c(\Lambda = 4) = 30$ and $n_z = 2$. SPT (dashed curve) also recovers the value $c_B = \pi^2/16$ for particle-hole symmetry.*

in Reference [4], one finds from Figure 5.2(a) that $T_{\rm K}^{\rm expt}/T_0^{(s)} \approx 1.18$, so one should expect $c_T^{\rm expt} \approx 7.5$, which is somewhat larger than the extracted value $c_T^{\rm expt} \approx 5.6 \pm 1.2$ [4].

As discussed in Section 5.3, $c_B$ is independent of the charging energy $U$ for the particle-hole symmetric case, where it takes the value $\pi^2/16 \approx 0.617$, which is also recovered exactly within SPT. However, experiments use the scale $T_{\rm K}^{\rm expt}$ and measure $c_B^{\rm expt}$ as given by Equation (5.14). This depends on $U$ through the ratio of Kondo scales $T_{\rm K}^{\rm expt}/T_0^{(s)}$. For completeness, we therefore show the $U$ dependence of $c_B^{\rm expt}$ in Figure 5.3. For $U/\Delta \approx 4.5$, relevant for the experiments in Ref. [4], we find $c_B^{\rm expt} \approx 0.89$ significantly smaller than the value $c_B^{\rm expt} \approx 5.1$ extracted from the measurements. As discussed in that paper, the large discrepancy between the measured and predicted values of $c_B^{\rm expt}$ could indicate the importance of the large spin-orbit interaction present in the InAs quantum dots investigated in Ref. [4].

### 5.5.2 Asymmetric case ($\varepsilon_d > -U/2$)

#### NRG results

For completeness, we show the dependence of $c_T$ on $\varepsilon_d$ for $\varepsilon_d \geq -U/2$ for $U$ ranging from weakly ($U/\Delta \ll 1$) to strongly ($U/\Delta \gg 1$) correlated quantum dots in Figure 5.4. For strong correlations $U/\Delta \gg 1$, $c_T$ decreases monotonically with increasing deviations from the Kondo regime, eventually becoming negative after the mixed valence regime is reached.

#### Comparison with SPT

Figure 5.5 compares SPT results for the local level dependence of $c_T'$, as defined in Equation (5.18), with correspondingly defined quantities in NRG. Figure 5.6 shows a similar comparison for the quantity $c_B'$ defined in Equation (5.19). We see in both cases, that agreement between NRG and SPT, holds for $\tilde{\varepsilon}_d \equiv (\varepsilon_d + U/2)/\Delta \lesssim 1$. For larger deviations from the symmetric point and with increasing Coulomb interactions, we see an increasing deviation of the SPT results from the NRG calculations. Although we show comparisons also in the region $\tilde{\varepsilon}_d \gg 1$, by construction the SPT calculation is perturbative in $\tilde{\varepsilon}_d$ and agreement can only be expected in the limit $\tilde{\varepsilon}_d \ll 1$, which we find.

## 5.6 Conclusions

In this chapter we investigated deviations from the universal Kondo scaling in the linear conductance of a correlated quantum dot due to a finite level asymmetry (i.e., deviation of gate voltage from mid-valley) and a finite local Coulomb repulsion (i.e., finite charging energy). In particular, we

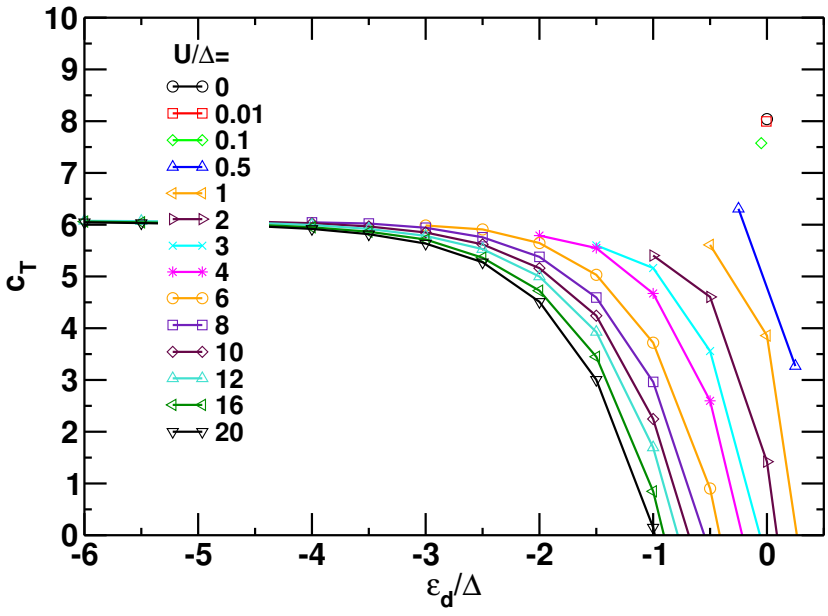


*Figure 5.4: $c_T$ vs $\varepsilon_d$ (in intervals of $0.5\Delta$) with $\varepsilon_d \geq -U/2$ for several $U/\Delta$, ranging from strong, $U \gg \Delta$, to weak, $U \ll \Delta$, correlations, and using the scale $T_0$. NRG parameters were for $\Lambda = 4$ with an energy cut-off $e_c(\Lambda = 4) = 30$ and $n_z = 2$.*

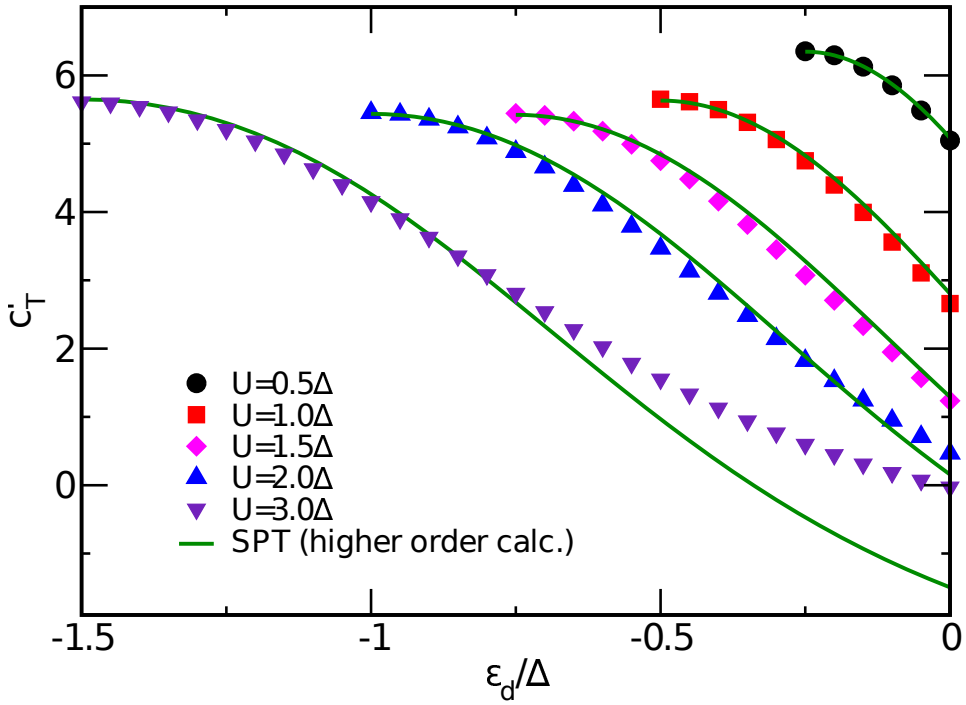


*Figure 5.5: $c'_T$ vs $\varepsilon_d/\Delta$ for several $U$ calculated within NRG (symbols) and SPT (lines). $c'_T$ is defined in Equation (5.18) using $T_0^{(s)}$ at the symmetric point as the Kondo scale for comparison with the SPT results. NRG parameters were for $\Lambda = 4$ with an energy cut-off $e_c(\Lambda = 4) = 30$ and $n_z = 2$.*

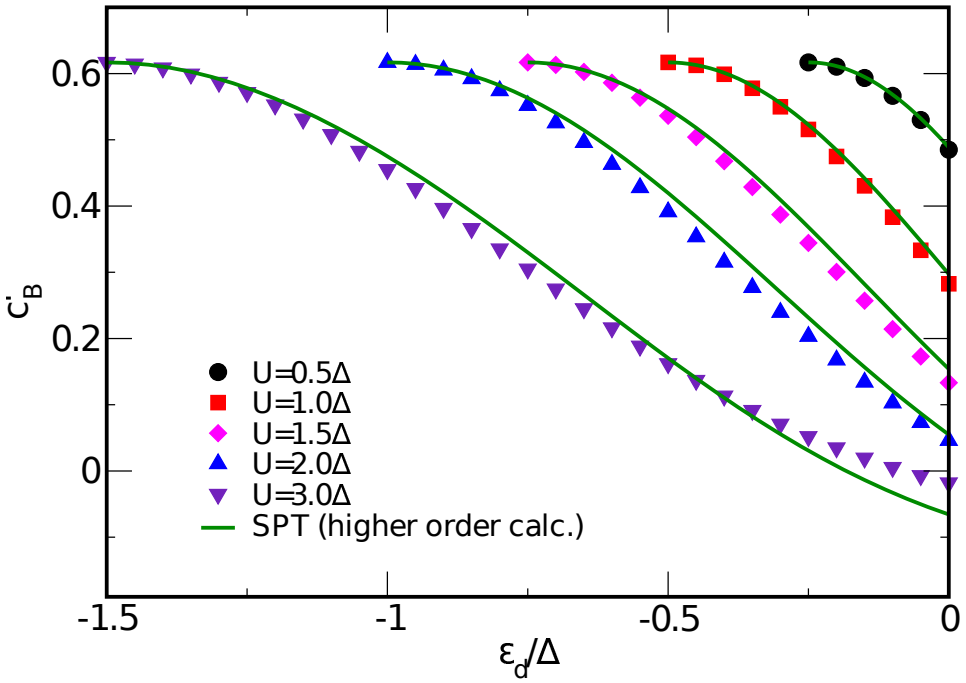


*Figure 5.6: $c'_B$ vs $\varepsilon_d/\Delta$ for several $U$ calculated within NRG (symbols) and SPT (lines). $c'_B$ is defined in Equation (5.19) using $T_0^{(s)}$ at the symmetric point as the Kondo scale for comparison with the SPT results. NRG parameters were for $\Lambda = 4$ with an energy cut-off $e_c(\Lambda = 4) = 30$ and $n_z = 2$.*

determined the behavior of the coefficients $c_T$ and $c_B$ as a function of $\varepsilon_d$ and $U$ within NRG and compared these with results from SPT [84], finding good agreement for all $U$ at the symmetric point and reasonable agreement for $\tilde{\varepsilon}_d = (\varepsilon_d + U/2)/\Delta \lesssim 1$ away from the symmetric point. Both $c_T$ and $c_B$ are monotonically decreasing functions of the deviation $\tilde{\varepsilon}_d$ from the symmetric point $\tilde{\varepsilon}_d = 0$ for all $U$ and an exact Fermi liquid expression for $c_B$ has been given which is valid for any $U$ and $\varepsilon_d$. In particular, the coefficients $c_T$ and $c_B$ become negative on entering the mixed valence regime, signaling the onset of thermally activated transport which becomes pronounced in the empty orbital limit $n_d \approx 0$.

For the mid-valley conductance, we also determined the ratio of the conductance to susceptibility Kondo scales $T_{\rm K}^{\rm expt}/T_0^{(s)}$, allowing us to relate our results for $c_T$ and $c_B$ in terms of $T_0^{(s)}$, to the measured coefficients $c_T^{\rm expt}$ and $c_B^{\rm expt}$ in terms of $T_{\rm K}^{\rm expt}$. While for quantum dots with $U/\Delta \gtrsim 6$, the difference between the two sets of coefficients is a constant factor of order unity (e.g., $c_{T,B}^{\rm expt}/c_{T,B} = (T_{\rm K}^{\rm expt}/T_0^{(s)})^2 \approx 1.08$ for $U/\Delta \gg 6$), for quantum dots with $U/\Delta \lesssim 6$ this difference becomes significant and should be carefully taken into account in detailed comparisons of theory with experiment. We expect this to be particularly important for semiconducting quantum dots since $U/\Delta$ is tunable to smaller values in these systems.

# Chapter 6

# Thermopower in a magnetic field

## 6.1 Introduction

The Anderson impurity model offers a good description of quantum dots connected by leads and dilute magnetic impurities in metals and it also gives some interesting insights into some heavy fermion systems. Thermoelectric properties like the Seebeck coefficient offer a sensitive tool to probe the low energy behavior of such systems [103]. Previous work in calculating the thermoelectric properties focused mainly on the effect of a gate voltage [20], the effect of an effective screening term [27] or on a negative U model [22]. The effects of a magnetic field have been studied for the low temperature scaling behavior of the conductance [39, 83, 104] (see Chapter 5).

In this chapter, the effects of a magnetic field on the thermopower of the SIAM (as well as other transport coefficients) will be considered. This extends the zero field results of Costi and Zlatić [20] to finite magnetic fields. Experimentally heavy fermion systems typically develop a high Seebeck coefficient (also known as thermopower) [62, 105]. A recent experiment of the group of von Löhneysen [21] measured the thermopower of $CeCu_{6-x}Au_x$ in a magnetic field. The low temperature behavior can be captured well by an Anderson impurity model. In this chapter we will discuss the effect of a magnetic field on the thermoelectric properties. The used method to calculate the thermoelectric coefficients within the NRG will be shown in Section 6.2. A set of curves displaying the results of a magnetic field on the thermoelectric properties will be presented in Section 6.3. In Section 6.4 we compare the experimental data for the Seebeck coefficient of $CeCu_{6-x}Au_x$ to the Anderson impurity model and show the predictiveness and limits of this simple representation.

## 6.2 Calculation of thermoelectric properties

Like in previous chapters the model for an Anderson impurity with a local magnetic field is given by

$$H = H_{\text{imp}} + H_0 + H_{\text{int}} + H_B, \tag{6.1}$$

where the impurity part is given by $H_{\text{imp}} = \sum_\sigma \varepsilon_d d_\sigma^\dagger d_\sigma + U n_{d\uparrow} n_{d\downarrow}$. The second term, $H_0 = \sum_{k\sigma} \epsilon_k c_{k\sigma}^\dagger c_{k\sigma}$, describes the non interacting conduction electron band. The interaction is given by $H_{\text{int}} = V \sum_{k\sigma} (c_{k\sigma}^\dagger d_\sigma + d_\sigma^\dagger c_{k\sigma})$ and the magnetic field term is described by $H_B = -g\mu_{\text{B}} B\, S_z$,

Within NRG we are limited to calculating thermoelectric properties in linear response. Either Keldysh formalism in the limit of zero voltage and temperature bias or linear response theory lead to the same result. For a quantum dot these properties can be calculated by first calculating the transport coefficients $L_{i,j}$ defined as [93, 101, 106, 107, 108, 20]

$$\begin{pmatrix} \delta I_C \\ \delta I_Q \end{pmatrix} = \begin{pmatrix} L_{11} & L_{12} \\ L_{21} & L_{22} \end{pmatrix} \begin{pmatrix} \delta V \\ \delta T \end{pmatrix}. \tag{6.2}$$

The matrix terms can be expressed in terms of moments of the transport matrix, where $L_{11} = e^2 I_0$, $L_{21} = T L_{12} = -e I_1$ and $L_{22} = I_2/T$. Here

$$I_n(T) = \sum_\sigma \frac{1}{h} \int \mathrm{d}\omega\, \omega^n\, \mathcal{T}_\sigma(\omega) \left(-\frac{\partial f}{\partial \omega}\right), \tag{6.3}$$

where $\mathcal{T}(\omega) \propto \mathcal{A}_{\mathrm{d},\mathrm{d}^\dagger}(\omega)$. We use the method described in Reference [91, 24, 50] to calculate the conductance and generalize it to the n-th moment of the spectral function.

$$I_n = \sum_\sigma \frac{\gamma}{h} \int \mathrm{d}\omega\, \omega^n\, \mathcal{A}_{\mathrm{d}_\sigma,\mathrm{d}_\sigma^\dagger}(\omega) \left(-\frac{\partial f}{\partial \omega}\right) \tag{6.4}$$

$$= \sum_\sigma \gamma \frac{\beta}{Z} \sum_{l,l'} (E_l - E_{l'})^n\, \frac{\left|\langle l | d_\sigma^\dagger | l' \rangle\right|^2}{\mathrm{e}^{-\beta E_l} + \mathrm{e}^{-\beta E_{l'}}}, \tag{6.5}$$

where $\gamma = 4\pi\Delta_L\Delta_R/(\Delta_L + \Delta_R) = \pi\Delta_0$, removing the need to broaden the spectral function. This sum was evaluated at the lowest NRG shell that fulfilled $t_n > T$ like in previous chapters.

Thermoelectric properties, conductance $G$, Seebeck coefficient $S$ and electron contribution to the thermal conductance $\kappa_e$, can be derived in terms

of these coefficients:

$$G(T) = L_{11} \tag{6.6}$$
$$= e^2 I_0(T) \tag{6.7}$$
$$S(T) = \frac{L_{12}}{L_{11}} \tag{6.8}$$
$$= -\frac{1}{eT}\frac{I_1(T)}{I_0(T)} \tag{6.9}$$
$$\kappa_e(T) = L_{12}L_{21}/L_{11} - L_{22} \tag{6.10}$$
$$= \frac{1}{T}\left[I_2(T) - \frac{I_1^2(T)}{I_0(T)}\right]. \tag{6.11}$$

Further we calculated a set of derived quantities

$$ZT_0 = \frac{GS^2T}{\kappa_e} \tag{6.12}$$
$$PF_0 = \frac{S^2G}{G_0} \tag{6.13}$$
$$L/L_0 = \frac{\kappa_e}{GT}. \tag{6.14}$$

$ZT_0$ is the dimensionless figure of merit, lacking the phonon contribution to the thermal conductance. For the full thermal conductance $\kappa_e + \kappa_{\mathrm{ph}}$ is not accessible in our calculations and depends on the setup. There is a close relation between the figure of merit and the efficiency of thermoelectric devices [109]

$$\eta = \frac{T_H - T_L}{T_H}\frac{\sqrt{1+Z\bar{T}}-1}{\sqrt{1+Z\bar{T}}+\frac{T_L}{T_H}}$$

where $T_H$ is the hotter, $T_L$ is the colder and $\bar{T}$ the average temperature. The power factor $PF_0$ is a measure for the effectiveness of a device, that does not need the knowledge of the total thermal conductance. $L/L_0$ is the Lorenz factor describing the relation between thermal and electrical conductance. These two are in linear relationship for metals according to the Wiedemann-Franz law

$$\frac{\kappa_e}{G} = LT$$

Keep in mind that we have no means to access the phonon contribution of the thermal conductance. Neglecting it is rather optimistic for real case scenarios, but at least for low temperatures the phonon contribution $\kappa_{\mathrm{ph}} \sim T^3$ becomes negligible.

## 6.3 Results

All curves have been calculated using $\Delta_0 = 0.001D$ where $D$ is the half bandwidth of a flat band, $U = 16\Delta_0$. The discretization parameters are

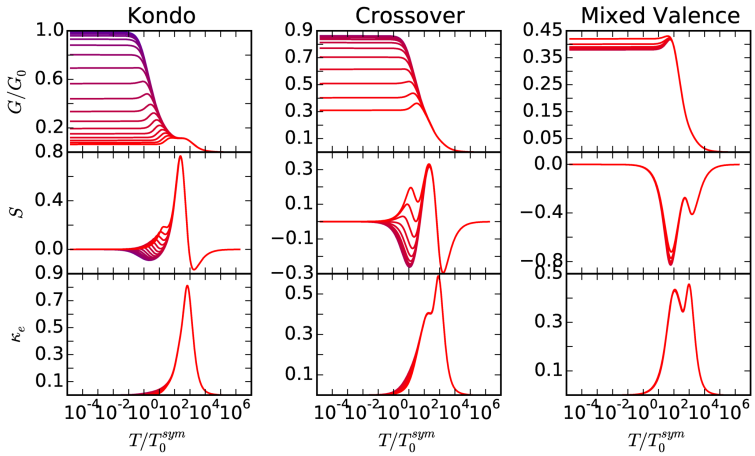


*Figure 6.1: The picture displays the effect of a magnetic field on conductance $G/G_0$ (top), Seebeck coefficient $S$ (middle) and electron contribution to the thermal conductance $\kappa_e/G_0$ (bottom) for different regimes: Kondo regime (left) using $\varepsilon_d = -4.5\Delta_0$, mixed valence regime (right) using $\varepsilon_d = 0$ and a position in between (middle) using $\varepsilon_d = -2\Delta_0$. The magnetic field was varied on a logarithmic scale $B_{loc} = 1.19 \times 10^{-2} T_0^{sym}(blue) \ldots 1.37 \times 10^{2} T_0^{sym}(red)$ in steps of a factor $\sqrt{2}$, where Kondo temperature for the symmetric case $T_0^{sym} = 5.83 \times 10^{-06}$ was derived from Equation (4.15).*

$\Lambda = 4, n_z = 4$, $N_{\text{keep}} \approx 1024$. As the local magnetic field $B_{\text{loc}}$ breaks the SU(2) symmetry, $N$ and $S_z$ have been used as quantization numbers. The temperature ranged from $T = 1 \times 10^{-10} D$ to $1 \times 10^{1} D$ (257 values). The gate voltage $v_g$ will be measured from the symmetric Anderson model $v_g = \varepsilon_d + \frac{1}{2}U$. The resulting curves are given in Figure 6.1 and Figure 6.4 with a close-up given in Figure 6.2 and Figure 6.5. The symmetric case $\varepsilon_d = -\frac{1}{2}U$ yields no thermopower as the spectral function is distributed symmetrically around $\omega = 0$. The curves are picked from the three regimes: $\varepsilon_d = -4.5\Delta_0$ still in the Kondo regime, $\varepsilon_d = 0$ the mixed valence regime and $\varepsilon_d = -2\Delta_0$ an intermediate local level energy showing the crossover between these two regimes.

Some general behaviors can be observed. The relevant temperature of the system $T_K$ increases from the Kondo temperature of the symmetric case $\sim T_0^{\text{sym}}$ to the hybridization strength $\Delta_0$ in the mixed valence regime. The Kondo temperature $T_0^{\text{sym}}$ used here is defined by $T_0 = 1/(4\chi_S^{\text{sym}}(T = 0))$ and has been calculated using Equation (4.15). Universal functions in the Kondo regime depend on $T/T_K$, $\omega/T_K$ and $B/T$, so $\Phi = \Phi(T/T_K, \omega/T_K, B/T)$. Similar behaviour can be found in all the thermoelectric properties, as the magnetic field dependence decreases as the temperature increases (dependence on $B/T$) and decreases as $T_K$ increases (dependence on $T/T_K$, see Figure 6.2

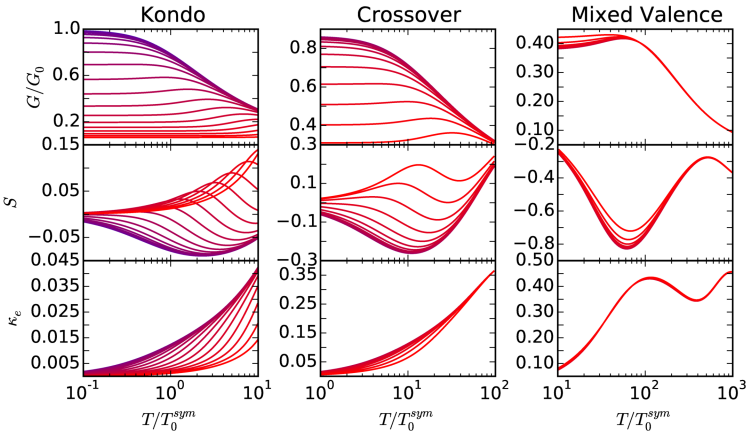


*Figure 6.2: A close up version of Figure 6.1. Note that when moving from the Kondo scale to Mixed valence regime the relevant low temperature scale shifts from the Kondo scale $T \approx T_0^{sym}$ to the hybridization strength $T \approx \Delta_0$.*

and Figure 6.4).

### Electrical conductance $G(T)$

In the Kondo regime the local magnetic field causes the Kondo effect to gradually break down. This causes the conductance to drop accordingly. In the mixed valence regime on the other hand we see a slight increase in the conductance. Here the Kondo effect plays no role. The resonant level around $\Delta_0$ gets split and part moves towards Fermi energy, resulting in the observed small increase of the conductance with magnetic field in this regime. The conductance is given in units of $G_0 = \frac{2e^2}{h} \approx 7.75 \times 10^{-5}\Omega^{-1}$.

### Thermopower $S(T)$

An increase in the gate voltage $v_g = \varepsilon_d + U/2$ results in a shift of the peak of the spectral function. This asymmetry gives a contribution to the first moment of the weighted spectral function and therefore gives raise to the thermopower. The magnetic field on the other hand splits the Kondo peak. In Figure 6.3 we show the zero temperature spectral function $\mathcal{A}_{\mathrm{d}_\sigma,\mathrm{d}_\sigma^\dagger}(\omega)$. The shift in the peak and the splitting can be identified. As a result of this splitting, the sign changes in the Seebeck coefficient $S(T)$ for the low temperature behavior in the Kondo regime when $B_{\mathrm{loc}} \approx T_K$. This sign change indicates that the local $B$-field gradually destroys the Kondo effect and we see the merging with the middle peak. The local minimum shifts towards higher temperatures in the process. In Section 6.4 we will see that these general trends with magnetic field in the Kondo induced thermopower

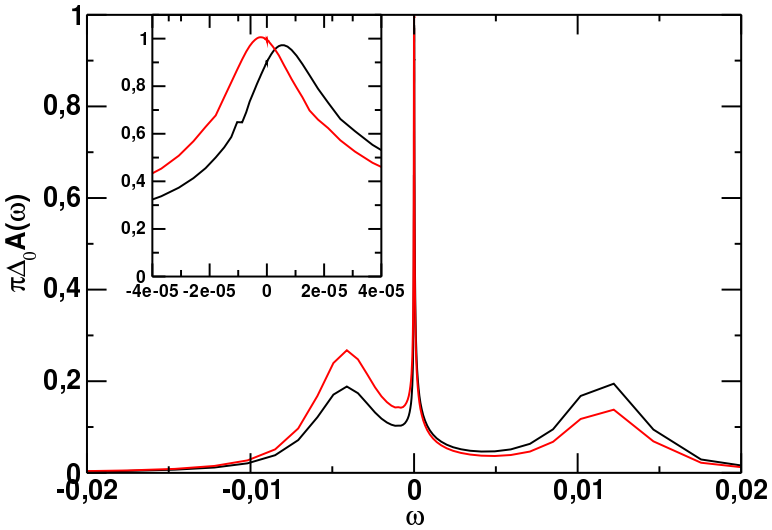


*Figure 6.3: The figure depicts the spectral function separated by up (red curve) and down (black curve) spin. The calculation was done using* $\Lambda = 8$, $e_C = 15$, $n_z = 16$ *for* $\varepsilon_d = -4.5\Delta_0$ *and* $B_{loc} = T_0^{sym} = 5.8 \times 10^{-6}$ *using a Gaussian broadening* ($\sigma_{rel} = 0.1$). *The total shift due to gate voltage and the splitting due to the* $B_{loc}$ *can be observed. This set of parameters was chosen to be near the transition from positive to negative thermopower.*

peak are in qualitative agreement with measurements of the thermopower of $CeCu_{6-x}Au_x$. The thermopower is given in units of $S[\frac{k_B}{e} \approx 86\mu V/K]$.

### Thermal conductance $\kappa_e$

The low temperature behavior of the electron contribution to the thermal conductance is fully covered by the Wiedemann-Franz law. In Figure 6.4 the Lorenz number is constant in the whole Fermi-liquid regime. The overall behavior of the thermal conductance is mainly shaped by the change in the gate voltage $v_g$, which causes a crossing point at $T \approx \Delta_0$ (see Costi and Zlatić [20]). The effects of a magnetic field can be better observed in the Lorenz number.

### Figure of merit $ZT_0$

The main effect of the local magnetic field on the figure of merit is at the Kondo temperature. The behavior of the Seebeck coefficient is reflected here too, leading to a shift and drop of the low temperature peak. Higher temperature behavior is largely unaffected by the local magnetic field. The Kondo induced low temperature peak only yields a $ZT < 0.025$ leading to $\eta \approx \frac{T_H - T_L}{T_H} 0.6\%$ efficiency.

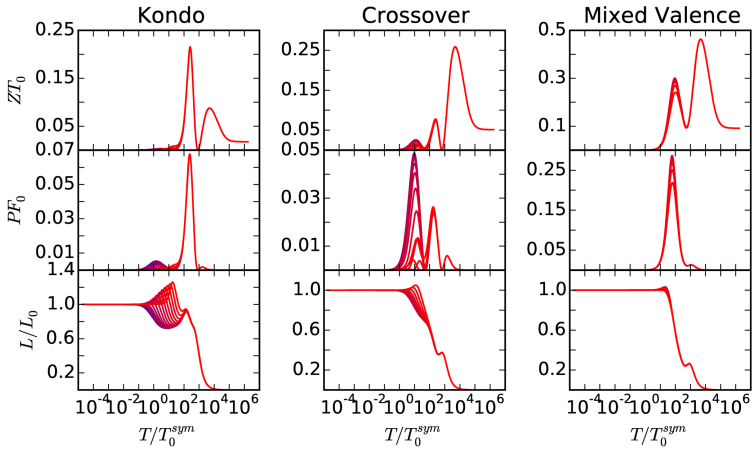


*Figure 6.4: The picture displays the effect of a magnetic field on the figure of merit $ZT$ (top), the power factor $PF_0$ (middle) and the Lorenz number $L/L_0$ (bottom). The magnetic field was varied on a logarithmic scale $B_{loc} = 1.19 \times 10^{-2} T_0^{sym}(blue) \ldots 1.37 \times 10^{2} T_0^{sym}(red)$. The parameters are the same as in Figure 6.1.*

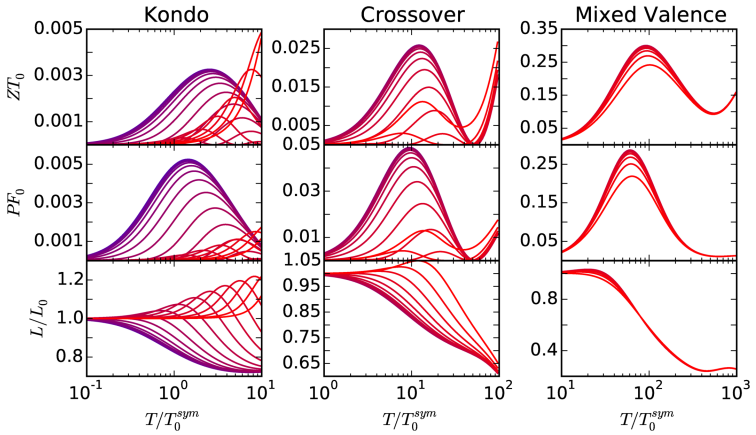


*Figure 6.5: A close up version of Figure 6.4. Note that when moving from the Kondo regime to Mixed valence regime the relevant system temperature shifts from the Kondo scale $T \approx T_0^{sym}$ to the hybridization strength $T \approx \Delta_0$.*

**Powerfactor** $PF_0$

At the Kondo temperature the power factor as well is mainly dominated by the behavior of the Seebeck coefficient. The powerfactor is given in units of $P[\frac{2k_B}{h} \approx 5.75 \times 10^{-13} W/K^2]$.

**Lorenz number** $L/L_0$

In the Fermi-liquid regime the Wiedemann-Franz law is fulfilled for any magnetic field. For higher temperatures we see deviations from the Wiedemann-Franz law. At small temperatures the deviations depend on the magnetic field similar to the behavior of the Seebeck coefficient. For $B_{\mathrm{loc}} \lesssim T_K$ the Lorenz number forms a valley ($L/L_0 < 1$) while for $B_{\mathrm{loc}} \gtrsim T_K$ a peak arises ($L/L_0 > 1$).

## 6.4 Thermopower of $CeCu_{6-x}Au_x$

In this section we will focus on the thermopower of the heavy Fermion material $CeCu_{6-x}Au_x$. The group of von Löhneysen investigated the Seebeck coefficient $S = -\frac{\Delta V}{\Delta T}$ of $CeCu_{6-x}Au_x$ for different doping concentrations $x = 0.0, 0.1, 0.3, 0.5$.

The thermoelectric properties have been of continuous experimental [105] and theoretical [103, 90, 20] interest. The Seebeck coefficient is a sensitive measure for low energy excitations in metallic systems [103]. In heavy Fermion systems we find an enhanced thermopower compared to ordinary metals [103].

### 6.4.1 Interpretation in terms of Kondo physics

Generally, in heavy Fermion systems like $CeCu_{6-x}Au_x$ local impurity screening of the magnetic Ce ions competes with magnetic RKKY interactions between the Ce ions. In this section we neglect the RKKY interaction and further assume a local impurity picture i.e., that the transport properties of this system can be approximated adequately as resulting from electron scattering from independent Ce impurities with the Ce impurities being described by the Anderson impurity model.

$CeCu_6$ does not develop antiferromagnetic ordering, but remains paramagnetic down to temperatures $T < 5\,\mathrm{mK}$ [110]. When increasing the Gold concentration the orthorhombic lattice expands lowering the hybridization of the Cerium atoms. This in turn allows the formation of local moments and the appearance of antiferromagnetic ordering below the Néel temperature $T_N$, which lies approximately below 1 K for all $x < 0.5$.

We assume that we can model the Ce atoms as a simple Anderson impurity coupling to a Cu/Au bath. We expect the most Kondo like behavior

in $CeCu_{5.5}Au_{0.5}$ as the excited crystal field state, that shows as an increase in the thermopower for higher temperatures, seems to interfere least with the ground state doublet in the $x = 0.5$ case (see Figure 6.6). On the other hand the Néel temperature is below 1 K for all concentrations investigated, justifying the dominance of the Kondo effect above this temperature.

As increasing Gold concentrations probably lead to a reduction of the coupling $J \propto \Delta/U$, we tried varying $U/\Delta$, but the $B = 0$ trends were best replicated by varying $\varepsilon_d$.

Though this is clearly not a text book example for an Anderson model, many additional effects may simply cause a renormalization of the local level energy $\varepsilon_d$ and the Kondo Temperature $T_K$. This is a very simplistic model, but nevertheless qualitatively captures the low temperature behavior and the effects of magnetic field in the systems.

It has to be noted here that opposed to Equation (6.9) the correct approach for a bulk material is given by [90, 72]

$$S(T) = -\frac{1}{|e|\,T}\frac{M_1(T)}{M_0(T)}, \tag{6.15}$$

where

$$M_n(T) = \int \mathrm{d}\omega\, \omega^n \tau(\omega, T)\left(-\frac{\partial f}{\partial \omega}\right),$$

where $\tau$ is the transport time of electron with $\frac{1}{\tau(\omega,T)} \propto \mathcal{A}_{\mathrm{d},\mathrm{d}^\dagger}(\omega)$. But in the Kondo regime for low temperatures the resulting curves are equivalent up to a sign and a shift in the effective Kondo temperature (see Costi and Zlatić [20]). As we do only expect a qualitative equivalence, the quantum dot formula (with negative sign) was used for the comparison.

### 6.4.2 Results

#### Parameter extraction and comparison

For the calculation we assume that the curves follow a universal behavior. The experimental measurements and the fitted curves can be seen in Figure 6.6. To find the corresponding values for the local level $\varepsilon_d$ we produced a set of different curves for varying $\varepsilon_d$ and compared it to the different Gold concentrations without magnetic field. As in the previous section, the Coulomb repulsion is given by $U = 16\Delta$, $\Delta = 0.001D$ using the half-bandwidth $D = 1$ as a unit of energy. As the Seebeck coefficient will be in units of $k_B/e \approx 86.17\,\mu\mathrm{V/K}$ the calculated curves were rescaled by this factor. The temperature was scaled down to fit the lowest peak of the experimental data. Table 6.1 summarizes the extracted values for $\varepsilon_d$ and the different Kondo temperature, measured as the low temperature peak of the thermopower.

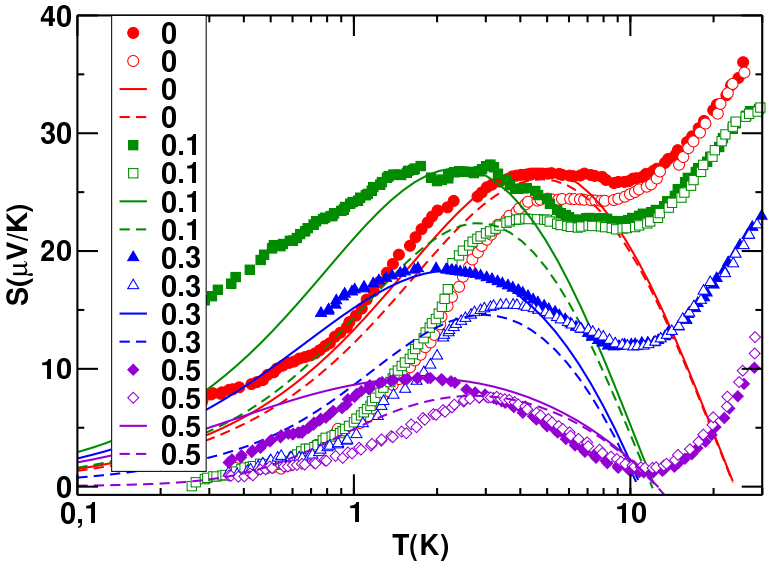


*Figure 6.6: Seebeck coefficients $S = -\frac{\Delta V}{\Delta T}$ of $CeCu_{6-x}Au_x$ for different concentrations ($x = 0, 0.1, 0.3, 0.5$). The filled symbols show the experimental data without magnetic field, the empty symbols show the Seebeck coefficients at $B = 5-6T$. The solid lines are the NRG data that fitted the experimental peak most closely. Only the purple dashed line ($x = 0.5$) is a fit in the B-field extracting the model parameters for $B = 5.5T$, for the other dashed curves.*

| $x$ | $\varepsilon_d$ | $T_K^{\text{theo}}[D]$ | $T_K^{\text{exp}}[K]$ | $\lvert E_Z\rvert\,[g\mu_B/\hbar]$ | $n_d$ |
|---|---|---|---|---|---|
| 0.5 | $-4\Delta_0$ | $1.8\times10^{-5}$ | 1.8 | $0.885\times10^{-5}$ | 0.915 |
| 0.3 | $-2.375\Delta_0$ | $4.9\times10^{-5}$ | 1.8 | $2.41\times10^{-5}$ | 0.803 |
| 0.1 | $-1.625\Delta_0$ | $1.0\times10^{-4}$ | 2.2 | $4.02\times10^{-5}$ | 0.704 |
| 0.0 | $-1.625\Delta_0$ | $1.0\times10^{-4}$ | 5.2 | $1.70\times10^{-5}$ | 0.704 |

*Table 6.1: Values for $\varepsilon_d$ that best fitted the experimental curves for different concentrations $x$, The theoretical curves where rescaled by a factor of $T_K^{exp}/T_K^{theo}$, where $T_K$ here is defined as lower temperature peak. The B-field is expected to scale with the Kondo temperature. Therefore only $B_{loc}(x = 0.5)$ was fitted to extract a g-factor of $g_{eff} \approx 0.3$, the other fields are rescaled according to the difference in Kondo temperature.*

In fitting the experimental data, we use in the theoretical calculations the same ratio of field to Kondo scale as in the experiment, i.e.,

$$B^{\mathrm{exp}}(x)/T_K^{\mathrm{exp}}(x) = B^{\mathrm{theo}}(x)/T_K^{\mathrm{theo}}(x), \tag{6.16}$$

where the Kondo scale is defined (both in theory and experiment) as the position of the low temperature Kondo induced peak in the thermopower (for given $x$) and is tabulated in Table 6.1. Thus, for the case $x = 0.5$, we would use in the calculation $B^{\mathrm{theo}}(x = 0.5) = 1.8 \times 10^{-5}\,\mathrm{D} \times 6\,\mathrm{T}/1.8\,\mathrm{K} = 6 \times 10^{-5}\,\mathrm{DT/K}$.

The magnetic field in the Hamiltonian $H_{\mathrm{B}} = -g_{\mathrm{eff}}\mu_B B S_z$ results in an energy shift of the up/down levels by a Zeemann energy $|E_Z| = \frac{1}{2} g_{\mathrm{eff}}\mu_B B^{\mathrm{theo}}$, which still requires the extraction of the g-factor. To find the corresponding factor a set of curves with varying magnetic field was produced for $\varepsilon_d = -4\Delta_0$ ($x = 0.5$). The curve that best described the experimental peak was for a Zeemann energy $|E_Z/\mu_B| = 0.885 \times 10^{-5}$. Comparing the values for $|E_Z/\mu_B|$ leads to $g_{\mathrm{eff}} \approx 0.3$.

To further strengthen the predictiveness of the theory we assume that all curves follow a universal behavior. This means that the effect of the $B_{\mathrm{loc}}$-field is only dependent on the ratio $B_{\mathrm{loc}}/T_K$ as described by Equation (6.16). We can therefore deduce the Zeemann energy $|E_Z/\mu_B|$ that corresponds to 6 T for the different curves, which are also given in Table 6.1.

The rescaled curves and the experimental data can be seen in Figure 6.6. We see qualitatively the trend in the experiment: curves calculated at a finite B-field have their maximum lowered and shifted to a higher temperature and the asymptotes of the curves for $B = 0$ and $B = 5 - 6T$ join at higher temperatures as in experiment. For higher temperatures the experiment observes a second peak, while the Anderson model typically develops a negative coefficient. This high temperature behavior cannot be captured by our theory as it probably stems from an excited crystal field state. Our model only describes the ground state doublet which is responsible for the observed low temperature Kondo induced peak in the thermopower. Adding a second spin degenerate local level, that hybridizes with a second band, could possibly capture this feature. For $x = 0$ we see a much smaller field dependence than in the experiment, which is not unexpected; this limit corresponds to a periodic array of Ce impurities, which therefore can no longer be considered a system of incoherent Kondo scatterers at low temperatures, Instead this limit should be modeled within a Kondo lattice description. In contrast, for $x \geq 0.1$, modeling the system as a collection of independent Kondo impurities, captures the main trends observed in the field dependence of the thermopower at temperatures of order $T_K$.

## 6.5 Conclusion

We described the effect of a magnetic field on the thermoelectric properties of a quantum dot in different regimes and could observe a general scaling behavior. We further applied the model to experimental measurement of the thermopower of $CeCu_{6-x}Au_x$. Though this is not a dilute system of magnetic impurities, we could reproduce the low temperature trends of the effect of a magnetic field on the thermopower and even have predictive power on the behavior at different concentrations, showing that the model can explain basic underlying trends observed. To fully describe the features of the experimental data (see Figure 6.6) would require a more sophisticated model.

# Chapter 7

# Two channel Anderson model with screening

## 7.1 Introduction

The Anderson impurity model focuses only on the most basic interactions. There are other effects that may play an important role. Phonon excitations and electron screening are some examples of how to extend the basic Anderson model. This chapter will focus on the effects of an electron screening term on the low temperature conductance and on charge and spin susceptibilities. The Anderson impurity model has been used to describe approximately local properties such as photo-emission and inverse photo-emission spectra of CuO materials [111] and of Ce [112] heavy fermion systems. Electron screening in these cases results in an effective renormalization of the Coulomb repulsion $U$, the local level energy $\varepsilon_d$ and the hybridization $\Delta$. Some work has been done on electron screening in the one channel Anderson model within NRG [26, 27]. Such an effective model breaks down for strong screening interactions. Moreover in most context screening is operative in more than one channel e.g in molecular quantum dots screening by two leads is required. In Reference [22, 27] it has been shown that a negative-U description of molecular quantum dots result in good thermoelectric performance. This motivates the detailed implementation of a conduction electron screening term in a two channel (i.e. two leads) Anderson description of a molecular quantum dot. The two channel Anderson model without any screening term has been studied previously within NRG, see for example Pruschke and Bulla [113], Sakai et al. [94] or Leo and Fabrizio [114].

In Section 7.2 we will describe the used model and discuss some of the difficulties. In Section 7.3 we verify our results and estimate its reliability by comparing to known exact results in limiting cases. The charge and spin susceptibilities and associated Kondo scales are discussed in Section 7.4

and 7.5. Last we compare our results for the local occupation and the conductance to fRG results of Hämmerle et al. [28] in Section 7.6

## 7.2 Two channel model

The two channel Anderson model for a quantum dot system coupled to a left and right lead, is given by

$$H = H_{\text{imp}} + H_{\text{int}} + H_{\text{cond}} \tag{7.1}$$

with

$$H_{\text{imp}} = U n_{d,\uparrow} n_{d,\downarrow} + \sum_{\sigma} \varepsilon_d n_{d,\sigma} \tag{7.2}$$

$$H_{\text{int}} = \sum_{k,\alpha,\sigma} V_\alpha c^\dagger_{k,\alpha,\sigma} d_\sigma + d^\dagger_\sigma c_{k,\alpha,\sigma} \tag{7.3}$$

$$H_{\text{cond}} = \sum_{k,\alpha,\sigma} \epsilon_{k,\alpha} c^\dagger_{k,\alpha,\sigma} c_{k,\alpha,\sigma}, \tag{7.4}$$

where the index $\alpha \in [L, R]$ represents the left or right lead. Without any additional terms this model can be reduced to a one channel model, by introducing even and odd conductance operator combinations (see e.g. Appendix A of Costi and Zlatić [20])

$$t a^\dagger_{e,k,\sigma} = V_L c^\dagger_{k,L,\sigma} + V_R c^\dagger_{k,R,\sigma} \tag{7.5}$$

$$t a^\dagger_{o,k,\sigma} = V_L c^\dagger_{k,R,\sigma} - V_R c^\dagger_{k,L,\sigma}. \tag{7.6}$$

This will lead to a one channel model and an uncoupled conduction electron Hamiltonian

$$H = H_{\text{SIAM},e} + H_{\text{cond},o}. \tag{7.7}$$

Here $H_{\text{SIAM},e}$ is the one channel SIAM Hamiltonian using the even operators in place of its conduction operators $c^\dagger_{k\sigma}$ and $H_{\text{cond},o}$ is just a one channel conduction band using the odd operators in place of $c^\dagger_{k\sigma}$. Thus $H_{\text{cond},o}$ introduces just a degeneracy to the one channel model whose occupation follows the usual Fermi distribution.

When introducing an additional screening term [26]

$$H_{\text{screen}} = \sum_{k,k',\alpha} U'(n_d - 1) \sum_{\sigma} (c^\dagger_{k,\alpha,\sigma} c_{k',\alpha,\sigma} - \delta_{k,k'}) \tag{7.8}$$

$$= U'(n_d - 1)(n_{0,L} - 1 + n_{0,R} - 1), \tag{7.9}$$

the odd and even Hamiltonian no longer decouple. Here we introduced the occupation of the conduction band Wannier orbitals $n_{0,\alpha} = f^\dagger_{0,\alpha,\sigma} f_{0,\alpha,\sigma}$, $\alpha \in [L, R]$ that coincide with first shell of the NRG chain. The screening term reflects that a non-occupied or doubly occupied quantum dot is electrically charged and will therefore attract nearby electrons.

### 7.2.1 Numerical Challenges

Within the NRG method, a two channel calculation is numerically demanding. In each iteration the Hilbert space does not increase by a factor $d = 4$, but by $d = 16$. Therefore keep in mind that $N_{\text{kept}} = 500$ kept states corresponds to 8000 states in each iteration. On top of that, degeneracies reduce the effective number of kept states. The program makes use of the SU(2) symmetry to reduce the number of needed eigenstates. The coefficients needed for the SU(2) symmetry can be found in Appendix A. To reduce the computation time (and to some extend increase the accuracy) a large discretization parameter $\Lambda$ was used. A few cases had been calculated with smaller $\Lambda$ to ensure that the error made remains within a few percent. This cut off scheme, depending on a fixed number of states, was used to ensure that each process ended in a similar amount of time. As the Message Passing Interface (MPI) was used to communicate between different z values, idle processes would else have occupied wasted processing time. When using an energy dependent cut off scheme, the first shells typically require more kept states than the last ones. To reflect this behavior we kept 4 times more states in the first five shells keeping all states up to shell $m_0 = 4$. The Hamiltonians of the first two shells (impurity and hybridization) are given in Appendix A. The sub-Hamiltonians where generated by a script using SymPy to avoid sign errors. The same script was also used to generate the initial matrix elements required for local observables.

## 7.3 Computational details

Due to technical details in the fRG calculation a semi-elliptical band was used instead of the usual flat band for two channel calculations

$$\Delta(\omega) = 2V^2\sqrt{1-\omega^2}. \tag{7.10}$$

The resonant level half-width is given by $\Gamma = \pi\rho(0)V^2 = 2V^2 = \Delta_L + \Delta_R$ and will be used frequently as an energy scale.

To verify that the NRG calculations for the semi-elliptical band work we compare the non-interacting Anderson Model ($U = 0$) with the one and two channel calculations of the NRG for a semi-elliptical band. The result for the local occupation of the non-interacting Anderson model at $T = 0$ is given by

$$n_d(\varepsilon_d) = -\int_{-\infty}^{0} \frac{1}{\pi} \operatorname{Im} \mathrm{G}_{d,d^\dagger}(\omega) \tag{7.11}$$

$$= \int_{-1}^{0} \frac{\Delta_I(\epsilon)/\pi}{(\epsilon - \varepsilon_d - \Delta_R(\epsilon))^2 + \Delta_I(\epsilon)^2}, \tag{7.12}$$

where $\Delta_I(\omega) = 2V^2\sqrt{1-\omega^2}$, $\Delta_R(\omega) = 2V^2\omega$ was integrated numerically. Figure 7.1 compares the NRG results to the exact ones. One channel and

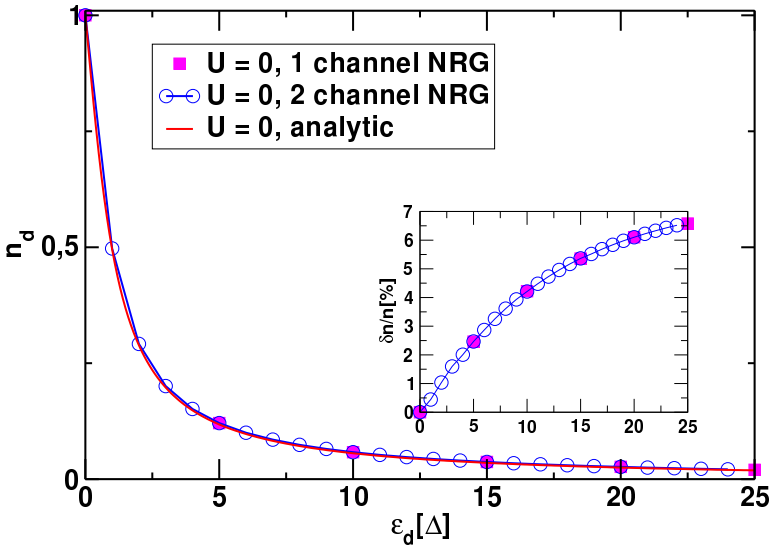


*Figure 7.1: Comparison of one and two channel NRG with analytic curve for semi elliptical band.* $N_{keep} = 500$ *(4 times in the first 5 shells, including impurity),* $\Lambda = 8$, $n_z = 16$. *The error stays below 7% for all values of* $\varepsilon_d$.

two channel calculations give almost identical results, showing that the two channel calculations converged. Nevertheless we can see a small deviation for larger $\varepsilon_d$ with a relative error $\Delta n_d/n_d < 7\%$. Lowering $\Lambda$ increases the accuracy, but also increases the computational effort significantly.

We tried two approaches to calculate the conductance in the two channel case with screening. The first one is the straightforward solution of linear response theory given in Appendix F (see also Reference [115]).

$$\mathrm{G}(T) = \frac{2}{h} \lim_{\omega \to 0} \frac{\mathrm{Im}\langle\langle I_C, I_C \rangle\rangle(\omega)}{\hbar\omega}, \tag{7.13}$$

where $I_C = -e\frac{\dot{N}_L - \dot{N}_R}{2}$, with is the electron charge $e$. The other method uses a Keldysh approach in the linear response limit (i.e. see Reference [116, 117])

$$\mathrm{G}(T) \propto \int \frac{\partial f(\omega)}{\partial \omega} \left| \mathrm{G}_{f_{0,L}, f_{0_R}^\dagger}(\omega) \right|^2 \mathrm{d}\omega\,. \tag{7.14}$$

This method requires the real and imaginary part of the Green's function. The real part was recovered by a Kramers-Kronig transform of the spectral function. A Python script that transforms arbitrarily spaced discrete signals using triangularization was used for the transformation. Figure 7.2 shows the comparison between both methods for a range of parameters. Though both curves behave similar, the results acquired using the linear response method are closer to the one-channel calculation, that has proven to deliver accurate results. A look at the spectral function $\mathcal{A}_{\mathrm{f}_{0,\mathrm{R}}, \mathrm{f}_{0,\mathrm{L}}^\dagger}(\omega)$ reveals that

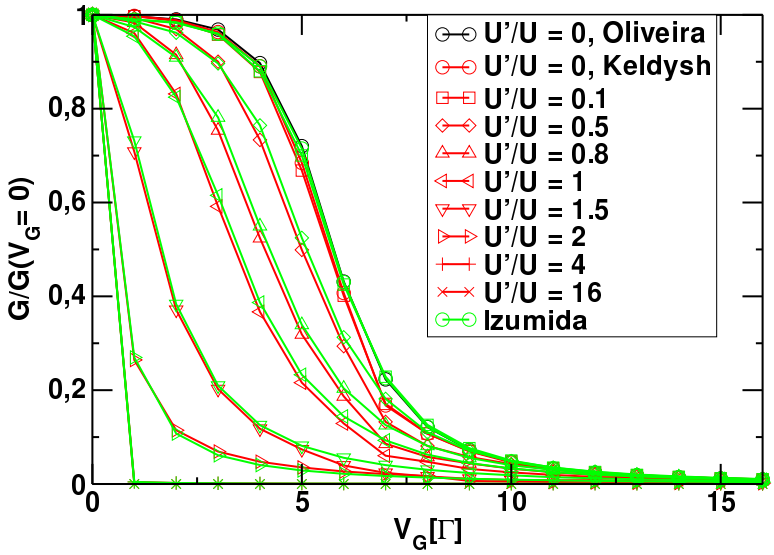


*Figure 7.2: The figure shows the comparison between different calculation methods.* $N_{keep} = 500$ *(4 times in the first 5 shells, including impurity),* $\Lambda = 8$, $n_z = 16$, $U = 12\Gamma$, $\Gamma = 0.01$. *Even though the trends are the same among the two methods, the linear response method (denoted Izumida) can better reproduce the one channel result for vanishing* $U'$ *(denoted Oliveira).*

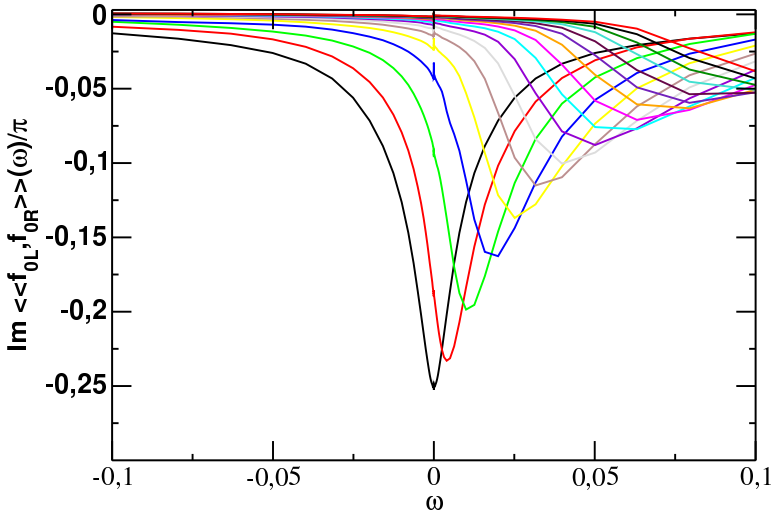


*Figure 7.3:* $\mathcal{A}_{\mathrm{f}_{0,\mathrm{R}},\mathrm{f}^{\dagger}_{0,\mathrm{L}}}(\omega)$ *for different values of* $\varepsilon_d = -\Gamma \ldots 15\Gamma$, $U = 2\Gamma$, $\Gamma = 0.01$, $U' = 0$. *There is a numerical problem at* $\omega \approx 0$ *even for* $\omega > T$.

at least the used Kernel has problems for $\omega \approx 0$ (see Figure 7.3). For $\omega < T$ this is a known problem, but it arises already at higher frequencies for this quantity. This error is probably the origin for the worse behavior of the method, as only the $\omega = 0$ part will contribute in the $T \to 0$ limit due to the Fermi window in the integral. Therefore the linear response method was used for further comparison with the fRG results. The general effect of a screening term is that it suppresses the conductance and renormalizes $\varepsilon_d$ higher values. This is in contrast to later results for small Coulomb interaction $U$ and small screening term $U'$. The conductance was normalized to one for $v_G = 0$, $v_G = \varepsilon_d + U/2$, therefore no direct statement about the conductance itself can be made, but the original data suggests that a screening term always results in a lowering of the conductance. As soon as $U' \gg U$ one can effectively see it as a negative-$U$ model. Here the gate voltage $v_G$ acts as a magnetic field that can quickly destroy the Kondo effect.

## 7.4 Charge susceptibility

Apart from low temperature conductance and local occupation number (see Section 7.6) we investigated the effect of the electron screening term on the charge and spin susceptibilities. The usual quantity, the impurity contribution of the (isothermal) charge susceptibility to the total system, needs two calculations, one with impurity and one for only the host system. We then subtract the two values (see also Chapter 3):

$$\chi_C = \beta\langle N - \langle N\rangle\rangle^2 \tag{7.15}$$

$$\chi_{C,0} = \beta\langle N - \langle N\rangle_0\rangle_0^2 \tag{7.16}$$

$$\chi_{C,\mathrm{imp}} = \chi_C - \chi_{C,0}. \tag{7.17}$$

If taking the FDM approach one has to be careful similarly to the spin susceptibility in Chapter 4. The uncoupled shells contribute to total electron number ($1 = (0+1+1+2)/4$ per uncoupled shell and channel in case the particle number $N$ is used instead of the total charge $Q$) as well as the total charge susceptibility ($0.5 = (1+0+0+1)/4$ per uncoupled shell and channel). The total charge susceptibility behaves badly for low temperatures as shown in Figure 7.4. Therefore we decided to focus on a similar quantity, the local charge susceptibility. In Chapter 4 it was reviewed that, for the Anderson model, the local spin susceptibility is equivalent to the impurity contribution of the total spin susceptibility in the wide band limit. Similarly the local charge susceptibility is equivalent to the impurity contribution [62].

Unlike the results in Chapter 4 the local susceptibilities were calculated directly using the method described in Chapter 2.6.4

$$\chi_c^{\mathrm{iso}} = -G^{(0)}_{n-\langle n\rangle,n}, \tag{7.18}$$

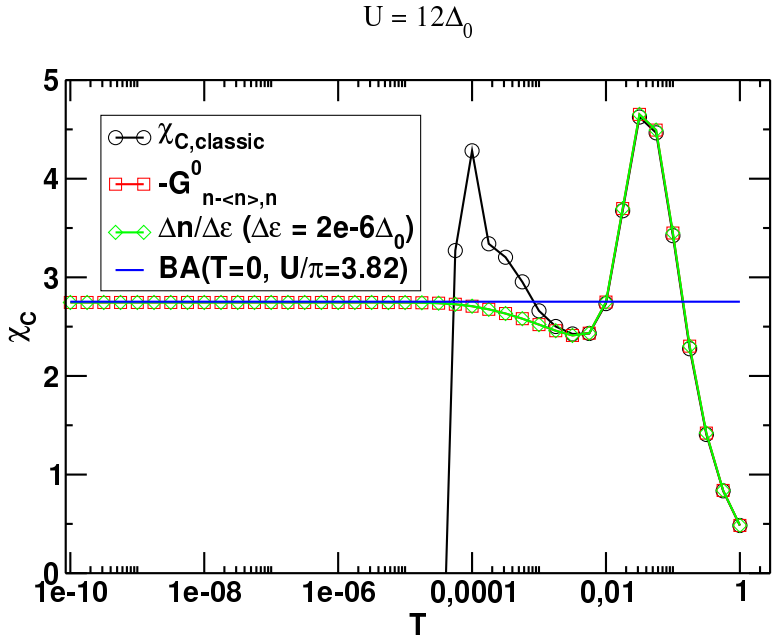


*Figure 7.4: This figure depicts the impurity contribution to the charge susceptibility. The traditional approach to take the difference of two NRG runs fails for small temperatures. The local charge susceptibility on the other hand has the same high temperature behavior as the impurity contribution to the charge susceptibility and recovers the Bethe-Ansatz results for the low temperature.*

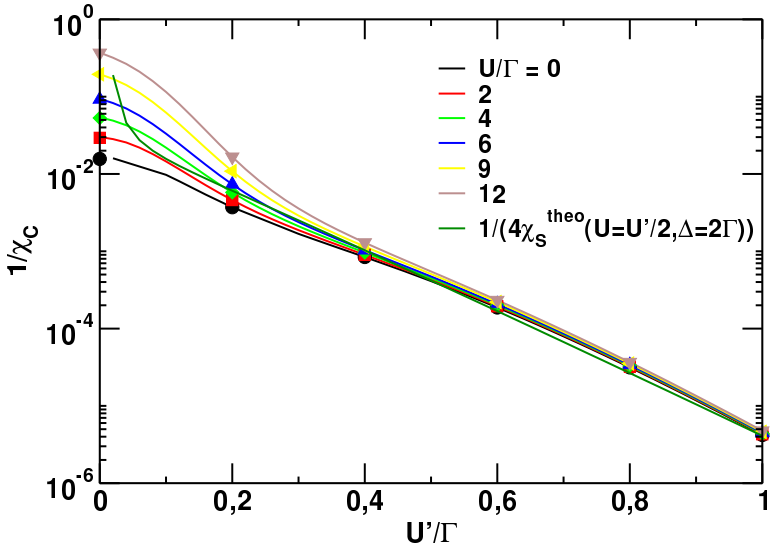


*Figure 7.5: This figure shows the charge susceptibility* $\chi_C(T = 0)$. $\Gamma = 1e - 2 = 2\Delta_0$, $N_{keep} = 500$, $\Lambda = 8$. *The lines are computed using discrete derivative* $\Delta n/\Delta\epsilon$, *where* $\Delta\epsilon = 2 \times 10^{-6}$. *As a further check the values for* $U'/\Gamma = 20, 40, \ldots, 100$ *were calculated as* $\chi_C^{iso} = -G^0_{n-\langle n\rangle,n}$ *and are displayed as filled dots. The dark green curve is equivalent to the charge susceptibility of a corresponding negative* $U$ *Anderson model.*

where $n$ is the local occupation operator. Figure 7.4 shows that the high temperature results are within 1% difference for both methods. Comparison with a Bethe-Ansatz result for zero temperature shows that this limit is also well captured. As a further check the isothermal susceptibility was compared to taking the discrete derivative $\Delta n/\Delta\varepsilon_d$.

The effect of a screening term on the local charge susceptibility has been investigated in Figure 7.5. Here the curves were calculated via discrete derivative and where checked using the linear response result of Equation (7.18) for selected points. The curves converge for high $U'$. An electron screening will reduce the Coulomb repulsion [26]. Therefore we expect to be able to describe the curves at some point by a negative $U$ Anderson model. The mapping between positive and negative $U$ Anderson model [63, 64] leads to a correspondence between charge and spin susceptibility. The modified spin susceptibility in Figure 7.5 therefore shows the charge susceptibility of a corresponds negative $U$ Anderson model. The spin susceptibility was multiplied by a factor 4 to compensate for the intrinsic prefactor $\frac{1}{2}$ of the spins. The parameters $\Delta = 2\Gamma$ and $U = U'/2$ in the analytic curve were chosen as the simplest numbers that fitted the curve. These results indicate that the two channel Anderson model at the particle-hole symmetric point behaves like a negative-$U$ Anderson model when $U' \gg U$. As expected for

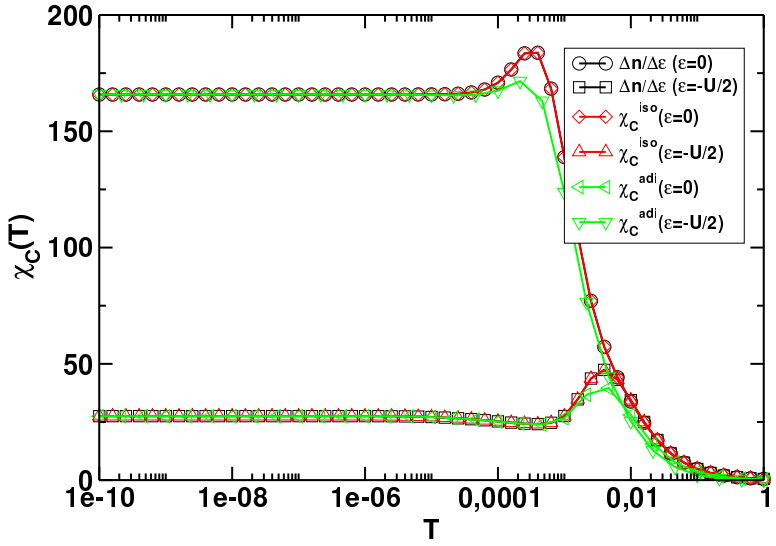


*Figure 7.6: This graph depicts the difference between the adiabatic and isothermal charge susceptibilities. The curves where produced in a one channel calculation using* $U = 12\Delta_0$,$\Delta_0 = 1 \times 10^{-3}$, $N_{keep} = 500$, $\Lambda = 4$ $n_z = 4$. *The adiabatic susceptibilities were calculated using* $\chi_C^{adi}(T) = -\mathrm{G}_{n,n}(+i0)$, *the isothermal curves where calculated using* $\chi_C^{iso}(T) = -\mathrm{G}^0_{n-\langle n\rangle,n}$. *Further the isothermal charge susceptibility was calculated from the discrete derivation* $\Delta n/\Delta\epsilon$ *using* $\Delta\epsilon = 1 \times 10^{-6}$.

the negative-$U$ Anderson model, one sees that the charge Kondo scale $1/\chi_C$ acquires an exponential dependence on $U'$. Though, keep in mind that the screening energy reaches the half band width $D = 100\Gamma = 1$ and derivations from any universal behavior are expected.

The delicate difference between adiabatic and isothermal susceptibility has been addressed in Figure 7.6. The adiabatic charge susceptibility (see Chapter 2.4) is given by

$$\chi_c^{\mathrm{adi}} = -\mathrm{G}_{n,n}(0 + i\delta). \tag{7.19}$$

Again, the isothermal susceptibility was calculated directly and by using discrete derivatives. Both adiabatic and isothermal curves give the same low temperature results but the high temperature peak behaves slightly differently.

## 7.5 Spin susceptibility

Like the charge susceptibility, the impurity contribution to the total spin susceptibility can develop bad behavior. Its definition is similar to the charge

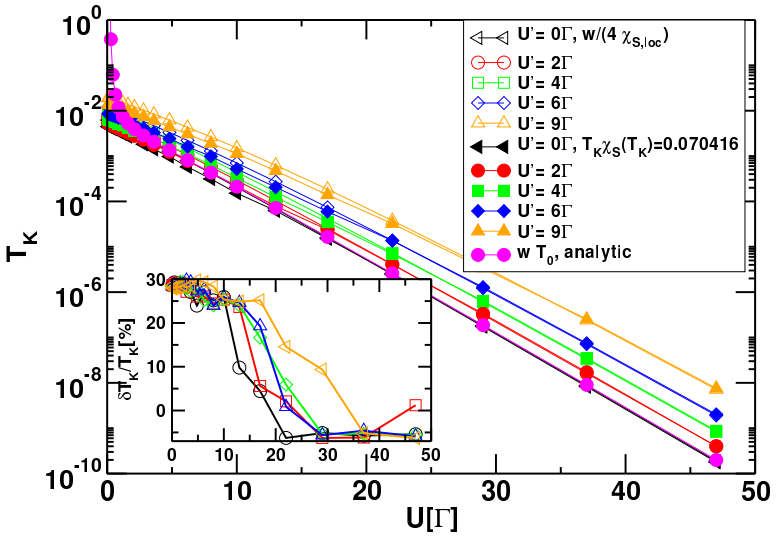


*Figure 7.7: Comparison between different methods to calculate the Kondo Temperature for the symmetric Anderson Model with screening. The Wilson number $w = 0.41071\ldots$ connects $T_0$ with the Kondo Temperature $T_K$. $T_K$ was extracted by linear interpolation of $T\chi_S(T)$ for $T = 1\times10^{-10}\ldots1\times10^{-1}$ using 51 values for $T$. Both methods give similar results in the Kondo limit. The calculation details are the same as in Figure 7.9.*

susceptibility and was discussed in Chapter 4 for the Anderson model. Independently Fang et al. [52] showed that the local spin susceptibility, which is equivalent to the impurity contribution in the wide band limit, can be calculated directly within the NRG. The local $s_z$ operator is a spin $S = 1$ tensor operator. Therefore three subspaces have to be considered when calculating it within $SU(2)$ symmetry. The details about the operator derivation can be seen in Appendix A.

Figure 7.7 shows the effect of a screening term on the Kondo temperature in the symmetric case $\varepsilon_d = -U/2$. The Kondo temperature was extracted using two different methods. As the impurity contribution to the total spin susceptibility $\chi_S$ behaves bad for low temperatures $T_0 = 1/(4\chi_S(T = 0))$, $T_0$ was evaluated using the local spin susceptibility $T_0 = 1/(4\chi_s(T = 0))$. The other method is by finding $T\chi_S(T) = 0.070416\ldots$ for the total spin [32, 62]. The two Kondo temperatures are connected by the Wilson number $\omega = 0.41071\ldots$ [62]. As a check the analytic curve $T_K = \frac{1}{4\chi_S(T=0)} = \sqrt{\frac{U\Gamma}{2}}\exp(-\frac{\pi U}{8\Gamma} + \frac{\pi\Gamma}{2U})$ was inserted for comparison in the Kondo regime. The inset shows the relative error between the two methods. The two methods become equivalent for large values of $U$. It can be seen that $U'$ competes with $U$ increasing the Kondo temperature as well as delaying the convergence of the two methods.

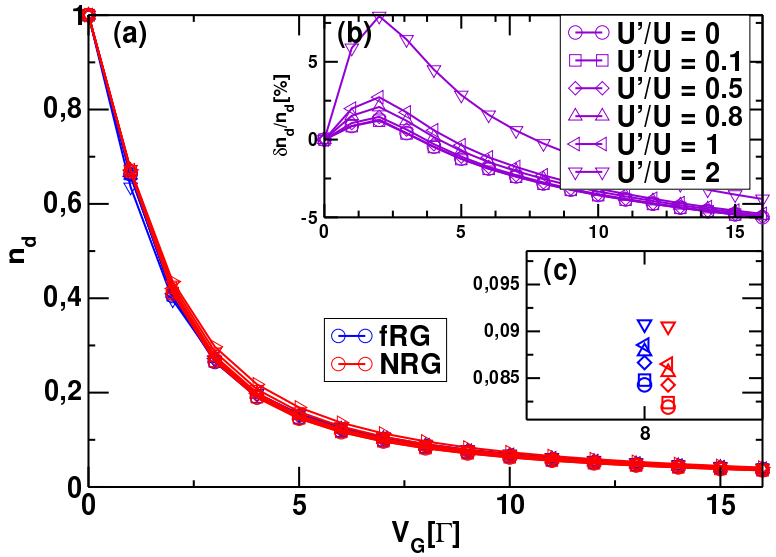


*Figure 7.8: Comparison between the fRG and NRG results for the local occupation number using $U = 0.02$, $\Gamma = 0.01$. Inset (b) shows the relative error between the two methods. Inset (c) is a close up on $v_G = 8\Gamma$. The NRG results have been shifted a bit to the right to make the results easier comparable.*

## 7.6 Comparison with fRG

The low temperature local occupation and the conductance have been compared with recent fRG results of Hämmerle et al. [28] (obtained within the static approximation). The fRG approach, see Metzner et al. [118], is expected to be quantitatively accurate for $U, U' \lesssim \Gamma$ and yield qualitatively correct trends as a function of $U$ and $U'$ in quantities like conductance and local occupation number. Hence it provides a useful test for our NRG calculations.

The local occupation number depending on the local level position $v_G = \varepsilon_d + \frac{1}{2}U$ and on the conductance electron screening term $U'$ can be viewed in Figure 7.8. On a larger scale both methods produce the same curve. Figure 7.1 suggests that part of the error for $U' = 0$ is due to the large discretization. For $U'/U < 0.5$ both methods can reproduce the same trends, only for larger values $U'/U \geq 1$ the two methods begin to diverge. The Inset (c) shows a close-up to points at $v_G = 8\Gamma$. The trend for higher conductance electron screening is a lower effective value for $v_G$. A screening term $U'$ is known to renormalize $U$, $\varepsilon_d$ and $\Gamma$. For small $U$ and $U'$ the effective increase of the hybridization [25] $\Gamma' > \Gamma$, which would lead to a lower effective $v_G$, seems to be the dominant effect.

Figure 7.9 shows results for the normalized conductance for $U = 2\Gamma$. The

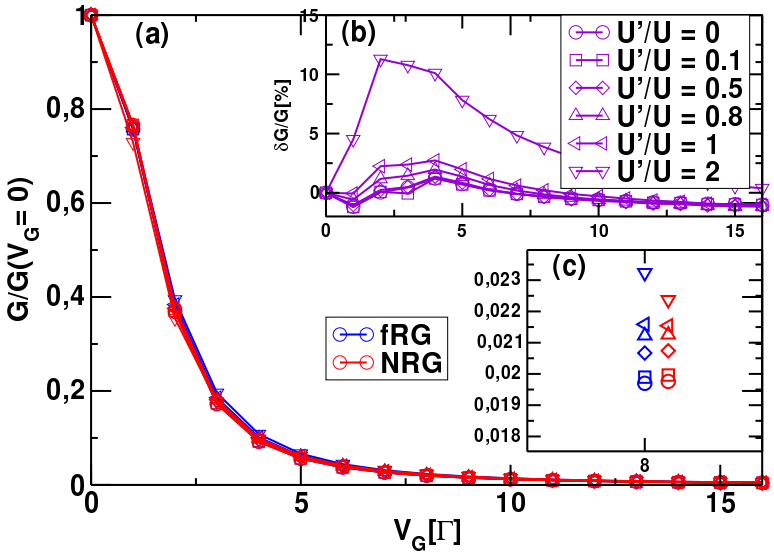


*Figure 7.9: Comparison between fRG and NRG results for the conductance using $U = 0.02$, $\Gamma = 0.01$. Inset (b) shows the relative error between the two methods. Inset (c) is a close up on $v_G = 8\Gamma$. The NRG results have been shifted a bit to the right to make the results easier comparable.*

results are very similar to the behavior of the occupation number. The two methods agree up to a small error in case of a small screening term and begin to diverge for $U'/U \geq 1$. The effect of the screening term as well is an effective reduction of $v_G$.

## 7.7 Conclusion

We showed that the NRG method is capable of calculating results for the two channel Anderson model. We noted the delicate difference between isothermal and adiabatic susceptibility at finite temperatures. The comparison with fRG showed that both methods agree for small screening terms, though the large discretization parameter $\Lambda$ needed to succeed with the NRG calculation induces a small bias error. Though the calculation of the real part of isothermal susceptibilities were shown to be unproblematic at all temperatures, the calculation of finite temperature spectral functions, within the FDM approach, are completely free of artifacts only at zero temperature. A discussion of this problem can be found in Appendix C.

# Chapter 8

# Conclusion and Outlook

After giving an introduction to the Anderson model, we gave a detailed description of the NRG method. Chapter 3 introduced a new method to calculate the specific heat in the Anderson model and related models. Further we saw the success of z-averaging, enabling the evaluation of specific heats on an arbitrary temperature grid and at large $\Lambda$. The numerical evaluation of the Bethe ansatz equations allowed the accuracy of the specific heats within the conventional and the new method to be assessed. In Chapter 4 the FDM approach for static correlation functions was applied to the specific heat and the impurity contribution to the uniform susceptibility. Within this method, a non negligible contribution from the environment degrees of freedom needs to be taken into account to recover the correct susceptibility. Chapter 5 implemented an accurate method to calculate the conductance of a quantum dot, enabling the extraction of the Fermi liquid scaling coefficients $c_T$ and $c_B$ to high accuracy. The results agreed very well with renormalized superperturbation theory. The introduction of the $U(1)$ symmetry enabled the investigation of the effect of a magnetic field on the thermoelectric properties of quantum dots (Chapter 6). The introduction of the two channel Hamiltonian (Chapter 7) brought a couple of challenges. A calculation for the $T = 0$ conductance via the Kubo formula was found to be more accurate than via the Keldysh approach (in the linear response limit). As the impurity contribution to the charge susceptibility exhibits artifacts for $T \to 0$ a new approach based on the local charge susceptibility was introduced which overcame this problem.

In future work it would be interesting to investigate the effect of the screening term on the thermoelectric properties for finite temperatures. The NRG faces problems for the calculation of these quantities when a temperature independent broadening scheme is used (see Appendix C), resulting in the need to strongly broaden the spectral functions (see also Appendix F). To increase the accuracy of the two channel calculations more symmetries can be used. Though the even and odd Hamiltonians no longer decouple,

electrons do not tunnel between them. Therefore an additional symmetry can be exploited allowing the use of a smaller discretization parameter $\Lambda$. Finally, a screening term is only one of the discussed mechanisms for the realization of a negative-U model, which is desirable for enhancing thermoelectric efficiency. Phonon modes as described by the Anderson-Holstein model can also lead to an effective reduction of the Coulomb repulsions, and offer an additional path to enhanced thermoelectric efficiency of quantum dots.

# Appendix A

# Coefficients for SU(2) symmetry

In this appendix we present detailed information about the prefactors involved in a NRG run using $SU(2)$ symmetry for the two channel case. Please note, that all prefactors in the two channel case have not been derived by hand as it is too easy to make sign errors. A self written Python script was used to calculate the basis for the first iterations, the general basis, the starting Hamiltonian and operator matrix entries and the prefactors for the diagonalization. It has the capabilities to calculate arbitrary many bands and/or impurity excitations in the $SU(2)$ symmetry. The symbolic calculations in the script were computed using SymPy (v. 0.7.2), the simplify routine was hand tuned as we are only interested in the well behaved cases. The routine for calculating Clebsch-Gordan coefficients can be found in Reference [119]. Not well behaving cases are excluded manually in the program (like the $S = 0$ triplet for the two-channel diagonalization). The coefficients for the diagonalization were checked with the ones given in Reference [120].

## A.1 Diagonalization

### A.1.1 Generating operators

Considering the Hamiltonian at a step during the diagonalization

$$\begin{aligned} H_{n+1} = H_n + \sum_{\sigma,\alpha} \epsilon_{n+1} f^\dagger_{n+1,\sigma,\alpha} f_{n+1,\sigma,\alpha} \\ + t_n \underbrace{\sum_{\sigma,\alpha} f^\dagger_{n+1,\sigma,\alpha} f_{n,\sigma,\alpha} + h.c.}_{H_H}. \end{aligned} \tag{A.1}$$

The states spanning the Hilbert space can be generated from the previous iteration by the creation operators $f^\dagger_{n+1,\sigma,\alpha}$. We want to make use of the full

$SU(2)$ symmetry. The combination of two angular momentums is given by

$$|J,M\rangle = \sum_{m_1=-j_1}^{j_1} \sum_{m_2=-j_2}^{j_2} \langle j_1, m_1, j_2, m_2 \mid J, M\rangle |j_1, m_1\rangle |j_2, m_2\rangle, \tag{A.2}$$

where $\langle j_1, m_1, j_2, m_2 \mid J, M\rangle$ is the corresponding Clebsch-Gordan coefficient. To ensure that the appended states will have well defined spin values the creation operators should fulfill the definition for a spherical tensor operator $T_q^k$

$$[J^{\pm}, T_q^k] = \sqrt{k(k+1) - q(q\pm 1)} \cdot T_{q\pm 1}^k \tag{A.3}$$

$$[J_z, T_q^k] = q \cdot T_q^k. \tag{A.4}$$

The operator sets will be arranged in groups accordingly. For the one channel case the Hilbert space can be spanned by

$$|N, S, S_z, r, \varnothing\rangle = 1|N, S, S_z, r\rangle \tag{A.5}$$

$$|N, S, S_z, r, \uparrow\rangle = f_{n+1,\uparrow}^{\dagger}|N, S, S_z, r\rangle \tag{A.6}$$

$$|N, S, S_z, r, \downarrow\rangle = f_{n+1,\downarrow}^{\dagger}|N, S, S_z, r\rangle \tag{A.7}$$

$$|N, S, S_z, r, \uparrow\downarrow\rangle = f_{n+1,\uparrow}^{\dagger} f_{n+1,\downarrow}^{\dagger}|N, S, S_z, r\rangle. \tag{A.8}$$

For the two channel case, this is provided by the following combinations

$$|N=0, S=0, S_z=0\rangle : \quad 1 \tag{A.9}$$

$$|N=1, S=\tfrac{1}{2}, S_z=-\tfrac{1}{2}\rangle : f_{n+1,\downarrow,1}^{\dagger} \tag{A.10}$$

$$|N=1, S=\tfrac{1}{2}, S_z=\tfrac{1}{2}\rangle : \quad f_{n+1,\uparrow,1}^{\dagger} \tag{A.11}$$

$$|N=1, S=\tfrac{1}{2}, S_z=-\tfrac{1}{2}\rangle : f_{n+1,\downarrow,2}^{\dagger} \tag{A.12}$$

$$|N=1, S=\tfrac{1}{2}, S_z=\tfrac{1}{2}\rangle : \quad f_{n+1,\uparrow,2}^{\dagger} \tag{A.13}$$

$$|N=2, S=0, S_z=0\rangle : \quad f_{n+1,\uparrow,1}^{\dagger} f_{n+1,\downarrow,1}^{\dagger} \tag{A.14}$$

$$|N=2, S=0, S_z=0\rangle : \quad f_{n+1,\uparrow,2}^{\dagger} f_{n+1,\downarrow,2}^{\dagger} \tag{A.15}$$

$$|N=2, S=0, S_z=0\rangle : \quad \frac{1}{\sqrt{2}}\left(f_{n+1,\uparrow,1}^{\dagger} f_{n+1,\downarrow,2}^{\dagger} - f_{n+1,\downarrow,1}^{\dagger} f_{n+1,\uparrow,2}^{\dagger}\right) \tag{A.16}$$

$$|N=2,S=1,S_z=-1\rangle : f^\dagger_{n+1,\downarrow,1} f^\dagger_{n+1,\downarrow,2} \tag{A.17}$$

$$|N=2,S=1,S_z=0\rangle : \frac{1}{\sqrt{2}}\left(f^\dagger_{n+1,\uparrow,1} f^\dagger_{n+1,\downarrow,2} + f^\dagger_{n+1,\downarrow,1} f^\dagger_{n+1,\uparrow,2}\right) \tag{A.18}$$

$$|N=2,S=1,S_z=1\rangle : f^\dagger_{n+1,\uparrow,1} f^\dagger_{n+1,\uparrow,2} \tag{A.19}$$

$$|N=3,S=\tfrac{1}{2},S_z=-\tfrac{1}{2}\rangle : f^\dagger_{n+1,\uparrow,1} f^\dagger_{n+1,\downarrow,1} f^\dagger_{n+1,\downarrow,2} \tag{A.20}$$

$$|N=3,S=\tfrac{1}{2},S_z=\tfrac{1}{2}\rangle : f^\dagger_{n+1,\uparrow,1} f^\dagger_{n+1,\downarrow,1} f^\dagger_{n+1,\uparrow,2} \tag{A.21}$$

$$|N=3,S=\tfrac{1}{2},S_z=-\tfrac{1}{2}\rangle : f^\dagger_{n+1,\downarrow,1} f^\dagger_{n+1,\uparrow,2} f^\dagger_{n+1,\downarrow,2} \tag{A.22}$$

$$|N=3,S=\tfrac{1}{2},S_z=\tfrac{1}{2}\rangle : f^\dagger_{n+1,\uparrow,1} f^\dagger_{n+1,\uparrow,2} f^\dagger_{n+1,\downarrow,2} \tag{A.23}$$

$$|N=4,S=0,S_z=0\rangle : f^\dagger_{n+1,\uparrow,1} f^\dagger_{n+1,\downarrow,1} f^\dagger_{n+1,\uparrow,2} f^\dagger_{n+1,\downarrow,2}. \tag{A.24}$$

### A.1.2 New Basis states

Using Equation (A.2) these states can now be used to create a new basis with well defined quantum numbers. For the one channel case the new basis states are given by

$$|N,S,S_z,r,1\rangle = |N,S,S_z,r\rangle|\varnothing\rangle \tag{A.25}$$

$$\begin{aligned}|N,S,S_z,r,2\rangle = {} & \frac{\sqrt{S+S_z+1}}{\sqrt{2}\sqrt{S+1}}|N-1,S+\frac{1}{2},S_z+\frac{1}{2},r\rangle|\Downarrow\rangle \\ & - \frac{\sqrt{S-S_z+1}}{\sqrt{2}\sqrt{S+1}}|N-1,S+\frac{1}{2},S_z-\frac{1}{2},r\rangle|\Uparrow\rangle\end{aligned} \tag{A.26}$$

$$\begin{aligned}|N,S,S_z,r,3\rangle = {} & \frac{\sqrt{S-S_z}}{\sqrt{2}\sqrt{S}}|N-1,S-\frac{1}{2},S_z+\frac{1}{2},r\rangle|\Downarrow\rangle \\ & + \frac{\sqrt{S+S_z}}{\sqrt{2}\sqrt{S}}|N-1,S-\frac{1}{2},S_z-\frac{1}{2},r\rangle|\Uparrow\rangle\end{aligned} \tag{A.27}$$

$$|N,S,S_z,r,4\rangle = |N-2,S,S_z,r\rangle|\Uparrow\downarrow\rangle. \tag{A.28}$$

In the two channel case the states are given by

$$|N,S,S_z,r,1\rangle = |N,S,S_z,r\rangle|\varnothing\rangle \tag{A.29}$$

$$|N,S,S_z,r,2\rangle = \frac{\sqrt{S+S_z+1}}{\sqrt{2}\sqrt{S+1}}|N-1,S+\frac{1}{2},S_z+\frac{1}{2},r\rangle\Downarrow,\varnothing\rangle + \frac{(-S+S_z-1)}{\sqrt{2}\sqrt{S+1}\sqrt{S-S_z+1}}|N-1,S+\frac{1}{2},S_z-\frac{1}{2},r\rangle\Uparrow,\varnothing\rangle \quad \text{(A.30)}$$

$$|N,S,S_z,r,3\rangle = \frac{\sqrt{S-S_z}}{\sqrt{2}\sqrt{S}}|N-1,S-\frac{1}{2},S_z+\frac{1}{2},r\rangle\Downarrow,\varnothing\rangle + \frac{\sqrt{S+S_z}}{\sqrt{2}\sqrt{S}}|N-1,S-\frac{1}{2},S_z-\frac{1}{2},r\rangle\Uparrow,\varnothing\rangle \quad \text{(A.31)}$$

$$|N,S,S_z,r,4\rangle = \frac{\sqrt{S+S_z+1}}{\sqrt{2}\sqrt{S+1}}|N-1,S+\frac{1}{2},S_z+\frac{1}{2},r\rangle|\varnothing,\downarrow\rangle + \frac{(-S+S_z-1)}{\sqrt{2}\sqrt{S+1}\sqrt{S-S_z+1}}|N-1,S+\frac{1}{2},S_z-\frac{1}{2},r\rangle|\varnothing,\uparrow\rangle \quad \text{(A.32)}$$

$$|N,S,S_z,r,5\rangle = \frac{\sqrt{S-S_z}}{\sqrt{2}\sqrt{S}}|N-1,S-\frac{1}{2},S_z+\frac{1}{2},r\rangle|\varnothing,\downarrow\rangle + \frac{\sqrt{S+S_z}}{\sqrt{2}\sqrt{S}}|N-1,S-\frac{1}{2},S_z-\frac{1}{2},r\rangle|\varnothing,\uparrow\rangle \quad \text{(A.33)}$$

$$|N,S,S_z,r,6\rangle = |N-2,S,S_z,r\rangle\Uparrow\downarrow,\varnothing\rangle \quad \text{(A.34)}$$

$$|N,S,S_z,r,7\rangle = \frac{1}{\sqrt{2}}|N-2,S,S_z,r\rangle\Downarrow,\uparrow\rangle + -\frac{1}{\sqrt{2}}|N-2,S,S_z,r\rangle\Uparrow,\downarrow\rangle \quad \text{(A.35)}$$

$$|N,S,S_z,r,8\rangle = |N-2,S,S_z,r\rangle|\varnothing,\uparrow\downarrow\rangle \quad \text{(A.36)}$$

$$
\begin{aligned}
|N,S,S_z,r,9\rangle = &-\frac{\sqrt{S+S_z+1}\sqrt{S+S_z+2}}{\sqrt{2}\sqrt{S+1}\sqrt{2S+3}}|N-2,S+1,S_z+1,r\rangle|\Downarrow,\downarrow\rangle \\
&+\frac{\sqrt{S-S_z+1}\sqrt{S+S_z+1}}{\sqrt{2}\sqrt{S+1}\sqrt{2S+3}}|N-2,S+1,S_z,r\rangle|\Downarrow,\uparrow\rangle \\
&+\frac{\sqrt{S-S_z+1}\sqrt{S+S_z+1}}{\sqrt{2}\sqrt{S+1}\sqrt{2S+3}}|N-2,S+1,S_z,r\rangle|\Uparrow,\downarrow\rangle \\
&+-\frac{\sqrt{S-S_z+1}\sqrt{S-S_z+2}}{\sqrt{2}\sqrt{S+1}\sqrt{2S+3}}|N-2,S+1,S_z-1,r\rangle|\Uparrow,\uparrow\rangle
\end{aligned}
\tag{A.37}
$$

$$
\begin{aligned}
|N,S,S_z,r,10\rangle = &-\frac{\sqrt{S-S_z}\sqrt{S+S_z+1}}{\sqrt{2}\sqrt{S}\sqrt{S+1}}|N-2,S,S_z+1,r\rangle|\Downarrow,\downarrow\rangle \\
&+-\frac{S_z}{\sqrt{2}\sqrt{S}\sqrt{S+1}}|N-2,S,S_z,r\rangle|\Downarrow,\uparrow\rangle \\
&+-\frac{S_z}{\sqrt{2}\sqrt{S}\sqrt{S+1}}|N-2,S,S_z,r\rangle|\Uparrow,\downarrow\rangle \\
&+\frac{\sqrt{S+S_z}\sqrt{S-S_z+1}}{\sqrt{2}\sqrt{S}\sqrt{S+1}}|N-2,S,S_z-1,r\rangle|\Uparrow,\uparrow\rangle
\end{aligned}
\tag{A.38}
$$

$$
\begin{aligned}
|N,S,S_z,r,11\rangle = &-\frac{\sqrt{2}\sqrt{S-S_z}\sqrt{S-S_z-1}}{2\sqrt{S}\sqrt{2S-1}}|N-2,S-1,S_z+1,r\rangle|\Downarrow,\downarrow\rangle \\
&+-\frac{\sqrt{S-S_z}\sqrt{S+S_z}}{\sqrt{2}\sqrt{S}\sqrt{2S-1}}|N-2,S-1,S_z,r\rangle|\Downarrow,\uparrow\rangle \\
&+-\frac{\sqrt{S-S_z}\sqrt{S+S_z}}{\sqrt{2}\sqrt{S}\sqrt{2S-1}}|N-2,S-1,S_z,r\rangle|\Uparrow,\downarrow\rangle \\
&+-\frac{\sqrt{S+S_z}\sqrt{S+S_z-1}}{\sqrt{2}\sqrt{S}\sqrt{2S-1}}|N-2,S-1,S_z-1,r\rangle|\Uparrow,\uparrow\rangle
\end{aligned}
\tag{A.39}
$$

$$
\begin{aligned}
|N,S,S_z,r,12\rangle = &\frac{\sqrt{S+S_z+1}}{\sqrt{2}\sqrt{S+1}}|N-3,S+\frac{1}{2},S_z+\frac{1}{2},r\rangle|\Uparrow\downarrow,\downarrow\rangle \\
&+\frac{(-S+S_z-1)}{\sqrt{2}\sqrt{S+1}\sqrt{S-S_z+1}}|N-3,S+\frac{1}{2},S_z-\frac{1}{2},r\rangle|\Uparrow\downarrow,\uparrow\rangle
\end{aligned}
\tag{A.40}
$$

$$
\begin{aligned}
|N,S,S_z,r,13\rangle = &\frac{\sqrt{S-S_z}}{\sqrt{2}\sqrt{S}}|N-3,S-\frac{1}{2},S_z+\frac{1}{2},r\rangle|\Uparrow\downarrow,\downarrow\rangle \\
&+\frac{\sqrt{S+S_z}}{\sqrt{2}\sqrt{S}}|N-3,S-\frac{1}{2},S_z-\frac{1}{2},r\rangle|\Uparrow\downarrow,\uparrow\rangle
\end{aligned}
\tag{A.41}
$$

$$|N,S,S_z,r,14\rangle = \frac{\sqrt{S+S_z+1}}{\sqrt{2}2\sqrt{S+1}}|N-3,S+\frac{1}{2},S_z+\frac{1}{2},r\rangle|\downarrow,\uparrow\downarrow\rangle + \frac{(-S+S_z-1)}{\sqrt{2}\sqrt{S+1}\sqrt{S-S_z+1}}|N-3,S+\frac{1}{2},S_z-\frac{1}{2},r\rangle|\uparrow,\uparrow\downarrow\rangle \tag{A.42}$$

$$|N,S,S_z,r,15\rangle = \frac{\sqrt{S-S_z}}{\sqrt{2}\sqrt{S}}|N-3,S-\frac{1}{2},S_z+\frac{1}{2},r\rangle|\downarrow,\uparrow\downarrow\rangle + \frac{\sqrt{S+S_z}}{\sqrt{2}\sqrt{S}}|N-3,S-\frac{1}{2},S_z-\frac{1}{2},r\rangle|\uparrow,\uparrow\downarrow\rangle \tag{A.43}$$

$$|N,S,S_z,r,16\rangle = |N-4,S,S_z,r\rangle|\uparrow\downarrow,\uparrow\downarrow\rangle. \tag{A.44}$$

Note that, as a singlet and a triplet never couple into a singlet[120], $|N,S,S_z,r,10\rangle_{n+1}$ only exist for $S \neq 0$. The states will occasionally be abbreviated as $|i\rangle$.

### A.1.3 Diagonalization Coefficients

The next step is to calculate $\langle i|H_{n+1}|j\rangle$. Like mentioned in Chapter 2, $H_n$ and $H_{\text{on-site}} = \sum_{\sigma,\alpha}\epsilon_{n+1}f^\dagger_{n+1,\sigma,\alpha}f_{n+1,\sigma,\alpha}$ will contribute to the diagonal matrix elements of $\langle i|H_{n+1}|j\rangle$. To calculate the remaining $\langle i|H_{\text{hopping}}|j\rangle$ and to make the diagonalization independent of $S_z$, we will have to use the Wigner-Eckart theorem on the creation/annihilation operators $f^{(\dagger)}_{n+1,\sigma,\alpha}$. For a spherical tensor operator $T^k_q$ it states that its z-component can be separated from the operator

$$\langle J',J'_z,r'|T^k_q|J,J_z,r\rangle = \langle J,J_z,k,q \mid J',J'_z\rangle\langle J',r'||\,T^k\,||J,r\rangle, \tag{A.45}$$

where $\langle J,J_z,k,q \mid J',J'_z\rangle$ represent the corresponding Clebsch-Gordan coefficients and $\langle J',r'||\,T^k\,||J,r\rangle$ are referred to as the reduced matrix elements of $T^k_q$.

We will calculate the emerging coefficients exemplary for $\langle 1|H_{\text{hopping}}|3\rangle$. A collection of all non-zero coefficients are listed in Table A.1.

$$\begin{aligned}
\langle 1|H_H|3\rangle &= \langle {}^0_0|\langle N,S,S_z,r|f^\dagger_{n,\uparrow,1}f_{n+1,\uparrow,1}|N-1,S-\tfrac{1}{2},S_z-\tfrac{1}{2},r'\rangle|{}^\uparrow_0\rangle\sqrt{\tfrac{S+S_z}{2S}}\\
&+ \langle {}^0_0|\langle N,S,S_z,r|f^\dagger_{n,\downarrow,1}f_{n+1,\downarrow,1}|N-1,S-\tfrac{1}{2},S_z+\tfrac{1}{2},r'\rangle|{}^\downarrow_0\rangle\sqrt{\tfrac{S-S_z}{2S}}\\
&= \langle {}^0_0|\langle N,S,S_z,r|f^\dagger_{n,\uparrow,1}|N-1,S-\tfrac{1}{2},S_z-\tfrac{1}{2},r'\rangle|{}^0_0\rangle\sqrt{\tfrac{S+S_z}{2S}}(-1)^{N-1}\\
&+ \langle {}^0_0|\langle N,S,S_z,r|f^\dagger_{n,\downarrow,1}|N-1,S-\tfrac{1}{2},S_z+\tfrac{1}{2},r'\rangle|{}^0_0\rangle\sqrt{\tfrac{S-S_z}{2S}}(-1)^{N-1}\cdot\\
&= \langle N,S,r||\,f^\dagger_{n,1}\,||N-1,S-\tfrac{1}{2},r'\rangle\tfrac{S+S_z}{2S}(-1)^{N-1}\\
&+ \langle N,S,r||\,f^\dagger_{n,1}\,||N-1,S-\tfrac{1}{2},r'\rangle\tfrac{S-S_z}{2S}(-1)^{N-1}\\
&= {}_n\langle N,S,r||\,f^\dagger_{n,1}\,||N-1,S-\tfrac{1}{2},r'\rangle_n(-1)^{N-1}
\end{aligned} \tag{A.46}$$

| $\langle i\|$ | $\|j\rangle$ | $\alpha$ | Coefficient $\times(-1)^N$ | $\langle i\|$ | $\|j\rangle$ | $\alpha$ | Coefficient $\times(-1)^N$ |
|---|---|---|---|---|---|---|---|
| 1 | 2 | 1 | $-1$ | 6 | 12 | 2 | $-1$ |
| 1 | 3 | 1 | $-1$ | 6 | 13 | 2 | $-1$ |
| 1 | 4 | 2 | $-1$ | 7 | 12 | 1 | $-\frac{1}{2}\sqrt{2}$ |
| 1 | 5 | 2 | $-1$ | 7 | 13 | 1 | $-\frac{1}{2}\sqrt{2}$ |
| 2 | 6 | 1 | $\frac{\sqrt{2S+2}}{\sqrt{2S+1}}$ | 7 | 14 | 2 | $-\frac{1}{2}\sqrt{2}$ |
| 2 | 7 | 2 | $-\frac{\sqrt{S+1}}{\sqrt{2S+1}}$ | 7 | 15 | 2 | $-\frac{1}{2}\sqrt{2}$ |
| 2 | 9 | 2 | 1 | 8 | 14 | 1 | $-1$ |
| 2 | 10 | 2 | $\frac{\sqrt{S}}{\sqrt{2S+1}}$ | 8 | 15 | 1 | $-1$ |
| 3 | 6 | 1 | $-\frac{\sqrt{2}\sqrt{S}}{\sqrt{2S+1}}$ | 9 | 12 | 1 | $\frac{\sqrt{4S+6}}{2\sqrt{S+1}}$ |
| 3 | 7 | 2 | $\frac{\sqrt{S}}{\sqrt{2S+1}}$ | 9 | 14 | 2 | $-\frac{\sqrt{4S+6}}{2\sqrt{S+1}}$ |
| 3 | 10 | 2 | $\frac{\sqrt{S+1}}{\sqrt{2S+1}}$ | 10 | 12 | 1 | $-\frac{\sqrt{2}\sqrt{S}}{2\sqrt{S+1}}$ |
| 3 | 11 | 2 | 1 | 10 | 13 | 1 | $\frac{\sqrt{2S+2}}{2\sqrt{S}}$ |
| 4 | 7 | 1 | $-\frac{\sqrt{S+1}}{\sqrt{2S+1}}$ | 10 | 14 | 2 | $\frac{\sqrt{2}\sqrt{S}}{2\sqrt{S+1}}$ |
| 4 | 8 | 2 | $\frac{\sqrt{2S+2}}{\sqrt{2S+1}}$ | 10 | 15 | 2 | $-\frac{\sqrt{2S+2}}{2\sqrt{S}}$ |
| 4 | 9 | 1 | $-1$ | 11 | 13 | 1 | $-\frac{\sqrt{4S-2}}{2\sqrt{S}}$ |
| 4 | 10 | 1 | $-\frac{\sqrt{S}}{\sqrt{2S+1}}$ | 11 | 15 | 2 | $\frac{\sqrt{4S-2}}{2\sqrt{S}}$ |
| 5 | 7 | 1 | $\frac{\sqrt{S}}{\sqrt{2S+1}}$ | 12 | 16 | 2 | $\frac{\sqrt{2S+2}}{\sqrt{2S+1}}$ |
| 5 | 8 | 2 | $-\frac{\sqrt{2}\sqrt{S}}{\sqrt{2S+1}}$ | 13 | 16 | 2 | $-\frac{\sqrt{2}\sqrt{S}}{\sqrt{2S+1}}$ |
| 5 | 10 | 1 | $-\frac{\sqrt{S+1}}{\sqrt{2S+1}}$ | 14 | 16 | 1 | $\frac{\sqrt{2S+2}}{\sqrt{2S+1}}$ |
| 5 | 11 | 1 | $-1$ | 15 | 16 | 1 | $-\frac{\sqrt{2}\sqrt{S}}{\sqrt{2S+1}}$ |

*Table A.1: None zero coefficients $C$ of $\langle i|H_{hopping}|j\rangle = C\langle i||\, f_{n,\alpha}\,||j\rangle$. Only results for $j > i$ are given as the final Hamiltonian will be hermitian.*

One can read the one channel coefficients from this table by realizing that the subset $|1\rangle$, $|2\rangle$, $|3\rangle$ and $|6\rangle$ from the two-channel calculation correspond to the one channel states. Entries only consisting of these combinations lead to the coefficients of the one channel case.

The elements ${}_n\langle m|\,|\, f^\dagger_{n,\alpha}\,|\,|n\rangle_n$ remaining still have to be calculated. The states $|m\rangle$ and $|n\rangle$ are already diagonalized and do not share the same quantum numbers. To access the occupation of the last added shell we will transform the states back. We will continue with the example from the previous step

$$
\begin{aligned}
&{}_n\langle N, S, r||\, f^\dagger_{n,1}\,||N-1, S-\tfrac{1}{2}, r'\rangle_n \\
&= \sum_{i,\omega,j,\omega'} {}_{n-1}\langle i, N, S, \omega||\, f^\dagger_{n,1}\,||N-1, S-\tfrac{1}{2}, \omega', j\rangle_{n-1} U^{N,S}_{i,\omega\to r} U^{N-1,S-\frac{1}{2}}_{j,\omega'\to r'}. \quad \text{(A.47)}
\end{aligned}
$$

| $\langle i\|$ | $\|j\rangle$ | $S-S'=-\frac{1}{2}$ | $\langle i\|$ | $\|j\rangle$ | $S-S'=\frac{1}{2}$ |
|---|---|---|---|---|---|
| 2 | 1 | 1 | 3 | 1 | 1 |
| 6 | 3 | $\frac{\sqrt{4S'+2}}{2\sqrt{S'}}$ | 6 | 2 | $-\frac{\sqrt{4S'+2}}{2\sqrt{S'+1}}$ |
| 7 | 5 | $-\frac{\sqrt{2S'+1}}{2\sqrt{S'}}$ | 7 | 4 | $\frac{\sqrt{2S'+1}}{2\sqrt{S'+1}}$ |
| 9 | 4 | 1 | 10 | 4 | $\frac{\sqrt{2S'+3}}{2\sqrt{S'+1}}$ |
| 10 | 5 | $\frac{\sqrt{2S'-1}}{2\sqrt{S'}}$ | 11 | 5 | 1 |
| 12 | 7 | $\frac{1}{2}\sqrt{2}$ | 12 | 9 | $-\frac{\sqrt{4S'+2}}{2\sqrt{S'+1}}$ |
| 12 | 10 | $\frac{\sqrt{2S'+2}}{2\sqrt{S'}}$ | 13 | 7 | $\frac{1}{2}\sqrt{2}$ |
| 13 | 11 | $\frac{\sqrt{4S'+2}}{2\sqrt{S'}}$ | 13 | 10 | $-\frac{\sqrt{2}\sqrt{S'}}{2\sqrt{S'+1}}$ |
| 14 | 8 | 1 | 15 | 8 | 1 |
| 16 | 15 | $\frac{\sqrt{4S'+2}}{2\sqrt{S'}}$ | 16 | 14 | $-\frac{\sqrt{4S'+2}}{2\sqrt{S'+1}}$ |

*Table A.2: The coefficients for* $\langle i||\, f^{\dagger}_{n,1}\,||j\rangle \times (-1)^{N'}$

To evaluate this let us first evaluate the corresponding $\langle i|f^{\dagger}_{n,\uparrow,1}|j\rangle$ and then use the Wigner-Eckart theorem. Further we will limit ourselves to $\langle 3|f^{\dagger}_{n,\uparrow,1}|1\rangle$ in this example. On the one hand,

$$
\begin{aligned}
&{}_{n-1}\langle 3,N,S,\omega|f^{\dagger}_{n,\uparrow,1}|N-1,S-\tfrac{1}{2},\omega',1\rangle_{n-1} && \text{(A.48)}\\
=&\langle {}^{\uparrow}_{0}|_{n-1}\langle N-1,S-\tfrac{1}{2},S_z-\tfrac{1}{2},\omega|f^{\dagger}_{n,\uparrow,1}|N-1,S-\tfrac{1}{2},S_z-\tfrac{1}{2},\omega'\rangle_{n-1}|\,{}^{0}_{0}\rangle\sqrt{\tfrac{S+S_z}{2S}}\\
+&\langle {}^{\downarrow}_{0}|_{n-1}\langle N-1,S-\tfrac{1}{2},S_z+\tfrac{1}{2},\omega|f^{\dagger}_{n,\uparrow,1}|N-1,S-\tfrac{1}{2},S_z-\tfrac{1}{2},\omega'\rangle_{n-1}|\,{}^{0}_{0}\rangle\sqrt{\tfrac{S-S_z}{2S}} && \text{(A.49)}\\
=&(-1)^{N-1}\sqrt{\tfrac{S+S_z}{2S}}\delta_{\omega,\omega'}, && \text{(A.50)}
\end{aligned}
$$

on the other hand,

$$
\begin{aligned}
&{}_{n-1}\langle 3,N,S,\omega|f^{\dagger}_{n,\uparrow,1}|N-1,S-\tfrac{1}{2},\omega',1\rangle_{n-1} && \text{(A.51)}\\
=&\langle {}^{\uparrow}_{0}|_{n-1}\langle N-1,S-\tfrac{1}{2},S_z-\tfrac{1}{2},\omega|f^{\dagger}_{n,\uparrow,1}|N-1,S-\tfrac{1}{2},S_z-\tfrac{1}{2},\omega'\rangle_{n-1}|\,{}^{0}_{0}\rangle\sqrt{\tfrac{S+S_z}{2S}}\\
=&{}_{n-1}\langle 3,N,S,\omega||\, f^{\dagger}_{n,1}\,||N-1,S-\tfrac{1}{2},\omega',1\rangle_{n-1}\sqrt{\tfrac{S+S_z}{2S}}, && \text{(A.52)}
\end{aligned}
$$

therefore

$$
\begin{aligned}
&{}_{n-1}\langle 3,N,S,\omega||\, f^{\dagger}_{n,1}\,||N-1,S-\tfrac{1}{2},\omega',1\rangle_{n-1}U^{N,S}_{3,\omega\to r}U^{N-1,S-\frac{1}{2}}_{1,\omega'\to r'} && \text{(A.53)}\\
=&(-1)^{N-1}U^{N,S}_{3,\omega\to r}U^{N-1,S-\frac{1}{2}}_{1,\omega\to r'}, && \text{(A.54)}
\end{aligned}
$$

The none zero elements are shown in table A.2 and A.3.

| $\langle i\|$ | $\|j\rangle$ | $S-S'=\frac{1}{2}$ | $\langle i\|$ | $\|j\rangle$ | $S-S'=-\frac{1}{2}$ |
|---|---|---|---|---|---|
| 5 | 1 | 1 | 4 | 1 | 1 |
| 7 | 2 | $\frac{\sqrt{2S'+1}}{2\sqrt{S'+1}}$ | 7 | 3 | $-\frac{\sqrt{2S'+1}}{2\sqrt{S'}}$ |
| 8 | 4 | $-\frac{\sqrt{4S'+2}}{2\sqrt{S'+1}}$ | 8 | 5 | $\frac{\sqrt{4S'+2}}{2\sqrt{S'}}$ |
| 10 | 2 | $-\frac{\sqrt{2S'+3}}{2\sqrt{S'+1}}$ | 9 | 2 | $-1$ |
| 11 | 3 | $-1$ | 10 | 3 | $-\frac{\sqrt{2S'-1}}{2\sqrt{S'}}$ |
| 13 | 6 | 1 | 12 | 6 | 1 |
| 14 | 9 | $\frac{\sqrt{4S'+2}}{2\sqrt{S'+1}}$ | 14 | 7 | $\frac{1}{2}\sqrt{2}$ |
| 15 | 7 | $\frac{1}{2}\sqrt{2}$ | 14 | 10 | $-\frac{\sqrt{2S'+2}}{2\sqrt{S'}}$ |
| 15 | 10 | $\frac{\sqrt{2}\sqrt{S'}}{2\sqrt{S'+1}}$ | 15 | 11 | $-\frac{\sqrt{4S'+2}}{2\sqrt{S'}}$ |
| 16 | 12 | $-\frac{\sqrt{4S'+2}}{2\sqrt{S'+1}}$ | 16 | 13 | $\frac{\sqrt{4S'+2}}{2\sqrt{S'}}$ |

*Table A.3: The coefficients for* $\langle i||\, f^{\dagger}_{n,2}\,||j\rangle \times (-1)^{N'}$

## A.2 FDM coefficients

As shown in Chapter 2.6 the full density matrix $R^{n}_{k,k'}$ can be calculated recursively from $\mathcal{R}^{n+1}_{x,x'} = |x\rangle_{n+1}\mathcal{R}^{n+1}{}_{n+1}\langle x'|$ a combination of $R^{n+1}_{k,k'}$ and the discarded Boltzmann factors of shell $n+1$. We will calculate the coefficients for the environmental state $|\Uparrow,\varnothing\rangle_{n+1}$

$$\sum_{N',S',S'_z,\omega,\omega'} \langle {}^{\uparrow}_{0}|\langle N,S,S_z,r \mid N',S',S'_z,w\rangle_{n+1}\times \\ \mathcal{R}^{n+1}{}_{n+1}\langle N',S',S'_z,w' \mid N,S,S_z,r'\rangle|\,{}^{\uparrow}_{0}\rangle. \tag{A.55}$$

When transforming $|N',S',S'_z,w\rangle = \sum_{i,k} U^{N',S'}_{i,k\to\omega}|N',S',S'_z,k,i\rangle$, the only basis states that can contribute are $i=2,3$, when comparing the environmental state. Further, when comparing the the quantum numbers for these states, $N'$, $S'$, $S'_z$ will be fixed to $N'=N+1$, $S'=S\pm\frac{1}{2}$ and $S'_z=S_z+\frac{1}{2}$. This leaves

$$\sum_{\omega,\omega'} \frac{S-S_z}{2S+1} U^{N+1,S-\frac{1}{2}\,T}_{2,k\to\omega} \left[\mathcal{R}(N+1,S-\tfrac{1}{2})\right]^{n+1}_{\omega,\omega'} U^{N+1,S-\frac{1}{2}}_{2,k'\to\omega'} \\ +\frac{S+S_z+1}{2S+1} U^{N+1,S+\frac{1}{2}\,T}_{3,k\to\omega} \left[\mathcal{R}(N+1,S+\tfrac{1}{2})\right]^{n+1}_{\omega,\omega'} U^{N+1,S+\frac{1}{2}}_{3,k'\to\omega'}. \tag{A.56}$$

Though this is still dependent on $S_z$ it can be easily verified that $S_z$ cancels out when the $|\Downarrow,\varnothing\rangle$ environmental state is added. The final coefficients can be seen in Table A.4.

| $N'$ | $S'$ | $\mathrm{c}(N',S')$ |
|---|---|---|
| $N$ | $S$ | $1$ |
| $N+1$ | $S+\frac{1}{2}$ | $\frac{2S+2}{2S+1}$ |
| $N+1$ | $S-\frac{1}{2}$ | $\frac{2S}{2S+1}$ |
| $N+2$ | $S$ | $1$ |
| $N+2$ | $S+1$ | $\frac{2S+3}{2S+1}$ |
| $N+2$ | $S-1$ | $\frac{2S-1}{2S+1}$ |
| $N+3$ | $S+\frac{1}{2}$ | $\frac{2S+2}{2S+1}$ |
| $N+3$ | $S-\frac{1}{2}$ | $\frac{2S}{2S+1}$ |
| $N+4$ | $S-\frac{1}{2}$ | $1$ |

*Table A.4: Prefactors* $\mathrm{c}(N',S')$ *for the calculation of* $R^n_{k,k'}(N,S) = \sum_{N',S',i,\omega,\omega'} \mathrm{c}(N',S') {U^{N',S'}_{i,k\to\omega}}^T U^{N',S'}_{i,k'\to\omega'} \mathcal{R}^{n+1}_{\omega,\omega'}(N',S')$*. Note that several states* $|i\rangle$*, e.g.* $i=2$ *and* $i=4$*, yield the same prefactor and quantum number combination.*

## A.3 Operator coefficients

There are some subtleties when calculating the operator elements of a local operator for lower shells. We will display this for the case of a spin-$\frac{1}{2}$ operator like $d^\dagger$.

Given a reduced operator $d^\dagger$ at shell $n$, to calculate the matrix elements at shell $n+1$, we will use the Wigner-Eckart theorem to obtain the $S_z$ dependent operator, transform it to the next shell and then reapply the Wigner-Eckart theorem. We will restrict ourselves to one operator subspace ${}_{n+1}\langle N,S||\, d^\dagger \,||N-1,S+\frac{1}{2}\rangle_{n+1}$.

$$
\begin{aligned}
&{}_{n+1}\langle N,S,\omega||\, d^\dagger \,||N-1,S+\tfrac{1}{2},\omega'\rangle_{n+1}\left(-\sqrt{\frac{S-S_z+1}{2S+2}}\right) && \text{(A.57)}\\
=&{}_{n+1}\langle N,S,S_z,\omega|d^\dagger_\uparrow|N-1,S+\tfrac{1}{2},S_z-\tfrac{1}{2},\omega'\rangle_{n+1} && \text{(A.58)}\\
=&\sum_{i,k,j,k'} {U^{N,S}_{i,k\to\omega}}^T U^{N-1,S+\frac{1}{2}}_{j,k'\to\omega'} \times\\
&\qquad {}_{n+1}\langle N,S,S_z,k,i|d^\dagger_\uparrow|N-1,S+\tfrac{1}{2},S_z-\tfrac{1}{2},k',j\rangle_{n+1}. && \text{(A.59)}
\end{aligned}
$$

Here, we restrict ourselves to $i=2$ and $j=3$. Only the following combina-

tions contribute

$$
\begin{aligned}
&{}_{n+1}\langle N, S, S_z, k, 2|d^\dagger_\uparrow|N-1, S+\tfrac{1}{2}, S_z-\tfrac{1}{2}, k', 3\rangle_{n+1} && \text{(A.60)}\\
=&\sqrt{\frac{S+S_z+1}{2S+2}}\sqrt{\frac{S-S_z+1}{2S+1}}\langle {}^{\downarrow}_{0}|\langle N-1, S+\tfrac{1}{2}, S_z+\tfrac{1}{2}, k'|d^\dagger_\uparrow|N-2, S, S_z, k\rangle|{}^{\downarrow}_{0}\rangle\\
-&\sqrt{\frac{S-S_z+1}{2S+2}}\sqrt{\frac{S+S_z}{2S+1}}\langle {}^{\uparrow}_{0}|\langle N-1, S+\tfrac{1}{2}, S_z-\tfrac{1}{2}, k'|d^\dagger_\uparrow|N-2, S, S_z-1, k\rangle|{}^{\uparrow}_{0}\rangle && \text{(A.61)}\\
=&\left(\sqrt{\frac{(S+S_z+1)(S-S_z+1)(S+S_z+1)}{(2S+2)(2S+1)(2S+1)}}-\sqrt{\frac{(S-S_z+1)(S+S_z)(S+S_z)}{(2S+2)(2S+1)(2S+1)}}\right)\times\\
&\langle N-1, S+\tfrac{1}{2}, k'||\, d^\dagger_\uparrow\,||N-2, S, k\rangle. && \text{(A.62)}
\end{aligned}
$$

Dividing by the Clebsch-Gordan coefficient from Equation (A.57) yields

$$\frac{-1}{2S+1}{}_n\langle N-1, S+\tfrac{1}{2}, k'||\, d^\dagger\,||N-2, S, k\rangle_n. \qquad \text{(A.63)}$$

Results for all coefficients for $d^\dagger$ (or generally a spin $\frac{1}{2}$ operator) can be found in Table A.5

Please note, that, when calculating any expectation value, a separate coefficient might appear when summing over the $S_z$ values.

| $i$ | $j$ | $\pm$ | c($S$) |
|---|---|---|---|
| 1 | 1 | + | 1 |
| 2 | 2 | + | 1 |
| 2 | 3 | − | $\frac{-1}{2S+1}$ |
| 3 | 3 | + | $\frac{\sqrt{2S(2S+2)}}{2S+1}$ |
| 4 | 4 | + | 1 |
| 4 | 5 | − | $\frac{-1}{2S+1}$ |
| 5 | 5 | + | $\frac{\sqrt{2S(2S+2)}}{2S+1}$ |
| 6 | 6 | + | 1 |
| 8 | 8 | + | 1 |
| 9 | 9 | + | 1 |
| 9 | 10 | − | $-\sqrt{\frac{2}{(2S+2)(2S+1)}}$ |
| 10 | 10 | + | $\sqrt{\frac{2S(2S+3)}{(2S+2)(2S+1)}}$ |
| 10 | 11 | − | $-\sqrt{\frac{1}{S(2S+1)}}$ |
| 11 | 11 | + | $\sqrt{\frac{(2S-1)(2S+2)}{2S(2S+1)}}$ |
| 12 | 12 | + | 1 |
| 12 | 13 | − | $\frac{-1}{2S+1}$ |
| 13 | 13 | + | $\frac{\sqrt{2S(2S+2)}}{2S+1}$ |
| 14 | 14 | + | 1 |
| 14 | 15 | − | $\frac{-1}{2S+1}$ |
| 15 | 15 | + | $\frac{\sqrt{2S(2S+2)}}{2S+1}$ |
| 16 | 16 | + | 1 |

| $i$ | $j$ | $\pm$ | c($S$) |
|---|---|---|---|
| 1 | 1 | − | 1 |
| 2 | 2 | − | $\frac{\sqrt{2S(2S+2)}}{2S+1}$ |
| 3 | 2 | + | $\frac{1}{2S+1}$ |
| 3 | 3 | − | 1 |
| 4 | 4 | − | $\frac{\sqrt{2S(2S+2)}}{2S+1}$ |
| 5 | 4 | + | $\frac{1}{2S+1}$ |
| 5 | 5 | − | 1 |
| 6 | 6 | − | 1 |
| 8 | 8 | − | 1 |
| 9 | 9 | − | $\sqrt{\frac{2S(2S+3)}{(2S+2)(2S+1)}}$ |
| 10 | 9 | + | $\sqrt{\frac{2}{(2S+2)(2S+1)}}$ |
| 10 | 10 | − | $\sqrt{\frac{(2S-1)(2S+2)}{2S(2S+1)}}$ |
| 11 | 10 | + | $\sqrt{\frac{1}{S(2S+1)}}$ |
| 11 | 11 | − | 1 |
| 12 | 12 | − | $\frac{\sqrt{2S(2S+2)}}{2S+1}$ |
| 13 | 12 | + | $\frac{1}{2S+1}$ |
| 13 | 13 | − | 1 |
| 14 | 14 | − | $\frac{\sqrt{2S(2S+2)}}{2S+1}$ |
| 15 | 14 | + | $\frac{1}{2S+1}$ |
| 15 | 15 | − | 1 |
| 16 | 16 | − | 1 |

*Table A.5: The results for the coefficients of* ${}_{n+1}\langle N, S||\, d^\dagger \,||N-1, S\pm\frac{1}{2}\rangle_{n+1}$ $= \sum_{i,k,j,k'} U^{N,S}_{i,k\to\omega}\ {}^T U^{N-1,S\pm\frac{1}{2}}_{j,k'\to\omega'}\, \mathrm{c}(S)\langle N, S, i||\, d^\dagger \,||N-1, S\pm\frac{1}{2}, j\rangle$. *The left table contains the* $S+\frac{1}{2}$ *case, the right table contains the* $S-\frac{1}{2}$ *case. The sign signals whether* $\langle N, S, i||\, d^\dagger \,||N-1, S\pm\frac{1}{2}, j\rangle$ *will connect a* $S$ *to a* $S+\frac{1}{2}$ *or a* $S-\frac{1}{2}$ *subspace.*

# Appendix B

# Initial Hamiltonian

The two channel SIAM Hamiltonian with screening takes the form

$$\begin{aligned} H_0 &= U n_{d,\uparrow} n_{d,\downarrow} + \epsilon_d n_d \\ &\quad + U_{dc}(n_d - 1)(n_{f_0,R} - 1 + n_{f_0,L} - 1) \\ &\quad + \sum_{\sigma=\uparrow,\downarrow} \sum_{\alpha=L,R} \tau_\alpha (d^\dagger_\sigma f_{0\sigma\alpha} + f^\dagger_{0\sigma\alpha} d_\alpha). \end{aligned} \tag{B.1}$$

The calculation of the Hamiltonian is straightforward once the basis states for each quantum number are found. Note, that this is true for the starting matrix elements of any operator, though the Wigner-Eckart theorem has to be used to obtain the z-spin independent reduced matrix elements. The basis states and their corresponding starting Hamiltonian are given below.

$N = 0, S = 0$

$|0, 0, 0\rangle$

$$\begin{pmatrix} 2U_{dc} \end{pmatrix}$$

$N = 1, S = 1/2$

$|\Downarrow, 0, 0\rangle$

$|0, \downarrow, 0\rangle$

$|0, 0, \downarrow\rangle$

$$\begin{pmatrix} e_d & \tau_R & \tau_L \\ \tau_R & U_{dc} + \epsilon_R & 0 \\ \tau_L & 0 & U_{dc} + \epsilon_L \end{pmatrix}$$

$N = 2, S = 0$

$|\Uparrow\downarrow, 0, 0\rangle$

$\frac{1}{2}\sqrt{2}|\Uparrow, \downarrow, 0\rangle + -\frac{1}{2}\sqrt{2}|\Downarrow, \uparrow, 0\rangle$

$\frac{1}{2}\sqrt{2}|\Uparrow, 0, \downarrow\rangle + -\frac{1}{2}\sqrt{2}|\Downarrow, 0, \uparrow\rangle$

$|0, \uparrow\downarrow, 0\rangle$

$\frac{1}{2}\sqrt{2}|0, \downarrow, \uparrow\rangle + -\frac{1}{2}\sqrt{2}|0, \uparrow, \downarrow\rangle$

$|0, 0, \uparrow\downarrow\rangle$

$$\begin{pmatrix} U - 2U_{dc} + 2e_d & \sqrt{2}\tau_R & \sqrt{2}\tau_L & 0 & 0 & 0 \\ \sqrt{2}\tau_R & \epsilon_R + e_d & 0 & \sqrt{2}\tau_R & -\tau_L & 0 \\ \sqrt{2}\tau_L & 0 & \epsilon_L + e_d & 0 & -\tau_R & \sqrt{2}\tau_L \\ 0 & \sqrt{2}\tau_R & 0 & 2\epsilon_R & 0 & 0 \\ 0 & -\tau_L & -\tau_R & 0 & \frac{1}{2}U_{dc} + \epsilon_L + \epsilon_R & 0 \\ 0 & 0 & \sqrt{2}\tau_L & 0 & 0 & U_{dc} + 2\epsilon_L \end{pmatrix}$$

$N = 2, S = 1$

$|\Downarrow, \downarrow, 0\rangle$

$|\Downarrow, 0, \downarrow\rangle$

$-1|0, \downarrow, \downarrow\rangle$

$$\begin{pmatrix} \epsilon_R + e_d & 0 & \tau_L \\ 0 & \epsilon_L + e_d & -\tau_R \\ \tau_L & -\tau_R & \epsilon_L + \epsilon_R \end{pmatrix}$$

$N = 3, S = 1/2$

$|\Uparrow\downarrow, \downarrow, 0\rangle$

$|\Uparrow\downarrow, 0, \downarrow\rangle$

$|\Downarrow, \uparrow\downarrow, 0\rangle$

$\frac{1}{2}\sqrt{2}|\Downarrow, \downarrow, \uparrow\rangle + -\frac{1}{2}\sqrt{2}|\Downarrow, \uparrow, \downarrow\rangle$

$|\Downarrow, 0, \uparrow\downarrow\rangle$

$-\frac{1}{3}\sqrt{6}|\Uparrow, \downarrow, \downarrow\rangle + \frac{1}{6}\sqrt{6}|\Downarrow, \downarrow, \uparrow\rangle + \frac{1}{6}\sqrt{6}|\Downarrow, \uparrow, \downarrow\rangle$

$|0, \uparrow\downarrow, \downarrow\rangle$

$|0, \downarrow, \uparrow\downarrow\rangle$

$$\begin{pmatrix} U - U_{dc} + \epsilon_R + 2e_d & 0 & -\tau_R & \frac{1}{2}\sqrt{2}\tau_L & 0 & \frac{1}{2}\sqrt{6}\tau_L & 0 & 0 \\ 0 & U - U_{dc} + \epsilon_L + 2e_d & 0 & \frac{1}{2}\sqrt{2}\tau_R & -\tau_L & -\frac{1}{2}\sqrt{6}\tau_R & 0 & 0 \\ -\tau_R & 0 & 2\epsilon_R + e_d & 0 & 0 & 0 & \tau_L & 0 \\ \frac{1}{2}\sqrt{2}\tau_L & \frac{1}{2}\sqrt{2}\tau_R & 0 & \epsilon_L + \epsilon_R + e_d & 0 & 0 & \frac{1}{2}\sqrt{2}\tau_R & \frac{1}{2}\sqrt{2}\tau_L \\ 0 & -\tau_L & 0 & 0 & 2\epsilon_L + e_d & 0 & 0 & \tau_R \\ \frac{1}{2}\sqrt{6}\tau_L & -\frac{1}{2}\sqrt{6}\tau_R & 0 & 0 & 0 & \epsilon_L + \epsilon_R + e_d & -\frac{1}{2}\sqrt{6}\tau_R & \frac{1}{2}\sqrt{6}\tau_L \\ 0 & 0 & \tau_L & \frac{1}{2}\sqrt{2}\tau_R & 0 & -\frac{1}{2}\sqrt{6}\tau_R & -U_{dc} + \epsilon_L + 2\epsilon_R & 0 \\ 0 & 0 & 0 & \frac{1}{2}\sqrt{2}\tau_L & \tau_R & \frac{1}{2}\sqrt{6}\tau_L & 0 & 2\epsilon_L + \epsilon_R \end{pmatrix}$$

$N = 3, S = 3/2$

$-1|\Downarrow, \downarrow, \downarrow\rangle$

$$\begin{pmatrix} \epsilon_L + \epsilon_R + e_d \end{pmatrix}$$

$N = 4, S = 0$

$|\Uparrow\downarrow, \uparrow\downarrow, 0\rangle$

$\frac{1}{2}\sqrt{2}|\Uparrow\downarrow, \downarrow, \uparrow\rangle + -\frac{1}{2}\sqrt{2}|\Uparrow\downarrow, \uparrow, \downarrow\rangle$

$|\Uparrow\downarrow, 0, \uparrow\downarrow\rangle$

$\frac{1}{2}\sqrt{2}|\Uparrow, \uparrow\downarrow, \downarrow\rangle + -\frac{1}{2}\sqrt{2}|\Downarrow, \uparrow\downarrow, \uparrow\rangle$

$\frac{1}{2}\sqrt{2}|\Uparrow, \downarrow, \uparrow\downarrow\rangle + -\frac{1}{2}\sqrt{2}|\Downarrow, \uparrow, \uparrow\downarrow\rangle$

$|0, \uparrow\downarrow, \uparrow\downarrow\rangle$

$$\begin{pmatrix} U + 2\epsilon_R + 2e_d & 0 & 0 & \sqrt{2}\tau_L & 0 & 0 \\ 0 & U - \frac{1}{2}U_{dc} + \epsilon_L + \epsilon_R + 2e_d & 0 & \tau_R & \tau_L & 0 \\ 0 & 0 & U - U_{dc} + 2\epsilon_L + 2e_d & 0 & \sqrt{2}\tau_R & 0 \\ \sqrt{2}\tau_L & \tau_R & 0 & \epsilon_L + 2\epsilon_R + e_d & 0 & \sqrt{2}\tau_L \\ 0 & \tau_L & \sqrt{2}\tau_R & 0 & 2\epsilon_L + \epsilon_R + e_d & \sqrt{2}\tau_R \\ 0 & 0 & 0 & \sqrt{2}\tau_L & \sqrt{2}\tau_R & -U_{dc} + 2\epsilon_L + 2\epsilon_R \end{pmatrix}$$

$N = 4, S = 1$

$-1|\Uparrow\downarrow, \downarrow, \downarrow\rangle$

$|\Downarrow, \uparrow\downarrow, \downarrow\rangle$

$|\Downarrow, \downarrow, \uparrow\downarrow\rangle$

$$\begin{pmatrix} U + \epsilon_L + \epsilon_R + 2e_d & \tau_R & -\tau_L \\ \tau_R & \epsilon_L + 2\epsilon_R + e_d & 0 \\ -\tau_L & 0 & 2\epsilon_L + \epsilon_R + e_d \end{pmatrix}$$

$N = 5, S = 1/2$

$|\Uparrow\downarrow, \uparrow\downarrow, \downarrow\rangle$

$|\Uparrow\downarrow, \downarrow, \uparrow\downarrow\rangle$

$|\Downarrow, \uparrow\downarrow, \uparrow\downarrow\rangle$

$$\begin{pmatrix} U + U_{dc} + \epsilon_L + 2\epsilon_R + 2e_d & 0 & -\tau_L \\ 0 & U + 2\epsilon_L + \epsilon_R + 2e_d & -\tau_R \\ -\tau_L & -\tau_R & 2\epsilon_L + 2\epsilon_R + e_d \end{pmatrix}$$

$N = 6, S = 0$

$\Uparrow\downarrow, \uparrow\downarrow, \uparrow\downarrow\rangle$

$\left( \quad U + U_{dc} + 2\epsilon_L + 2\epsilon_R + 2e_d \quad \right)$

# Appendix C

# Broadening

Motivated by the inability to calculate susceptibilities at zero frequency for finite temperatures we looked into finding a solution. Apart from the general interest, these susceptibilities are needed when calculating thermoelectric properties in the two channel model with screening. This appendix describes some of the failed approaches tried to overcome the problem and ends with a proposal on how it might be possible.

## C.1 Common Schemes

As shown in Chapter 2.6 the spectral function of the NRG is given as a set of delta functions. Denoting by $\mathcal{A}_{\mathrm{A,B}}(\omega) = -\frac{1}{\pi}\,\mathrm{Im}(G_{A,B}(\omega))$ the spectral function of the retarded Green's function $G_{A,B}(\omega) \equiv \langle\langle A, B\rangle\rangle$. We have for $\mathcal{A}_{\mathrm{A,B}}(\omega)$:

$$\mathcal{A}_{\mathrm{A,B}}(\omega) = -\frac{1}{\pi}\sum_{m,n,N_{\mathrm{shell}}} \delta(\omega - (E_m - E_n)) \underbrace{\sum_k (R_{k,m}B_{n,m} \pm R_{n,k}B_{n,m})A^0_{m,n}}_{C_{m,n}}\,. \tag{C.1}$$

$R_{m,n}$ is the combination of the diagonal Boltzmann factors and the full reduced density matrix (FDM). $A^0_{m,n}$ is the $A$ operator where the kept-kept entries are set to zero to avoid overcounting in this compact representation. This discrete form is a consequence of the logarithmically discretized conduction band. For real systems with continuous conduction bands the spectrum is a smooth function of energy. Such a smooth spectral function can be recovered in the NRG by replacing

$$\delta(\omega - (E_m - E_n)) \to \eta_{m,n}(\omega, E_m, E_n) \tag{C.2}$$

The simplest approach is to replace each delta function by a Gaussian

$$\eta_{m,n}(\omega, \mu_{m,n} = E_m - E_n, \sigma_{m,n}) = \frac{1}{\sqrt{2\pi\sigma^2_{m,n}}} \mathrm{e}^{-\frac{(\omega-(E_m-E_n))^2}{2\sigma^2_{m,n}}} \tag{C.3}$$

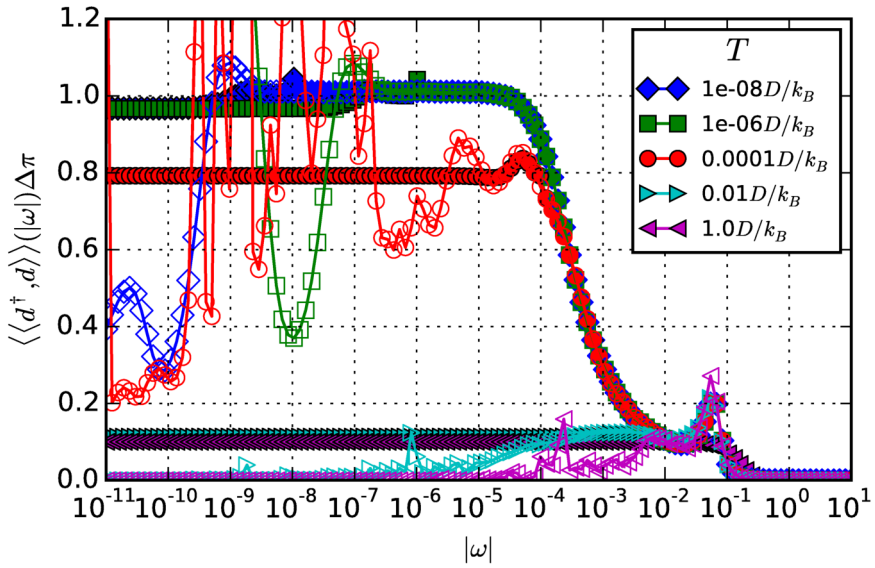


*Figure C.1: The spectral function $\mathcal{A}_{\mathrm{d}^\dagger,\mathrm{d}}(\omega)$ calculated using a Gaussian broadening ($b = 0.1$ see Equation (C.4)) at the symmetric point using different Temperatures. $\Lambda = 8$, $\Delta = 1 \times 10^{-2} D$, $e_d = -6\Delta$, $U = -2e_d$, 16 $z$-values and $N_{shells} = 2\lceil \ln(T_{min} \cdot 10^{-4}) / \ln \Lambda \rceil + 3 = 31$. The Kondo Temperature is $T_K \approx 2.5 \times 10^{-4} D$. The filled symbols show the curve when a constant broadening is used below $T$. The empty symbols show a purely energy dependent broadening $\sigma_{m,n} = b|E_m - E_n|$. For low temperatures the limit $\pi\Delta\,\mathcal{A}_{\mathrm{d}^\dagger,\mathrm{d}}(\omega = 0) = 1$ is better obtained for $\omega > T$ showing that both approaches have problems for low frequencies. The results were calculated for the one-channel Anderson model using an energy dependent cut-off scheme with $e_c = 10$.*

To have a good resolution on each energy scale while also broadening away any artifacts a typical scheme for $\sigma_{m,n}$ is

$$\sigma_{m,n} = b \max(T, |E_m - E_n|) \tag{C.4}$$

A different choice to make $\sigma$ dependent on $|\omega|$ instead of $|E_m - E_n|$ is also possible but it will not conserve the weight of each delta function thus sum rules might be violated. The temperature dependence is a problem in the NRG calculations for frequencies below the temperature. Commonly these artifacts are being suppressed by using a constant broadening for frequencies below the Temperature. Figure C.1 shows the problems that arise with and without the temperature dependent broadening for the $\mathcal{A}_{\mathrm{d}^\dagger,\mathrm{d}}$ spectral function.

Typically susceptibilities have an even worse behavior, as linear behavior around $\omega = 0$ can drop much faster to zero (see Osolin and Žitko [121] or

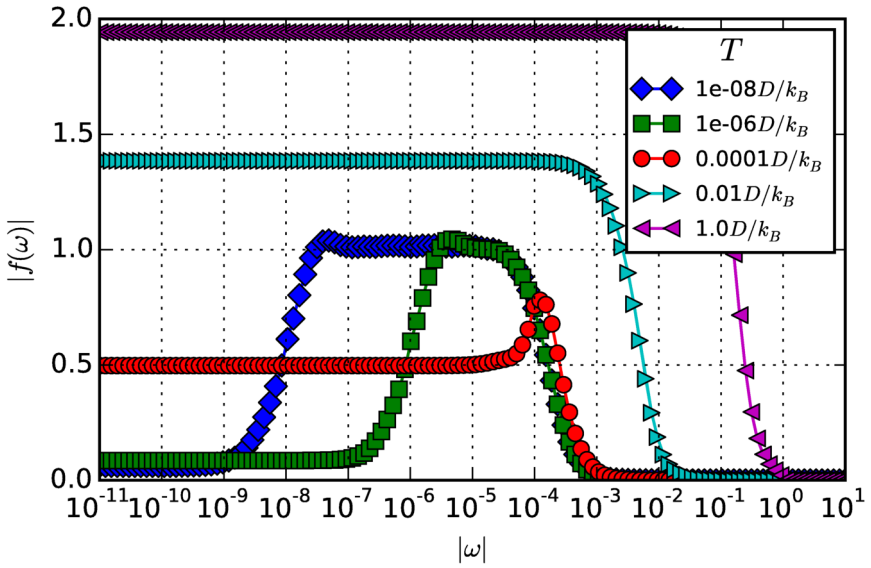


*Figure C.2: This figure shows the imaginary part of the local spin Green's function* $\mathrm{Im}\langle\langle s_z, s_z\rangle\rangle$ *at different temperatures. The same model and parameter set as in Figure C.1 is used except* $\Lambda = 4$*, using the temperature dependent broadening. The limit seen for low temperatures for* $T > \omega \gg T_K$ *is not at all captured by this method at lower frequencies. This is an example of poorly defined behavior even when using this broadening scheme.* $f(x) = \mathrm{Im}(\chi_s(\omega))/(2\pi\omega[\mathrm{Re}(\chi_s(0))]^2)$ *on the y axis normalizes the expression according to the Korringa-Shiba relation and should equal one at zero frequency for* $T \ll T_K$ *(see Equation* (C.5)*).*

Figure C.2). The figure has been normalized according to the Korringa-Shiba relation [122, 62]:

$$\lim_{\omega\to 0} \frac{\mathrm{Im}\,\chi(\omega)}{\omega} = 2\pi\left[\mathrm{Re}\,\chi(0)\right]^2 \tag{C.5}$$

though it only valid for $T \ll T_K$. We see the correct value of 1 is only reached for $\omega \gg T$. As the relation is not valid for higher temperatures, we can not compare to an exact limit here. But as the results for higher temperatures strongly depend on the broadening method used, we can conclude that the low frequency limit can not be safely extracted for high temperatures.

Another successful broadening scheme is to incorporate the logarithmic nature of the NRG scheme into the broadening by making the following transformation. To ensure that the total weights of each delta function does

not change the transformation is done under the integral.

$$\int_{-\infty}^{\infty} \frac{1}{\sqrt{2\pi\sigma^2}} \mathrm{e}^{-\frac{(\omega-\mu)^2}{2\sigma^2}} d\omega \tag{C.6}$$

$$\overset{\omega,\mu\to\ln(\omega),\ln(\mu)}{=} \int_{0}^{\infty} \frac{1}{\sqrt{2\pi\sigma^2}|\omega|} \mathrm{e}^{-\frac{(\ln(\omega/\mu))^2}{2\sigma^2}} d\omega, \tag{C.7}$$

therefore

$$\eta_{m,n}(\omega, E_m - E_n) = \begin{cases} \frac{1}{\sqrt{2\pi\sigma^2}|\omega|} \mathrm{e}^{-\frac{\ln(\omega/(E_m-E_n))^2}{2\sigma^2}} & \text{if } \omega/(E_m - E_n) > 0 \\ 0 & \text{else} \end{cases}. \tag{C.8}$$

This distribution can be refined to conserve a second weight $\int \eta_\mu(\omega, \mu)d\mu = 1$ by instead substituting $\mu \to \ln(\mu) + \sigma^2/2$ in Equation (C.7) (see Weichselbaum and von Delft[50]):

$$\eta_{m,n}(\omega, E_m - E_n) = \frac{\theta(\omega(E_m - E_n))}{\sqrt{2\pi\sigma^2}|\omega|} \mathrm{e}^{-\frac{(\ln(\omega/(E_m-E_n))-\sigma^2/2)^2}{2\sigma^2}} \tag{C.9}$$

$$= \frac{\theta(\omega(E_m - E_n))}{\sqrt{\pi}\alpha|\omega|} \mathrm{e}^{-(\frac{\ln(\omega/(E_m-E_n))}{\alpha} - \frac{\alpha}{4})^2}. \tag{C.10}$$

A small broadening parameter $\sigma$ should be used as the peak of these distributions is shifted by a small factor from $E_m - E_n$: $\mathrm{e}^{-\sigma^2}$ in Equation (C.8) or $\mathrm{e}^{-\sigma^2/2}$ in Equation (C.9). Furthermore all energies are shifted by a factor $\mathrm{e}^{\sigma^2/2}$ in Equation (C.9). As an energy difference can only contribute to the frequency of the same sign, there is an intrinsic problem with this broadening for $\omega \to 0$. But usually artifacts due to a finite temperature are more severe.

## C.2 Low Frequency Problems

To overcome the Problems for $\omega < T$ several attempts have been made.

### C.2.1 Relative Error

One attempt was to assume that there is a relative error in each energy level.

$$E_n \to \eta_n(\omega) = \frac{1}{\sqrt{2\pi(E_n\sigma_{\mathrm{rel}})^2}} \mathrm{e}^{-\frac{(\omega-E_n)^2}{2(E_n\sigma_{\mathrm{rel}})^2}}. \tag{C.11}$$

Substituting this into Equation (C.1) yields

$$G_{A,B}(\omega) = \int_{-\infty}^{\infty}\int_{-\infty}^{\infty} \sum_{m,n,N_{\mathrm{shell}}} \delta(\omega - (\omega' - \omega''))\eta_m(\omega')\eta_n(\omega'')C_{m,n}d\omega' d\omega'' \tag{C.12}$$

$$= \int_{-\infty}^{\infty} \sum_{m,n,N_{\mathrm{shell}}} \eta_m(\omega')\eta_n(\omega' - \omega)C_{m,n}d\omega'. \tag{C.13}$$

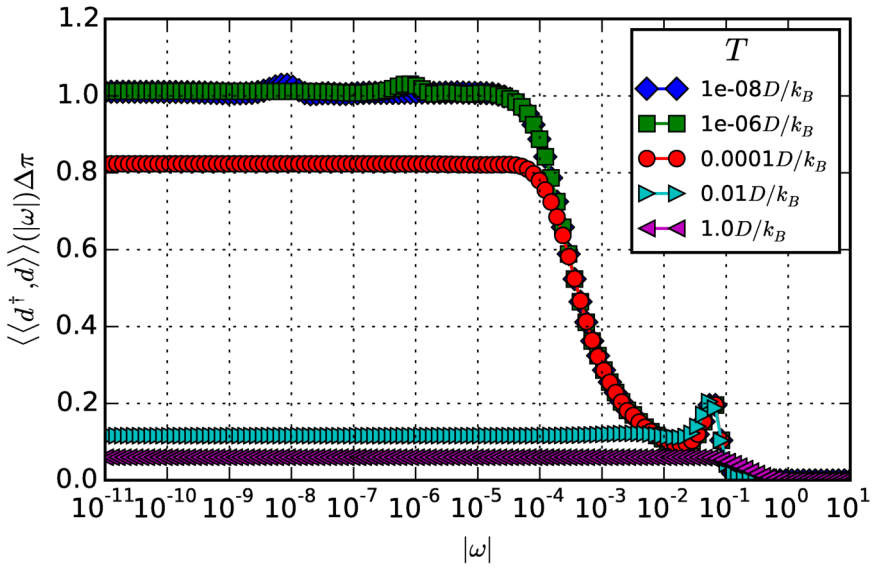


*Figure C.3: Example of the local level spectral function $\mathcal{A}_{\mathrm{d}^\dagger,\mathrm{d}}(\omega)$ broadened by the relative energy error approach. The same model and parameters are used as in Figure C.2. There is a divergence from the correct value at $\omega = T$ and for high temperatures as the satellites should not disappear.*

This is apart from the sign in $\eta_n(\omega' - \omega)$ a convolution of two Gaussian functions. The result is again a Gaussian function.

$$G_{A,B}(\omega) = \sum_{m,n,N_{\mathrm{shell}}} \eta(\omega, \mu_{m,n}, \sigma_{m,n}) C_{m,n}, \tag{C.14}$$

where $\mu_{m,n} = E_m - E_n$ and $\sigma^2_{m,n} = \sigma^2_m + \sigma^2_n = \sigma^2_{\mathrm{rel}}(E^2_m + E^2_n)$. Keep in mind that this broadening is only directly applied to the energies. Including it into the Boltzmann factors used to calculate $R_{m,n}$ produces its own problem as

$$\mathrm{e}^{-\beta E_n} \to \int_{-\infty}^{\infty} \eta_n(\omega)\mathrm{e}^{-\beta\omega} = \mathrm{e}^{-\beta(E_n - \beta\sigma^2_{\mathrm{rel}}E^2_n/2)} \tag{C.15}$$

can become arbitrary large for small temperatures. Attempts to make better guesses for the shift have been made in connection with Section C.2.4 leading to a well working approximation for the FDM approach (see Appendix D). The broadening scheme results in finite constant values for low frequencies (see Figure C.3, C.4) without depending on the temperature, but the zero frequency limit does usually not yield the correct values. As a side note, in the limit of $T \to 0$ this approach is identical to the usual Gaussian

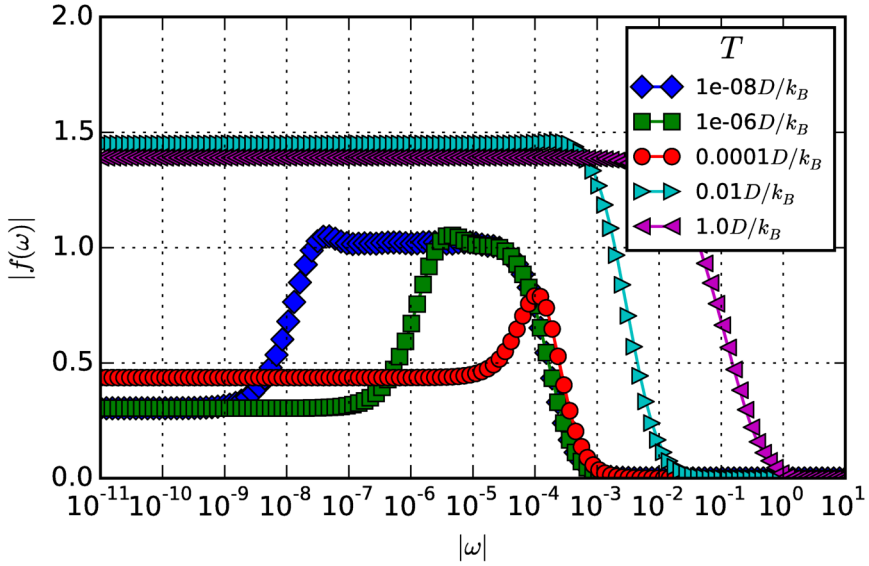


*Figure C.4: Local spin spectral function $\mathcal{A}_{S_z,S_z}(\omega)$ (see Figure C.2), but using the relative energy error as broadening scheme. The zero frequency behavior is improved but still unreliable. The same model and parameters are used as in Figure C.2.*

broadening. It can be easily shown using the Lehman representation

$$G_{A,B}(\omega) = \frac{1}{Z}\sum_{m,n}\delta(\omega-(E_m-E_n))(\mathrm{e}^{-\beta E_m}\pm\mathrm{e}^{-\beta E_n})A_{m,n}B_{n,m} \tag{C.16}$$

$$\overset{T\to 0}{=}\sum_{n}\delta(\omega+E_n)A_{g,n}B_{n,g}\pm\delta(\omega-E_n)A_{n,g}B_{g,n}, \tag{C.17}$$

where $g$ denotes the index for the ground state. As all other Boltzmann factors are zero, one of the energy levels has to be the ground state (= zero). Therefore $\sigma_{m,n} = \sigma_{\mathrm{rel}}\max(E_m, E_n)$ in both cases.

### C.2.2 Density sensitive

This approach tries to make the broadening anti-proportional to the number of delta function weighted by the Boltzmann factors around a frequency. Regions with less dense information will receive a larger broadening. This density will be defined as

$$\rho(\omega) = \frac{1}{Z}\delta(\omega-(E_m-E_n))(\mathrm{e}^{-\beta E_m}+\mathrm{e}^{-\beta E_n}) \propto \frac{1}{\sigma_{m,n}(\omega=E_m-E_n)}. \tag{C.18}$$

Further we will assume the following density for the energies [1]

$$n(\omega) \propto \begin{cases} 1/\omega_{\min} & 0 < \omega < \omega_{min} \\ 1/\omega & \omega_{\min} < \omega < 1 \\ 0 & \text{else} \end{cases} . \tag{C.19}$$

We make this choice because in the NRG scheme the number of states in each shell is more or less constant. The energies of the discarded states will more or less lie in the region $ct_n < E_l < ct_{n-1}$. Furthermore $t_n$ is proportional to $\lambda^{-n/2}$. So there is a constant number of states between $c\lambda^{-n/2}$ and $c\lambda^{-(n-1)/2}$. As the integral

$$\int_{c\lambda^{-n/2}}^{c\lambda^{-(n-1)/2}} \frac{1}{x} dx = \log(\lambda)/2 = \text{const}, \tag{C.20}$$

we chose it as the approximate energy density and constant density for the last shell whose energies shall lie below $\omega_{min}$.

Substituting Equation (C.19) into (C.18) will lead to

$$\rho(\omega) = \frac{1}{Z} \int_{-\infty}^{\infty} \int_{-\infty}^{\infty} \delta(\omega - (\omega' - \omega'')) n(\omega') n(\omega'') (\mathrm{e}^{-\beta\omega'} + \mathrm{e}^{-\beta\omega''}) d\omega' d\omega'' \tag{C.21}$$

$$= \frac{1}{Z} \int_{-\infty}^{\infty} n(\omega') n(\omega' - \omega) (\mathrm{e}^{-\beta\omega'} + \mathrm{e}^{-\beta(\omega' - \omega)}) d\omega'. \tag{C.22}$$

The result is a rather lengthy multiple case solution that can be calculated using standard symbolic math programs (e.g. Maple). The exponential integral appearing in the result was calculated using the Expint routine from "Recipes in Fortran". Figure C.5 shows an example curve for this integral. Again this method will be identical to the Gaussian broadening for low temperatures. To prove this consider that $\mathrm{e}^{-\beta\omega}$ will be zero for all frequencies except $\omega = 0$. Below $\omega = 0$ $n(\omega)$ will be zero. Therefore $\mathrm{e}^{-\beta\omega}$ (or $\mathrm{e}^{-\beta(\omega'-\omega)}$) can be replaced by a delta function $\delta(\omega)$ (or $\delta(\omega'-\omega)$). This leads to $\rho(\omega) \propto 1/|\omega|$ for $\omega_{\min} < |\omega| < 1$ which in turn is identical to Equation (C.4).

This approach seems to have the same shortcomings as the usual approach (see Figure C.6). As a further downside we introduced a second arbitrary proportionality factor in Equation (C.18) that may depend on the temperature. To achieve the reliable high frequency behavior we chose it to be

$$\frac{1}{\sigma(\omega)} = \frac{2\rho(\omega)}{b\rho(0.5D)} \tag{C.23}$$

Fixing the result for a high frequency $\omega = 0.5D$ to be identical to Equation (C.4).

[1] An attempt to estimate this directly from the subspaces used for the operators failed as the difference between different z values was too big and artifacts appeared even for $\omega > T$. The quantity used for this attempt was $\Delta(\int_0^{\omega} \rho(\omega')d\omega' - \int_{\omega}^{\infty} \rho(\omega')d\omega')/\Delta\omega$

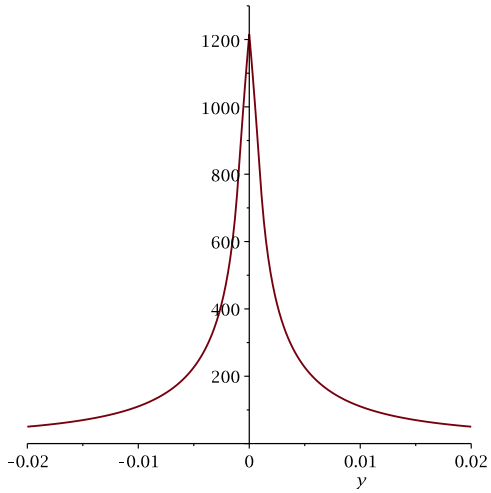


*Figure C.5: Example of $\frac{1}{\sigma(\omega)}$ for the density sensitive approach. Here $\omega_{min} = 10^{-3}$ and $T = 10^{-2}$ was chosen. The figure is zoomed in to the part that differs from the usual approach.*

### C.2.3 Padé Approximation

Another approach tested to solve the low frequency issue was the Padé Approximation introduced by Osolin and Žitko [121] for the NRG. Opposed to the calculating the imaginary part of the real axis directly, the Greens function is calculated at a set of Matsubara frequencies $i\omega_n = i(2n+1)\pi T$. After z-averaging the function values $G_{A,B}(i\omega_n)$ will be used to fit the function

$$f(z) = \frac{p_0 + p_1 z + \cdots + p_{r-1} z^{r-1}}{q_0 + q_1 z + \cdots + q_{r-1} z^{r-1} + z^r}. \tag{C.24}$$

It will be an approximate continuation of the Greens function. The highest power of the two polynomials is chosen to account for the long range behavior $G_{A,B}(z) \propto \frac{1}{z}$ for $|z| \to \infty$. Spectral functions can be simply evaluated as $\mathrm{Im}(f(\omega))$.

The advantage of this approach is that this method avoids any arbitrary broadening parameters. On the other hand one has to choose how many Matsubara frequencies should be evaluated and which ones to take. Figure C.7 shows the problem of using only frequencies close to $z = 0$ for low temperatures. The curve are significantly improved if the frequencies are taken in a range between $[0 \ldots 1i]$ for low temperatures. In fact the restriction to Matsubara frequencies is not needed. We found

$$i\omega_n = i\alpha\beta^n \tag{C.25}$$

where $\alpha$ and $\beta$ are define by $\omega_0 = \pi T$ and $\omega_N = 10D$ give results comparable to other methods.

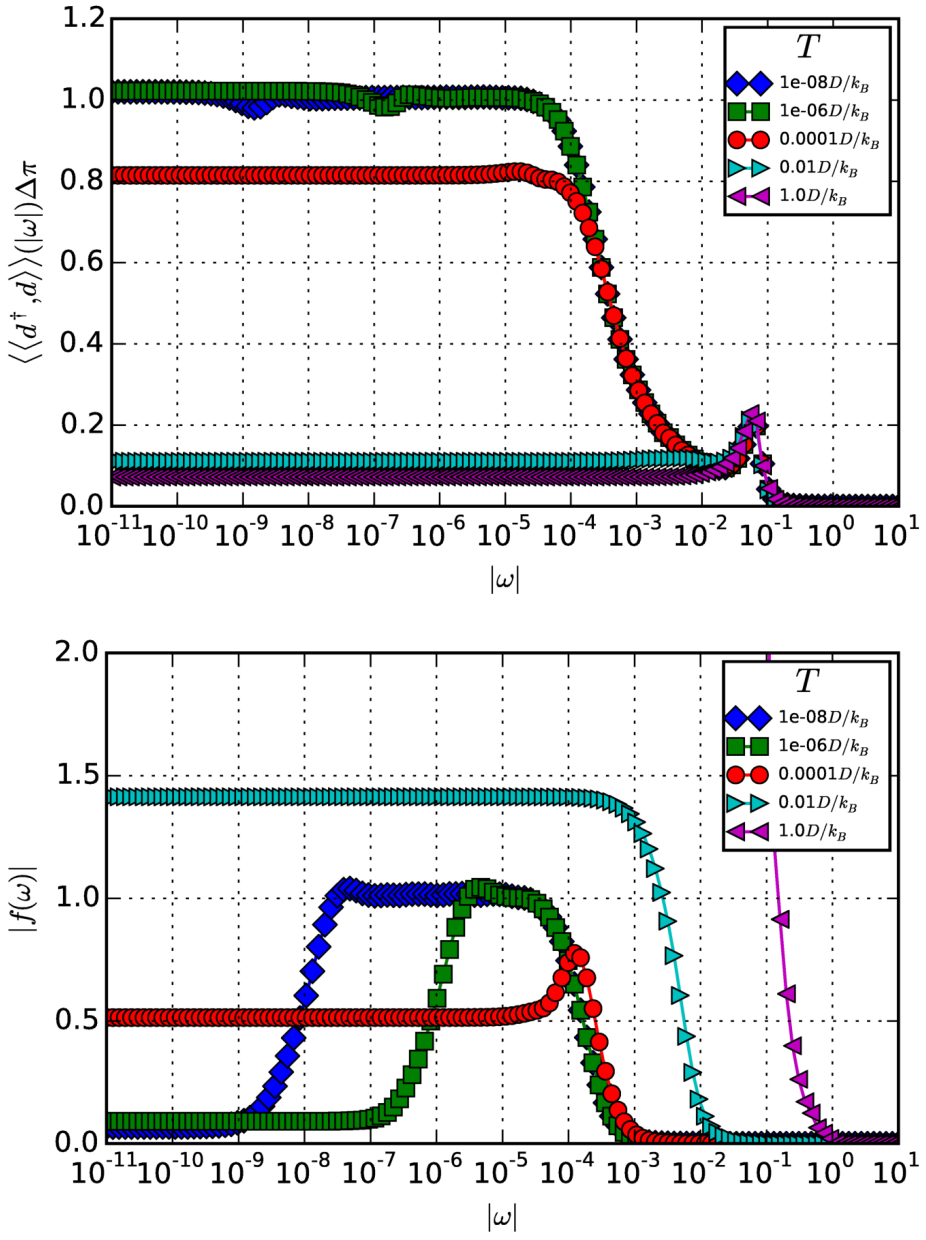


*Figure C.6: Broadening results for the density sensitive approach. The resulting curves show a similar behavior as the standard approach. The model and parameters were chosen like in Figure C.2.*

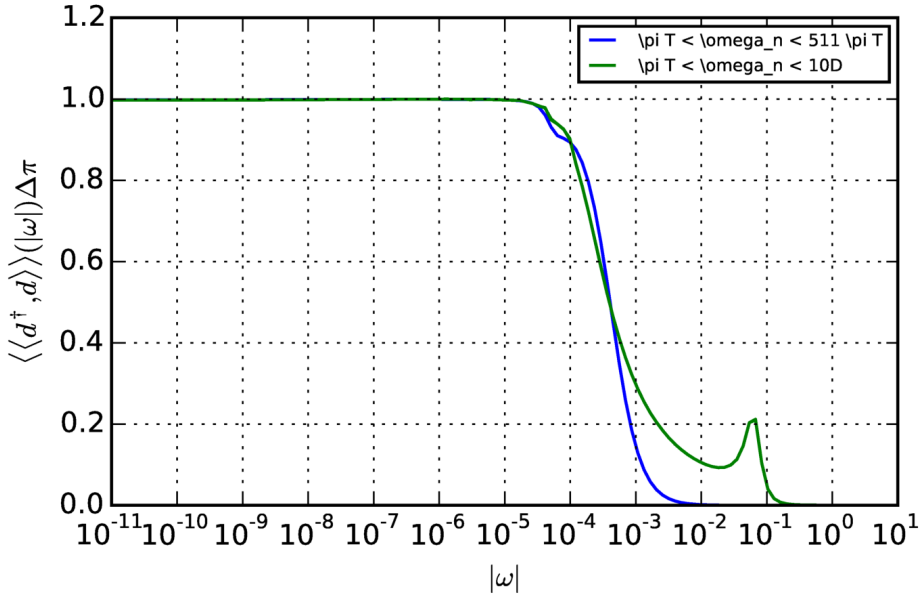


*Figure C.7: The image shows the comparison between the first 256 Matsubara frequencies $i\omega_n = i\pi(2n-1)$ and logarithmically spaced frequencies $i\omega_n = i\alpha\beta^n$ (see Equation (C.25)). If the points are only chosen close to the origin the spectral function can not be completely recovered. The curves are calculated at $T = 10^{-8}D$. The low frequency artifacts are very small. The same model and parameters are used as in Figure C.2.*

The Padé Approximation is very sensitive to errors. In Quantum Monte Carlo simulations this is a problem so the maximum entropy method is preferred. NRG calculations on the other hand return very accurate results for $G_{A,B}(i\omega_n)$ so the Padé Approximation gives good results without using any symmetries. Nevertheless a lot of care has to be taken in evaluating the coefficients $p_i, q_i$. The system of linear equations that has to be solved

$$Ax = b, \tag{C.26}$$

where

$$A = \begin{pmatrix} 1 & z_0 & \cdots & z_0^{r-1} & -f_0 & -f_0 z_0 & \cdots & -f_0 z_0^{r-1} \\ 1 & z_1 & \cdots & z_1^{r-1} & -f_1 & -f_1 z_1 & \cdots & -f_1 z_1^{r-1} \\ \vdots & \vdots & & \vdots & \vdots & \vdots & & \vdots \end{pmatrix}, \tag{C.27}$$

$$b = \begin{pmatrix} f_0 z_0^r & f_1 z_1^r & \cdots & f_{2r-1} z_{2r-1}^r \end{pmatrix}, \tag{C.28}$$

$$z = \begin{pmatrix} p_0 & p_1 & \cdots & p_{r-1} & q_0 & q_1 & \cdots & q_{r-1} \end{pmatrix}, \tag{C.29}$$

behaves badly and must be solved using multiple precision arithmetic. To solve these equations we used the Python mpmath package from Symbolic Python for development and the BOOST libraries (which in turn used the GMP library) with a Gaussian elimination algorithm with pivoting to solve the equation using OpenMP.

The Padé Approximation works well for the local $d$ level Greens functions. Without exploiting symmetries the method is not well suited for $\lim_{\omega\to 0} \chi(\omega)/\omega$ calculations as it is not guaranteed that the curves will be antisymmetric. If the symmetry is enforced by setting the imaginary part of $f(i\omega_n)$ to zero, a similar behavior occurs as with the other approaches. To achieve linear behavior one can use unreliable few points for the approximation which has a similar effect as a large broadening. But this behavior hints to a problem within the NRG method. To find further proof, Osolin and Žitko [121] looked at the cumulant function of the spin susceptibility

$$C(x) = \int_0^x \mathrm{Im}(\langle\langle S_z, S_z \rangle\rangle(\omega))\, \mathrm{d}\omega\,. \tag{C.30}$$

It did not fulfill the expected quadratic behavior at high temperatures despite being a quantity that is independent of any broadening or fitting.

### C.2.4 Possible Error Source

We will now take a closer look into the errors leading to this badly defined behavior at low frequencies. The energies provided by the NRG are a good

description of the real energies at their energy scale. To have an estimate for the error we look at the perturbation added in each shell:

$$H_{n+1} = H_n + \underbrace{t_n(f^\dagger_{\sigma,n} f_{\sigma,n+1} + f^\dagger_{\sigma,n+1} f_{\sigma,n})}_{t_n V_n}. \tag{C.31}$$

Standard perturbation theory states the the correction to the energies will be

$$E^1_m = t_n \langle m^0 | V_n | m^0 \rangle. \tag{C.32}$$

The degenerate energies will split with a magnitude of the order of $t_n$.

Due to the symmetry of the problem the discussion will assume that $\omega > 0$ therefore $E_m > E_n$. First we will consider the case of frequencies higher than the temperatures $\omega \gg T$. The spectral function generally reads

$$\mathcal{A}_{\mathrm{A,B}}(\omega) = \delta(\omega - (E_m - E_n))(\mathrm{e}^{-\beta E_m} \pm \mathrm{e}^{-\beta E_n}) A_{m,n} B_{n,m} \tag{C.33}$$

$$= \delta(\omega - (E_m - E_n))\mathrm{e}^{-\beta E_n}(\mathrm{e}^{-\beta(E_m - E_n)} \pm 1) A_{m,n} B_{n,m}, \tag{C.34}$$

as $\omega \gg T$ the energies will be restricted by

$$\beta(E_m - E_n) \gg 1 \tag{C.35}$$

$$\beta E_m \gg 1 + \beta E_n. \tag{C.36}$$

Only energy differences will contribute that have a low energy state $\beta E_n < 1$ (Equation (C.34)) and an energy state $\beta E_m \gg 1$ (Equation (C.36)). In the FDM scheme only discarded-discarded, kept-discarded and discarded-kept state combination contribute. Therefore these differences will be a kept-discarded or discarded-kept combination. Taking the difference $E_m - E_n$ is therefore unproblematic because the error of order $t_n$ will usually be small compared to the difference.

For frequencies equal to or lower than the temperature $\omega \lesssim T$, energies that are close to each other (in terms of the relevant perturbation $t_n$) can contribute as the restriction of Equation (C.36) no longer holds. In these cases the error on the energy difference may be larger than the energy scale one is interested in.

To provide evidence for this theory one can look at the spectral functions for different values of $\Lambda$. As $t_n \propto \Lambda^{-n/2}$ the splitting in the energies should be reduced by $\sqrt{\Lambda_1/\Lambda_2}$. This factor should also predict the difference in frequency for the irregular behavior to occur. Figure C.8 compares the local level spectral function for two different values of $\Lambda$. The expected difference in the frequency at which the irregularity occurs is quite well observed.

### Less than linear behaviour

Using this one can explain why Osolin and Žitko [121] can not find the quadratic behavior in the cumulant. The Lehmann representation for susceptibilities is represented by a Bosonic Greens function. Its imaginary part

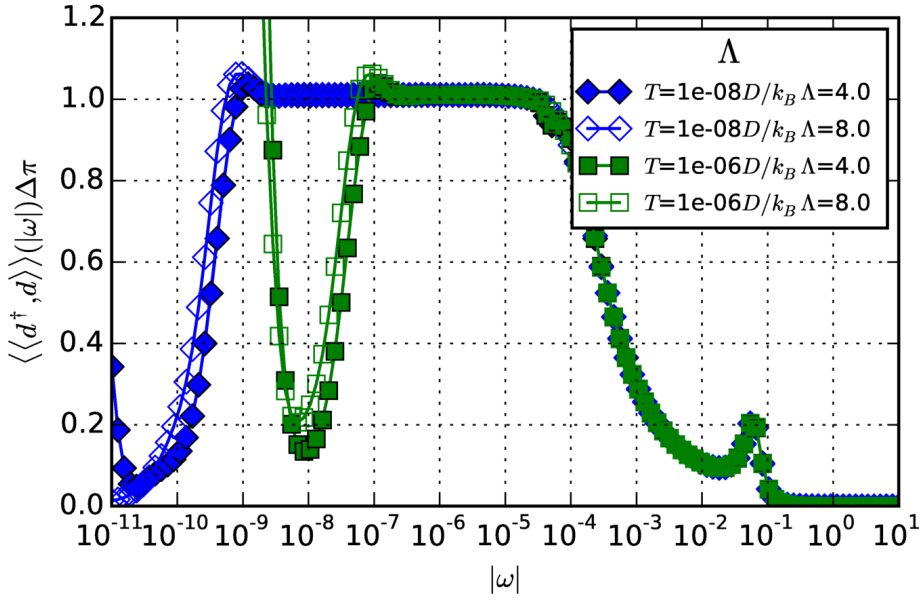


*Figure C.8: Spectral function at several temperatures. Comparing the naive Gaussian Kernel with $\sigma = 0.1|E_n - E_m|$ for two different $\Lambda$. The relative distance between the two curves, when the method breaks down, is approximately $\sqrt{\Lambda_1/\Lambda_2} = \sqrt{2}$.*

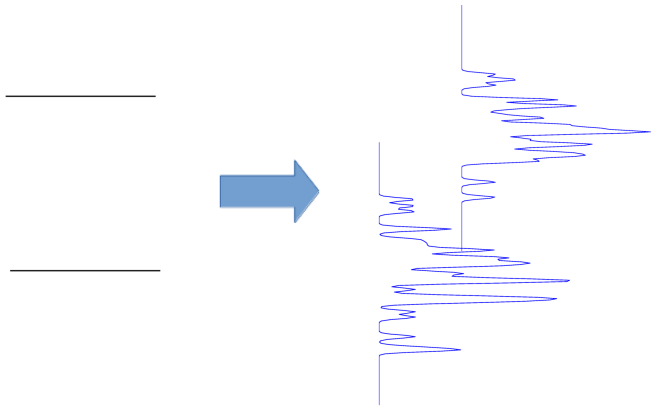

*Figure C.9: The left side should display the energy levels given by the NRG. The right side is a possible splitting if the state was not discarded. There is an overlap that might contribute to the zero frequency part of a spectral function that is lost due to the bad resolution.*

is given by

$$\mathcal{A}_{\mathrm{A,B}}(\omega) = \pi\delta(\omega - (E_m - E_n))(\mathrm{e}^{-\beta E_m} - \mathrm{e}^{-\beta E_n})A_{m,n}B_{n,m}. \tag{C.37}$$

In lower shells (with $E_n \ll T$) the Boltzmann factors are equal to one and therefore cancel out. Higher shells with $E_n \gg T$ will describe the high frequency range. Only shells containing discarded states of order $E_n \approx T$ will shape the zero frequency behavior. Figure C.9 shows a possible explanation for the less than linear behavior. The energies will split into energies that partly lie closer to each other and therefore contributing to the zero frequency part. But this overlap is missing in the energies provided by the NRG. The obvious choice to broaden every energy depending proportional to the perturbation $\sigma_{m,n} \propto t_N$ is too sensitive to the proportionality factor and does not yield any consistent results.

### Energy shift

Lastly we look into the effect of the splitting on the Boltzmann factors. As will be mentioned in Appendix D the splitting of the energies leads to an effective energy drop in the Boltzmann factors. Applying this shift to the Boltzmann factors did not change the behavior of the curves. This approach on the other hand had another surprising outcome. It can be used to make Green's functions calculations on the whole spectrum of discarded states without the need of the FDM, as shown in Appendix D.

# Appendix D

# Alternative to FDM

A different approach of how to use the full set of discarded states to calculate a Green's function will be shown here. We will see that it is possible to replace the reduced full density matrix by simple diagonal matrix. It will only contain Boltzmann factors that have a shift in the energy. The idea is that an energy at shell $n$ will split into more states in shell $n+1$. These energies are a good approximation at energies that are higher than the corresponding hopping term $t_n$. The corresponding Boltzmann factors on the other hand may vary largely for low temperatures. A simple example demonstrates this. When you consider a spinless 2 site model where the two sites are connected via a hopping term, the energies will split into

$$4 \times E = 0 \rightarrow \begin{cases} E &= t \\ 2 \times E &= 0 \\ E &= -t \end{cases} \tag{D.1}$$

The partition function $Z$ therefore will either be $Z = 4$ or

$$Z = 2 + \mathrm{e}^{-\beta t} + \mathrm{e}^{\beta t} > 4. \tag{D.2}$$

To negate this difference one could lower the energies of the unperturbed system slightly by an energy $E^n_{\text{shift}}$ so the partition functions become equal. In the NRG scheme the kept states of a shell will split into all states in the next shell. Therefore we shift the energies so that

$$\mathrm{e}^{-\beta E^n_{\text{shift}}} Z_{\text{kept},n} = Z_{n+1}, \tag{D.3}$$

where $Z_{\text{kept},N}$ is the sum of the Boltzmann factors of the kept states of shell $N$. This shift is then applied to all Boltzmann factors of shell $n$ and the next shell $n-1$ can be reweighted. The energies shifts are themselves depending on the temperature.

When using this method the degeneracy factor $n_e^{N-n}$ and energy difference to the ground state $E^n_{GS} = E^n_0 - E^N_0$ can be ignored in the calculation

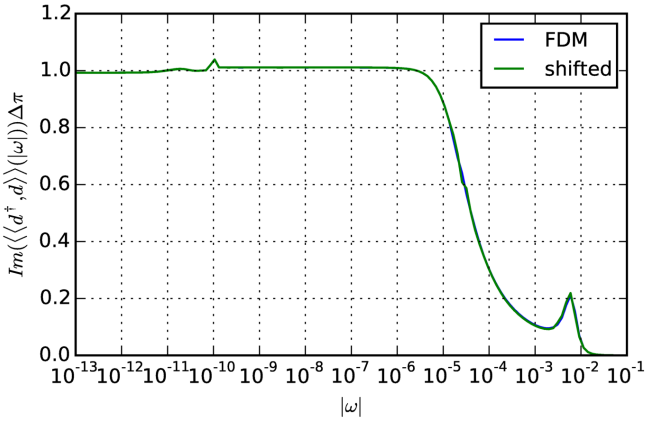


*Figure D.1: The comparison between the established FDM curves and the curves calculated without FDM but with an effective energy shift do not show significant differences. The used NRG parameter were 1-channel,* $\Lambda = 8$, $n_z = 16$, $\Delta = 10^{-3}D$, $U = 12\Delta$, $\varepsilon_d = -\frac{1}{2}U$, $e_C = 15$.

as they automatically are included in $E^n_{\text{shift}}$. In Chapter 2.6 we noted that the approximation

$$\mathrm{e}^{-\beta H}|k_n\rangle = \mathrm{e}^{-\beta E^n_k}|k_n\rangle$$

is not valid, therefore the full density matrix was introduced to relate different shells. The results suggest that these relations can be incorporated by the introduced energy shift. Using the nomenclature of Chapter 2.6 the simplified method to calculate the Green's function or spectral function therefore is $\mathrm{G}_{A,B}(\omega) = \mathrm{G}^I_{A,B}(\omega) + \mathrm{G}^{II}_{A,B}(\omega)$, where

$$\mathrm{G}^I_{A,B}(\omega) = \sum_n \frac{\mathrm{e}^{-\beta E^n_{\text{shift}}}}{Z'} \sum_{l,x} \frac{\mathrm{e}^{-\beta E^n_l} \pm \mathrm{e}^{-\beta E^n_x}}{\omega + E^n_l - E^n_x} A^n_{l,x} B^n_{x,l} \tag{D.4}$$

$$\mathrm{G}^{II}_{A,B}(\omega) = \sum_n \frac{\mathrm{e}^{-\beta E^n_{\text{shift}}}}{Z'} \sum_{x,l} \frac{\mathrm{e}^{-\beta E^n_x} \pm \mathrm{e}^{-\beta E^n_l}}{\omega + E^n_x - E^n_l} A^n_{x,l} B^n_{l,x}. \tag{D.5}$$

Here $x \in \{l, k\}$ and the partition function $Z' = \sum_n \mathrm{e}^{-\beta E^n_{\text{shift}}} \sum_l \mathrm{e}^{-\beta E^n_l}$ was calculated with respect to the shifted energies.

A comparison between the FDM method and this simplified version can be seen in Figure D.1. There are no significant differences between both methods. Further the method avoids the matrix multiplication and can therefore be evaluated faster.

# Appendix E

# Alternative Green's function

The target of this section is to derive a formula for the spectral function in the Lehmann-representation. We will use the fact that the discarded states of each iteration step (plus the kept states of the last iteration) form a complete basis set. The complete set has the form

$$\mathbb{I} = \sum_{n=n_c}^{N} \sum_{\{e\}_{n\to N}} \sum_{l_n} |e_N\rangle \dots |e_{n+1}\rangle |l_n\rangle\langle l_n| \langle e_{n+1}| \dots \langle e_N|, \tag{E.1}$$

where $n_c$ denotes the first shell where a cut-off is used and $N$ the number of iterations. $|e_n\rangle$ are the environment that are not yet coupled to the impurity. $\sum_{\{e\}_{n\to N}}$ is short for $\sum_{e_{n+1}} \cdots \sum_{e_N}$, the sum over all environment states. Further the discarded states of iteration $n$ will be called $l_n$ and the kept states $k_n$ To simplify the derivation we assume that:

$$\begin{aligned} |l_n\rangle &= \sum_{k_{n-1},e_n} U_{k_{n-1},e_n\to l_n} |k_{n-1}\rangle |e_n\rangle \\ |k_n\rangle &= \sum_{k_{n-1},e_n} U_{k_{n-1},e_n\to k_n} |k_{n-1}\rangle |e_n\rangle. \end{aligned} \tag{E.2}$$

The Lehmann representation of the spectral function has the form:

$$G_{A,B}(\omega) = \sum_{m,n} \langle m|A|n\rangle\langle n|B|m\rangle \cdot (\mathrm{e}^{-\beta E_m} + \mathrm{e}^{-\beta E_n}) \cdot \delta(\omega - (E_m - E_n)) \tag{E.3}$$

$$\begin{aligned} = \sum_{n=n_c}^{N} \sum_{l_n} \sum_{\{e\}_{n\to N}} \sum_{m=n_c}^{N} \sum_{l'_m} \sum_{\{e'\}_{m\to N}} \times \\ \langle e_N| \dots \langle e_{n+1}|\langle l_n|A|l'_m\rangle |e'_{m+1}\rangle \dots |e'_N\rangle \times \\ \langle e'_N| \dots \langle e'_{m+1}|\langle l'_m|B|l_n\rangle |e_{n+1}\rangle \dots |e_N\rangle \times \\ (\mathrm{e}^{-\beta E_{l_n}} + \mathrm{e}^{-\beta E_{l'_m}}) \cdot \delta(\omega - (E_{l_n} - E_{l'_m})). \end{aligned} \tag{E.4}$$

We will split this sum into 3 parts. One containing $m = n$, a second one with $m > n$ and a last one with $m < n$. In the first part all environments can

be reduced to a factor $d^{N-n}$

$$G^1_{A,B}(\omega) = d^{N-n} \sum_{n=n_c}^{N} \sum_{l_n,l'_n} \langle l_n|A|l'_n\rangle\langle l'_n|B|l_n\rangle\times (\mathrm{e}^{-\beta E_{l_n}} + \mathrm{e}^{-\beta E_{l'_n}}) \cdot \delta(\omega - (E_{l_n} - E_{l'_n})). \tag{E.5}$$

In the second part only the environment variables $> m$ can be reduced to a factor

$$G^2_{A,B}(\omega) = d^{N-m} \sum_{m=n_c}^{N} \sum_{l'_m} \sum_{n=m+1}^{N} \sum_{\{e\}_{n\to m}} \sum_{l_n} \times \langle e_m|\ldots\langle e_{n+1}|\langle l_n|A|l'_m\rangle\langle l'_m|B|l_n\rangle|e_{n+1}\rangle\ldots|e_m\rangle\times (\mathrm{e}^{-\beta E_{l_n}} + \mathrm{e}^{-\beta E_{l'_m}}) \cdot \delta(\omega - (E_{l_n} - E_{l'_m})). \tag{E.6}$$

We transform the lower shell $(m)$ into the next higher shell

$$= d^{N-m} \sum_{m=n_c}^{N} \sum_{l'_m} \sum_{n=m+1}^{N} \sum_{\{e\}_{n\to m}} \sum_{l_n} \sum_{k^A_{m-1},e^A_m} \sum_{k^B_{m-1},e^B_m} \times \langle e_m|\ldots\langle e_{n+1}|\langle l_n|AU_{k^A_{m-1},e^A_m\to l'_m}|k^A_{m-1}\rangle|e^A_m\rangle\times \langle e^B_m|\langle k^B_m|U_{k^B_{m-1},e^B_m\to l'_m}B|l_n\rangle|e_{n+1}\rangle\ldots|e_m\rangle\times (\mathrm{e}^{-\beta E_{l_n}} + \mathrm{e}^{-\beta E_{l'_m}}) \cdot \delta(\omega - (E_{l_n} - E_{l'_m})), \tag{E.7}$$

$$= d^{N-m} \sum_{m=n_c}^{N} \sum_{l'_m} \sum_{n=m-1}^{N} \sum_{\{e\}_{n\to m+1}} \sum_{l_n} \sum_{k^A_{m-1}} \sum_{k^B_{m-1}} \sum_{e_m} \times \langle e_{m-1}|\ldots\langle e_{n+1}|\langle l_n|AU_{k^A_{m-1},e_m\to l'_m}|k^A_{m-1}\rangle\times \langle k^B_m|U_{k^B_{m-1},e_m\to l'_m}B|l_n\rangle|e_{n+1}\rangle\ldots|e_{m-1}\rangle\times (\mathrm{e}^{-\beta E_{l_n}} + \mathrm{e}^{-\beta E_{l'_m}}) \cdot \delta(\omega - (E_{l_n} - E_{l'_m})). \tag{E.8}$$

We continue to transform until we reach the $n$-th shell

$$= d^{N-m} \sum_{m=n_c}^{N} \sum_{l'_m} \sum_{n=m-1}^{N} \sum_{\{e\}_{n\to m}} \sum_{l_n} \sum_{k^A_{m-1}} \cdots \sum_{k^A_n} \sum_{k^B_{m-1}} \cdots \sum_{k^B_n} \times \langle l_n|AU_{k^A_{m-1},e_m\to l'_m}\ldots U_{k^A_n,e_{n+1}\to k^A_{n+1}}|k^A_n\rangle\times \langle k^B_n|U_{k^B_n,e_{n+1}\to k^B_{n+1}}\ldots U_{k^B_{m-1},e_m\to l'_m}B|l_n\rangle\times (\mathrm{e}^{-\beta E_{l_n}} + \mathrm{e}^{-\beta E_{l'_m}}) \cdot \delta(\omega - (E_{l_n} - E_{l'_m})). \tag{E.9}$$

To clarify what this means in term of matrix multiplications we will rename $\langle l_n|A|k^A_n\rangle =: A_{l_n,k^A_n}$, $\langle k^A_n|B|l_n\rangle =: B_{k^B_m,l_n}$, $U_{k^A_n,e_{n+1}\to k^A_{n+1}} =: U^{e_{n+1}}_{k^A_n,k^A_{n+1}}$ and

$(\mathrm{e}^{-\beta E_{l_n}} + \mathrm{e}^{-\beta E_{l'_m}}) \cdot \delta(\omega - (E_{l_n} - E_{l'_m})) =: F_{l_n,l'_m}(\omega)$ and reorder the transformations and sums

$$
\begin{aligned}
= \quad & d^{N-m} \sum_{m=n_c}^{N} \sum_{l'_m} \sum_{n=m-1}^{N} \sum_{l_n} \sum_{k^A_{m-1}} \cdots \sum_{k^A_n} \sum_{k^B_{m-1}} \cdots \sum_{k^B_n} \times \\
& A_{l_n,k^A_n} \sum_{e_{n+1}} (U^{e_{n+1}}_{k^A_n,k^A_{n+1}} \cdots \sum_{e_m} (U^{e_m}_{k^A_{m-1},l'_m} U^{e_m}_{k^B_{m-1},l'_m}) \ldots U^{e_{n+1}}_{k^B_n,k^B_{n+1}}) B_{k^B_m,l_n} F_{l_n,l'_m}(\omega).
\end{aligned}
\tag{E.10}
$$

For a specific lower shell state $l'_m$ we define $M^{1,l'_m}_{k^A_{m-1},k^B_{m-1}} := \sum_{e_m} U^{e_m}_{k^A_{m-1},l'_m} U^{e_m}_{k^B_{m-1},l'_m}$. This Matrix can be used to calculate the contributions to the Green's function for a shell difference $m - n = 1$. For the higher differences we can define new matrices $M^{m-n,l'_m}_{k^A_n,k^B_n} = \sum_{e_{n+1}} \sum_{k^A_{n+1}} U^{e_{n+1}}_{k^A_n,k^A_{n+1}} \sum_{k^B_{n+1}} M^{m-n-1,l'_m}_{k^A_{n+1},k^B_{n+1}} U^{e_{n+1}}_{k^B_n,k^B_{n+1}}$ recursively. This can be written in Matrix form as

$$
\underline{\underline{M}}^{m-n,l'_m} = \sum_{e_{n+1}} \underline{\underline{U}}^{n+1,e_{n+1}} \underline{\underline{M}}^{m-n-1,l'_m} \underline{\underline{U}}^{n+1,e_{n+1}\,\dagger}
$$

This leads to:

$$
G^2_{A,B}(\omega) = \quad d^{N-m} \sum_{m=n_c}^{N} \sum_{l'_m} \sum_{n=m-1}^{N} \sum_{l_n} \sum_{k^A_n} \sum_{k^B_n} A_{l_n,k^A_n} M^{m-n,l'_m}_{k^A_n,k^B_n} B_{k^B_m,l_n} F_{l_n,l'_m}(\omega).
\tag{E.11}
$$

For $G^3_{A,B}(\omega)$ we can use the same derivation except that the Operators $A$ and $B$ will interchanged

$$
G^3_{A,B}(\omega) = \quad d^{N-m} \sum_{m=n_c}^{N} \sum_{l'_m} \sum_{n=m-1}^{N} \sum_{l_n} \sum_{k^B_n} \sum_{k^A_n} B_{l_n,k^B_n} M^{m-n,l'_m}_{k^B_n,k^A_n} A_{k^A_m,l_n} F_{l_n,l'_m}(\omega).
\tag{E.12}
$$

This method was not implemented as it seemed time intensive and not promising to improve any problems discussed in Appendix C.

# Appendix F

# Linear response for thermoelectric properties

In this section we will touch briefly on the derivation for the conductance formula used in Chapter 7 as well as extending this method to all thermoelectric properties for future calculations. Following Mahan [43], for the energy current $I_E$ and the particle current $I_C$ the linear equations are given by

$$I_C = -M^{(11)}\left[\frac{e}{T}\nabla V + \nabla\left(\frac{\mu}{T}\right)\right] + M^{(12)}\nabla\left(\frac{1}{T}\right) \tag{F.1}$$

$$I_E = -M^{(21)}\left[\frac{e}{T}\nabla V + \nabla\left(\frac{\mu}{T}\right)\right] + M^{(22)}\nabla\left(\frac{1}{T}\right), \tag{F.2}$$

where $M^{(12)} = M^{(21)}$. The coefficients $M^{(ij)}$ can be calculated as

$$M^{(ij)} = \pi \sum_{n,m} \mathrm{e}^{-\beta E_n}\langle n|I_i|m\rangle\langle m|I_j|n\rangle\delta(E_n - E_m), \tag{F.3}$$

where we defined $I_1 = I_C$ and $I_2 = I_E$. From these coefficients the thermoelectric properties, the conductance $G$, the Seebeck coefficient $S$ and the thermal conductance $\kappa$, can be calculated:

$$G = \frac{e^2}{T}M^{(11)} \tag{F.4}$$

$$S = \frac{1}{eT}\left(\frac{M^{(12)}}{M^{(11)}} - \mu\right) \tag{F.5}$$

$$\kappa = \frac{1}{T^2}\left(M^{(22)} - \frac{{M^{(12)}}^2}{M^{(11)}}\right). \tag{F.6}$$

The formula used in Chapter 7 is equivalent to Equation (F.4). In the following sections we will calculate the needed current operators for the Anderson model with conduction electron screening.

## F.1 Electrical current

The conductance is the response of the current to the voltage. The voltage introduces an energy difference in between the bands $-e\,\mathrm{d}V\,(\lambda N_L - (1-\lambda)N_R)$. If the hybridization of the two leads is proportional to each other, the particle current can be expressed as [108]:

$$I_C = \left(\lambda' \dot{N}_L - (1-\lambda')\dot{N}_R\right), \tag{F.7}$$

where

$$\langle \dot{N}_\alpha \rangle = \frac{i}{\hbar}\langle [H, N_\alpha] \rangle \tag{F.8}$$

$$= \frac{i}{\hbar}\langle \left[H_{hyb} + H_{screen}, N_\alpha\right] \rangle. \tag{F.9}$$

In case of the conductance only $[H_{hyb}, N_\alpha]$ remains.

$$\left[H_{hyb}, N_\alpha\right] = \sum_{\sigma,i} t_{0,\alpha,i}\left(d^\dagger_{\sigma,i} f_{0,\alpha,\sigma} - f^\dagger_{0,\alpha,\sigma} d_{\sigma,i}\right), \tag{F.10}$$

where $f_{0,\alpha,\sigma} = \sum_k c_{k,\alpha,\sigma}$. The freedom in the factor $\lambda$ can be used to simplify the expression in the one-channel case.

## F.2 Energy current

For the energy current we define, similar to the electrical current:

$$I_E = \dot{E} = \frac{i}{\hbar}[H, E], \tag{F.11}$$

where

$$E = x' H_{\mathrm{Band},L} - (1-x') H_{\mathrm{Band},R}, \tag{F.12}$$

where $x$ and $x'$ can be any number between 1 and 0. This degree of freedom can be exploited in absence of a screening term. For the case that a screening term is added to the Hamiltonian it is no longer possible to reduce the model to a one-channel model that can be further simplified. To calculate these operators for the 2-channel case with screening we will define $H_{\mathrm{Band},\alpha}$ in terms of the tridiagonal Hamiltonian of the NRG calculation:

$$H_{\mathrm{Band},L} = \sum_{n,\sigma} t_{n,L}(f^\dagger_{n,\sigma,L} f_{n+1,\sigma,L} + \mathrm{h.c}) + \epsilon_{n,L} f^\dagger_{n,\sigma,L} f_{n,\sigma,L}. \tag{F.13}$$

The Hamiltonian is divided into it 4 parts $H = H_{\text{imp}} + H_{\text{hyb}} + H_{\text{screen}} + H_{\text{band}}$. The results of each term of the commutator in Equation (F.11) are:

$$[H_{\text{imp}}, H_{\text{Band},L}] = [H_{\text{Band}}, H_{\text{Band},L}] = 0 \tag{F.14}$$

$$\begin{aligned}
[H_{\text{hyb}}, H_{\text{Band},L}] &= \sum_\sigma \xi_{0,L} t_{0,L} [d_\sigma^\dagger f_{0,\sigma,L} + f_{0,\sigma,L}^\dagger d, f_{0,\sigma,L}^\dagger f_{1,\sigma,L} + f_{1,\sigma,L}^\dagger f_{0,\sigma,L}] \\
&\quad + \xi_{0,L}\epsilon_{0,L} [d_\sigma^\dagger f_{0,\sigma,L} + f_{0,\sigma,L}^\dagger d, f_{0,\sigma,L}^\dagger f_{0,\sigma,L}] \\
&= \sum_\sigma \xi_{0,L} t_{0,L} (d_\sigma^\dagger f_{0,\sigma,L} f_{0,\sigma,L}^\dagger f_{1,\sigma,L} + f_{0,\sigma,L}^\dagger d f_{1,\sigma,L}^\dagger f_{0,\sigma,L} \\
&\quad - f_{0,\sigma,L}^\dagger f_{1,\sigma,L} d_\sigma^\dagger f_{0,\sigma,L} - f_{1,\sigma,L}^\dagger f_{0,\sigma,L} f_{0,\sigma,L}^\dagger d) \\
&\quad + \xi_{0,L}\epsilon_{0,L} (d_\sigma^\dagger f_{0,\sigma,L} f_{0,\sigma,L}^\dagger f_{0,\sigma,L} - f_{0,\sigma,L}^\dagger f_{0,\sigma,L} f_{0,\sigma,L}^\dagger d) \\
&= \sum_\sigma \xi_{0,L} t_{0,L} (d^\dagger f_{1,\sigma,L} - f_{1,\sigma,L}^\dagger d) \\
&\quad + \xi_{0,L}\epsilon_{0,L} (d_\sigma^\dagger f_{0,\sigma,L} - f_{0,\sigma,L}^\dagger d)
\end{aligned} \tag{F.15}$$

$$\begin{aligned}
[H_{\text{screen}}, H_{\text{Band},L}] &= \sum_\sigma U_{dc} t_{0,L} (n_d - 1) [f_{0,\sigma,L}^\dagger f_{0,\sigma,L}, f_{0,\sigma,L}^\dagger f_{1,\sigma,L} + f_{1,\sigma,L}^\dagger f_{0,\sigma,L}] \\
&= \sum_\sigma U_{dc} t_{0,L} (n_d - 1) (f_{0,\sigma,L}^\dagger f_{0,\sigma,L} f_{0,\sigma,L}^\dagger f_{1,\sigma,L} - f_{1,\sigma,L}^\dagger f_{0,\sigma,L} f_{0,\sigma,L}^\dagger f_{0,\sigma,L}) \\
&= \sum_\sigma U_{dc} t_{0,L} (n_d - 1) (f_{0,\sigma,L}^\dagger f_{1,\sigma,L} - f_{1,\sigma,L}^\dagger f_{0,\sigma,L}).
\end{aligned} \tag{F.16}$$

All results are $S = 0$ operators, that can be computed within the NRG.

# Appendix G

# Thermodynamic Bethe Ansatz

## G.1 TBA Equations

Using the thermodynamic Bethe ansatz Kawakami and Okiji [66] and Tsvelick, Filyov and Wiegmann [123, 69, 55] solved the Anderson-Model analytically and provided details to of the numerical solution (published in Merker and Costi [54]). The thermodynamic Bethe Ansatz (TBA) produces a set of coupled integral equations describing the charge and spin excitations of the system:

$$\begin{aligned}
\epsilon(k) - T \cdot (s * \ln(f(\kappa_1))) \circ (g(k)) = \\
\epsilon_0(k) - T \cdot (s * \ln(f(\kappa_1'))) \circ (g(k)) \qquad \text{(G.1a)} \\
\kappa_n + T \cdot s * (\ln(f(\kappa_{n-1})) + \ln(f(\kappa_{n-1}))) = \\
\delta_{n,1} \cdot T \cdot \int_{-\infty}^{\infty} s(g(k) - \Lambda) \ln(f(\epsilon(k))) g'(k) \, \mathrm{d}k \qquad \text{(G.1b)} \\
\kappa_n' + T \cdot s * (\ln(f(\kappa_{n-1}')) + \ln(f(\kappa_{n-1}'))) = \\
\delta_{n,1} \cdot T \cdot \int_{-\infty}^{\infty} s(g(k) - \Lambda) \ln(f(-\epsilon(k))) g'(k) \, \mathrm{d}k \qquad \text{(G.1c)}
\end{aligned}$$

where

$$\begin{aligned}
g(k) &= \frac{(k - e_d - \frac{1}{2}U)^2}{2\Gamma \mathrm{U}}, \quad s(\Lambda) = \frac{1}{2\cosh(\pi\Lambda)}, \quad f(k) = \frac{1}{1 + \mathrm{e}^{k/T}} \\
R(x) &= \frac{1}{\pi} \int_0^{\infty} \frac{\cos(\omega x)}{1 + \mathrm{e}^{\omega}} \mathrm{d}\omega \\
\epsilon_0(k) &= k - e_d - \frac{1}{2}U + \int_{-\infty}^{\infty} R(g(k) - g(p)) p g'(p) \mathrm{d}p.
\end{aligned}$$

Here, $g'(x)$ marks the first derivative of $g(k)$ with respect to $k$, $*$ is the convolution and $\circ$ the composition of two functions. $\kappa_0$ and $\kappa_0'$ equal $-\infty$.

For $\lim n \to \infty$ the functions approach the values:

$$\lim_{n\to\infty} \kappa_n = n \cdot H, \qquad \lim_{n\to\infty} \kappa'_n = n \cdot (2e_d + U). \tag{G.2}$$

The thermodynamic potential $\Omega$ can be calculated via:

$$\Omega = T \int_{-\infty}^{\infty} \rho_0 \ln(f(-\epsilon(k)))\mathrm{d}k + T \int_{-\infty}^{\infty} \sigma_0 \ln(\kappa'_1(\Lambda))\mathrm{d}\Lambda + E_0. \tag{G.3}$$

The functions $\rho_0$ and $\sigma_0$ are given by:

$$\begin{aligned}
\Delta(k) &= \frac{\Gamma}{\pi(\Gamma + (k - e_d)^2)} \\
\sigma_0(\Lambda) &= \int_{-\infty}^{\infty} s(\Lambda - g(k))\Delta(k)\mathrm{d}k \\
\rho_0(k) &= \Delta(k) + g'(k) \int_{-\infty}^{\infty} R(g(k) - g(p))\Delta(p)\mathrm{d}p,
\end{aligned}$$

where $E_0$ is the ground state energy of the symmetric Anderson model see Kawakami and Okiji [66]. Note that the ground state energy is not needed for specific heat calculations. In this set of equations two mistakes where corrected from the paper of A.M. Tsvelick and P.B. Wiegmann [55]: First, a sign in equation G.1c was changed, and second, the boundary value for $\kappa'_n$ (see equation G.2) was doubled.

## G.2 Reformulations of the Equations

For the calculations we use a transform similar to T.A. Costi and G. Zaránd [124]. After substituting $\xi_n = \ln(1 + \mathrm{e}^{\kappa_n})$ we get the following coupled equations:

$$\xi_n(\Lambda) = \ln(1 + \exp(s * (\xi_{n-1}(\Lambda) + \xi_{n+1}(\Lambda)))), \qquad n > 1 \tag{G.4a}$$
$$\xi_1(\Lambda) = \ln(1 + \exp(s * (\xi_2(\Lambda) + I_1(\Lambda)))) \tag{G.4b}$$
$$\xi'_n(\Lambda) = \ln(1 + \exp(s * (\xi'_{n-1}(\Lambda) + \xi'_{n+1}(\Lambda)))), \qquad n > 1 \tag{G.4c}$$
$$\xi'_1(\Lambda) = \ln(1 + \exp(s * (\xi'_2(\Lambda) + I'_1(\Lambda)))) \tag{G.4d}$$
$$I_1(\Lambda) = \int_{-\infty}^{\infty} s(g(k) - \Lambda) \ln(f(-\epsilon(k)))g'(k)\,\mathrm{d}k \tag{G.4e}$$
$$I'_1(\Lambda) = \int_{-\infty}^{\infty} s(g(k) - \Lambda) \ln(f(\epsilon(k)))g'(k)\,\mathrm{d}k \tag{G.4f}$$
$$I(k) = (s * (\xi_1(\Lambda) - \xi'_1(\Lambda))) \circ (g(k)) \tag{G.4g}$$
$$e(k) = e_0(k) + T \cdot I(k). \tag{G.4h}$$

The dependence of these equations is depicted in figure G.1.

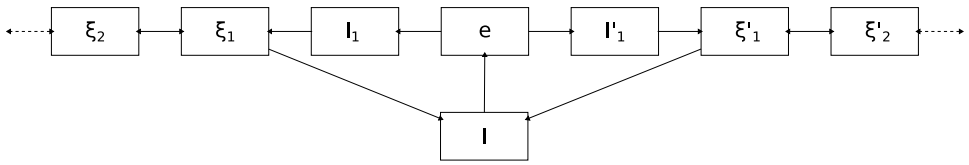


*Figure G.1: Diagram depicting the dependence between the equations.*

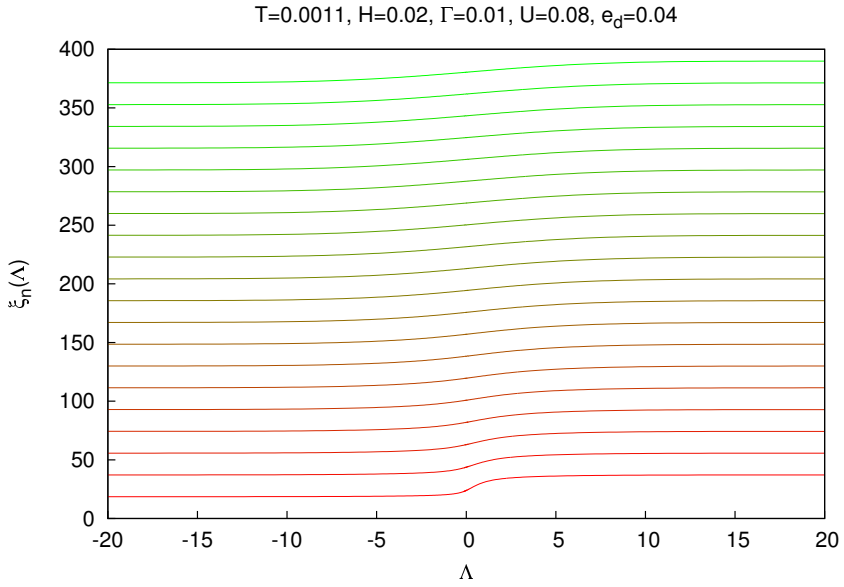


*Figure G.2: The figure shows a set of $\xi_n$ for the symmetric case ($e_d + \frac{1}{2}U = 0$) zoomed to range of $\Lambda = -20 \ldots 20$. The functions become smoother with higher $n$ due to the convolution with $s(x)$.*

## G.3 Boundary Conditions

For calculation purposes the equations $\xi_n$ and $\xi'_{n'}$ have to be truncated at some finite value $n = N$ and $n' = N'$. One has to calculate the functions at the truncation with care, to avoid wrong results. We use the same method as M. Takahashi and M. Shiroishi [125]. It is assumed that the function $s(x)$ can be approximated by $\frac{1}{2}\delta(x)$ for large $n$ or $n'$. This is justified as the functions become smoother in this region (see figure G.2). Rewritten for the Anderson Model and for $\xi_N$ and $\xi'_N$ the corresponding truncation functions are calculated by:

$$\xi_N = \ln\left(\left(\cosh(\frac{H}{2})\cdot\sqrt{2+\mathrm{e}^{\xi_{N-1}}}+\sqrt{1+\sinh^2(\frac{H}{2})\cdot[2+\mathrm{e}^{\xi_{N-1}}]}\right)^2\right) \tag{G.5a}$$

$$\xi'_{N'} = \ln\left(\left(\cosh(\frac{2e_d+U}{2})\cdot\sqrt{2+\mathrm{e}^{\xi'_{N'-1}}}+\sqrt{1+\sinh^2(\frac{2e_d+U}{2})\cdot[2+\mathrm{e}^{\xi'_{N'-1}}]}\right)^2\right). \tag{G.5b}$$

As a further check and to ensure the correct behaviour the TBA equations were calculated in the limits of $\Lambda, k \to \pm\infty$. As the functions are smooth in this limit one can assume $s(x) \to \frac{1}{2}\delta(x)$ and $\lim_{k\to\infty}\epsilon_0(k) = 2(k - e_d - \frac{1}{2}U)$, $\lim_{k\to-\infty}\epsilon_0(k) = 0$. This leads to an new set of coupled equations:

$$\lim_{\Lambda\to-\infty}$$

$$\xi_1 = \ln(1+\exp(\frac{1}{2}\xi_2))) \tag{G.6a}$$

$$\xi_n = \ln(1+\exp(\frac{1}{2}(\xi_{n-1}+\xi_{n+1}))) \tag{G.6b}$$

$$\xi'_1 = \ln(1+\exp(\frac{1}{2}\xi'_2)) \tag{G.6c}$$

$$\xi'_n = \ln(1+\exp(\frac{1}{2}(\xi'_{n-1}+\xi'_{n+1}))) \tag{G.6d}$$

$$\lim_{\Lambda\to\infty}$$

$$\xi_1 = \ln(1+\exp(\frac{1}{2}(\xi_2 - \ln(1+\exp(\frac{1}{2}\xi_1))))) \tag{G.6e}$$

$$\xi_n = \ln(1+\exp(\frac{1}{2}(\xi_{n-1}+\xi_{n+1}))) \tag{G.6f}$$

$$\xi'_1 = 0 \tag{G.6g}$$

$$\xi'_n = \ln(1+\exp(\frac{1}{2}(\xi'_{n-1}+\xi'_{n+1}))). \tag{G.6h}$$

$$\tag{G.6i}$$

The cut-off bounds $\xi_N$ and $\xi'_{N'}$ are calculated like in equation G.5. These boundaries where calculated using a modification of the Powell hybrid method [126].

## G.4 Numerical Details

For the calculations a logarithmic grid was used that is centered around $e_d+\frac{1}{2}U$. The start values of $\xi_n$ and $\xi'_{n'}$ were chosen to fit a tanh-function with boundary values fitting the boundaries of the $\xi_n$ and $\xi'_n$. The integrations were made by a continuous integrations over a spline interpolation of the grid. As the $\xi_n$ and $\xi'_{n'}$ only depend on their neighbors and not themselves, the function jump in a zigzag pattern. To smooth this behaviour 10% of the old iteration values are kept in each step. To represent mainly smooth functions as splines, $\xi_1$ and $\xi'_1$ are not stored, but $s*\xi_2$ and $s*\xi'_2$ respectively. The values of $\xi_1$ and $\xi'_1$ are then calculated from the stored values and from $I_1$ and $I'_1$. $N = N' = 20$ functions were used and iterated 200 times for the figures in this chapter. The growth-rate of the grid was 1.05 and consisted of 801 points. The mid 400 values lie in a range of $[-40, 40]$. After a certain temperature dependent cut-off ($\pm 40 \pm 40 \cdot T/T_0$) the boundary values were used instead of being calculated to ensure numerical stability. The thermodynamic potential was calculated in a range of $T_0 \cdot 10^{-3}$ to $T_0 \cdot 10^6$ on a logarithmic distance (factor $2^{1/8}$ as step width) where $T_0$ is defined as $T_0 = \sqrt{U\Gamma/2} \cdot \exp(-\frac{\pi U}{8\Gamma} + \frac{\pi\Gamma}{2U})$ which is similar to the Kondo temperature for the symmetric case. It is defined by the magnetic susceptibility at zero temperature $\chi_{imp}(T = 0) = \frac{(g\mu)^2}{4k_B T_0}$(see Hewson [62] p. 165).

## G.5 Results

From the thermodynamic potential we can calculate the entropy, the specific heat, the magnetization or the magnetic susceptibility. Non equilibrium terms as the thermopower are not accessible via the thermodynamic potential.

### G.5.1 Specific Heat

The specific heat $C(T)$ and the Entropy $S(T)$ can be calculated from the thermodynamic potential by:

$$S(T) = -\frac{\partial\Omega(T)}{\partial T} \tag{G.7}$$

$$C(T) = T \cdot \frac{\partial S(T)}{\partial T}. \tag{G.8}$$

The derivatives in equation G.7 and equation G.8 are calculated using discrete differences. Figure G.3 shows an example for the specific heat curve. The dashed blue curve shows the specific heat for the s-d model. In the local moment limit ($U \to \infty$) these curves coincide. Figure G.4 shows the variation of the gate voltage. In the mixed valence regime the Kondo effect breaks down. In figure G.5 the magnetic field is changed for the symmetric

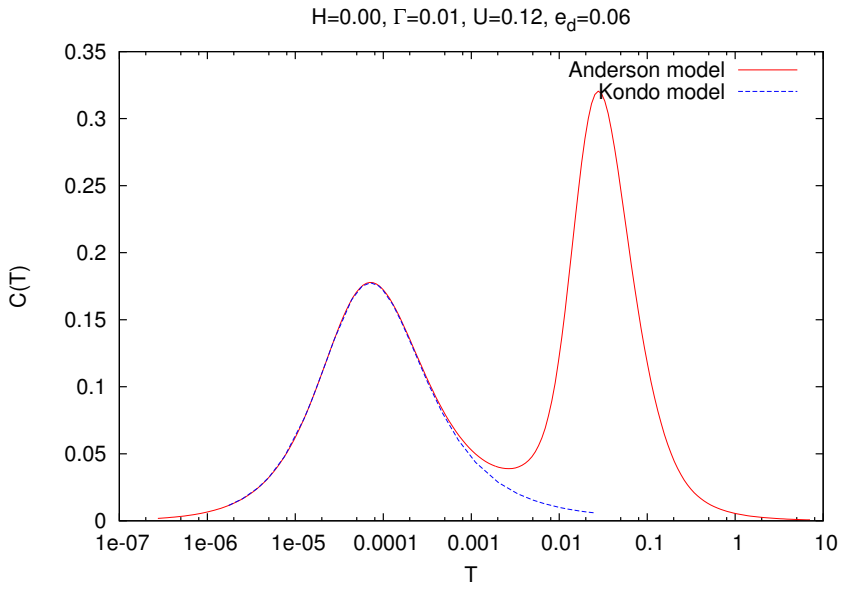


*Figure G.3: The figure shows the specific heat for the symmetric case ($e_d + \frac{1}{2}U = 0$). The dashed blue line corresponds the Kondo peak of the s-d model. For low temperatures these lines agree with each other.*

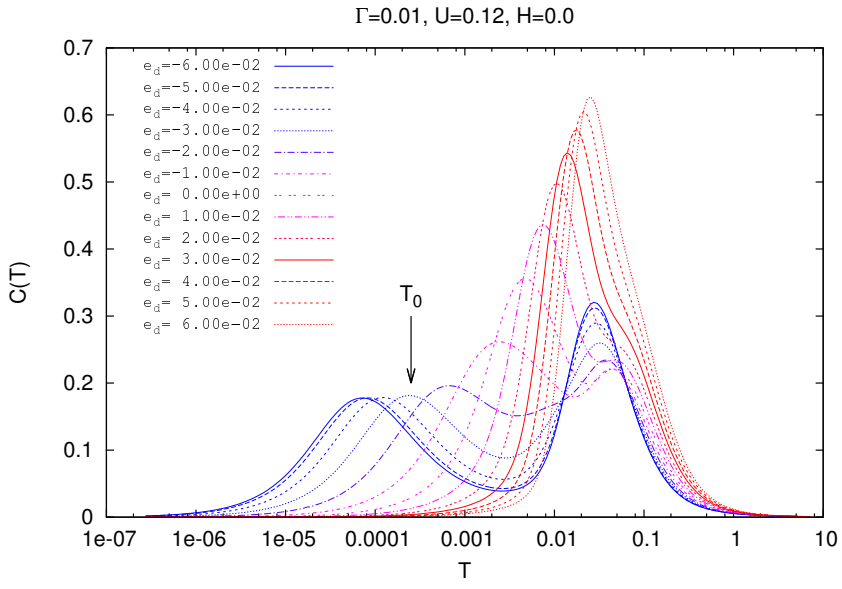


*Figure G.4: The plot shows the specific heat varying the gate voltage. Different colors correspond to different parameter regions. The blue lines from $e_d = -6\Gamma \cdots -2\Gamma$ shows the Kondo region. $e_d = -\Gamma \ldots \Gamma$ (pink) depicts the mixed valence region and values of $e_d > \Gamma$ (red) show the empty orbital region.*

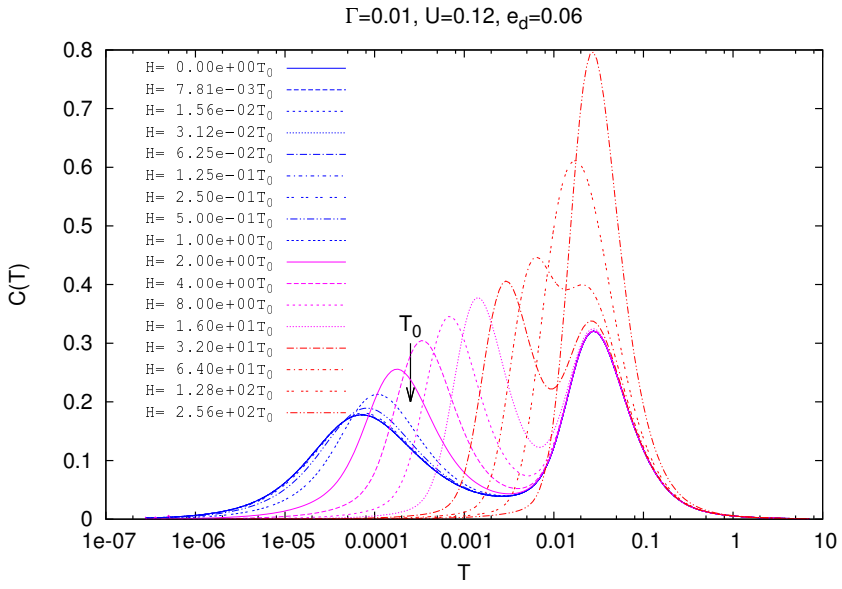


*Figure G.5: The plot shows the specific heat varying the magnetic field. After a certain magnetic field about the Kondo Temperature the two peaks merge and develop a shift like a Schottky type specific heat.*

Anderson model. For the symmetric model this model can be mapped to an equivalent asymmetric model with negative $U$.

# Bibliography


[1] D. Goldhaber-Gordon, J. Göres, M. A. Kastner, Hadas Shtrikman, D. Mahalu, and U. Meirav. From the Kondo Regime to the Mixed-Valence Regime in a Single-Electron Transistor. *Phys. Rev. Lett.*, 81:5225–5228, Dec 1998. doi: 10.1103/PhysRevLett.81.5225. URL `http://link.aps.org/doi/10.1103/PhysRevLett.81.5225`.

[2] S.M. Cronenwett, T.H. Oosterkamp, and L.P. Kouwenhoven. A tunable Kondo effect in quantum dots. *Science*, 281(5376):540–544, 1998.

[3] R. M. Potok, I. G. Rau, Hadas Shtrikman, Yuval Oreg, and D. Goldhaber-Gordon. Observation of the two-channel Kondo effect. *Nature*, 446(7132):167–171, Mar 2007. ISSN 0028-0836. doi: 10.1038/nature05556. URL `http://dx.doi.org/10.1038/nature05556`.

[4] Andrey V. Kretinin, Hadas Shtrikman, David Goldhaber-Gordon, Markus Hanl, Andreas Weichselbaum, Jan von Delft, Theo Costi, and Diana Mahalu. Spin-$\frac{1}{2}$ Kondo effect in an InAs nanowire quantum dot: Unitary limit, conductance scaling, and Zeeman splitting. *Phys. Rev. B*, 84:245316, Dec 2011. doi: 10.1103/PhysRevB.84.245316. URL `http://link.aps.org/doi/10.1103/PhysRevB.84.245316`.

[5] D. Goldhaber-Gordon, Hadas Shtrikman, D. Mahalu, David Abusch-Magder, U. Meirav, and M. A. Kastner. Kondo effect in a single-electron transistor. *Nature*, 391(6663):156–159, Jan 1998. ISSN 0028-0836. doi: 10.1038/34373. URL `http://dx.doi.org/10.1038/34373`.

[6] Sebastian Mehl and David P. DiVincenzo. Noise-protected gate for six-electron double-dot qubit. *Phys. Rev. B*, 88:161408, Oct 2013. doi: 10.1103/PhysRevB.88.161408. URL `http://link.aps.org/doi/10.1103/PhysRevB.88.161408`.

[7] Tuukka Hiltunen, Hendrik Bluhm, Sebastian Mehl, and Ari Harju. Charge-noise tolerant exchange gates of singlet-triplet qubits in asymmetric double quantum dots. *Phys. Rev. B*, 91:075301, Feb 2015. doi: 10.1103/PhysRevB.91.075301. URL `http://link.aps.org/doi/10.1103/PhysRevB.91.075301`.

[8] J. Park, A. N. Pasupathy, J. I. Goldsmith, C. Chang, Y. Yaish, J. R. Petta, M. Rinkoski, J. P. Sethna, H. D. Abruna, P. L. McEuen, and D. C. Ralph. Coulomb blockade and the Kondo effect in single-atom transistors. *NATURE*, 417(6890):722–725, JUN 13 2002. ISSN 0028-0836. doi: 10.1038/nature00791.

[9] Lam H. Yu, , and Douglas Natelson. The Kondo Effect in C60 Single-Molecule Transistors. *Nano Letters*, 4(1):79–83, 2004. doi: 10.1021/nl034893f. URL `http://dx.doi.org/10.1021/nl034893f`.

[10] Nicolas Roch, Serge Florens, Theo A. Costi, Wolfgang Wernsdorfer, and Franck Balestro. Observation of the Underscreened Kondo Effect in a Molecular Transistor. *Phys. Rev. Lett.*, 103:197202, Nov 2009. doi: 10.1103/PhysRevLett.103.197202. URL `http://link.aps.org/doi/10.1103/PhysRevLett.103.197202`.

[11] J. J. Parks, A. R. Champagne, T. A. Costi, W. W. Shum, A. N. Pasupathy, E. Neuscamman, S. Flores-Torres, P. S. Cornaglia, A. A. Aligia, C. A. Balseiro, G. K.-L. Chan, H. D. Abruña, and D. C. Ralph. Mechanical Control of Spin States in Spin-1 Molecules and the Underscreened Kondo Effect. *Science*, 328(5984):1370–1373, 2010. doi: 10.1126/science.1186874. URL `http://www.sciencemag.org/content/328/5984/1370.abstract`.

[12] G. D. Scott, D. Natelson, S. Kirchner, and E. Muñoz. Transport characterization of Kondo-correlated single-molecule devices. *Phys. Rev. B*, 87:241104, Jun 2013. doi: 10.1103/PhysRevB.87.241104. URL `http://link.aps.org/doi/10.1103/PhysRevB.87.241104`.

[13] Pramod Reddy, Sung-Yeon Jang, Rachel A. Segalman, and Arun Majumdar. Thermoelectricity in Molecular Junctions. *Science*, 315(5818):1568–1571, 2007. ISSN 0036-8075. doi: 10.1126/science.1137149. URL `http://science.sciencemag.org/content/315/5818/1568`.

[14] Kenneth G. Wilson. The renormalization group: Critical phenomena and the Kondo problem. *Rev. Mod. Phys.*, 47:773–840, Oct 1975. doi: 10.1103/RevModPhys.47.773. URL `http://link.aps.org/doi/10.1103/RevModPhys.47.773`.

[15] Jun Kondo. Resistance Minimum in Dilute Magnetic Alloys. *Progress of Theoretical Physics*, 32(1):37–49, 1964. doi: 10.1143/PTP.32.37. URL `http://ptp.oxfordjournals.org/content/32/1/37.abstract`.

[16] L. I. Glazman and M. E. Raikh. Resonant Kondo transparency of a barrier with quasilocal impurity states. *jETP Lett*, 47(8):452–455, 1988.

[17] Tai Kai Ng and Patrick A. Lee. On-Site Coulomb Repulsion and Resonant Tunneling. *Phys. Rev. Lett.*, 61:1768–1771, Oct 1988. doi: 10.1103/PhysRevLett.61.1768. URL `http://link.aps.org/doi/10.1103/PhysRevLett.61.1768`.

[18] Ralf Bulla, Theo A. Costi, and Thomas Pruschke. Numerical renormalization group method for quantum impurity systems. *Rev. Mod. Phys.*, 80:395–450, Apr 2008. doi: 10.1103/RevModPhys.80.395. URL `http://link.aps.org/doi/10.1103/RevModPhys.80.395`.

[19] M. Grobis, I. G. Rau, R. M. Potok, H. Shtrikman, and D. Goldhaber-Gordon. Universal Scaling in Nonequilibrium Transport through a Single Channel Kondo Dot. *Phys. Rev. Lett.*, 100:246601, Jun 2008. doi: 10.1103/PhysRevLett.100.246601. URL `http://link.aps.org/doi/10.1103/PhysRevLett.100.246601`.

[20] T. A. Costi and V. Zlatić. Thermoelectric transport through strongly correlated quantum dots. *Phys. Rev. B*, 81:235127, Jun 2010. doi: 10.1103/PhysRevB.81.235127. URL `http://link.aps.org/doi/10.1103/PhysRevB.81.235127`.

[21] H. von Löhneysen, J. Benz, T. Tomanic, C. Sürgers, C. Pleiderer, O. Stockert, L. Merker, and Costi T.A. unpublished.

[22] S. Andergassen, T. A. Costi, and V. Zlatić. Mechanism for large thermoelectric power in molecular quantum dots described by the negative-$U$ Anderson model. *Phys. Rev. B*, 84:241107, Dec 2011. doi: 10.1103/PhysRevB.84.241107. URL `http://link.aps.org/doi/10.1103/PhysRevB.84.241107`.

[23] V.L. Campo Jr and L.N. Oliveira. Alternative discretization in the numerical renormalization-group method. *Physical Review B*, 72(10): 104432, 2005. doi: 10.1103/PhysRevB.72.104432. URL `http://link.aps.org/doi/10.1103/PhysRevB.72.104432`.

[24] A. C. Seridonio, M. Yoshida, and L. N. Oliveira. Universal zero-bias conductance through a quantum wire side-coupled to a quantum dot. *Phys. Rev. B*, 80:235318, Dec 2009. doi: 10.1103/PhysRevB.80.235318. URL `http://link.aps.org/doi/10.1103/PhysRevB.80.235318`.

[25] T. A. Costi. Spectral density of the local Cu-O model. *Phys. Rev. B*, 55:6670–6673, Mar 1997. doi: 10.1103/PhysRevB.55.6670. URL `http://link.aps.org/doi/10.1103/PhysRevB.55.6670`.

[26] I. E. Perakis and C. M. Varma. Non-Fermi-liquid states of a magnetic ion in a metal: Particle-hole symmetric case. *Physical Review B*, 49

(13):9041, 1994. doi: 10.1103/PhysRevB.49.9041. URL http://link.aps.org/doi/10.1103/PhysRevB.49.9041.

[27] V. Schöps, V. Zlatić, and T. A. Costi. Thermoelectric effects in correlated quantum dots and molecules. *Journal of Physics: Conference Series*, 273(1):012155, 2011. URL http://stacks.iop.org/1742-6596/273/i=1/a=012155.

[28] David Hämmerle, Lukas Merker, T.A. Costi, and Sabine Andergassen. preprint, 2016.

[29] W.J. de Haas, J. de Boer, and G.J. van den Berg. The electrical resistance of gold, copper and lead at low temperatures. *Physica*, 1(7):1115 – 1124, 1934. ISSN 0031-8914. doi: http://dx.doi.org/10.1016/S0031-8914(34)80310-2. URL http://www.sciencedirect.com/science/article/pii/S0031891434803102.

[30] P. W. Anderson. Localized Magnetic States in Metals. *Phys. Rev.*, 124:41–53, Oct 1961. doi: 10.1103/PhysRev.124.41. URL http://link.aps.org/doi/10.1103/PhysRev.124.41.

[31] J. R. Schrieffer and P. A. Wolff. Relation between the Anderson and Kondo Hamiltonians. *Phys. Rev.*, 149:491–492, Sep 1966. doi: 10.1103/PhysRev.149.491. URL http://link.aps.org/doi/10.1103/PhysRev.149.491.

[32] H. R. Krishna-murthy, J. W. Wilkins, and K. G. Wilson. Renormalization-group approach to the Anderson model of dilute magnetic alloys. I. Static properties for the symmetric case. *Phys. Rev. B*, 21:1003–1043, Feb 1980. doi: 10.1103/PhysRevB.21.1003. URL http://link.aps.org/doi/10.1103/PhysRevB.21.1003.

[33] H. R. Krishna-murthy, J. W. Wilkins, and K. G. Wilson. Renormalization-group approach to the Anderson model of dilute magnetic alloys. II. Static properties for the asymmetric case. *Phys. Rev. B*, 21:1044–1083, Feb 1980. doi: 10.1103/PhysRevB.21.1044. URL http://link.aps.org/doi/10.1103/PhysRevB.21.1044.

[34] M. Hanl, A. Weichselbaum, T. A. Costi, F. Mallet, L. Saminadayar, C. Bäuerle, and J. von Delft. Iron impurities in gold and silver: Comparison of transport measurements to numerical renormalization group calculations exploiting non-Abelian symmetries. *Phys. Rev. B*, 88:075146, Aug 2013. doi: 10.1103/PhysRevB.88.075146. URL http://link.aps.org/doi/10.1103/PhysRevB.88.075146.

[35] R. Bulla, Th. Pruschke, and A. C. Hewson. Anderson impurity in pseudo-gap Fermi systems. *Journal of Physics: Condensed Matter*,

9(47):10463, 1997. URL http://stacks.iop.org/0953-8984/9/i=47/a=014.

[36] H. O. Frota and L. N. Oliveira. Photoemission spectroscopy for the spin-degenerate Anderson model. *Phys. Rev. B*, 33:7871–7874, Jun 1986. doi: 10.1103/PhysRevB.33.7871. URL http://link.aps.org/doi/10.1103/PhysRevB.33.7871.

[37] Wanda C. Oliveira and Luiz N. Oliveira. Generalized numerical renormalization-group method to calculate the thermodynamical properties of impurities in metals. *Phys. Rev. B*, 49:11986–11994, May 1994. doi: 10.1103/PhysRevB.49.11986. URL http://link.aps.org/doi/10.1103/PhysRevB.49.11986.

[38] M. Yoshida, M. A. Whitaker, and L. N. Oliveira. Renormalization-group calculation of excitation properties for impurity models. *Physical Review B*, 41(13):9403, 1990. doi: 10.1103/PhysRevB.41.9403. URL http://link.aps.org/doi/10.1103/PhysRevB.41.9403.

[39] L. Merker, S. Kirchner, E. Muñoz, and T. A. Costi. Conductance scaling in Kondo-correlated quantum dots: Role of level asymmetry and charging energy. *Phys. Rev. B*, 87:165132, Apr 2013. doi: 10.1103/PhysRevB.87.165132. URL http://link.aps.org/doi/10.1103/PhysRevB.87.165132.

[40] O. Sakai and Y. Kuramoto. Application of the numerical renormalization group method to the hubbard model in infinite dimensions. *Solid State Communications*, 89(4):307 – 311, 1994. ISSN 0038-1098. doi: http://dx.doi.org/10.1016/0038-1098(94)90589-4. URL http://www.sciencedirect.com/science/article/pii/0038109894905894.

[41] Rok Žitko and Thomas Pruschke. Energy resolution and discretization artifacts in the numerical renormalization group. *Phys. Rev. B*, 79:085106, Feb 2009. doi: 10.1103/PhysRevB.79.085106. URL http://link.aps.org/doi/10.1103/PhysRevB.79.085106.

[42] E. Müller-Hartmann. Einführung in die Vielteilchenphysik, 1977/78. URL www.thp.uni-koeln.de/thphysik/vtp.pdf. /Promotion/Papers/Background.

[43] Gerald D. Mahan. *Many Particle Physics*. Springer, 2000.

[44] W. Nolting. *Grundkurs: Theoretische Physik, Bd. 7: Viel-Teilchen-Theorie, 3*, volume 48. Springer, 1995.

[45] G. Czycholl. *Theoretische Festkörperphysik*. Springer Verlag, 2007. ISBN 3540747893.

[46] T. A. Costi and A. C. Hewson. Resistivity cross-over for the non-degenerate Anderson model. *Philosophical Magazine Part B*, 65(6): 1165–1170, 1992. doi: 10.1080/13642819208215080. URL http://dx.doi.org/10.1080/13642819208215080.

[47] Walter Hofstetter. Generalized Numerical Renormalization Group for Dynamical Quantities. *Phys. Rev. Lett.*, 85:1508–1511, Aug 2000. doi: 10.1103/PhysRevLett.85.1508. URL http://link.aps.org/doi/10.1103/PhysRevLett.85.1508.

[48] Frithjof B. Anders and Avraham Schiller. Real-Time Dynamics in Quantum-Impurity Systems: A Time-Dependent Numerical Renormalization-Group Approach. *Phys. Rev. Lett.*, 95:196801, Oct 2005. doi: 10.1103/PhysRevLett.95.196801. URL http://link.aps.org/doi/10.1103/PhysRevLett.95.196801.

[49] Robert Peters, Thomas Pruschke, and Frithjof B. Anders. Numerical renormalization group approach to Green's functions for quantum impurity models. *Phys. Rev. B*, 74:245114, Dec 2006. doi: 10.1103/PhysRevB.74.245114. URL http://link.aps.org/doi/10.1103/PhysRevB.74.245114.

[50] Andreas Weichselbaum and Jan von Delft. Sum-Rule Conserving Spectral Functions from the Numerical Renormalization Group. *Phys. Rev. Lett.*, 99:076402, Aug 2007. doi: 10.1103/PhysRevLett.99.076402. URL http://link.aps.org/doi/10.1103/PhysRevLett.99.076402.

[51] A. I. Tóth, C. P. Moca, Ö. Legeza, and G. Zaránd. Density matrix numerical renormalization group for non-Abelian symmetries. *Phys. Rev. B*, 78:245109, Dec 2008. doi: 10.1103/PhysRevB.78.245109. URL http://link.aps.org/doi/10.1103/PhysRevB.78.245109.

[52] Tie-Feng Fang, Ning-Hua Tong, Zhan Cao, Qing-Feng Sun, and Hong-Gang Luo. Spin susceptibility of Anderson impurities in arbitrary conduction bands. *Phys. Rev. B*, 92:155129, Oct 2015. doi: 10.1103/PhysRevB.92.155129. URL http://link.aps.org/doi/10.1103/PhysRevB.92.155129.

[53] Markus Hanl and Andreas Weichselbaum. Local susceptibility and Kondo scaling in the presence of finite bandwidth. *Phys. Rev. B*, 89: 075130, Feb 2014. doi: 10.1103/PhysRevB.89.075130. URL http://link.aps.org/doi/10.1103/PhysRevB.89.075130.

[54] L. Merker and T. A. Costi. Numerical renormalization group calculation of impurity internal energy and specific heat of quantum impurity models. *Phys. Rev. B*, 86:075150, Aug 2012. doi: 10.1103/PhysRevB.

86.075150. URL http://link.aps.org/doi/10.1103/PhysRevB.86.075150.

[55] A. M. Tsvelick and P. B. Wiegmann. Low-temperature properties of the asymmetric Anderson model (exact solution) II. *Physics Letters A*, 89(7):368–372, 1982. doi: 10.1016/0375-9601(82)90195-5.

[56] P. B. Wiegmann and A. M. Tsvelick. Exact solution of the Anderson model: I. *Journal of Physics C: Solid State Physics*, 16:2281, 1983. doi: 10.1088/0022-3719/16/12/017.

[57] A. Okiji and N. Kawakami. Thermodynamic properties of the Anderson model. *Physical review letters*, 50(15):1157–1159, 1983. doi: 10.1103/PhysRevLett.50.1157. URL http://link.aps.org/doi/10.1103/PhysRevLett.50.1157.

[58] V. T. Rajan, J. H. Lowenstein, and N. Andrei. Thermodynamics of the Kondo Model. *Phys. Rev. Lett.*, 49:497–500, Aug 1982. doi: 10.1103/PhysRevLett.49.497. URL http://link.aps.org/doi/10.1103/PhysRevLett.49.497.

[59] H.U. Desgranges. Thermodynamics of the n-channel Kondo problem (numerical solution). *Journal of Physics C: Solid State Physics*, 18:5481, 1985. doi: 10.1088/0022-3719/18/28/017.

[60] P. D. Sacramento and P. Schlottmann. Low-temperature properties of a two-level system interacting with conduction electrons: An application of the overcompensated multichannel Kondo model. *Phys. Rev. B*, 43:13294–13304, Jun 1991. doi: 10.1103/PhysRevB.43.13294. URL http://link.aps.org/doi/10.1103/PhysRevB.43.13294.

[61] C. J. Bolech and N. Andrei. Solution of the Two-Channel Anderson Impurity Model: Implications for the Heavy Fermion ube$_{13}$. *Phys. Rev. Lett.*, 88:237206, May 2002. doi: 10.1103/PhysRevLett.88.237206. URL http://link.aps.org/doi/10.1103/PhysRevLett.88.237206.

[62] A.C. Hewson. *The Kondo problem to heavy fermions*, volume 2. Cambridge Univ Pr, 1997. ISBN 0521599474.

[63] Georges Iche and A. Zawadowski. Partial cancellation in the electron-hole and electron-electron correlation in the symmetric anderson model. *Solid State Communications*, 10(11):1001 – 1004, 1972. ISSN 0038-1098. doi: http://dx.doi.org/10.1016/0038-1098(72)90882-4. URL http://www.sciencedirect.com/science/article/pii/0038109872908824.

[64] A. C. Hewson, J. Bauer, and W. Koller. Field dependent quasiparticles in a strongly correlated local system. *Phys. Rev. B*, 73:045117, Jan 2006. doi: 10.1103/PhysRevB.73.045117. URL http://link.aps.org/doi/10.1103/PhysRevB.73.045117.

[65] L. Merker, A. Weichselbaum, and T. A. Costi. Full density-matrix numerical renormalization group calculation of impurity susceptibility and specific heat of the Anderson impurity model. *Phys. Rev. B*, 86: 075153, Aug 2012. doi: 10.1103/PhysRevB.86.075153. URL http://link.aps.org/doi/10.1103/PhysRevB.86.075153.

[66] N. Kawakami and A. Okiji. Exact expression of the ground-state energy for the symmetric Anderson model. *Physics Letters A*, 86(9): 483–486, 1981. doi: 10.1016/0375-9601(81)90663-0.

[67] N. Kawakami and A. Okiji. Ground State of Anderson Hamiltonian. *Journal of the Physical Society of Japan*, 51(4):1145–1152, 1982. doi: 10.1143/JPSJ.51.1145. URL http://jpsj.ipap.jp/link?JPSJ/51/1145/.

[68] A. M. Tsvelick and P. B. Wiegmann. Exact solution of the Anderson model. II. Thermodynamic properties at finite temperatures. *Journal of Physics C: Solid State Physics*, 16:2321, 1983. doi: 10.1088/0022-3719/16/12/018.

[69] V. M. Filyov, A. M. Tsvelick, and P. B. Wiegmann. Low-temperature thernodynamics of the Anderson model. I. Symmetric case. *Physics Letters A*, 89(3):157–162, 1982. doi: 10.1016/0375-9601(82)90881-7. URL http://www.sciencedirect.com/science/article/pii/0375960182908817.

[70] S. C. Costa, C. A. Paula, V. L. Líbero, and L. N. Oliveira. Numerical renormalization-group computation of specific heats. *Physical Review, B: Condensed Matter*, 55(1):30–33, Jan 1997. doi: 10.1103/PhysRevB.55.30. URL http://link.aps.org/doi/10.1103/PhysRevB.55.30.

[71] A. Weichselbaum. Discarded weight and entanglement spectra in the numerical renormalization group. *Phys. Rev. B*, 84:125130, Sep 2011. doi: 10.1103/PhysRevB.84.125130. URL http://link.aps.org/doi/10.1103/PhysRevB.84.125130.

[72] T. A. Costi, A. C. Hewson, and V. Zlatic. Transport coefficients of the Anderson model via the numerical renormalization group. *Journal of Physics: Condensed Matter*, 6(13):2519, 1994. URL http://stacks.iop.org/0953-8984/6/i=13/a=013.

[73] F. D. M. Haldane. Scaling Theory of the Asymmetric Anderson Model. *Phys. Rev. Lett.*, 40:416–419, Feb 1978. doi: 10.1103/PhysRevLett.40.416. URL http://link.aps.org/doi/10.1103/PhysRevLett.40.416.

[74] P. B. Vigman and A. M. Finkelstein. Resonant-level model in the Kondo problem. *Sov. Phys. JETP*, 48:102–107, Jul 1978.

[75] F. Guinea, V. Hakim, and A. Muramatsu. Bosonization of a two-level system with dissipation. *Phys. Rev. B*, 32:4410–4418, Oct 1985. doi: 10.1103/PhysRevB.32.4410. URL http://link.aps.org/doi/10.1103/PhysRevB.32.4410.

[76] P. W. Anderson and A. M. Clogston. Antiferromagnetic Contribution to the Polarization of Free Electrons by Inner Shell Spins. *Bulletin of the American Physical Society*, 6(1):124, 1961.

[77] Robert Jördens, Niels Strohmaier, Kenneth Günter, Henning Moritz, and Tilman Esslinger. A Mott insulator of fermionic atoms in an optical lattice. *Nature*, 455(7210):204–207, 2008. URL http://dx.doi.org/10.1038/nature07244.

[78] U. Schneider, L. Hackermüller, S. Will, Th. Best, I. Bloch, T. A. Costi, R. W. Helmes, D. Rasch, and A. Rosch. Metallic and Insulating Phases of Repulsively Interacting Fermions in a 3D Optical Lattice. *Science*, 322(5907):1520–1525, 2008. doi: 10.1126/science.1165449. URL http://www.sciencemag.org/content/322/5907/1520.abstract.

[79] Gabriel Kotliar and Dieter Vollhardt. Strongly correlated materials: Insights from dynamical mean-field theory. *Physics Today*, 57(3):53–59, 2004. doi: http://dx.doi.org/10.1063/1.1712502. URL http://scitation.aip.org/content/aip/magazine/physicstoday/article/57/3/10.1063/1.1712502;jsessionid=8l6jsinmpe9tc.x-aip-live-03.

[80] Antoine Georges, Gabriel Kotliar, Werner Krauth, and Marcelo J. Rozenberg. Dynamical mean-field theory of strongly correlated fermion systems and the limit of infinite dimensions. *Rev. Mod. Phys.*, 68:13–125, Jan 1996. doi: 10.1103/RevModPhys.68.13. URL http://link.aps.org/doi/10.1103/RevModPhys.68.13.

[81] D. Vollhardt. Dynamical mean-field theory for correlated electrons. *Annalen der Physik*, 524(1):1–19, 2012. ISSN 1521-3889. doi: 10.1002/andp.201100250. URL http://dx.doi.org/10.1002/andp.201100250.

[82] Baoming Tang, Thereza Paiva, Ehsan Khatami, and Marcos Rigol. Short-Range Correlations and Cooling of Ultracold Fermions in the Honeycomb Lattice. *Phys. Rev. Lett.*, 109:205301, Nov 2012. doi: 10.1103/PhysRevLett.109.205301. URL http://link.aps.org/doi/10.1103/PhysRevLett.109.205301.

[83] L. Merker, S. Kirchner, E. Muñoz, and T. A. Costi. Reply to "Comment on 'Conductance scaling in Kondo-correlated quantum dots: Role of level asymmetry and charging energy"'. *Phys. Rev. B*, 90:077102, Aug 2014. doi: 10.1103/PhysRevB.90.077102. URL http://link.aps.org/doi/10.1103/PhysRevB.90.077102.

[84] Enrique Muñoz, C. J. Bolech, and Stefan Kirchner. Universal Out-of-Equilibrium Transport in Kondo-Correlated Quantum Dots: Renormalized Dual Fermions on the Keldysh Contour. *Phys. Rev. Lett.*, 110:016601, Jan 2013. doi: 10.1103/PhysRevLett.110.016601. URL http://link.aps.org/doi/10.1103/PhysRevLett.110.016601.

[85] A. C. Hewson. Renormalized perturbation expansions and Fermi liquid theory. *Phys. Rev. Lett.*, 70:4007–4010, Jun 1993. doi: 10.1103/PhysRevLett.70.4007. URL http://link.aps.org/doi/10.1103/PhysRevLett.70.4007.

[86] Akira Oguri. Fermi Liquid Theory for the Nonequilibrium Kondo Effect at Low Bias Voltages. *Journal of the Physical Society of Japan*, 74(1):110–117, 2005. doi: 10.1143/JPSJ.74.110. URL http://dx.doi.org/10.1143/JPSJ.74.110.

[87] A. N. Rubtsov, M. I. Katsnelson, and A. I. Lichtenstein. Dual fermion approach to nonlocal correlations in the Hubbard model. *Phys. Rev. B*, 77:033101, Jan 2008. doi: 10.1103/PhysRevB.77.033101. URL http://link.aps.org/doi/10.1103/PhysRevB.77.033101.

[88] H. Hafermann, C. Jung, S. Brener, M. I. Katsnelson, A. N. Rubtsov, and A. I. Lichtenstein. Superperturbation solver for quantum impurity models. *EPL (Europhysics Letters)*, 85(2):27007, 2009. URL http://stacks.iop.org/0295-5075/85/i=2/a=27007.

[89] C. Jung, A. Lieder, S. Brener, H. Hafermann, B. Baxevanis, A. Chudnovskiy, A.N. Rubtsov, M.I. Katsnelson, and A.I. Lichtenstein. Dual-fermion approach to non-equilibrium strongly correlated problems. *Annalen der Physik*, 524(1):49–61, 2012. ISSN 1521-3889. doi: 10.1002/andp.201100045. URL http://dx.doi.org/10.1002/andp.201100045.

[90] T. A. Costi and A. C. Hewson. Transport coefficients of the Anderson model. *Journal of Physics: Condensed Matter*, 5(30):L361, 1993. URL `http://stacks.iop.org/0953-8984/5/i=30/a=001`.

[91] M. Yoshida, A. C. Seridonio, and L. N. Oliveira. Universal zero-bias conductance for the single-electron transistor. *Phys. Rev. B*, 80: 235317, Dec 2009. doi: 10.1103/PhysRevB.80.235317. URL `http://link.aps.org/doi/10.1103/PhysRevB.80.235317`.

[92] Selman Hershfield, John H. Davies, and John W. Wilkins. Probing the Kondo resonance by resonant tunneling through an Anderson impurity. *Phys. Rev. Lett.*, 67:3720–3723, Dec 1991. doi: 10.1103/PhysRevLett.67.3720. URL `http://link.aps.org/doi/10.1103/PhysRevLett.67.3720`.

[93] Yigal Meir, Ned S. Wingreen, and Patrick A. Lee. Low-temperature transport through a quantum dot: The Anderson model out of equilibrium. *Phys. Rev. Lett.*, 70:2601–2604, Apr 1993. doi: 10.1103/PhysRevLett.70.2601. URL `http://link.aps.org/doi/10.1103/PhysRevLett.70.2601`.

[94] Osamu Sakai, Yukihiro Shimizu, and Tadao Kasuya. Single-Particle and Magnetic Excitation Spectra of Degenerate Anderson Model with Finite f–f Coulomb Interaction. *Journal of the Physical Society of Japan*, 58(10):3666–3678, 1989. doi: 10.1143/JPSJ.58.3666. URL `http://dx.doi.org/10.1143/JPSJ.58.3666`.

[95] R. Bulla, T. A. Costi, and D. Vollhardt. Finite-temperature numerical renormalization group study of the Mott transition. *Phys. Rev. B*, 64: 045103, Jun 2001. doi: 10.1103/PhysRevB.64.045103. URL `http://link.aps.org/doi/10.1103/PhysRevB.64.045103`.

[96] Frithjof B. Anders. Renormalization-group approach to spectral properties of the two-channel Anderson impurity model. *Phys. Rev. B*, 71:121101, Mar 2005. doi: 10.1103/PhysRevB.71.121101. URL `http://link.aps.org/doi/10.1103/PhysRevB.71.121101`.

[97] P. Nozières. A "fermi-liquid" description of the Kondo problem at low temperatures. *Journal of Low Temperature Physics*, 17(1-2):31–42, 1974. ISSN 0022-2291. doi: 10.1007/BF00654541. URL `http://dx.doi.org/10.1007/BF00654541`.

[98] A. A. Aligia. Comment on "Conductance scaling in Kondo-correlated quantum dots: Role of level asymmetry and charging energy". *Phys. Rev. B*, 90:077101, Aug 2014. doi: 10.1103/PhysRevB.90.077101. URL `http://link.aps.org/doi/10.1103/PhysRevB.90.077101`.

[99] Robert M. Konik, Hubert Saleur, and Andreas Ludwig. Transport in quantum dots from the integrability of the Anderson model. *Phys. Rev. B*, 66:125304, Sep 2002. doi: 10.1103/PhysRevB.66.125304. URL http://link.aps.org/doi/10.1103/PhysRevB.66.125304.

[100] Ayao Okiji and Norio Kawakami. Magnetic Properties of Anderson Model at Zero Temperature. *Journal of the Physical Society of Japan*, 51(10):3192–3196, 1982. doi: 10.1143/JPSJ.51.3192. URL http://dx.doi.org/10.1143/JPSJ.51.3192.

[101] Selman Hershfield, John H. Davies, and John W. Wilkins. Resonant tunneling through an Anderson impurity. I. Current in the symmetric model. *Phys. Rev. B*, 46:7046–7060, Sep 1992. doi: 10.1103/PhysRevB.46.7046. URL http://link.aps.org/doi/10.1103/PhysRevB.46.7046.

[102] T. Micklitz, A. Altland, T. A. Costi, and A. Rosch. Universal Dephasing Rate due to Diluted Kondo Impurities. *Phys. Rev. Lett.*, 96:226601, Jun 2006. doi: 10.1103/PhysRevLett.96.226601. URL http://link.aps.org/doi/10.1103/PhysRevLett.96.226601.

[103] V. Zlatić, T. A. Costi, A. C. Hewson, and B. R. Coles. Thermoelectric power of concentrated Kondo systems. *Phys. Rev. B*, 48:16152–16155, Dec 1993. doi: 10.1103/PhysRevB.48.16152. URL http://link.aps.org/doi/10.1103/PhysRevB.48.16152.

[104] A.M. Tsvelick and P.B. Wiegmann. Exact results in the theory of magnetic alloys. *Advances in Physics*, 32(4):453–713, 1983. doi: 10.1080/00018738300101581. URL http://dx.doi.org/10.1080/00018738300101581.

[105] M. Falkowski and A. Kowalczyk. Thermopower and thermal conductivity of Kondo lattice CeCu4Al. *Journal of Applied Physics*, 110 (4):043709, 2011. doi: http://dx.doi.org/10.1063/1.3624748. URL http://scitation.aip.org/content/aip/journal/jap/110/4/10.1063/1.3624748;jsessionid=7pjot0dkj0k3m.x-aip-live-06.

[106] Bing Dong and X L Lei. Effect of the Kondo correlation on the thermopower in a quantum dot. *Journal of Physics: Condensed Matter*, 14(45):11747, 2002. URL http://stacks.iop.org/0953-8984/14/i=45/a=316.

[107] Tae-Suk Kim and S. Hershfield. Thermoelectric effects of an Aharonov-Bohm interferometer with an embedded quantum dot in the Kondo regime. *Phys. Rev. B*, 67:165313, Apr 2003. doi: 10.1103/PhysRevB.67.165313. URL http://link.aps.org/doi/10.1103/PhysRevB.67.165313.

[108] Antti-Pekka Jauho, Ned S. Wingreen, and Yigal Meir. Time-dependent transport in interacting and noninteracting resonant-tunneling systems. *Phys. Rev. B*, 50:5528–5544, Aug 1994. doi: 10.1103/PhysRevB.50.5528. URL `http://link.aps.org/doi/10.1103/PhysRevB.50.5528`.

[109] H. J. Goldsmid. Conversion efficiency and figure-of-merit. *CRC Handbook of Thermoelectrics*, pages 19–25, 1995.

[110] Hilbert v. Löhneysen, Achim Rosch, Matthias Vojta, and Peter Wölfle. Fermi-liquid instabilities at magnetic quantum phase transitions. *Rev. Mod. Phys.*, 79:1015–1075, Aug 2007. doi: 10.1103/RevModPhys.79.1015. URL `http://link.aps.org/doi/10.1103/RevModPhys.79.1015`.

[111] H. Eskes and G. A. Sawatzky. Tendency towards Local Spin Compensation of Holes in the High-$T_c$ Copper Compounds. *Phys. Rev. Lett.*, 61:1415–1418, Sep 1988. doi: 10.1103/PhysRevLett.61.1415. URL `http://link.aps.org/doi/10.1103/PhysRevLett.61.1415`.

[112] O. Gunnarsson and K. Schönhammer. Electron spectroscopies for Ce compounds in the impurity model. *Phys. Rev. B*, 28:4315–4341, Oct 1983. doi: 10.1103/PhysRevB.28.4315. URL `http://link.aps.org/doi/10.1103/PhysRevB.28.4315`.

[113] Th. Pruschke and R. Bulla. Hund's coupling and the metal-insulator transition in the two-bandHubbard model. *The European Physical Journal B - Condensed Matter and Complex Systems*, 44(2):217–224, 2005. ISSN 1434-6036. doi: 10.1140/epjb/e2005-00117-4. URL `http://dx.doi.org/10.1140/epjb/e2005-00117-4`.

[114] Lorenzo De Leo and Michele Fabrizio. Spectral properties of a two-orbital Anderson impurity model across a non-Fermi-liquid fixed point. *Phys. Rev. B*, 69:245114, Jun 2004. doi: 10.1103/PhysRevB.69.245114. URL `http://link.aps.org/doi/10.1103/PhysRevB.69.245114`.

[115] Wataru Izumida, Osamu Sakai, and Yukihiro Shimizu. Many Body Effects on Electron Tunneling through Quantum Dots in an Aharonov-Bohm Circuit. *Journal of the Physical Society of Japan*, 66(3):717–726, 1997. doi: 10.1143/JPSJ.66.717. URL `http://dx.doi.org/10.1143/JPSJ.66.717`.

[116] C. Karrasch. Transport Through Correlated Quantum Dots - A Functional Renormalization Group Approach. Master's thesis, Universität Göttingen, November 2006.

[117] C. Karrasch, M. Pletyukhov, L. Borda, and V. Meden. Functional renormalization group study of the interacting resonant level model in and out of equilibrium. *Phys. Rev. B*, 81:125122, Mar 2010. doi: 10.1103/PhysRevB.81.125122. URL http://link.aps.org/doi/10.1103/PhysRevB.81.125122.

[118] Walter Metzner, Manfred Salmhofer, Carsten Honerkamp, Volker Meden, and Kurt Schönhammer. Functional renormalization group approach to correlated fermion systems. *Rev. Mod. Phys.*, 84:299–352, Mar 2012. doi: 10.1103/RevModPhys.84.299. URL http://link.aps.org/doi/10.1103/RevModPhys.84.299.

[119] William O. Straub. Efficient Computation of Clebsch-Gordan Coefficients. 2014. URL http://vixra.org/abs/1403.0263.

[120] Rok Zitko. *NRG Ljubljana*, 2007. URL http://nrgljubljana.ijs.si/manual_1.3.pdf.

[121] Žiga Osolin and Rok Žitko. Padé approximant approach for obtaining finite-temperature spectral functions of quantum impurity models using the numerical renormalization group technique. *Phys. Rev. B*, 87:245135, Jun 2013. doi: 10.1103/PhysRevB.87.245135. URL http://link.aps.org/doi/10.1103/PhysRevB.87.245135.

[122] Hiroyuki Shiba. The Korringa Relation for the Impurity Nuclear Spin-Lattice Relaxation in Dilute Kondo Alloys. *Progress of Theoretical Physics*, 54(4):967–981, 1975. doi: 10.1143/PTP.54.967. URL http://ptp.oxfordjournals.org/content/54/4/967.abstract.

[123] P. B. Wiegmann. Exact solution of the sd exchange model (Kondo problem). *Journal of Physics C: Solid State Physics*, 14:1463, 1981. doi: 10.1088/0022-3719/14/10/014. URL http://iopscience.iop.org/0022-3719/14/10/014.

[124] T. A. Costi and G. Zarand. Thermodynamics of the dissipative two-state system: A Bethe-ansatz study. *Physical Review B*, 59(19):12398, 1999. doi: 10.1103/PhysRevB.59.12398. URL http://link.aps.org/doi/10.1103/PhysRevB.59.12398.

[125] Minoru Takahashi and Masahiro Shiroishi. Thermodynamic Bethe ansatz equations of one-dimensional Hubbard model and high-temperature expansion. *Phys. Rev. B*, 65:165104, Apr 2002. doi: 10.1103/PhysRevB.65.165104. URL http://link.aps.org/doi/10.1103/PhysRevB.65.165104.

[126] The Numerical Algorithms Group (NAG) library. URL www.nag.com.